# Characterisation and Investigation of the Antimicrobial Properties of Graphene using Raman Spectroscopy

**Jennifer Ferguson**

Doctor of Philosophy

University of York

Physics

January 2020

# Abstract

The need for antimicrobial materials is more prevalent than ever given the current antimicrobial resistance crisis. Graphene is an excellent material candidate for use as an antibacterial agent, in places where stopping the spread of bacteria is of the utmost importance, such as within healthcare establishments and on equipment used during operations due to its ability to kill microbes. The mechanism via which graphene causes cell death is, however, not fully understood. This project utilises Raman spectroscopy for investigation into the biomolecular interactions between *Escherichia coli* (*E. coli*) and graphene formed via chemical vapour deposition (CVD).

Raman spectroscopy is a powerful tool for investigation into the metabolic state of microbes. Within this work Raman spectroscopy is also utilised for characterisation and analysis of three *E. coli* samples. Single point spectra and spectral averages at a population level display band variation pertaining to natural heterogeneity within biological samples, and due to different toxicity responses to desiccation and cell death. The level of characterisation of the samples is investigated through convergence of the statistical quantities, such as the standard error of the mean for increasing numbers of spectra in the average, to ensure full representation of the heterogeneity in the spectral average.

Raman spectroscopy is also utilised for characterisation of CVD graphene, which uncovers significant levels of heterogeneity both within and across samples. Bands shifts of up to 28 cm$^{-1}$ were recorded for bands in the Raman spectra of graphene, due to the presence of defects, such as grain boundaries and strain resultant from the CVD formation process. This level of heterogeneity could have serious repercussions for interactions of biological samples with graphene. Novel methods for determination of the level of characterisation and investigation of the level of heterogeneity are proposed within this work, with potential application to other systems.

# Declaration

I declare that this thesis is a presentation of original work and I am the sole author. This work has not previously been presented for an award at this, or any other, University. All sources are acknowledged as References.

# Acknowledgements

I would firstly like to thank both of my supervisors, Dr Yvette Hancock and Dr Marjan van der Woude. Their guidance and support throughout the years has been immeasurable in both time and quantity, and I am incredibly grateful to them both. Gabh raibh míle maith agaibh! To both of their research groups who helped throughout the years, especially within the biology lab for the constant support and help, which was never too much trouble. I would particularly like to thank Raquel and Andre, their help and training at the beginning of the PhD made the physics world seem a little less scary for a clueless mathematician! Also to Ioannis for all the help with the bacteria growth and around the lab. And to Marcus, for all the moral support through the mountains of analysis that we faced together!

Thanks to all my office pals, from all around the physics department, and to everyone who helped me make it through the last four years in one piece! Particularly to Razak, my neighbouring office friend for the entire four years, who always kept the positivity levels up. Also to Mike, for always being around to go to the pub with and for always taking the best care of Jeff, the most spoiled cat in York. Finally to Chris, for being one of the most dependable pals in physics.

Thanks to my family, to whom this thesis is dedicated. Particularly to my parents, whose support has been unwavering over the years and without whom this thesis would not have been possible. Thanks to my brother, Ciaran, for the many long discussions about physics and the struggles of PhD life, and to my sister, Fiona, for the much needed distraction from the physics world with fighting for the problems in the real world! Thank you for putting up with all me during this whole process!

Finally a special thanks to Steve, without whom I couldn't have made it through the past two years. His constant reassurance and support has made this thesis possible. Thank you for helping me stay sane through this whole process!

# Abbreviations

**A** adenine

**AMR** Antimicrobial Resistance

**BZ** Brillouin zone

**C** cytosine

**CFUs** colony forming units

**CVD** chemical vapour deposition

**Cyro-EM** cryo-electron microscopy

***E. coli*** *Escherichia coli*

***E. faecalis*** *Enterococcus faecalis*

***E. faecium*** *Enterococcus faecium*

**EM** electromagnetic

**FAs** fatty acids

**FWHM** full width at half maximum

**G** guanine

**GO** Graphene oxide

**GQDs** graphene quantum dots

**HCAI** Healthcare associated infections

**hMSCs** human mesenchymal stem cells

**HP35** chicken villin headpiece subdomain

**HPLC** high-performance liquid chromatography

**IM** inner membrane

**IPA** isopropyl alcohol

**LPS** lipopolysaccharides

**ME** micromechanically exfoliated

**NA** numerical aperture

**NMR** nuclear magnetic resonance

**OM** outer membrane

**OMPs** outer membrane proteins

**PCs** principal components

**PCA** principal component analysis

**PIR** peak intensity ratio

**PMMA** polymethyl methacrylate

**pSE** percent standard error of the mean

**RCF** relative centrifugal force

**ROS** reactive oxygen species

**rpm** revolutions per minute

***S. aureus*** *Staphylococcus aureus*

**2SD** second order standard deviation

**SE** standard error

**SEM** scanning electron microscopy

***S. epidermidis*** *Staphylococcus epidermidis*

**SERS** surfaced enhanced Raman spectroscopy

**SLG** single layer graphene

**SR** spatial resolution

**SWCNT** single-wall carbon nanotubes

**T** thymine

**U** uracil

**UTIs** urinary tract infections

# Contents

# List of Figures

# List of Tables

# 1

# Introduction

## 1.1 Overview

The development of new methods of bacterial containment and demise is more crucial than ever in order to combat the current Antimicrobial Resistance (AMR) crisis [1, 2, 3]. Increasing numbers of bacteria are becoming resistant to antibiotics, with new multi-drug resistant bacteria emerging around the world [4]. A report published in 2015 which analysed the effects of AMR on the population of people in the European Union and European Economic Area, estimated that 671,689 cases of antibiotic resistant bacterial infections occurred in 2015, resulting in 33,110 deaths [5], while it is estimated that globally AMR contributes to 700,000 deaths per year [6]. If the crisis continues along its current trajectory, it is estimated that by 2050, AMR will surpass cancer as the leading cause of death worldwide, and will be attributable to 10 million deaths per year compared with 8.2 million deaths from cancer [6].

The extensive overuse and misuse of antibiotics as medications, alongside the lack of development of new drugs and methods of containment are the main causes for the AMR crisis [1, 7]. For example, the overuse of antibiotics in animal food is a serious contributor. Antibiotics are used in animal feed to prevent the spread of bacteria, while also promoting an increase in the growth rates of animals, meaning more meat can be produced for a lesser number of animals [8]. This has resulted in many antibiotic resistant strains of bacteria emerging in the gut of animals [9]. A report published in 2005 found that significant amounts of antimicrobial resistant strains of *Enterococcus faecium* (*E. faecium*) were detected in farm animals, which were fed with feed containing the antibiotics quinupristin and dalfopristin over a five year period, with bacterial resistance rates of around 2% in beef cattle, 8% in dairy cattle, 21% in swine, 52% in turkey farms and 85% in chickens [9].

Overuse of antibiotics for human consumption is also a serious issue, with an increase of 65 % in the amount of antibiotics consumed between the years 2000 and 2015 [4, 10, 11]. This overuse of antibiotics can result in the bacteria evolving to achieve resistance. For instance, in the case of *Mycobacterium tuberculosis*, the pathogen responsible for tuberculosis, the bacteria have undergone chromosomal evolution, resulting in bacterial cells with this mutation being resistant to rifampicin and isoniazid, the antibiotics commonly used to treat tuberculosis [12]. Currently bacteria are evolving faster than new antibiotics are being developed [2]. Further contributing factors to the AMR crisis are rising world population and increasing urbanisation, with more than half of all humans living in cities [13], and more accessible global travel, helping to promote easier spread of microbes [14].

A serious issue for the spread of AMR bacteria is within healthcare associated establishments. Healthcare associated infections (HCAI) are an ever-increasing threat due to the growing numbers of people that hospitals are housing, allowing bacteria to spread more easily [15]. HCAIs are a particularly serious issue for low- and middle-income countries due to over-crowding in hospitals, misuse of limited resources and equipment, and lack of protocols to prevent the spread of bacteria [16, 17, 18]. The number of HCAIs in developing countries was found to be at least double the rate of infection compared with European countries, which is equivalent to 15.5 infections in every 100 patients [19]. *Escherichia coli* (*E. coli*) was noted to be among one of the ten most common pathogens to cause a HCAI, accounting for 10 % of 28,501 HCAIs reported among 25,384 patients from 463 hospitals in the US between 2006 and 2007 [20].

*E. coli* is studied in this project as a model bacterium. There are many different strains of *E. coli*, and while most are harmless, some can cause ailments, such as vomiting, diarrhoea, and urinary tract infections (UTIs) [21]. In the United States alone, *E. coli* is the cause of around 73,000 illnesses per year, resulting in around 61 deaths [21]. In the 2018 - 2019 report for the English Surveillance Programme for Antimicrobial Utilisation and Resistance by Public Health England, it was found that there was a 22 % increase in rate of bloodstream infections for all pathogens studied in the period from 2014 to 2018, and *E. coli* was found to be the most common cause of such infections [22].

The AMR crisis is becoming increasingly worse, with current options of antibacterial treatments limited and the sole reliance of bacterial demise continually being placed on antibiotic treatment alone [23]. For instance, a report published by Department of Health laid out a five year plan for the UK to combat AMR from 2013 to 2018, which focused primarily on the development of new antibiotics [24].

Kelly *et al.* published a report which, along with others, concluded that it is not be enough to rely solely on research into the development of new antibiotics, rather, a novel, multi-disciplinary approach is required to overcome this global crisis [3, 11, 25, 26]. Therefore, it is necessary to look for ways to contain and kill *E. coli* to avoid such infections particularly within healthcare settings; the application of an antimicrobial material in this setting could be paramount to ensure the demise of bacteria.

## 1.2 Properties of graphene

A material candidate that could assist in tackling the AMR crisis, and help to reduce the number of HCAIs is graphene. For example, a proposed application in this thesis is antimicrobial graphene coatings for application to surfaces and medical equipment

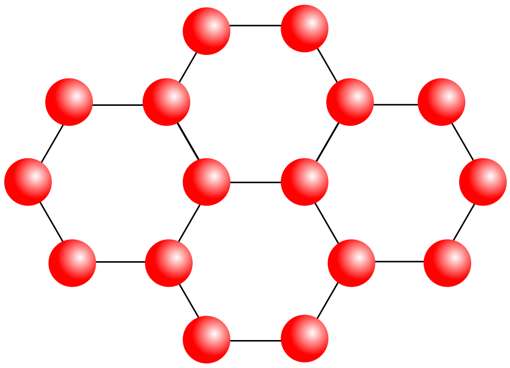

**Figure 1.1:** Honeycomb lattice structure of graphene. The red circles represent the carbon atoms.

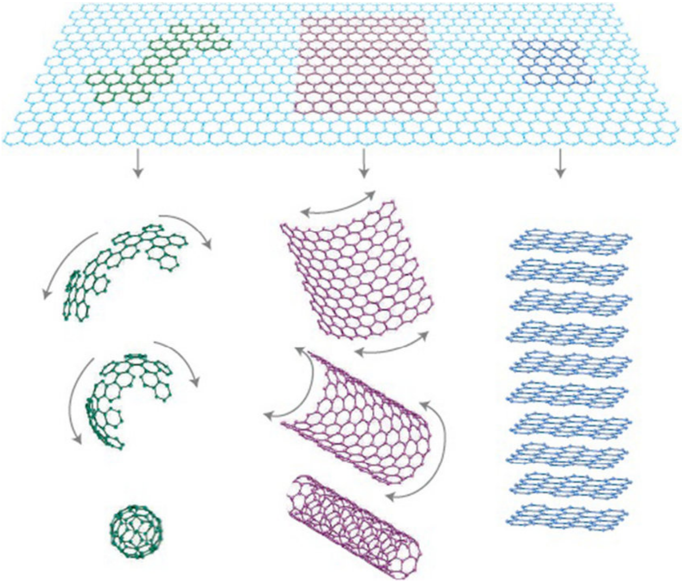

**Figure 1.2:** Image depicting the different sp$^2$ carbon allotrope formations that graphene comprises: wrapped into 0D fullerenes, rolled into 1D nanotubes or stacked into 3D graphite. Figure obtained from [27].

used during operations to reduce the number of infections, and to avoid additional financial burdens, which result from extra stays in hospitals due to AMR bacteria [23]. Other applications of graphene as an antimicrobial agent would include on food packaging, on food preparation surfaces and temporary wound dressings. Graphene could be critical in helping to reduce the number of infections and subsequent deaths by bacterial infections, its potential in the biomedical and healthcare industry is limitless. For example, graphene has been investigated for use as coating on catheters, which would help reduce UTIs, one of the leading causes of HCAIs [15, 28].

Graphene is a two-dimensional, $sp^2$-hybridised carbon allotrope, with carbon atoms arranged a honeycomb lattice structure (Figure 1.1) [27, 29]. It is the basis of other forms of carbon allotropes, and has been described as the "Mother of all graphitic forms", as it can be wrapped into 0D fullerenes, rolled into 1D nanotubes, and stacked to form 3D graphite (Figure 1.2) [27].

Before the isolation and experimental verification of a single layer of graphene in 2004 by Geim and Novoselov *et al.*, planar graphene was thought not to exist in the free state, as it was believed to be unstable when not in the form of a curved structure (Fig. 1.2) [27, 30]. Following this breakthrough, research into the properties of graphene accelerated at an unprecedented rate, the so-called 'graphene-explosion' [31].

It is the honeycomb lattice structure of graphene that gives rise to its band structure, which is attributable to graphenes unique properties [32]. The unit cell consists of two carbon atoms (Figure 1.3a), A and B, which are invariant under rotation of 120° around the lattice. Spaced 1.42 Å apart, the carbon atoms are located at the corners of the hexagons, where $a_1$ and $a_2$ are unit vectors (Fig. 1.3a) [32, 33, 34]. The Cartesian coordinates for the real space unit vectors $\vec{a}_1$ and $\vec{a}_2$ are defined as [32]

$$\vec{a}_1 = \left(\frac{\sqrt{3}}{2}a, \frac{a}{2}\right) \quad \vec{a}_2 = \left(\frac{\sqrt{3}}{2}a, -\frac{a}{2}\right)$$

The real space atom structure gives rise to the same symmetry in reciprocal space. The two atom basis corresponds to two inequivalent points in the Brillouin zone (BZ), K and K′, shown in Figure 1.3b [35]. The unit vectors $b_1$ and $b_2$ correspond

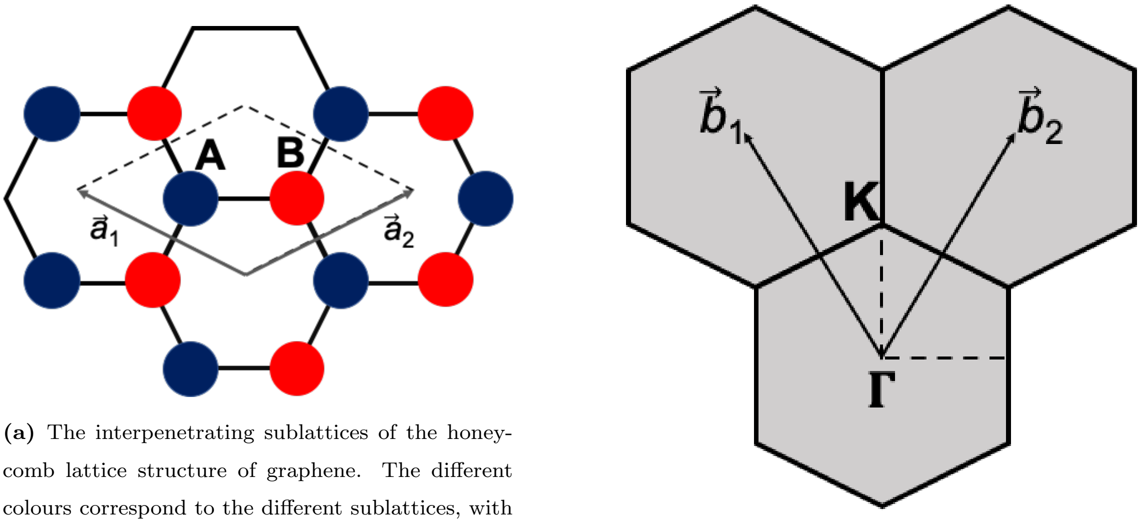

**(a)** The interpenetrating sublattices of the honeycomb lattice structure of graphene. The different colours correspond to the different sublattices, with one red and one blue atom being the basis of the two carbon atom unit cell. The carbon atoms are spaced 1.42 Å apart and are invariant under 120 ° rotation around the sublattice.

**(b)** The Brillouin zone (BZ) for SLG graphene, defined by the unit vectors $\vec{b}_1$ and $\vec{b}_2$. Points of high symmetry are labelled: Γ the zone center, M the mid point of the hexagon and K and K′ the BZ corners.

**Figure 1.3:** Graphene in real and reciprocal space.

to rotations of the $\vec{a}_1$ and $\vec{a}_2$ in real space of 30° respectively, and are defined as

$$\vec{b}_1 = \left( \frac{2\pi}{\sqrt{3}a}, \frac{2\pi}{a} \right) \quad \vec{b}_2 = \left( \frac{2\pi}{\sqrt{3}a}, -\frac{2\pi}{a} \right)$$

with a lattice constant of length $4\pi/\sqrt{3}a$ [32]. The points of high symmetry of the BZ are labelled on Figure 1.3b, those being Γ at the zone centre, the M point located in the middle of the hexagonal edges and the K and K′ points, the inequivalent points at the zone corners [36]. The lines along these points are also areas of high symmetry: $\Gamma K$ called $T$, $KM$ called $T'$ and $\Gamma M$ known as Σ [36].

Each carbon atom has one s orbital and three p orbitals. The s and two of the in-plane p orbitals of the carbon atoms are sp$^2$-hybridised in-plane via $\sigma$ bonds with neighbouring carbon atoms [34]. It is these bonds that are attributable to graphene's extreme mechanical strength [34].

Single layer pristine graphene is the strongest material tested to date. Graphene has a measured tensile strength of ∼125 GPa, compared with diamond which has an approximate tensile strength of 2800 MPa [37, 38]. Along with this extreme tensile strength, graphene is the thinnest and lightest material, therefore, such qualities have made it an excellent candidate for applications where strength and being lightweight are paramount, for example, for applications in the aerospace industry

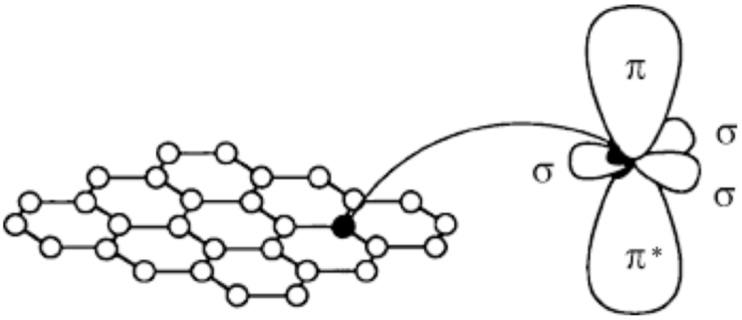

**Figure 1.4:** The bonding of the carbon atoms in graphene. The s-orbital and two of the in-plane p-orbitals of the carbon atoms form $sp^2$ hybridised in-plane $\sigma$ bonds with the neighbouring carbon atoms. The final p orbital of the carbon atoms, perpendicular to the molecular plane, forms the $\pi$ (valence) and $\pi^*$ (conduction) bands [34].

[37, 39].

The final p orbital of the carbon atoms, perpendicular to the molecular plane, forms the $\pi$ (valence) and $\pi^*$ (conduction) band [34]. We can therefore treat graphene as having one conductance electron arising from the $2p_z$ state (Fig. 1.4). Graphene is a zero gap semi-conductor, meaning the valence and conduction bands meet at the Fermi energy, crossing at the K and K′ points, or so-called Dirac points, and demonstrate a linear dispersion relationship, as indicated by the conical band structure shown in Figure 1.5, also known as a “Dirac cone” [32, 40].

About the Dirac points, the energy dispersion varies linearly, in contrast to other semiconductors, which generally display a parabolic dispersion relation near the Fermi energy [34]. The charge carriers in graphene act as relativistic particles with zero rest mass [32, 41]. Similarly to photons, the speed of the electrons in graphene is constant, independent of momentum. Graphenes charge carriers move at extremely high speeds, up to $\sim$ 15,000 $cm^2$/ V s, compared with 1000 $cm^2$/ V s for diamond [30, 32, 41, 42].

Furthermore, the flexibility of graphene and its high Young’s modulus, which has a measured value of $\sim$1100 GPa have also made it an attractive candidate for application in biomedical devices [37]. Its flexibility coupled with its high carrier mobility mean the potential applications in electronics is vast, such as in energy and storage devices [43] and in flexible circuits [44], which have been proposed for appli-

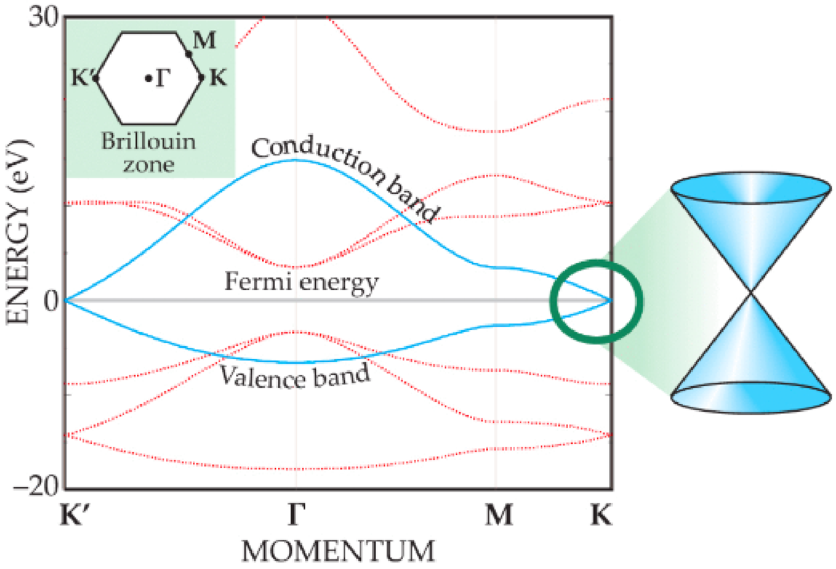

**Figure 1.5:** Graphene's electronic band structure. The $\pi$ and $\pi^*$ bands are shown in blue and the $\sigma$ and $\sigma^*$ bands in red. The Fermi energy is labelled, separating the occupied and empty states. The valence and conduction bands meet at the Fermi energy, at the K and K′ points and demonstrate a linear dispersion relationship, as indicated by the conical band structure or Dirac cone shown on the right. Image obtained from [34].

cation in wearable biomedical devices [45]. Its flexibility has also resulted in it being suggested for application as an antimicrobial agent in flexible food packaging [46], and would allow for graphene to be wrapped around surfaces or medical equipment, as is being proposed in this thesis.

The carrier mobility of graphene is, however, limited by the quality of the graphene sample and the substrate on which the sample is deposited [47]. For instance, for suspended graphene the charge carrier mobility has been reported to reach values of 200,000 $cm^2$/ V s [48]. For graphene formed via chemical vapour deposition (CVD) on an $Si/SiO_2$ substrate the mobility is approximately 3,760 $cm^2$/ V s, as reported by Graphenea for the graphene used in this work [49]. CVD graphene contains currently unavoidable inherent defects in the sample which hinder the charge carrier mobility [50]. These defects arise due to the formation process of CVD graphene [51]. For example, grain boundaries form due to the coalescence of the graphene domains, the size of which are controlled by the temperature used during the CVD process [51, 52].

### 1.2.1 CVD graphene

In this project we are investigating graphene formed via CVD, also known as large area graphene, as it can be produced on scales up to m$^2$ [53]. This scalability of the graphene sample is essential for the applications proposed in this thesis, such on surfaces and equipment in hospitals and healthcare establishments to stop the spread of infectious diseases. As well as this, CVD graphene is said to be able to detect cells with even more sensitivity than graphene made by other methods, due to increased chemical stability, and an enhanced charge carrier mobility, making it more advantageous for application in the biomedical field, such as in drug delivery for which it has previously been investigated [54, 55].

The inherent defects and, thus heterogeneous quality, of CVD graphene samples may, however, be a hindrance for the use of graphene in biomedical applications [56, 57]. The level of heterogeneity of samples may effect the way in which graphene interacts with cells. For example, it is thought that the defects may act as a binding site for proteins, resulting in denaturing of proteins [56, 57]. Therefore, thorough investigation into the level of heterogeneity of graphene samples is necessary, and is something which is explored within this work. A standard of characterisation is proposed which determines the number of spectra necessary to ensure proper characterisation of a sample. Within literature as few as ten spectra are collected for full characterisation of a given sample [58], with some works presenting the analysis performed on only a single spectrum for representation of the entire sample [59]. The levels of heterogeneity presented in this work demonstrate the need for collection of sufficient spectra, such that the sample is fully represented, and also highlights the need for standards of characterisation throughout literature to ensure reliability of data.

## 1.3 Raman spectroscopy of Graphene

Raman spectroscopy is utilised in this work to investigate the heterogeneity of graphene samples. Raman spectroscopy has been widely used for characterisation of carbon allotropes for decades, and is one of the most fast and definitive methods

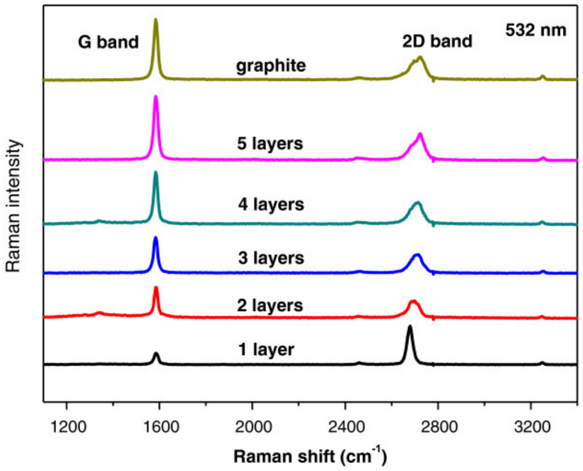

**Figure 1.6:** Raman spectra of graphene samples with different numbers of layers. The relative intensity of the G-band increases with respect to the 2D-band (also known as the G′-band), which also broadens with increasing numbers of layers. All spectra were collected using a 532 nm laser. Figure obtained from [60].

for characterisation of graphene [61]. Raman spectroscopy is a vibrational method based on the inelastic scattering of light from matter, known as the Raman effect. The Raman effect occurs when photons interact with the electron density of the chemical bonds of a molecule causing excitation into a virtual state. This results in emission of a photon of a frequency different than the incident light, which produces a Raman spectrum unique to the analyte [62].

There are two prominent bands in the Raman spectrum of graphene (Fig. 1.6), the first of these is the G-band which arises at around 1590 cm$^{-1}$. It is the main signature observed in the spectra of all sp$^2$ carbon structures, arising from the in-plane vibrations of the C-C bond stretching mode [36, 63, 64, 65]. The second feature in the Raman spectrum is the G′-band, located at ∼2685cm$^{-1}$ (Fig. 1.6), which arises from second order two-phonon scattering processes [36, 65]. It originates from the in-plane breathing mode of the carbon rings [66]. The G′-band is highly dependent on the electronic structure and phonon dispersion of the sample [36, 65, 67].

Two additional bands may also be present in the Raman spectrum of graphene as a result of defects in the sample. These are the D-band and D′-bands. The D-band is located at ∼ 1350 cm$^{-1}$, and is due to the ring-breathing modes of the carbon atoms [36]. The D′-band is located at $\sim$ 1610 cm$^{-1}$. Both bands arise from the scattering due to defects in the sample, and require an impurity to be activated [36, 64, 68].

Raman spectroscopy is the gold standard for characterisation of graphene as the Raman spectrum provides specific information on the number of layers, strain, crystallite size, defects, crystal disorder, edge structure and doping of the sample [36, 61, 63, 64, 66, 69]. It also provides precise information on the electronic states, phonon dispersion, and the electron-phonon interaction in sp$^2$-hybridised carbon systems that other methods of characterisation cannot [68, 70]. For example, the splitting of electronic band structure near the Fermi energy for increasing numbers of layers in the graphene sample is reflected through splitting of the bands in the Raman spectrum of graphene, specifically the G′-band splits into four components [64]. Raman spectra obtained from literature for increasing numbers of layers is shown in Figure 1.6.

## 1.4 Antimicrobial Properties of Graphene

Graphene has previously been shown to be antimicrobial and has excellent potential for application within healthcare associated environments, to stop the spread of micro-organisms and aid in the combat against resistant strains [71, 72, 73]. The antibacterial mechanism of graphene is, however, not yet understood. Most methods of analysis of bacteria cell death by graphene have assessed the cells viability by examining the cell morphology. For example, Li *et al.* used scanning electron microscopy (SEM) by when examining the antimicrobial efficiency of CVD graphene [71], and Akhavan *et al.* counted colony forming units (CFUs) of bacteria before and after being interfaced with graphene, when investigating bacteria cell death by graphene nanowalls [74, 75]. The former can determine the morphology changes, while the latter the number of viable cells, however, neither methods of analysis can investigate the biochemical changes of the cells due to interaction with graphene. The lack of specific and quantitative investigation into the biomolecular compositional changes of the bacterial cells after being interfaced with graphene means the mechanisms for cell death are inconclusive and contradictory [71, 74].

Published works have claimed antimicrobial mechanisms of graphene are due to destruction of the cell wall, while other works have reported that graphene possess little to no antibacterial properties [71, 74]. For instance, a paper published in 2014 by Li *et al.* analysed the ability of CVD graphene on copper (Cu), germanium (Ge) and silicon/ silicon dioxide (Si/$SiO_2$) substrates to cause the death of *E. coli* and *S. aureus* [71]. This work counted CFU and utilised fluorescence staining to determine the number of live cells after being interfaced with graphene. SEM was also used to image changes in the cellular morphology [71]. The group found that the number of viable cells after being interfaced with graphene on the Cu substrate decreased most, followed by the cells on the graphene on the Ge substrate, with the graphene on the Si/$SiO_2$ killing the least numbers of cells [71].

The loss of cell viability following interaction with graphene on Cu and Ge was concluded to be due to the role of the substrate on which the graphene is deposited [71]. They hypothesised that due to the negative resting membrane potential of the microbial cells (-200 mV to -20 mV), the substrate and graphene could induce electron transfer from the membrane, thus, cell death resulted from the disruption of the cell membrane due to the loss of electrons. In other words, graphene's antibacterial properties are dependent on the conductivity of the substrate [71].

In contrast, and indicative of the contradictions in the understanding the mechanism of graphenes antimicrobial properties, Dellieu *et al.* rejected the hypothesis that graphene killed cells by charge manipulation as proposed by Li *et al.* [71, 74]. The paper by Dellieu *et al.* also looked at interfacing *S. aureus* and *E. coli* with graphene on Cu and gold (Au). Again, fluorescence staining, counting CFU and SEM were used for determination of cell death. After 24 hours incubation of the cells with the graphene it was found that at least 91% of cells were viable, compared with 94% - 97% viability of the control cell cultures [74]. Viability tests were also carried out on bacteria interfaced with a Cu foil partially covered in graphene and a bare Cu foil. The former resulted in 46% of *E. coli* surviving, while the latter resulted in 94% of the *E. coli* cells being killed. Thus, they concluded it was not the graphene that killed the cells, rather the Cu-substrate, which caused the bacterial

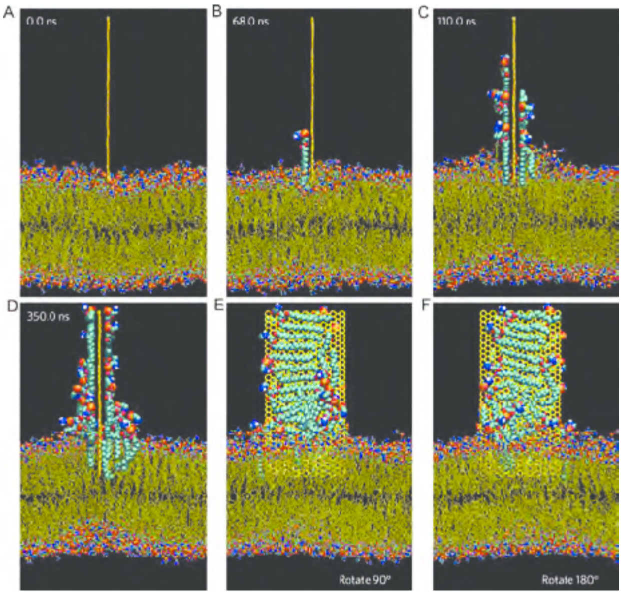

**Figure 1.7:** Simulation of lipid extraction from the lipid bilayer of the cell by a graphene nanosheet. The image shows snapshots of different times during the interaction of the nanosheet and the cell. The time is included on each image. (A) The nanosheet approaches the lipid bilayer of the cell, it is orientated perpendicular to it, represented at this point by a single orange line. (B) Some phospholipids begin climbing up the graphene nanosheet, due to the strong interactions of the graphene, as the nanosheet slightly penetrates the membrane. (C) More phospholipids are extracted from the cell. (D - F) Different orientations of the nanosheet showing the extracted lipids attached to the graphene surface. Figure obtained from [73].

cell death [74].

Another method of analysis which has been used to investigate graphene-bacteria cell death is field emission SEM, utilised by Krishnamoorthy *et al.* to image *E. coli* cells after graphene nanosheet exposure [72]. Their study imaged graphene nanosheets physically penetrating the bacteria, puncturing the cell membrane and causing cell death [72]. This finding was in agreement with a paper published in 2013 by Tu *et al.*, which used molecular dynamics simulation to study how graphene nanosheets interact with *E. coli* [73]. It was demonstrated through these simulations that the graphene nanosheets act as a blade, slicing into the membrane of the cell, following which the lipids are extracted from the lipid bilayer of the cell (Fig. 1.7). The mechanism for graphene nanosheet insertion has been attributed to the strong van der Waals interactions with the membrane lipids [73].

A similar hypothesis proposed by Luan *et al.* in a paper published in 2015, which utilised large-scale all-atom molecular dynamics simulations, showed graphene nanosheets caused cell-degradation, not by lipid constituents, but by interrupting the protein-protein interactions, which are essential in the bacterial cell membrane, therefore resulting in cell death [76]. The simulations showed graphene nanosheet insertion between two connecting proteins to be the most energetically favourable mechanism. However, no experimental work was performed to corroborate these predictions by Luan *et al.* [76].

The proposed idea that graphene does not possess any antimicrobial properties is not a view that is widely shared in the field [71, 72, 73, 76]. Many papers claim that graphene causes cell death by destruction of the cell membrane [72, 73]. However, many of these works have investigated the antimicrobial properties of nanographene [72, 73]. For instance the work by Krishnamoorthy *et al.* which showed graphene nanosheets penetrating the cell membrane [72]. Few works have been produced investigating the antibacterial properties of CVD graphene, used in this work, with the proposed hypotheses for the antimicrobial properties of CVD graphene being the change transfer out of the cell membrane amongst the only current hypotheses for CVD graphene [71].

The clear ambiguity which is present in relation to the exact mechanism which causes cell death could be answered by Raman spectroscopy. The thesis aims to gain an insight into the biomolecular interactions between graphene and *E. coli* through investigation of the Raman spectra prior to and post interaction of the cells with graphene. Raman spectroscopy does not appear to have previously been used for this purpose, and will provide detailed biochemical information on the mechanism of cell death by graphene. For instance, Raman spectroscopy has previously been utilised for investigation into the different changes due to cell death death by antibiotics, alcohols and heavy metals [77]. Only when the interactions between the cells and graphene are fully understood can the material be utilised within applications.

### 1.4.1 The biocompatibility of graphene

The biocompatibility of graphene, however, is a major concern for biomedical applications, particularly wearable devices. Conflicting reports have been published stating differing conclusions in regards to its biocompatibility. Zhang *et al.* found that the toxicity of graphene grown by radio frequency catalytic CVD and single-wall carbon nanotubes (SWCNT) to cell line, PC12, was dependent on concentration and shape of the carbon nanostructure [78]. It was found that the tubular shape of SWCNT promotes penetration of the cell membrane, while graphene sheets were found bind to the surface of the cells, which resulted in oxidative stress of the cell [78]. At the lowest dose of graphene (0.1 $\mu$g/mL) there were no toxic effects on the cells, while at the highest dose (10 $\mu$g/mL) the graphene induced cytotoxicity [78].

Sasidharan *et al.* found that the toxicity of the graphene to monkey renal cells was dependent on functionalisation of the samples [79]. Pristine graphene resulted in aggregation of the graphene on the cell membrane, which is likely to be a result of strong hydrophobic interactions between it and the cell membrane [79]. Whereas, carboxyl-functionalised hydrophilic graphene flakes were found not to accumulate on the cell surface, but became internalised by the cell, however, they claimed this did not cause any cellular damage [79].

In disagreement with these papers, Nayak *et al.* found that CVD graphene had no toxic response to human mesenchymal stem cells (hMSCs), but in fact found that graphene aided the differentiation of the hMSCs to bone tissue, proposing it as a biocompatible scaffold for tissue engineering [80]. In agreement with this, Rastogi *et al.* found that graphene enhanced cell adhesion and growth of both nonneuronal (monkey renal fibroblast) and neuronal (rat hippocampal neuron) cells [81]. They demonstrated that pristine graphene does not have any detrimental effects on the morphology of the cell by using live-dead assays, a fluorescence technique to assess the integrity of the cell membrane [81]. Similarly to the biomolecular interactions of graphene and bacteria, the interactions with biological samples is not fully understood. Therefore, future work of this project would be investigation into the effects of graphene on eukaryotic cells using Raman spectroscopy.

The biocompatability of graphene could have an impact on the use of graphene in surfaced enhanced Raman spectroscopy (SERS). SERS involves the use of substrates for enhancement of biological signals during the collection of Raman data [82]. However, the unknown interactions between graphene and biological samples make its use in SERS unsuitable. That is, the enhancement of signals of cells on graphene could be due to toxicity response of the cells, which has been shown to occur, for example, for the band at 1660 $\mathrm{cm}^{-1}$ increased in relative intensity due to inhibited protein synthesis by antibiotic ampicillin [77].

Graphene oxide (GO) is commonly used as an SERS substrate, such as by Liu *et al.* who investigated GO based SERS for investigation of cancer cells [83]. GO has also previously been reported to possess antibacterial properties [75, 84]. Many papers have been published which hypothesise the cause of cell death by GO, such as the work by Akhavan *et al.* which suggests GO nanowalls penetrate the cell membrane, physically damaging the cell and leading to cell lysis, similarly to the proposed antimicrobial mechanism of graphene nanowalls [72, 73, 75]. Other work has suggested the antimicrobial mechanism is due to oxidative stress of the cells which can lead to DNA degradation [84].

The antimicrobial properties of GO has been investigated more thoroughly than graphene within literature [85]. For instance, in a review paper by Szunerits *et al.* which looked at published works analysing the antimicrobial properties of graphene-based materials, a selection of the literature indicated that approximately 85 % of the papers investigated GO and around 14 % included work on graphene, with some papers including work on both materials [85]. Thus, this thesis is investigating graphene as opposed to GO, as it is under-represented and less understood within the literature at present [85].

## 1.5 *Escherichia coli*

*E. coli* is a Gram-negative bacterium, used as a model bacterium in this thesis, which is normally found in the digestive tracts of humans and animals [86]. *E. coli* is widely used within the literature for investigation of the antimicrobial properties of graphene [71, 72, 73, 74, 76]. For example, Li *et al.* compared the effect of graphene interaction on *E. coli* and *S. aureus* [71]. Additionally, Tu *et al.* simulated the effects of graphene nanosheets on *E. coli* cells [73].

The *E. coli* strain studied in this work is MG1655, a K-12 strain derivative [87].

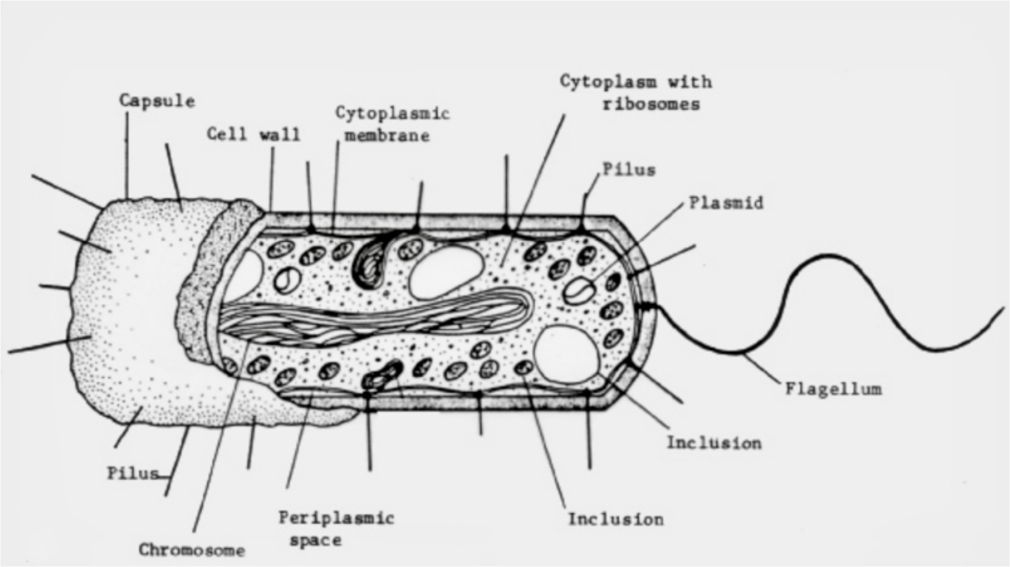

**Figure 1.8:** Structure of *E. coli* showing the main components of the cell [88].

MG1655 was the first strain of *E. coli* genomes to be sequenced in full, published in 1997 [87]. MG1655 has been maintained as a standard laboratory strain with minimal genetic manipulation.

*E. coli* is a rod shaped bacterium of approximately 1 $\mu$m in width and up to 3 $\mu$m in length [90]. *E. coli* is a prokaryotic cell, its basic structure is shown in Figure 1.8 [91]. *E. coli* has thin filaments around the outside, known as pili which enable it to attach to specific surfaces or to other cells. For example, the presence of pili was found to enhance the ability of *E. coli* to attach to human urinary tract epithelial cells, resultant in UTIs [92]. *E. coli* are capable of swimming due to their flagella, motorary structures which rotate clockwise to propel the bacteria forwards. *E. coli* have several flagella distributed over the cell [93].

The cell wall of *E. coli* is a complex structure (Fig. 1.9) responsible for the bacteria maintaining its shape. The cell wall is significant in this study as it is one of the main responders for cell stress, it protects the cells from threatening conditions by altering the membrane permeability, thus, will be a focus for the interactions of graphene with *E. coli* [94]. The main component of the cell wall which maintains its shape is the peptidoglycan, a polymer of sugar and amino acids, specifically a mesh of glycans and stretchable peptides, which helps protect from cell lysis [95, 96].The peptioglycan is bound to the outer membrane via lipoproteins

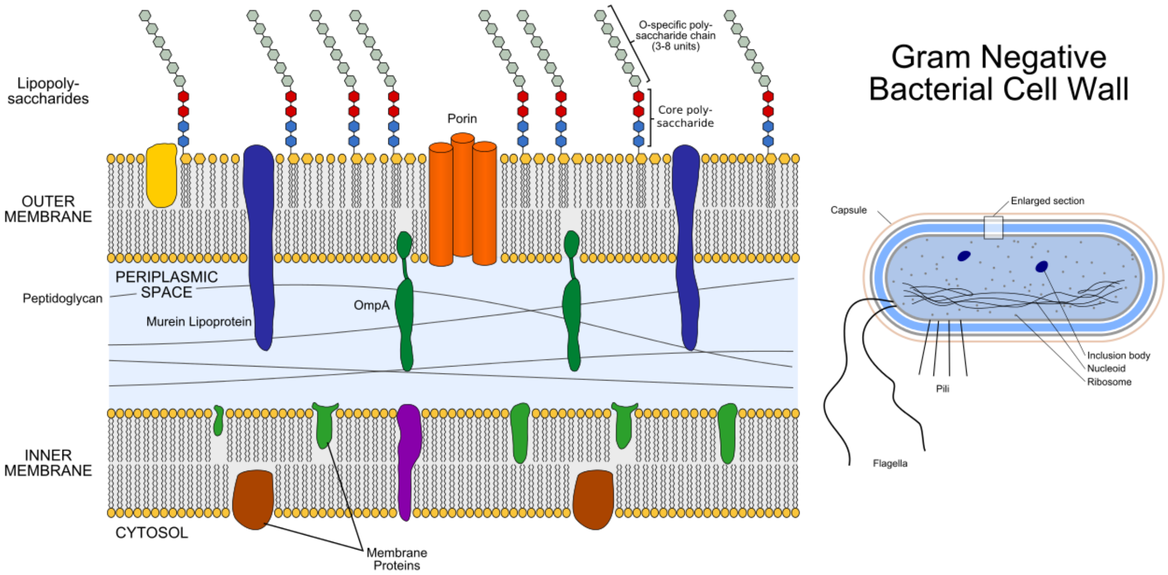

**Figure 1.9:** Representation of the cell wall of a Gram negative bacterium. The right shows an *E. coli* cell, some of the components of the cell are labelled, including the pili, flagella and ribosomes. The section of the cell wall which has been enlarged is shown on the cell. The cell wall shows the inner and outer membranes, which are composed by two lipid sheets, known as lipid bilayers. The periplasm is the space between the two membranes, which is filled with a compressible gel. The lipopolysaccharides (LPS) are anchored to the outer membrane via lipoproteins. Membrane proteins are shown in the figure, particularly OmpA is labelled. Its main function is to maintain cell integrity. Figure obtained from [89].

[96]. It has been shown that some antibiotics cause cell death through destruction of the peptioglycan, thus, comparison of cell death in this way with cells lysis by graphene will give an indication whether the cells are killed in a similar way [97].

The outer membrane (OM) and inner membrane (IM) of the cell wall is comprised of lipid bilayers (Fig. 1.9). Lipids are made up of a hydrophilic head and a hydrophobic tail or tails. The tails are usually fatty acids, differing in size, generally one is saturated and one unsaturated [98]. Different bacteria has different lipid membrane compositions, and even for like-species, the membrane composition may vary from cell to cell, and can be dependent on environmental conditions [99]. The lipid bilayer of the *E. coli* is thought to be one of the main mechanisms which undergoes degradation due to interaction with graphene, specifically graphene nanosheets were believed to cut into the cell membrane and extract lipids from the lipid bilayer of the cells [73]. Thus, the bilayer of the cell will be significant in the study, to determine if CVD graphene causes cell death by a similar method.

The IM and OM of *E. coli* is made up of different constituents. The IM is a bilayer containing $\alpha$-helical proteins, and phospholipids making up more than 95% of the lipid bilayer. The OM is an asymmetric bilayer made up of phospholipids and glycolipids, principally lipopolysaccharides (LPS) [100, 101]. The OM proteins can be divided into two classes, with some exceptions, $\beta$-barrel proteins and lipoproteins. There are more than 90 species of lipoproteins in the OM of *E. coli* which contribute to cellular processes, such as cell division [102]. The composition of lipids in bacterial cells can differ even within genetically identical cultures [103].

The transmembrane proteins in the OM generally assume a $\beta$-barrel conformation, referred to as outer membrane proteins (OMPs). Some membrane proteins are highlighted in the diagram of the cell wall (Fig. 1.9). OMPs have different jobs, such as the porins, OmpF and OmpC which allow uptake of small molecules like amino acids across the membrane through the porins [104]. The OMP labelled, OmpA is essential for outer membrane stability and its function is largely to maintain the structural integrity of the cell [105]. The OM proteins may also play a role in the interaction of graphene and *E. coli*. Specifically, interaction of the proteins with graphene may cause denaturing of the proteins as reported for interaction of graphene with eukaryotic cells [57].

LPS plays a role in the cell structure and also protects the cell from any toxins in its surroundings [106]. Lipid A, the innermost component of LPS, is hydrophobic, and anchors the LPS to the outer membrane (Fig. 1.9). The O-antigen consists of a series of three to six sugars which are repeated [104]. The core is also made up of sugars [107]. LPS can naturally vary within cultures of *E. coli* [103]. This can also cause heterogeneity of the Raman spectra from one area in the sample to the next. This heterogeneity is problematic for application of Raman spectroscopy in clinical settings when it could lead to misclassification of bacteria [108].

Heterogeneity can also arise in bacterial samples due to conformational changes of the cells, which is a naturally occurring phenomenon as the bacteria attempt to prepare themselves for unknown environmental changes or attacks [109]. For example, sub-populations of cells within a culture have even been found to resist prolonged dosages of penicillin which caused the death of the majority of cells in the population [109]. These sub-populations of cells were found to be able to overcome the penicillin, despite never having been in contact with the antibiotic [109].

Gover *et al.* explored this heterogeneity in an attempt to understand the rate of change of these cells [110]. Investigation of the changes in *E. coli* colonies was performed using time lapse fluorescence microscopy before and after semi-lethal heat treatment, which caused the death of approximately half the cells. It was found that post-heat treatment the survival probability and post-stress physiology of sister cells was altered from highly similar to uncorrelated within the first decile of their cell cycles [110]. The heterogeneity has been suggested to be a result of cells stochastically transitioning among different phenotypes in order to enhance the overall fitness of the cell population, in an attempt to be prepared for any unforeseen environmental fluctuations [111].

In this thesis the heterogeneity both within and across *E. coli* samples is explored using Raman spectroscopy. The effect of heterogeneity on the Raman spectra is investigated, in addition to the need for collection of sufficient data that the samples are properly represented by the spectral average, taking this heterogeneity into account. Such fluctuations in cells as a defensive technique may result in different toxicity responses following interaction with graphene. Thus, such heterogeneity is significant within this thesis which analyses the metabolic changes in cells due to cell death by graphene.

## 1.6 Raman spectroscopy

Raman spectroscopy is ideal for use in the biomedical field [112] as it can be used non-invasively and non-destructively [113]. For example, Raman spectroscopy has been utilised for non-destructive testing of biofilms [114]. Raman spectroscopy has previously been used to characterise and discriminate microbes [115, 116]. It it advantageous for use in microbiology due to its ability to provide information of the chemical composition and molecular structure of microbes [115, 117]. An example of this is the use of Raman spectroscopy to identify bacteria which have become resistant to antibiotics [117]. The changes in the Raman spectra of antibiotic-resistant *E. coli* compared with non-antimicrobial resistant *E. coli* is indicative of the mode of action which the cell had undertaken to achieve resistance, which could be linked to the evolutionary modifications of the genetic basis [117].

### 1.6.1 Raman spectroscopy for the analysis of cell death

Raman spectroscopy is becoming increasingly prevalent, not only for its ability to characterise cell types, but also to provide information on the metabolic state of the cell. It has been used to detect relative changes in cellular composition as a result of cell death [118], and has previously been used to detect *E. coli* cell death after toxic substances or conditions have been applied, such as antibiotics, heat and alcohols [77, 119, 120, 121]. For example, a paper published in 2016 by Teng *et al.* [77] analysed the Raman spectra of *E. coli* after being subjected to alcohols (ethanol and *n*-butanol), antibiotics (ampicillin and kanamycin) and heavy metals ($Cu^{2+}$ and $Cr^{6+}$). Teng *et al.* found that a reduction in the normalised intensity of bands associated with nucleic acids, such as the bands at 728 $cm^{-1}$, 782 $cm^{-1}$, 811 $cm^{-1}$, 1481 $cm^{-1}$ and 1574 $cm^{-1}$ occurred due to *E. coli* coming into contact with the alcohols, resulting from an increased cell-size due to stress, hence nucleic acid dilution [77]. Increased cell size due to stress has previously been reported in relation to cell stress by salts, with the cell size increasing up to ten-fold, and is thought to be linked to the induction of additional stress proteins in the cell [122]. A similar toxicity response may be employed by the cells following interaction with graphene, which could be monitored through the evolution of these bands in the Raman spectra [77].

A band which has been commonly noted to change as a result of cell death is the band representing RNA/ DNA at 782 cm$^{-1}$ in the Raman spectra of *E. coli* [77, 119, 120, 121]. Xie *et al.* and Escoriza *et al.* found this band changed due to the degradation of nucleic acids as a result of *E. coli* heat treatment [119, 120]. Teng *et al.* also observed a gradual reduction in intensity of the normalised 782 cm$^{-1}$ band due to cell death by alcohols, antibiotics and heavy metals indicating an alteration of the physiological development of the cell [77]. Thus, investigation of the bands at 782 and 813 cm$^{-1}$ following bacterial interaction with graphene will allow insight into any degradation of nucleic acids in the cells and changes of physiological development [119, 120].

Denaturing of proteins has previously been found to occur following interaction of graphene with protein HP35 in chicken villin subdomain due to defects in the samples [57]. Specifically, interaction of proteins with the defects results in proteins becoming anchored to the sample [57]. Thus, given the defects present in CVD graphene from the formation process, a similar interaction of the proteins in the cell membrane of *E. coli* with the defects in the graphene could cause protein denaturing [57]. This could be monitored through relative changes in the bands at 1004 cm$^{-1}$, 1610 cm$^{-1}$, 1670 cm$^{-1}$ and 1250 cm$^{-1}$, reported to change due to denaturing of proteins from heat treatment of *E. coli* cells at high temperatures of 60 - 121 °C [119, 120]. Unfortunately, in each of these papers, the high wavenumber region (2800 - 3100 cm$^{-1}$) of the cell spectra is not considered, despite being rich in prominent protein signatures [119, 120]. In this work, quantitative analysis will be performed on both fingerprint (600 - 1800 cm$^{-1}$) and high wavenumber regions of the spectra to gain thorough insight into the metabolic changes of the cells.

It was discovered that death by a bactericide (EDTA) and a disinfectant (sodium hypochlorite) resulted in a reduction in all normalised bands in the fingerprint region of the Raman spectrum, due to the dissolution of cell tissue [120]. Therefore, significant cell degradation by graphene will be reflected through general decrease in intensity of bands between 600 - 1800 cm$^{-1}$ in the Raman spectra of *E. coli* [120]. Unfortunately, however, no quantitative analysis is performed on the spectra for determination of the specific bands in the Raman spectra which change [120]. In this work both peak intensity ratio (PIR) analysis and principal component analysis (PCA) will be performed on all bands in the Raman spectra of *E. coli* following interaction with graphene, to determine specifically which components of the cell are changing due to cell death.

This lack of quantitative analysis of Raman spectra is common among other published work, and is also shown in a paper published in 2016 by Nanda *et al.* which investigated *E. coli* and *Enterococcus faecalis* (*E. faecalis*) cell death by GO nanosheets using Raman spectroscopy [123]. This work published Raman spectra of *E. coli* before and after being interfaced with GO suspended in solution at concentrations of 50 $\mu$/mL, 100 $\mu$/mL and 150 $\mu$/mL. It was found that there were changes in the relative intensity of the bands at 490 cm$^{-1}$ representing the S-S stretching vibration of proteins, at 610 cm$^{-1}$ attributable to CO-NH bending vibration of Amide IV and an A band at 729 cm$^{-1}$ [123]. There is a lack of quantitative analysis, such as peak fittings, PIRs or comparison of relative intensities to demonstrate the changes in these bands following interaction with GO, with the focus primarily on other methods of analysis for changes in morphology of the cell, such as SEM, with no attempt to determine the reason for the changes of the bands [123]. Furthermore, much of the spectra is not considered or analysed, with only the region between 450 cm$^{-1}$ and 800 cm$^{-1}$ being shown within the publication, and the three mentioned bands the only considered changes in the spectra [123]. This means there is a large amount of lost information due to the lack of analysis of other bands in the Raman spectra. In this thesis, quantitative analysis will be performed on the full spectral range between 600 cm$^{-1}$ to 3100 cm$^{-1}$ for thorough analysis of the changes due to cell death by graphene.

To investigate if the cause of cell death by graphene is due to inhibition of the cell wall, the Raman spectra after interaction with graphene will be compared against published works which analyse cell death in this way using Raman spectroscopy. For example, cell death by the antibiotic ampicillin was reported to inhibit the synthesis of the cell wall, which was reflected through the change in normalised intensity of the lipid containing bands at 957 $cm^{-1}$, 1302 $cm^{-1}$, 1449 $cm^{-1}$ and 1660 $cm^{-1}$ [77]. The monitoring of these bands will allow for investigation into the inhibition of the cell membrane following *E. coli* interaction with graphene, a hypothesised cause of cell death by graphene, according to literature [71, 73].

*E. coli* cell death by heavy metals also resulted in an increase in lipid signatures, such as the lipid band at 1449 $cm^{-1}$, and the band at 1128 $cm^{-1}$, which represents saturated lipids, while a decrease in protein bands suggested inhibition of protein synthesis [77]. Unfortunately, this work also does not analyse the high wavenumber region of the Raman spectra of *E. coli*, which is rich in protein and lipid signatures [124]. Monitoring of this region would provide further insight into changes in the lipids and proteins of the cells, as will be performed in this work.

Published work by Zu *et al.* did consider the high wavenumber region when analysing cell death by an alcohol, 1-butanol [121]. This work analysed the changes in three PIRs in the high wavenumber region of the spectra $I_{2870}/I_{2954}$, $I_{2852}/I_{2880}$, and $I_{2852}/I_{2924}$ to assess how alcohols affect the fluidity of the cell membrane, a noted change in the cell due to death by alcohols [77, 121, 125]. These bands were chosen as they are representative of symmetric and asymmetric stretching of C-H bonds of lipids and proteins in the cell membrane [121]. All three PIRs exhibited an eventual increase, thought to be due to the expected increase in membrane fluidity [121]. Consideration of such PIRs in this work following *E. coli* interaction with graphene will give insight into changes in membrane fluidity [126, 127]. It does not appear as though such investigations have been performed following *E. coli* interaction with CVD graphene. Thus, monitoring of these bands will allow investigation into the defence mechanisms of *E. coli* cells interfaced with graphene in a way which does not appear to have been done before [121].

The wealth of literature on the analysis of *E. coli* cell death by lethal substances, such as antibiotics and alcohols, using Raman spectroscopy will aid the investigation of this thesis into the biomolecular interactions between graphene and *E. coli*. Specifically, such interactions with known mechanisms for cell death will allow for comparison and parallels to be drawn against the mechanism utilised by graphene to kill the microbial cells, which will be reflected through the same changes in the Raman spectra, such as changes in the bands due to cell death by ampicillin, an antibiotic known to kill cells by inhibition of the cell wall [77]. The information provided by Raman spectroscopy promises to provide a level of detail which has not previously been obtained from methods such as counting of CFUs, which only allows determination of the number of viable cells.

This thesis will begin by presenting the background theory of Raman spectroscopy in Chapter 2. This chapter will also provide detail on the instrumentation, and the methods and protocols used throughout this work, including experimental and data analysis. Chapter 3 will present the investigation and characterisation of CVD graphene using Raman spectroscopy. Specifically this will involve comparison of the obtained quantities against published literature results, and exploration of the reliability of methods for characterisation of CVD graphene. The level of heterogeneity presented in the chapter is significant, and brings into question the possible repercussions of such extreme levels of heterogeneity, which does not appear to be reported previously for graphene formed via CVD.

The heterogeneity of *E. coli* samples using Raman spectroscopy is also explored in Chapter 4 of this thesis. The level of heterogeneity both within and across the three *E. coli* replicates is investigated in this chapter through PIR analysis, band fittings and PCA. The effect of the heterogeneity on the level of data collection necessary to ensure the sample is properly characterised is also explored, through consideration of the standard error and second order standard deviation of the data for increasing number of spectra in the spectral average. Standards for characterisation are proposed in this work, which could ensure reliability of data throughout literature.

The final results chapter presents the investigation of the biomolecular interactions of *E. coli* and CVD graphene. Comparison against the *E. coli* control samples will allow determination of the difference following interaction with graphene.

Furthermore, two different experiments are performed to determine the differences between *E. coli* interfaced with and cultured with graphene. PIR analysis, PCA and band shifts are all utilised to investigate the metabolic changes of the cells due to graphene. This thesis then finishes with conclusions and discussions on future work.

# 2

# Methods

## 2.1 The Theory of Raman Spectroscopy

### 2.1.1 The Raman Effect

Raman spectroscopy is a label-free method for characterising samples, which can be used non-invasively and non-destructively [113]. The Raman effect was first predicted by Smekal using quantum theory in 1923, and later experimentally verified by Chandrashekhara Venkata Raman in 1928, for which he was awarded the Nobel Prize in physics in 1930 [128, 129]. The Raman effect involves the inelastic scattering of photons following interaction with the molecules in a sample [62]. The interaction of the light and molecular bonds is dependent on the electronic and vibrational properties of the material, providing detailed spectroscopic information unique to the sample.

Photons, of frequency $\nu_0$, which undergo Raman scattering result in a frequency

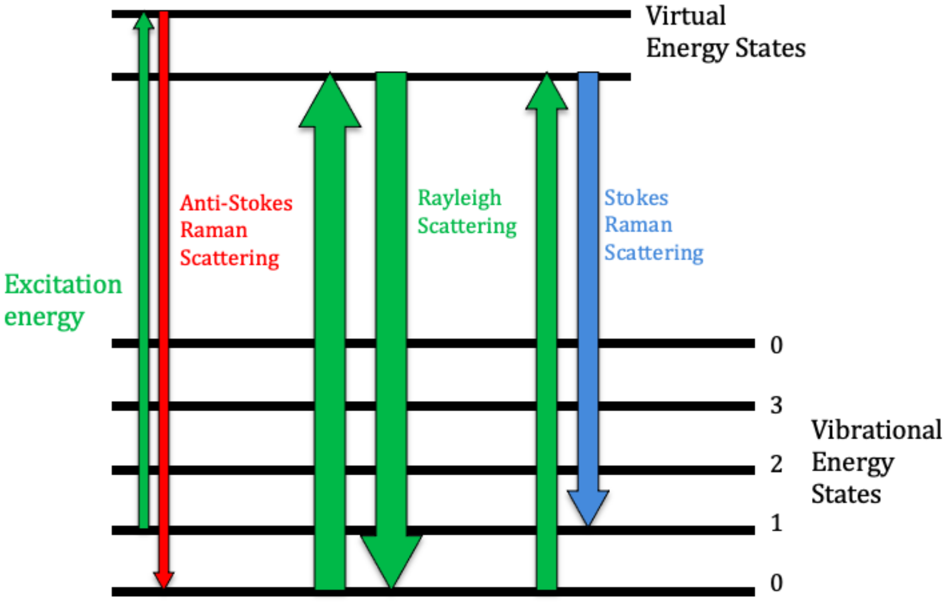

**Figure 2.1:** Jablonski diagram showing the different light scattering processes following molecule interaction. Rayleigh (elastic) scattering results in scattered photons of the same frequency as the incident light. Raman (inelastic) scattering produces light of a different frequency to the frequency of the incident light. Stokes (Anti-Stokes) scattering produces photons of frequency less (greater) than the incident radiation. Stokes scattering is most commonly studied as it produces more intense spectra [130].

change of $\nu_0 \pm \Delta\nu$, where $\Delta\nu$ is the frequency difference compared with the incident light. Raman scattering accounts for a very small percentage of the total light scattered, due to the requirement that the molecules are Raman active for Raman scattering to occur. For example, approximately one in $10^6$ to $10^8$ photons are Raman scattered, with most photons being Rayleigh scattered. Rayleigh scattering, or elastic scattering, is when the photons are scattered with unchanged energy from the incident light $\nu_0$ [62].

A schematic of the different possible light scattering processes following interaction with a molecule is shown in Figure 2.1. Raman scattering results in two scattering processes. The first process (Stokes scattering) involves the photon-induced excitation of the molecule to a higher vibrational state. The molecule relaxes back to a real state, emitting a photon with less energy than the incident photon. This process results in scattered photons of frequency $\nu_0 - \Delta\nu$ where $\Delta\nu$ represents the Raman (frequency) shift. The second scattering process (Anti-Stokes scattering)

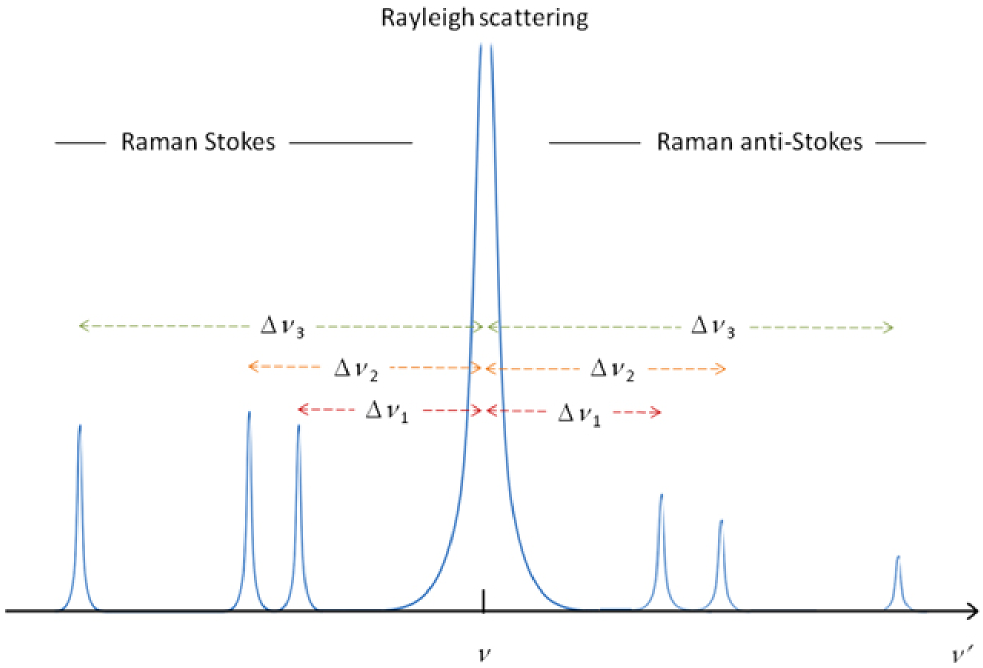

**Figure 2.2:** Schematic Raman spectrum. The intense Rayleigh line representative of the Rayleigh scattered light ($\nu = \nu'$) where $\nu$ is the incident frequency and $\nu'$ is the frequency of the scattered light. $\Delta\nu_1$, $\Delta\nu_2$ and $\Delta\nu_3$ represent wavenumber shifts due to interaction of photons with Raman active molecules. The Stokes and anti-Stokes lines provide the same spectroscopic information, however, the anti-Stokes lines are less intense that their Stokes counterparts. Figure obtained from [131].

involves a molecule in an already excited vibrational state, resulting in further excitation to a higher energy virtual state. Then relaxation of the molecule to the ground state produces an emitted photon of greater energy than the incident light, which has frequency $\nu_0 + \Delta\nu$. The same spectroscopic information is obtained for Stokes and Anti-Stokes scattering, i.e., band shifts arising at the same wavenumber (Fig. 2.2) [62]. As most molecules will be found in the ground state at room temperature, according to the Maxwell Boltzmann distribution, Stokes scattering will be the more probable Raman scattering process, resulting in more intense spectra, thus it is most commonly studied.

The Raman effect can be explained using classical theory, within the framework of classic electromagnetism [62]. Consider an electromagnetic (EM) wave, such as the incident light source of a laser beam (Fig. 2.3). The phenomena being discussed here does not involve the magnetic component of the EM wave and so will not be

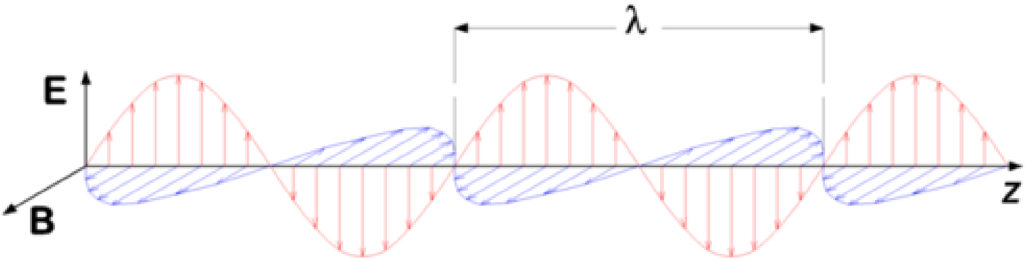

**Figure 2.3:** Electromagnetic wave showing the perpendicular electrical and magnetic components, with the electrical component represented by the y-axis (E) and the magnetic component represented by the x-axis (B) propagating along the z-axis. $\lambda$ is the wavelength [62].

considered. The electric field strength at time $t$ is

$$E = E_0 \cos(2\pi\ \nu_0\ t) \tag{2.1}$$

where $E_0$ is the amplitude and $\nu_0$ is the frequency. When the laser light radiates a sample a change in molecular dipole moment can be induced from the interaction of the EM radiation with the so-called Raman active molecule. The induced dipole moment is defined as

$$P = \alpha\ E \tag{2.2}$$

where $\alpha$ is the polarizability of the molecule. Molecular polarizability results from the electric field of the laser light distorting the electron distribution of a bond or molecule. An oscillating electric field induces an oscillating molecular dipole moment, thus combing Equations 2.1 and 2.2 for a diatomic molecule gives [62]

$$P = \alpha E = \alpha E_0\ \cos\ (2\pi\,\nu_0\ t) \tag{2.3}$$

The polarizability of the molecule can be described as a function of its static (equilibrium) polarizability, $\alpha_0$, and the vibrational displacement of the molecule, $q$, such that $\alpha = f(\alpha_0, q)$. For small displacements $q$, this equation can be written as a Taylor expansion

$$\alpha = \alpha_0 + \left.\frac{d\alpha}{dq}\right|_0 q + \ldots.., \tag{2.4}$$

where $\frac{d\alpha}{dq}$ is the rate of change of polarizability with respect to the change in displacement evaluated at the equilibrium position. As $q$ is small terms of higher order are negligible.

As the laser continually interacts with the molecule, it continually induces a dipole moment at the frequency of the incident light. For a molecule vibrating at a frequency, $\Delta\nu$, the nuclear displacement is given as

$$q = q_0 \ \cos(2\pi \ \Delta\nu \ t) \tag{2.5}$$

where $q_0$ denotes the maximum vibrational displacement. Combining this expression with Equation 2.4 yields

$$\implies \alpha = \alpha_0 + \left.\frac{\partial\alpha}{\partial q}\right|_0 q_0 \cos(2\pi \ \Delta\nu \ t). \tag{2.6}$$

Hence the polarizability from Equation 2.3 becomes

$$P = \alpha_0 E_0 \cos(2\pi\nu_0 t) + \left.\frac{\partial\alpha}{\partial q}\right|_0 q_0 E_0 \cos(2\pi\nu_0 t) \cos(2\pi\Delta\nu t), \tag{2.7}$$

which can be further written as

$$P = \alpha_0 \ E_0 \ \cos(2\pi \ \nu_0 \ t) + \left.\frac{\partial\alpha}{\partial q}\right|_0 \frac{q_0 \ E_0}{2} \cos\left(2\pi \ (\nu_0 - \Delta\nu) \ t\right) + \left.\frac{\partial\alpha}{\partial q}\right|_0 \frac{q_0 E_0}{2} cos\left(2\pi(\nu_0 + \Delta\nu) \ t\right). \tag{2.8}$$

The first term in this equation denotes the static/ equilibrium term representative of the Rayleigh elastic scattering. The second term corresponds to the Raman scattering resulting in the $\nu_0 - \Delta\nu$ frequency shift, which defines Stokes scattering. The last term represents the scattering associated with the $\nu_0 + \Delta\nu$ anti-Stokes frequency shift [62]. For a molecule to be Raman active, i.e., to produce a Raman shift, the following condition, associated with a change in polarizability, must be satisfied [62]:

$$\left.\frac{\partial\alpha}{\partial q}\right|_0 \neq 0. \tag{2.9}$$

## 2.2 Preparation of Bacterial Target Samples

*Escherichia coli* (*E. coli*) has been used in this work for characterisation and investigation of heterogeneity using Raman spectroscopy, and as a model bacterium for investigation into the bactericidal activity of graphene. *E. coli* strain MG1655 was

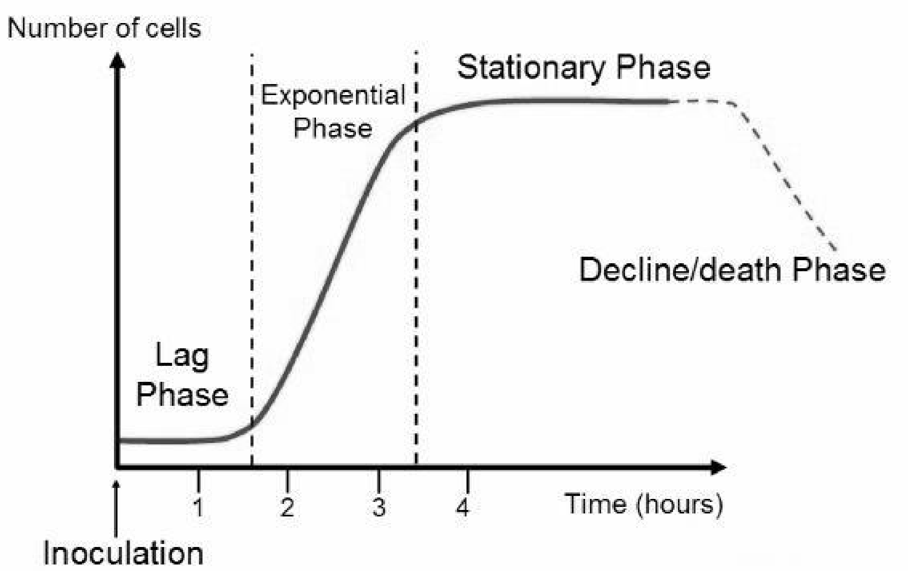

**Figure 2.4:** Bacteria growth curve showing the different growth stages. The first growth stage is the lag phase during which the bacteria adapt themselves to the growth conditions, the cells are not yet multiplying [134]. Following this stage is the logarithmic phase, also known as the exponential phase, during which the cells divide. The logarithmic phase is the main growth stage of the cells when they are most viable and have a good supply of nutrients. Then comes the stationary growth phase when the growth and death rates become equal. The last stage is the death phase, when bacteria begin to die off due to depleted nutrients [135].

used throughout all experiments. The *E. coli* strain was maintained as a glycerol stock (16 % glycerol) at -80 °C. A bacteria culture was produced by streaking the strain onto an LB agar plate, typically used for growth of bacterial microcolonies [75], and left to incubate overnight at 37 °C. A single colony was selected from the plate and inoculated in 3 mL of EZ rich media, obtained from Teknova [132], with 0.4 % glucose. EZ rich media is a defined media, meaning that each batch is made up of the same constituents, i.e, the quantities of all ingredients are known [133]. Undefined media, such as LB, is made up of unknown constituents [133]. Defined media produces much less variability between samples compared with undefined media [132]. The bacteria were grown overnight in a rotating incubator at 37 °C.

After overnight growth, 30 $\mu$l of the bacteria culture was diluted in 3 mL of fresh EZ rich media, and was left to incubate at 37 °C until the optical density ($OD_{600}$) reached a value of around $\sim 0.4 - 0.6$. This optical density has also been used by other works which assess cell viability following exposure to toxic substances or

**Figure 2.5:** Optical image of *E. coli* cell dried onto $CaF_2$ undergoing Raman analysis. The scale bar is 2 $\mu$m. An 100 x objective lens was used here.

conditions, such as exposure to alcohols, antibiotics and heavy metals [77, 121, 136]. At $OD_{600} = 0.4 - 0.6$ the *E. coli* cells are at the exponential phase of their growth (Fig. 2.4) [135]. This $OD_{600}$ was also found to give the best distribution of cells for Raman analysis, providing regions of single cells and clumps of bacteria for thorough analysis of different cell distributions in the bacteria culture (Fig. 2.5).

The exponential phase was chosen for examining the bacterial cells in this work as this is when the cells have most of their nutrients and are the most optimal stage of growth. Hence, when cells are grown to test the antimicrobial properties of graphene, cell death will take place when they are most viable and content [137]. This is the most robust time in the growth phase to assess antibacterial activity. Many papers carry out analysis following the growth of bacteria for 24 h at 37 °C [71, 74, 123]. After this length of growth time, nutrients are becoming depleted, meaning some cells will be in the stationary growth phase or entering into the death phase and will not as viable as earlier in the growth cycle (Fig. 2.4) [135].

Following growth, 1 mL of the bacteria culture was then centrifuged for five minutes at 6000 revolutions per minute (rpm) until a pellet of cells formed. Centrifugation is a commonly used method for harvesting bacteria, with a range of forces or rpm chosen, often without reasoning [138]. The relative centrifugal force (RCF), also known as the G-force, can be determined from the rpm using the following equation

$$\mathrm{RCF} = 1.12 * r * \left(\frac{\mathrm{rpm}}{1000}\right)^2, \tag{2.10}$$

where r is the radius of the centrifuge. For harvesting of the bacteria studied in this thesis a Heraeus Biofuge Pico centrifuge with a radius of 8.5 cm was used. From Equation 2.10, centrifuging bacterial cells at a rate of 6000 rpm results in a RCF of $\sim$ 3427 x $g$, where $g$ is the gravitational constant.

Pembery *et al.* found that centrifugation at high speeds of 15,000 x $g$ resulted in the culturability of *E. coli* being significantly diminished [139]. Furthermore, it was also shown by Bell that centrifugation of certain bacteria for longer periods of 30 min, compared with shorter times of 10 min, can have a detrimental effect on the ability of the cells to adhere to glass [140]. Despite this, papers still utilise prolonged periods of fast centrifugation when harvesting cells [123]. For example, a paper published by Nanda *et al.*, which investigated the antimicrobial properties of graphene oxide (GO) using Raman spectroscopy, centrifuged the *E. coli* and *S. aureus* cells at 10,000 rpm for 30 min. Given the findings by Pembery *et al.* and Bell it is thus likely to have modified the cells [123, 139, 140]. Bittel *et al* also performed centrifugation at 10,000 x $g$ , however, for a shortened period of 3 min, on *E. coli* cells when analysing the affect of arsenic exposure to the cell using Raman spectroscopy [136]. Comparatively, Teng *et al.* centrifuged the bacteria cells at 5,200 rpm for 1 - 2 min, chosen to avoid harming the cells [77]. Similarly to Teng *et al.* in this work gentler centrifugation speeds such as 6000 rpm were chosen to avoid doing the cells harm.

Following centrifugation, the supernatants were pipetted out and the *E. coli* cells were re-suspended in 1 ml of sterilised water. Washing cells using sterilised water is required prior to carrying out Raman analysis to avoid the media forming salts and affecting the Raman analysis [77, 120]. Washing was performed twice to ensure all EZ rich media was washed off the cells. 10 $\mu$l of the cell culture was diluted in 900 $\mu$L of sterilised water to ensure the sample was not too dense for Raman measurements, and that single cell analysis would be possible. An optical image of

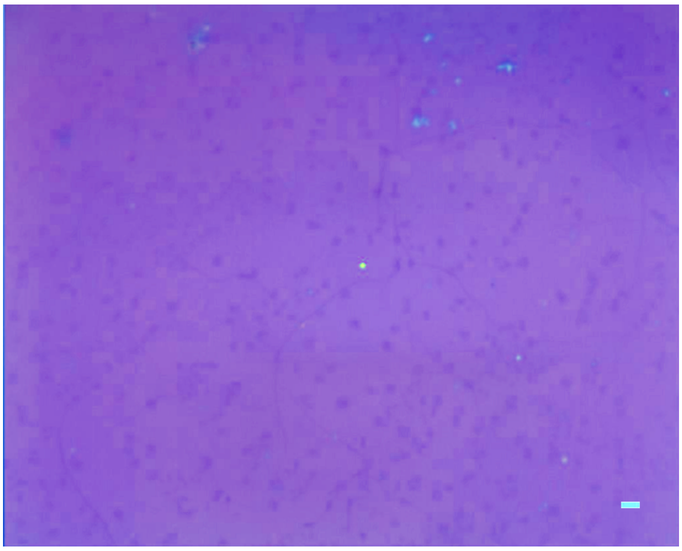

**Figure 2.6:** Optical image of one of the four CVD graphene sample studied in this work. The samples are monolayer graphene, deposited on an Si/SiO$_2$ substrate. The scale bar is 2 $\mu$m.

the cells can be seen in Figure 2.5.

## 2.3 Properties of CVD graphene

Four CVD monolayer graphene samples were studied in this project, all of which were purchased from Graphenea [49]. All samples are 1 cm$^2$ on a Si/SiO$_2$ substrate. The sample is p-doped with boron, with a resistivity of 450 ± 40 Ohms/sq. The covering of graphene on the Si/SiO$_2$ substrate is $> 95\%$. The domain sizes of the sample are up to 20 $\mu$m. An optical image can be seen in Figure 2.6.

The CVD samples were fabricated by heating methane gas molecules in a reaction chamber to 1000 °C [49]. Temperatures of 900 to 1000 °C are optimum for CVD growth of graphene, with lower temperatures found to be less efficient. The use of high temperatures (900 to 1000 °C) during growth results in monolayer graphene containing both fewer defects and less multilayer flakes [141, 142]. Furthermore, higher temperature produces graphene samples of larger domain size, correlating to higher quality graphene [141]. For example, grain sizes of 1 - 5 $\mu$m were reported for graphene grown at 850 °C compared with domain sizes of up to 20 $\mu$m for the graphene studied in this work [142].

For the CVD graphene used in this work, an 18 $\mu$m thick copper foil was used a catalyst for the graphene growth. Cu is the most commonly used catalyst in CVD formation due to its low solubility, which reduces the chance of absorption of hydrocarbons onto the Cu surface, compared with other catalysts which have been used within literature [143, 144, 145, 146, 147]. Without a catalyst the reactions require temperature of over 2500 °C [49].

According to Graphenea, the carbon atoms are deposited in graphene's honeycomb lattice structure onto the surface of the Cu foil catalyst in the reaction chamber and the waste products are pumped out of the chamber. Following growth of the monolayer graphene film, it is protected with a polymer layer, polymethyl methacrylate (PMMA), which is put over the graphene sample [49]. The bottom layer of the sample is then removed, and a ferric chloride solution is used to etch the Cu foil catalyst. The graphene is then transferred onto its final substrate (in this work $Si/SiO_2$) using a so-called PMMA wet transfer assisted process. The PMMA is then removed using organic solvents, acetone and isopropyl alcohol (IPA) [49].

## 2.4 Instrumentation

All spectra were collected using an HORIBA XploRA micro-Raman instrument (Figure 2.7). A schematic of the components of the Raman instrument are shown in Figure 2.8. Within the following section the setting for each component will be discussed, as chosen to achieve the best spatial resolution (SR) and spectral quality. The SR of the Raman spectrometer is the ability of the instrument to resolve features and bands into separate components. It can be found using the following equation [148]:

$$SR = \frac{0.61\lambda}{NA} \tag{2.11}$$

A 100 x objective lens was used for all experiments, with a numerical aperture (NA) of 0.9, and a laser wavelength of 532 nm to obtain the best SR, achieving a value of 361 nm. However, Raman scattering of the laser and interactions with light and the sample can result in reduced accuracy, thus, the SR of a Raman spectrometer is usually rounded up, often quoted as 1 $\mu$m, according to instrument manufacturer

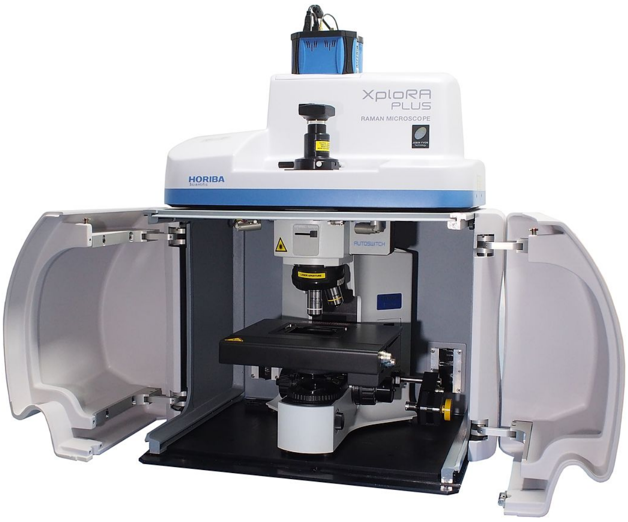

**Figure 2.7:** Raman micro-instrument XploRA PLUS. The motorised xyz-stage allowed for repositioning of the laser to random points in the sample for each spectrum. The adjustment of the hole and slit allows for confocal microscopy to be performed. The instrument is equipped with a 100 x/ 0.9 NA objective lens, used for all experiments. The 532 nm wavelength was used for the collection of all spectral data. Figure obtained from HORIBA [148].

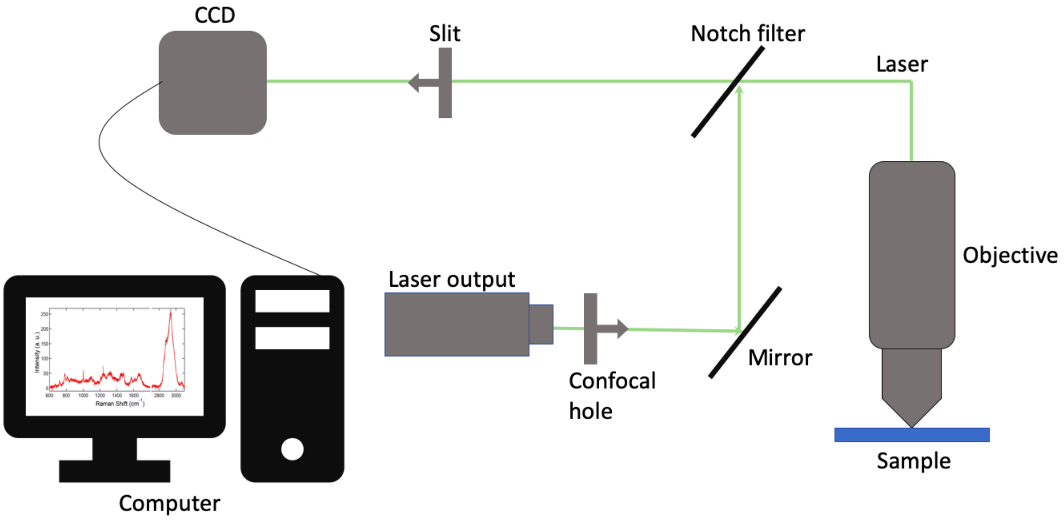

**Figure 2.8:** Schematic of a Raman spectrometer. A 532 nm green laser is used for experiments performed in this thesis. The hole and slit are adjusted to achieve confocal microscopy. A 100 x / 0.9 NA is used for data collection.

**Table 2.1:** Table of the parameters used for the acquisition of Raman spectra in this work. The laser power at the sample is an approximation.

| | **Experimental Parameters** |
|---|---|
| **Laser wavelength** | 532 nm |
| **Laser filter** | 50 % |
| **Laser power at sample** | 3.5 mW |
| **Hole** | 100 $\mu$m |
| **Slit** | 200 $\mu$m |
| **Diffraction grating** | 2400 gr/mm |
| **Exposure time** | 90 s |
| **Accumulations** | 2 |

HORIBA [148].

The equation for calculating laser spot size, in any optic system, is given by [149]:

$$d_l = \frac{1.22\lambda}{NA} \tag{2.12}$$

Therefore, the use of the green laser (532 nm) and the x 100 / 0.90 NA lens, results in a laser spot size of 721.16 nm.

All experimental parameters are in Table 2.1, including the time of acquisition, the number of accumulations and the hole and slit size used for collection of Raman spectra.

The HORIBA XploRA provides a maximum laser power-at-the-sample of 7 mW. Use of the variable notch filter allowed the power-at-the-sample to be controlled. For the experiments in this work the 50% variable filter was chosen to give an approximate laser power of 3.5 mW at the sample, as this was determined to prevent laser induced damage of the biological and graphene samples. Similar laser powers have been used by other works in literature for collection of Raman spectra, for example Keeler *et al.* and Walter *et al.* achieved laser powers of 2 - 5 mW and 5 mW at the sample respectively [150, 151]. Other works use higher laser powers. Table 2.2 includes the laser powers use by other works investigating biological samples, as well as other experimental details. Five of the 17 papers use a laser power of between 10 mW - 30 mW [77, 121, 136, 152, 153], while a similar amount utilise greater powers of between 70 mW and 200 mW [120, 123, 154, 155, 156]. A lower laser power is used in this work to ensure no laser induced damage to the cells.

Patzold *et al.* studied the effect of laser powers on biofilms and found that powers of less than 10 mW had no effect on the cells, whereas powers of 100 mW and more caused disruption of the biofilm [114, 157]. Cherney *et al.* found that laser powers of less than 30 mW did not damage biological samples [158]. The use of the laser power 3.5 mW utilised in this thesis is much less than this threshold. Both spectra and samples were checked to ensure no laser induced damage following collection.

For the collection of spectral data from graphene samples in published works, lower laser powers are used compared with those used for collection of biological spectra. For instance, as included in Table 2.3, laser powers of between 0.04 to 4 mW have been used [64]. The laser power of 3.5 mW used for the collection of data in this work falls in that range, and so is comparable with collection of Raman spectra from graphene in literature [64].

The adjustment of the hole and the slit in the Raman spectrometer allows for confocal microscopy to be performed. Specifically hole and slit sizes of 100 $\mu$m and 200 $\mu$m respectively. These settings were used for the collection of all spectra in this thesis (Table 2.1). Confocal microscopy allows for spatial filtering and control of the volume of the samples which is being analysed [148]. Higher resolution images can be obtained using confocal microscopy due to its efficiency in blocking out of focus fluorescent light [171]. Thus, confocal Raman spectroscopy is commonly used in literature [114, 172]. For example, Hermelink *et al.* used confocal Raman spectroscopy to investigate the heterogeneity within microbial populations due to the high spectral resolution of using a confocal set-up, which was 4 cm$^{-1}$, less than most other literature works (Table 2.2) [172]. Similarly a confocal set-up was used in this work, and a comparable spectral resolution achieved (3 cm$^{-1}$), however, only three spectra were collected from each bacterial sample in the work by Hermelink *et al.*, compared with the 55 collected in this work [172].

For all spectra collected in this work, an exposure time of 90 s and two accumulations were used. Increasing numbers of accumulations increases spectral quality as

**Table 2.2:** Table of details of the methods used for the collection of Raman spectra of bacteria throughout published work. This includes the bacteria and strain studied, the exposure time of the laser and accumulations (accum.) used for the collection of each Raman spectrum. The laser power, $\lambda$ the laser wavelength, and the spectral range over which the data is collected are included. The magnification and numerical aperture (NA) of the lens, the grating used and the corresponding spectral resolution (res.) for the data are listed. The growth time of the bacteria and cell state (live or dead) is stated. The bacteria are *Staphylococcus epidermidis* (*S. epidermidis*), *Escherichia coli* (*E. coli*), *Staphylococcus aureus* (*S. aureus*) and *Enterococcus faecium* (*E. faecium*).

| **Bacteria** | **Strain** | **Power (mW)** | **Exposure / Accum.** | **Lens / NA** | **Growth time or OD** | **Dried or live** | **Spectral range (cm$^{-1}$)** | **$\lambda$ (nm)** | **Res. (cm$^{-1}$)** | **Ref.** |
|---|---|---|---|---|---|---|---|---|---|---|
| *S. epidermidis*<br>*E. coli* | 1457 & 9142<br>K12 & Top 10 | 110 | 72 s | 50 x | 24 hr | Live - in agar | 600 - 1600 | 785 | - | [154] |
| *S. aureus*<br><br>*S. epidermidis*<br>*E. coli*<br>*E. faecium* | ATCC 29213 & UHR 28624<br>UHR 29489,<br>ATCC 25922<br>BM 4147 | 100 | 30 s | 80 x / 0.75 | 6 hr & 24hr | Both | 250 - 2150 | 830 | 8 | [155] |
| *E. coli*<br>*S. aureus*<br>*S. epidermidis*<br>*Candida albicans* | CCM 3988<br>D 47<br>STO 60<br>CCM 8261 | - | 15 s | 50 x | 24 hr | - | 600 - 1700 | 785 | - | [159] |
| *Clostridium* | - | - | 60 - 200 s | 100 x | - | - | - | 632.8 | - | [160] |
| *E. coli* | JM109 | 2 - 5 | 5 mins | 60 x & 100 x | 12 - 15 hr | Dried | 600 - 1800 | 514 | 1 - 2 | [151] |
| *E. coli* | ATCC 25922 | 28 | 60 s | 60 x | Various times | - | - | 785 | - | [152] |
| *E. coli* | DH5$\alpha$ | 5 | 60 s | - | - | - | 650 - 1703<br>2831 - 3017 | 244<br>532 | 10 | [150] |
| *E. coli* | ATCC 700926 | 30 | 5 s<br>8 accum. | - | OD600 = 0.1 | Dried | 400 - 1800 | 785 | 7 | [136] |
| *E. coli* | MG1655 | 30 | 10 s<br>3 accum. | 50 x | 15 hr | Dried | 500 - 2000 | 785 | 6 | [153] |
| | | 10 | 20 s<br>3 accum. | 50 x | - | - | - | 532 | - | |
| *E. coli* | - | - | - | 100 x<br>1.25 | - | - | - | 785 | 6 | [119] |
| *E. coli* | - | 200 | 60s<br>3 accum. | 100 x<br>1.3 | 4 - 5 hr<br>0.6 - 0.8 OD | Live - in solution | 600 - 1800 | 633 | - | [156] |
| *E. coli*<br>*E. faecalis* | KACC 10005 | 70 | 2 - 10 s | 10 x<br>0.55 | 0.17 OD | - | 400 - 800 | 633 | - | [123] |
| *S. epidermidis*<br>*E. coli* | ATCC 35984<br>ATCC 11775 | 200 | 60 s<br>3 accum. | 100 x | 18 - 20 hrs | Dried | 600 - 1800 | 532 | 6 | [120] |
| *E. coli* | DH5$\alpha$ | 20 | 25 s | 100 x | 0.4 - 0.5 OD | Dried | 600 - 3100 | 532 | 9 - 15 | [121] |
| *E. coli* | DH5$\alpha$ | 25 | 10 s | 100 x<br>0.9 | 0.3 OD | Dried | 600 - 1800 | 532 | 1 | [77] |

**Table 2.3:** Table of details of the methods used for the collection of Raman spectra of graphene throughout published work. This includes the type of graphene studied, where ME is graphene formed via mechanically exfoliation and CVD is chemical vapour deposition. The laser wavelength used and the power of the laser is included. The number of spectra collected for characterisation and the total acquisition time for each spectra, where these have been included in the papers, are also listed in the table. The magnification and numerical aperture (NA) of the lens, the grating of the instrument used and the corresponding spectral resolution for the data are listed also.

| Type of graphene | No. of spectra | Laser (nm) | Power (mW) | Lens | Grating (gr/mm) | Spectral resolution ($\mu$m) | Acquisition time (s) | Ref. |
|---|---|---|---|---|---|---|---|---|
| CVD | - | 532 | - | 50 x | - | - | - | [161] |
| ME | - | 514<br>633 | 0.04 - 4 | 100 x | - | - | - | [64] |
| CVD | - | 633 | $<$ 2 mW | 50 x | 600 | 4.6 | - | [162] |
| ME | - | 514.4 | 1 | 50 x | 1800 | 0.7 | - | [163] |
| CVD | - | - | 2 | - | - | - | - | [164] |
| CVD | - | 532 | - | - | - | - | - | [165] |
| ME | - | 514.5 | 1 | 100 x | 1800 | 5 | - | [166] |
| ME | - | - | 0.45 | - | - | - | 180 | [167] |
| ME | 100 | 532 | - | - | 1800 | 1 | - | [168] |
| CVD | 10 | 532 | - | 50 x | - | 1 | - | [58] |
| CVD | Maps | 514 | - | 50 x | - | 2 | - | [169] |
| ME | 20 | 514.5 | 0.3 | 100 x | - | - | - | [170] |

the Raman instrument accumulates a given number of measurements and averages them to produce a higher quality final result [148]. The number of accumulations were chosen to obtain the best signal-to-noise ratio without causing laser damage to the sample. Similar settings are used in literature, as can be seen in the experimental details of published works in Table 2.2. For example, both Chan *et al.* and Escoriza *et al.* perform spectral collection using 60 s acquisition over three accumulations, corresponding to the same overall collection time [120, 156]. A similar acquisition time was also used by Huang *et al.* of 180 s per spectra when investigating the effect of the substrate on graphene sample [167]. However, often the information about the acquisition time of the spectra is not included in published works, particularly for Raman studies investigating graphene (Table 2.3).

The diffraction grating, among other components such as the hole and slit, affects the spectral resolution of the instrument, a diffraction grating with more grooves per mm achieves high accuracy. The 2400 gr/mm was used for all experiments to achieve the best spectral resolution. If the resolution is too low then information could be lost, high resolution is necessary to distinguish changes in peak positions or shapes [148]. Often a 1800 gr/mm grating is used for the collection of spectral data from graphene samples, which can result in the collection less accurate spectra (Table 2.3). For instance, Bukowska *et al.* used a 1800 gr/mm for the collection of spectra from graphene samples, achieving a spectral resolution of 5 $\text{cm}^{-1}$ [166].

For collection of spectra from single *E. coli* cells Muhamadali also used a grating of 2400 gr/mm to achieve more accurate spectra, however, the exact spectral resolution is not included in the work [153]. A 600 gr/mm grating was also used in the work for collection of spectra from colonies [153]. Lack of consistent protocols results in the inability to compare data across experiments. In this thesis, the same procedures are followed for all experiments allowing for comparison across all data sets.

Prior to the collection of Raman spectra the instrument was calibrated using an Si standard sample, to ensure reliability of data. The calibration allowed for measurement accuracy of 3 $\text{cm}^{-1}$, which is the maximum error associated with the instrument [148]. Alignment of the laser was also performed prior to Raman

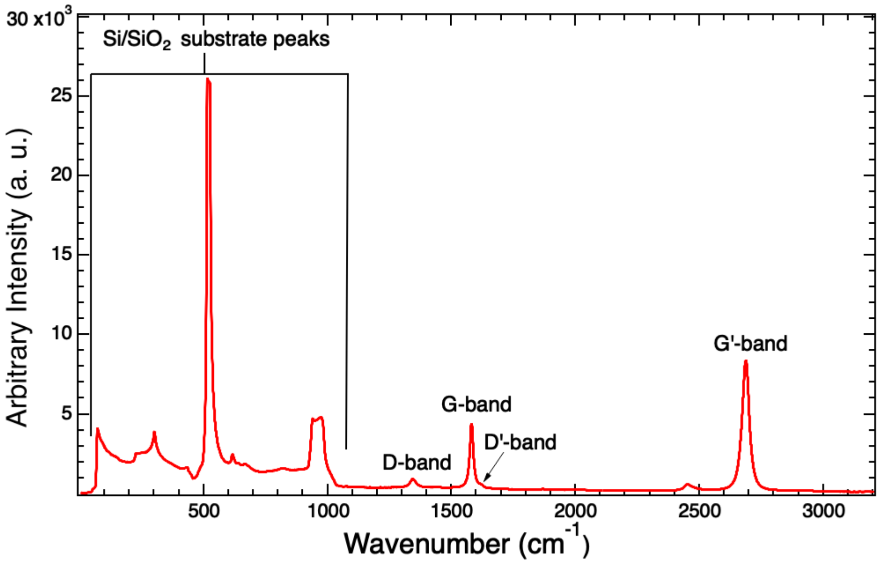

**Figure 2.9:** Full Raman spectra of graphene showing the main graphene signatures and the intense Si/SiO$_2$ signatures from the substrate. These spectral features correspond to collection of data between the wavenumbers 1200 - 1800 cm$^{-1}$ and 2400 - 2900 cm$^{-1}$.

measurements being taken for precision. Labspec 6, provided by HORIBA, was the software used for collection of all spectra. This software allowed for real time data collection of data.

To improve the quality of spectra acquired the software had a so-called dark correction which was applied to all spectra during collection. Some detectors have a fixed pattern artefact signal which is present in spectra, and can interfere with spectra with low signal. Therefore, a “dark” spectrum is acquired by the instrument, that is, a spectrum with the shutter closed so no light is actually radiating the sample, producing the fixed pattern signal only. This dark spectrum is then subtracted from the spectra, leaving only the sample signal and improving the spectral quality. This can also get rid of any external background light [148].

### 2.4.1 Raman Measurements of graphene

Four graphene samples were studied in this work using the parameters shown in Table 2.1. Three of the samples were used for the graphene interfaced with *E. coli* experiments as detailed in Section 2.5.1 for which three biological replicates were performed. One sample was used for an experiment investigating *E. coli* cultured with graphene as described in Section 2.5.2 for which one biological replicate was carried out due to PhD time restraints.

The Raman spectra of graphene were collected in ranges between 1200 - 1800 $cm^{-1}$ and 2400 - 2900 $cm^{-1}$, as this is where the predominate bands in the Raman spectra of graphene are found (Fig. 2.9) [64, 68]. The samples was checked optically following spectral acquisition to check for any laser-induced damage. Each spectrum was also monitored during collection to ensure no damage to the sample, such as the absence of the G- or G′-bands found to be characteristic of the Raman spectrum of laser-damaged graphene samples [173].

A total of 100 spectra were collected for the characterisation of each graphene sample. Most papers collect fewer spectra compared with the 100 spectra collected in this work (Table 2.3) [58, 170]. For example, Wu *et al.* collected only ten spectra at random points across the graphene sample for characterisation [58]. Comparatively Roscher *et al.* collected 100 Raman spectra when studying the differences in graphene compared with graphite powder, the same number as collected in this work [168]. However, Roscher *et al.* used a grating of 1800 grooves/mm, and so it was likely that they had a lower spectral resolution than in this work, though the spectral resolution is not stated within the work [168]. Often papers do not include the number of spectra collected for characterisation, more consistent standards are needed throughout literature to ensure reliability and clarity of data (Table 2.3) [161, 174, 175].

Random point sampling was performed in this work across the whole graphene sample, to ensure all areas of the sample are represented in the spectral average. Not all works perform characterisation of the sample in this way, some works collect spectra only from small areas of the sample [169]. For example, Zhou *et al.* collected spectra from maps focusing on small regions of the sample, limiting the level of characterisation of the sample, which is unrepresentative of the sample as a whole (Table 2.3) [169].

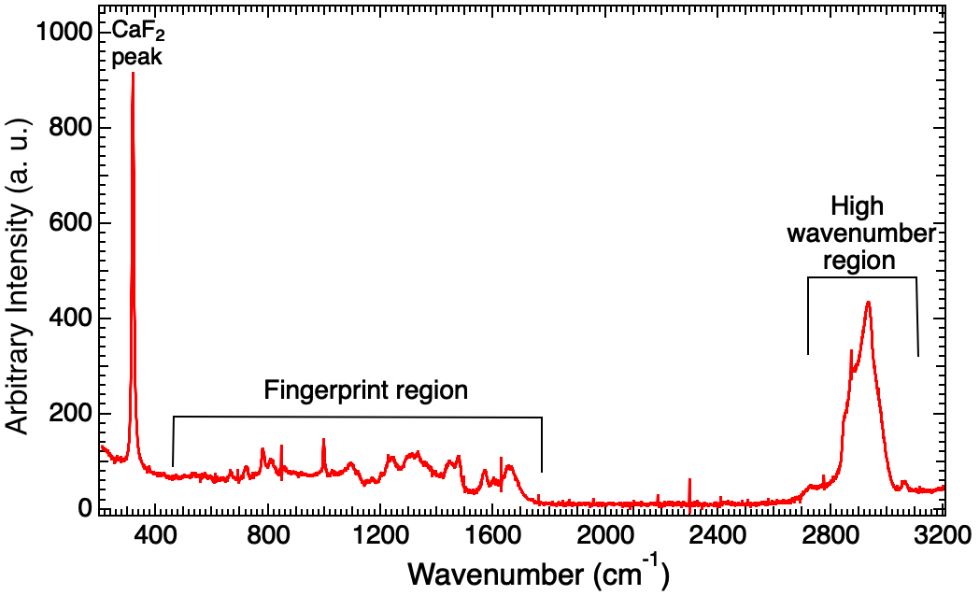

**Figure 2.10:** Raman spectrum of *E. coli* on $CaF_2$. The intense band at 319 $cm^{-1}$ is the $CaF_2$ band which does not interrupt the bands in the Raman spectrum of *E. coli*. The fingerprint region (600 - 1800 $cm^{-1}$) and the high wavenumber region (2800 - 3100 $cm^{-1}$) are labelled on the graph.

## 2.4.2 Raman measurements of *E. coli*

Following growth as described in Section 2.2, the cells were pipetted onto a $CaF_2$ disc of 1.2 mm in diameter in 5 $\mu$l droplets, and air-dried under a fume hood, ready for Raman analysis. The substrate on which the cells are deposited is of importance as Raman signatures can interfere with the bands in the Raman spectrum of the sample which is being investigated [176]. $CaF_2$ is commonly used for collection of spectra from biological samples as its Raman signal has only one band at 319 $cm^{-1}$ (Fig. 2.10) [153]. This is beneficial compared with the collection of spectra from biological samples deposited on glass, as the Raman spectra of glass has intense bands between 0 and 1500 $cm^{-1}$ which interrupt the Raman signals in the *E. coli* spectra [154, 156, 177].

The spectral range was chosen for the collection of *E. coli* spectra as it is in these regions that the bands in the Raman spectra of *E. coli* arise, 600 - 1800 $cm^{-1}$ is the so-called fingerprint region and 2800 - 3100 $cm^{-1}$ the high wavenumber region (Fig. 2.10). Published works analyse spectra collected over similar ranges, however, many works do not collect the high wavenumber region of the Raman spectra. For instance, of the published works shown in Table 2.2 only two of the twelve works have collected the high wavenumber region in the Raman spectra [121, 150]. Information could be lost due to the disregard of this region of the spectra. For example, Mlynarikova *et al.* studied the effect of the bacterial growth culture on the Raman spectra of different bacteria (Table 2.2) [159]. The high wavenumber region is rich in lipid signatures, which have been shown to vary significantly depending on growth parameters [124, 159, 178, 179]. For example, lowering the growth temperature of bacteria has been shown to cause an increase in the amount of saturated fatty acids in the cells [178, 179]. Thus, the changes in the high wavenumber region could be significant in the work by Mlynarikova *et al.*, despite this, it is not considered [159]. Both high wavenumber and fingerprint region are analysed in this thesis to ensure no information in the Raman spectra is overlooked.

A total of 55 individual Raman spectra were collected from each *E. coli* sample. Each sample is representative of a biological replicate, of which three were performed. This is more thorough characterisation than has been performed by any other work in literature. For example, Keeler *et al.* collected only 3 to 4 spectra from clusters of cells in a sample of *E. coli* when analysing the affect of UV-B and violet light on the cells (Table 2.2) [151]. This is insufficient data to represent the full population of cells, and is unlikely to fully represent the natural heterogeneity of the sample. Comparatively, Bittel *et al.* collected 45 spectra per sample when analysing the toxicity of the cells to arsenic exposure [136]. While this is similar to the amount collected in this work, Bittel *et al.* only achieved a spectral resolution of 7 $\text{cm}^{-1}$, compared with 3 $\text{cm}^{-1}$ in this work [136]. Moritz *et al.* collected 75 Raman spectra for characterisation of *E. coli*, however, only one biological replicate was performed, thus reproducibility has not been demonstrated [152].

Many works do not provide information on the number of spectra collected for characteriation purposes. For example, Wu *et al.* refers to “several” spectra being collected per sample, but does not specify exactly how many when analysing nucleic acids in *E. coli* using Raman spectroscopy [180]. The number of spectra collected from bacterial samples is significant due to the heterogeneity that can be present in samples of bacteria. It is necessary to collect sufficient amounts of data that

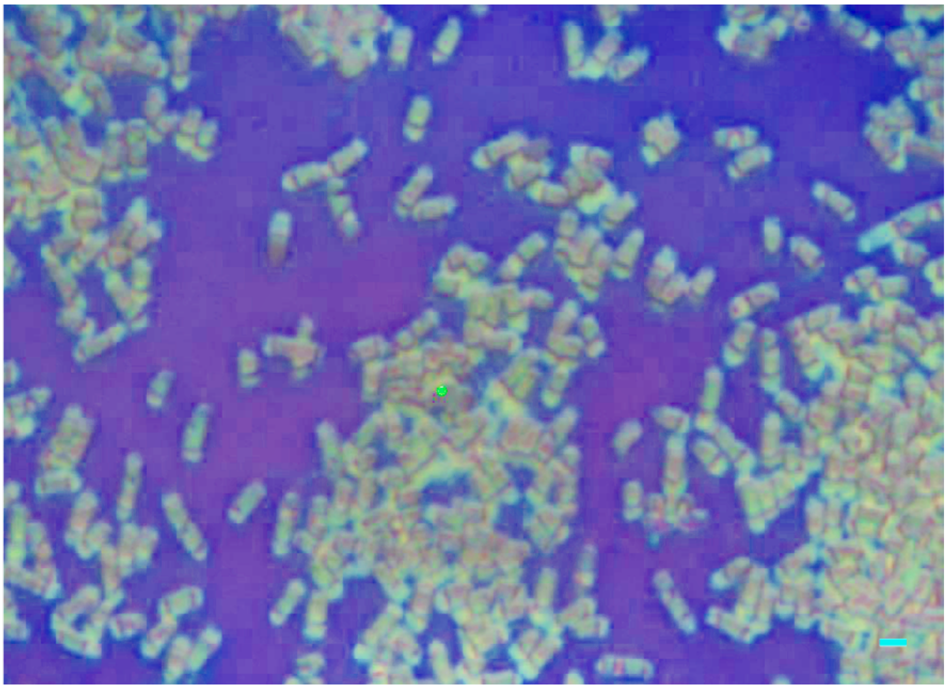

**Figure 2.11:** *E. coli* interfaced with graphene. The *E. coli* was grown to $OD_{600}$ = 0.4 - 0.6, when the cells are in the exponential growth stage. The cells were then pipetted onto CVD graphene to interface and left to dry, ready for Raman analysis. The scale bar is 2 $\mu$m.

this heterogeneity is represented in the spectral average, as is done in this work through collection of 55 Raman spectra from random cells per biological replicate. The standard error and second order standard deviation were analysed to ensure thorough characterisation was achieved.

## 2.5 Assessment of the Antimicrobial Properties of graphene

### 2.5.1 *E. coli* Interfaced with Graphene

Following growth of *E. coli* as described in Section 2.2, the bacterial culture was pipetted onto the 1 $cm^2$ graphene sample in 5 $\mu$l droplets, and left to dry under the fume hood. This is the same method as was done for the characterisation of *E. coli*, however, a $CaF_2$ disc was used instead of the graphene (Sect. 2.2).

After preparation of the graphene-cell sample the Raman spectra were then collected from random cells across the graphene sample. The *E. coli* on $CaF_2$ will be used as a control for this experiment, therefore, any changes in the Raman spectra compared with the *E. coli* dried on the $CaF_2$ can be assumed to be caused by cell death due to graphene. Three biological replicates were carried out on three separate graphene samples. The graphene samples were characterised prior to use, the details of which can be found in Section 2.4.1. A total of 45 - 55 individual Raman spectra were collected from each replicate. This was the maximum possible number of spectra it was possible to collect for each experiment due to the overall time required for experimental set-up and spectral collection. A optical image of the *E. coli* on the graphene surface can be seen in Figure 2.11.

Li *et al.* also used the approach of spreading bacteria onto a CVD graphene surface to test the antimicrobial properties [71]. The bacteria was left to incubate on the surface for 24 hours at 37°C, following which the viability of the bacterial cells were tested using scanning electron microscopy, however, given the long incubation time much of the nutrients in the cell media would have become depleted, with cells entering the so-called death phase (Section 2.2) [135]. Therefore, cell death may also be attributed to depleted nutrients due to 24 hour growth period [71]. The growth time used in this work was chosen to produce cells at their most viable state, in the exponential growth stage (Section 2.2), more appropriate for use in antimicrobial testing.

### 2.5.2 *E. coli* Cultured on Graphene

This experimental design involves analysis of *E. coli* cultured with CVD graphene samples. Following growth of the *E. coli* as described in Section 2.2, 20 $\mu$l of the bacterial culture was pipetted onto the CVD graphene sample, which was placed in a 24 well plate. The volume of 20 $\mu$l was used as this was sufficient bacterial culture to cover the graphene sample without immersing the graphene in liquid. The 24 well plate was then placed into a swing-out rotor centrifuge, and the samples were spun at 2010 rpm for 10 min. A gentler centrifugal force was chosen compared with the spinning down of cells (6,000 rpm) for harvesting during the cleaning process (Section 2.2) due to the cells undergoing centrifugation for a longer period.

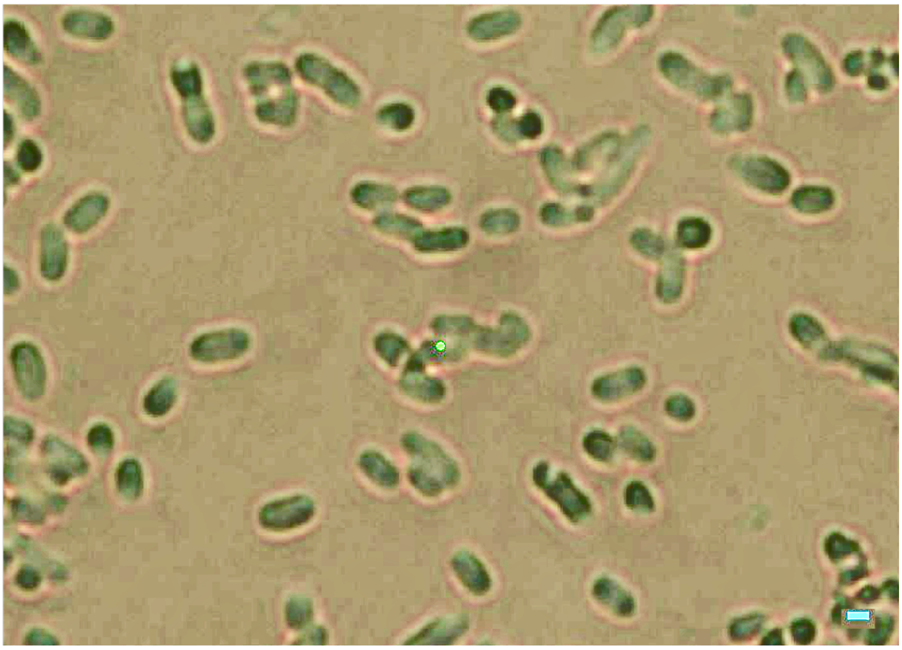

**Figure 2.12:** *E. coli* dried onto $CaF_2$ after being cultured on graphene. The bacteria culture was been spun down onto the CVD graphene in a 24 well plate which was left to interface for 1.5 hours in an incubator at 37 °C. The cells were then washed from the surfaced and pipetted onto $CaF_2$ for Raman analysis. The scale bar is $1\mu$m.

The centrifuge was evenly weighted with a further 24 well plate containing sterilised water. This process was required to spin the *E. coli* cells down onto the graphene samples, ensuring that cells were in direct contact with the graphene. This does not appear to have been done previously within published works. By spinning the cells down onto the graphene the chance of interaction between the cells and graphene is significantly increased.

Following spinning the cells down onto the sample, the 24 well plate was placed in the incubator for 1.5 hours to allow the bacteria time to interface with the graphene. The other wells were filled with sterilised water to avoid evaporation of media.

After the interfacing period, the bacteria culture was pipetted from the graphene surface. The cells were spun down at 6000 rpm for 5 min and washed twice in sterilised water to ensure all EZ rich media was washed off the cells. Following this, the *E. coli* was pipetted onto a $CaF_2$ disc of 1.2 mm in diameter, in $5\mu$l droplets, and air-dried under a fume hood, ready for Raman analysis, as was done with the *E. coli* cells for characterisation purposes in Section 2.2. A total of 55 individual

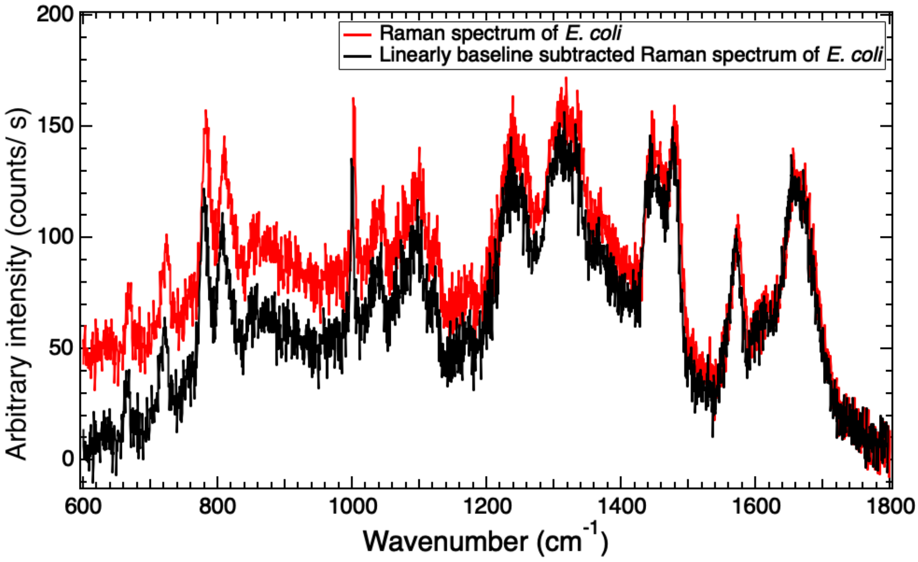

**Figure 2.13:** Graph showing a single Raman spectrum of *E. coli* before (red) and after (black) linear baseline subtraction for the purpose of removal of auto-fluorescence. Linear baseline subtraction is performed in Raman Toolset prior to any analysis being carried out on the spectra.

Raman spectra were collected from random points all across the sample, using the parameters shown in Table 2.1. A optical image can be seen in Figure 2.12. Only one biological replicate was performed for this experiment due to time limitations of the PhD.

## 2.6 Data Analysis

Data analyses including peak fittings, convergence tests, interpolation and averages were performed using Igor Pro 6, 7 and 8. Linear baseline subtraction, cutting spectra, normalisation and smoothing was carried out using Raman Tooslet. Principal component analysis (PCA) was performed using R Studio. Graphs and figures were made in Igor Pro, with the exception of the PCA plots which were produced in R studio.

## 2.7 Peak fittings

Prior to fittings being performed all Raman spectra are averaged and linear baseline subtracted using Raman Toolset, to remove background fluorescence from the sample. An image of the fingerprint region (600 - 1800 cm$^{-1}$) for a single *E. coli* spectrum before and after linear baseline subtraction is shown in Figure 2.13.

Linear baseline subtraction has also been performed in published works, for example Frank *et al.* carried out linear baseline subtraction on the Raman spectra of graphene when performing characterisation using Raman spectroscopy [181]. However, higher order baseline subtractions are also used in published works, particularly for use on the Raman spectra of biological samples [182]. For example, Ho *et al.* performed fifth order polynomial baseline subtraction when utilising Raman spectroscopy for identification of bacteria [182]. For the spectra in this thesis, linear baseline subtractions of the data were compared with other higher order polynomial baseline subtractions, such as third and fifth order polynomials, however, it was found that baseline subtractions using higher order polynomials were not as reproducible as those carried out with a linear line, and so linear baseline subtraction was chosen, and performed on all data prior to fittings.

Fittings were performed on the average spectrum for each sample. From these fittings, three quantities were obtained: the location, amplitude and full width at half maximum (FWHM) of the bands. In order to determine the most optimal fit for the bands in the Raman spectra, the residuals of fittings performed using different models were compared. The residual is the difference between the original wave and the model fit, therefore the worse the fit, the larger discrepancy between the model and the data. The fit which produces the residual of lowest magnitude indicates that the variance between the fit and the original data is lowest, i.e., it gives the best fit, and is chosen. All fittings are performed using a linear baseline.

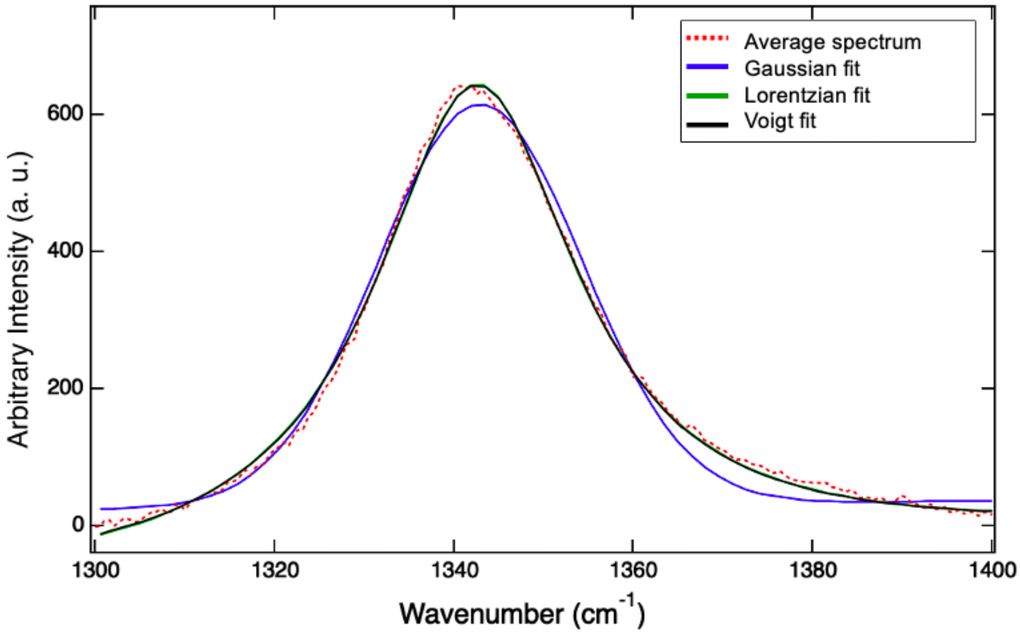

**Figure 2.14:** Fitting of the D-band using Gaussian, Lorentzian and Voigt peaks. Comparison of these fittings shows that the Gaussian results in the least optimal fit of the original data, while Lorentzian and Voigt models produce equally optimal fittings of the data.

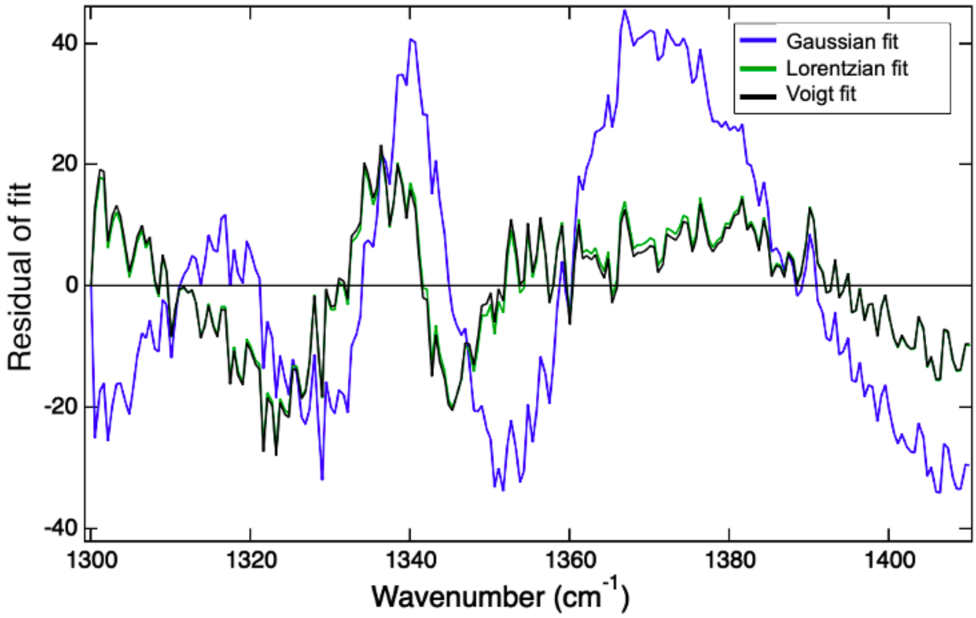

**Figure 2.15:** Residuals produced from fittings of the D-band shown in Figure 2.14. The Gaussian fit produces the residual of the largest magnitude, meaning it is the least optimal. The Lorentzian and Voigt fittings result in residuals of the same magnitude, and so give equally good fits of the data.

### 2.7.1 Peak fittings of CVD graphene

#### Peak fittings of the D-band

The so-called D-band in the Raman spectrum of graphene is located at ~1350 cm$^{-1}$ (Fig. 2.9). For the D-band three model fittings were performed, Gaussian, Lorentzian and Voigt. The fitting results are shown in Figure 2.14, and the corresponding residuals are shown in Figure 2.15.

The Gaussian fit gives the worst result for the data (Fig. 2.14), the fit is least similar to the original data and produces a residual of the highest magnitude (Fig. 2.15). The fittings of the D-band in the Raman spectrum using Lorentzian and Voigt models are of comparable quality, producing residuals of similarly low magnitudes (Fig. 2.15). Both provide a close representation of the original data, therefore it is possible that either of these fits could be chosen for this band.

A Lorentzian fit is chosen for fitting of the D-band, as this fit is commonly utilised throughout the literature [181, 183, 184]. For example, Frank *et al.* fitted the D-band with a Lorentzian profile following linear baseline subtraction of the data, when investigating defects in graphene samples [181]. The fit also produced one of the residuals of lowest magnitude (Fig. 2.15).

#### Peak fittings of the G- and D′-bands

The G-band arises in the Raman spectra of graphene at ~1590 cm$^{-1}$ (Fig. 2.9). Defects in a graphene sample results in the emergence of the D′-band in the Raman spectra of graphene which appears as a “shoulder” on the G-band at ~1620 cm$^{-1}$ [36]. Therefore, the G- and D′-bands must be fitted together and deconvolved [66].

It is essential to first deduce which fit is best for the D′-band. The fittings of the D′-band with a single Lorentzian and Gaussian profile can be seen in Figure 2.16, with the corresponding residuals in Figure 2.17. From these fittings it appears that the Gaussian is a much better representation of the data. Examining the residuals (Fig. 2.17) indicates that the Gaussian fit produces a marginally smaller residual than the Lorentzian. Consideration of the residual alongside the fitting in Figure 2.16 indicates that the Gaussian is the most optimal fit of the D′-band.

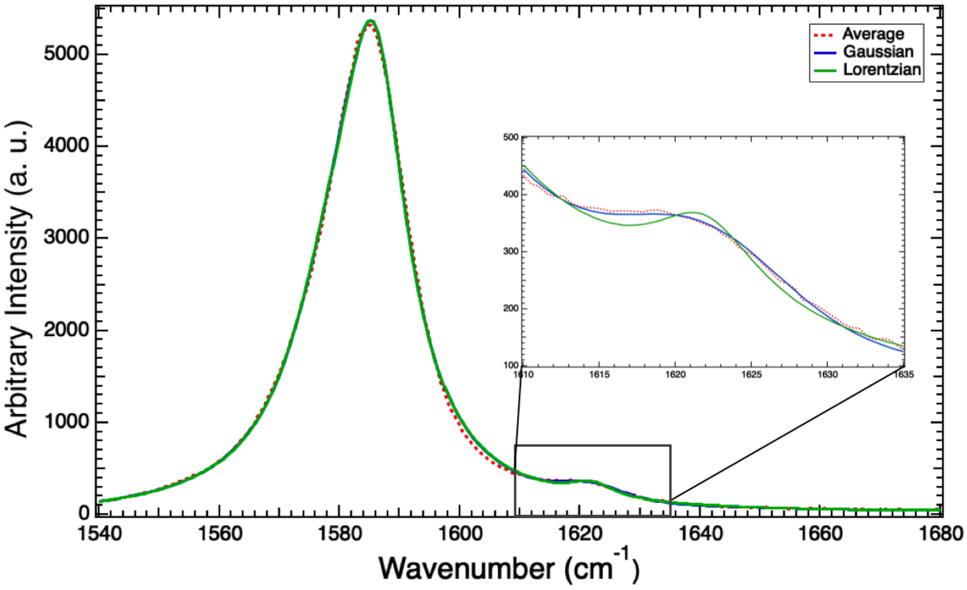

**Figure 2.16:** Fittings of the D′-band in the average Raman spectrum of graphene which comprises 100 individual Raman spectra. The fittings have been performed using a Gaussian and a Lorentzian model to determine which gives the most optimal fit. The fitting of the G-band has been performed using a double Lorentzian. The inset image shows a zoomed in picture of the fit of the D′-band.

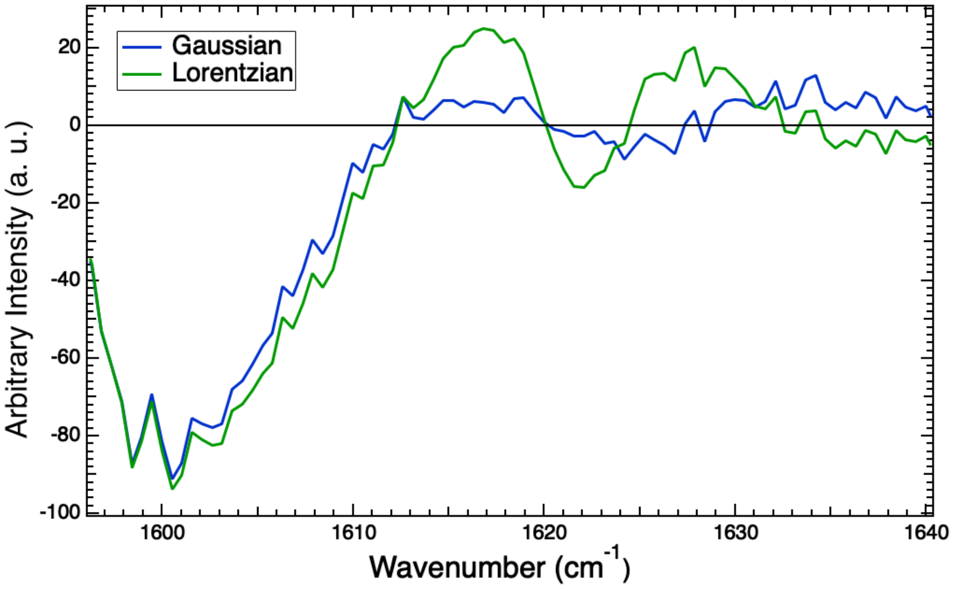

**Figure 2.17:** Residuals of the fittings of the D′-band in the Raman spectrum of graphene using a Lorentzian and a Gaussian. The Gaussian produces the small residual, thus gives the more optimal fit.

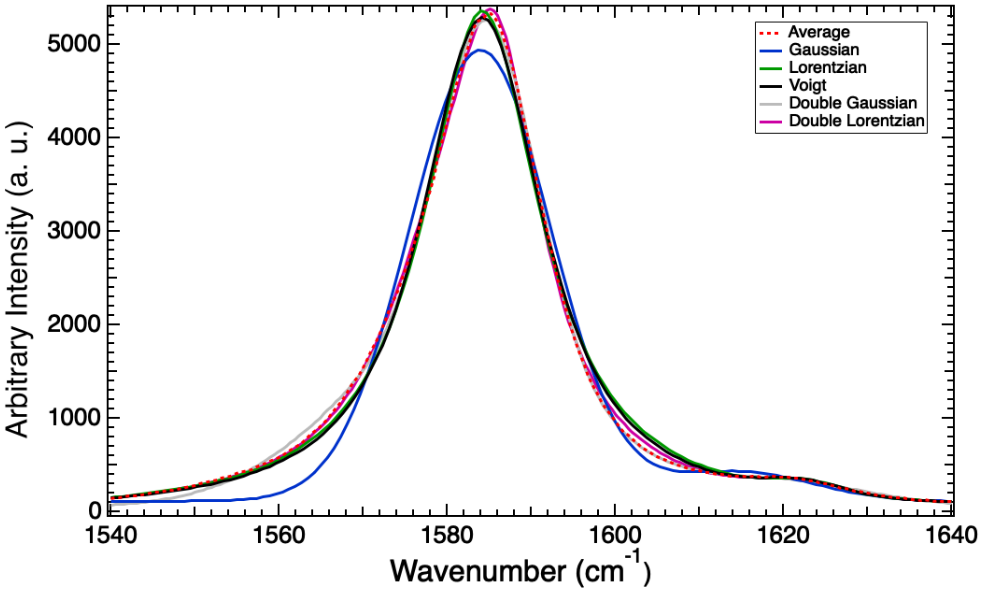

**Figure 2.18:** Fittings of the G-band in the average Raman spectrum of graphene which comprises 100 individual Raman spectra. The fittings have been performed using different models to determine which achieves the most optimal fit. The D′-band has been fitted with a Gaussian.

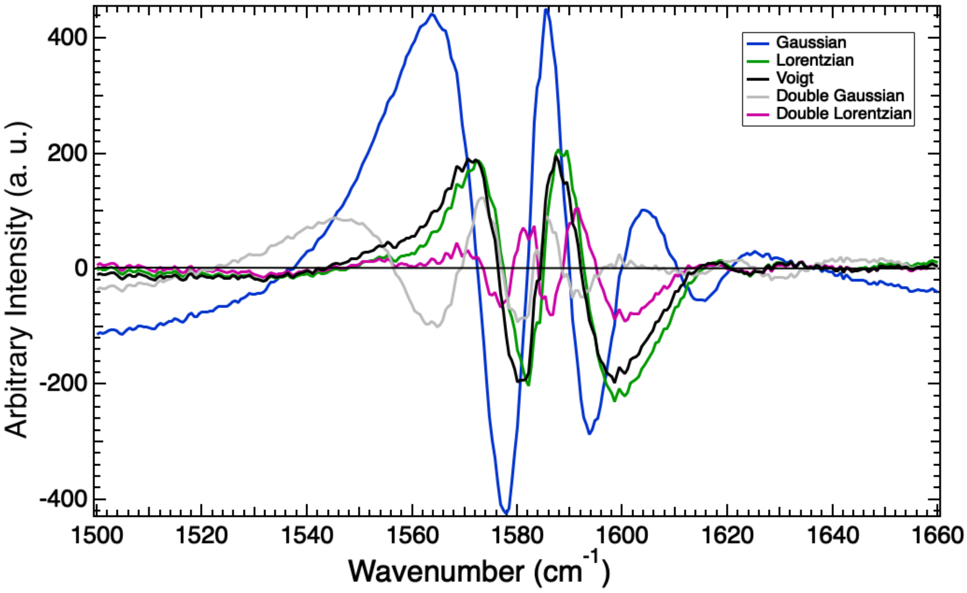

**Figure 2.19:** Residuals of the fittings of the G-band and the D′-band in the Raman spectrum of graphene. The double Lorentzian produces the small residual, thus gives the more optimal fit. The fitting of the D′-band is performed using a Gaussian.

The G-band in the Raman spectra of graphene is fitted with many different models, including single Lorentzian, double Lorentzian, Voigt and Gaussian to determine which provides the best fit for the data. The fittings can be seen in Figure 2.18, with the resultant residuals in Figure 2.19. For these fittings the D′-band has been fitted with a Gaussian as this was deemed the best fit for this band (Fig. 2.16).

The G-band fit using a Gaussian profile produces the worst result (Fig. 2.18). The model is not a good representation of the data and it produces a residual of large magnitude. The fitting using a single Lorentzian produces the second worst fit for the data, despite this being widely accepted as the best fit for the G-band in the Raman spectra of graphene [170, 174, 185]. For example, Kalbac *et al.* performs the fittings of all bands in the Raman spectra with a Lorentzian profile when investigating the electron-hole doping of graphene [174]. Fittings of the G-band with a single Lorentzian model was also reported by Graf *et al.* due to the G-band appearing as a single symmetrical band when performing characterisation of micromechanical exfoliated graphene [185]. However, neither of the works perform any analysis to determine if this is the best fit for the data [174, 185].The fitting of the G-band shown in this thesis using a Lorentzian profile is not appropriate given the large residual it produces.

A Voigt profile produces an equally bad fit for the G-band in the Raman spectrum (Fig. 2.18). A Voigt fit is also commonly used in published works for fitting of the G-band [166, 167, 186, 187, 188]. For instance, Wang *et al.* fitted the G-band with a Voigt profile when analysing the effect of substrates on the Raman spectra [188]. Berciaud *et al.* and Bukowska *et al.* fitted the G-band with a Voigt model, however, within both works the Gaussian component of the Voigt profile is kept at a constant FWHM of 8 cm$^{-1}$ in order to account for the spectral resolution of the instrument [166, 187]. However, this limits the amount of data which can be obtained from the fitting of the G-band in these works. This is also a high spectral resolution, almost three times the value achieved in this work (3 cm$^{-1}$) [166, 187]. For the spectra presented in this thesis, the fitting of the G-band with a Voigt profile is not a good representation of the data, given the large residual the fitting produces (Fig. 2.19).

The best fitting for the G-band is with a double Lorentzian profile (Fig. 2.18).

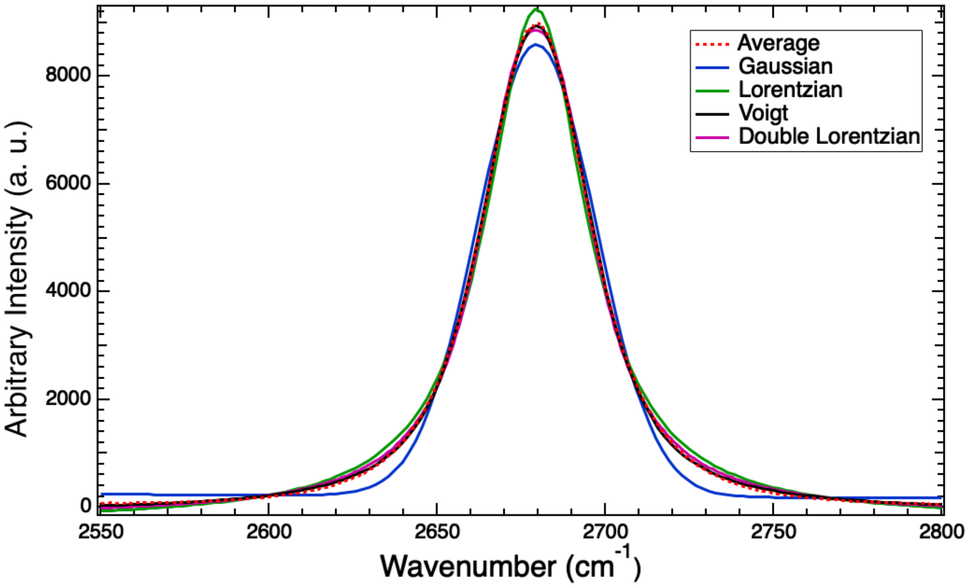

**Figure 2.20:** Fittings of the G′-band in the average Raman spectrum of graphene which comprises 100 individual Raman spectra. The fittings have been performed using a Gaussian, Lorentzian, Voigt and double Lorentzian model to determine which gives the most optimal fit.

This fitting produces the best representation of the data and also achieves the smallest residual compared with the other fittings (Fig. 2.19). Fitting of the G-band with a double Lorentzian has been reported in literature [59, 162]. Matsubayashi *et al.* fitted the G-band with a double Lorentzian due to the asymmetric contributions of the band, which are attributed to localized charge inhomogeneity within the laser probe area and inhomogeneous doping of the graphene sample from the Si/SiO$_2$ substrate, likely to also be the cause of the double Lorentzian being the optimal fit in this work [189] Therefore, the double Lorentzian fitting for the G-band and a single Gaussian for the D′-band are chosen, as they are the best representation of the data and produced the residual of lowest magnitude.

### Peak fittings of the G′-band

The fittings of the G′-band were tested with a single Lorentzian, double Lorentzian, single Gaussian and Voigt model to determine the most optimal fit (Fig. 2.20). The corresponding residuals are shown in Figure 2.21. The fitting of the G′-band with a single Lorentzian and a single Gaussian are the least optimal for the data, reflected in the large residuals produced (Fig. 2.21). Many papers performed fitting

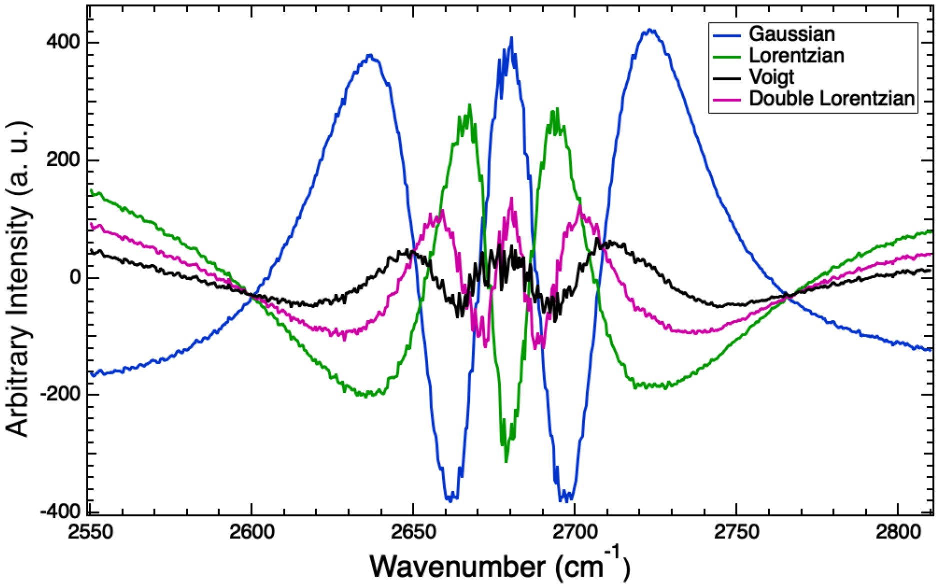

**Figure 2.21:** Residuals of the fittings of the G′-band in the Raman spectrum of graphene using a Gaussian, Lorentzian, Voigt and double Lorentzian. The Voigt produces the small residual, thus gives the more optimal fit for this sample.

of the G′-band in the Raman spectra of graphene with a single Lorentzian profile [36, 162, 164, 170, 174, 175, 187]. It has been noted that fitting of the G′-band with a single Lorentzian is characteristic of single layer graphene (SLG) [162, 175]. For example, Boyd *et al.* fits the G′-band in the Raman spectra of graphene with a single Lorentzian due to its symmetric shape, however, no analysis is performed to determine the best fit for the data [175]. Given the large residuals obtained for both the Lorentzian and Gaussian fits, neither of these profiles will be used for fitting of the G′-band in this work.

The fitting of the G′-band is most optimal when performed using a Voigt fitting, with the double Lorentzian profile producing the second best fit of the data (Fig. 2.20). This is reflected in the residuals, with the Voigt fitting producing the smallest residual and the double Lorentzian the second smallest residual (Fig. 2.21). However, this is not the case for all graphene samples that have been studied within this work. The sample shown here, and one further sample are best fitted with a Voigt fitting, however, for two of the other samples more optimal fits of the G′-band were achieved with double Lorentzian models (Appendix: Figure A.1). The fitting of the G′-band with a Voigt model has been used before in literature [166, 167, 168, 188].

For instance, Bukowska performed the fittings of all bands with a Voigt profile when investigating the Raman spectra of graphene on different substrates [166]. Roscher *et al.* used the symmetric Voigt profile to fit the G′-band in the Raman spectra of graphene and graphite, when utilising fitting methods to characterise the number of layers in a graphene sample [168]. Roscher *et al.* found that the Voigt fitting was optimal for the graphene spectra, similarly to the fitting results seen in this work.

The fit of the G′-band with a double Lorentzian is not often seen in literature. Thus, this work appears to be the only work which utilises a double Lorentzian fit on the G′-band. The fitting with a double Lorentzian is seen for polarised Raman spectroscopy, due to splitting of the G′-band from strain in the sample [190]. For instance, Yoon *et al.* examined strain in a graphene sample using polarised Raman spectroscopy and found the G′-band splits into two bands, best fitted with a double Lorentzian model [190]. Thus, the most optimal fit being achieved with a double Lorentzian may be indicative of strain in the sample.

In this work, due to the Voigt and double Lorentzian fits being the most optimal for two of the graphene samples each, the fittings of the G′-band is performed using both models, and the analysis of both is performed accordingly. Following extensive literature searches it does not appear that any other work has performed more than one type of fit on the bands in the Raman spectra of graphene, as has been done here. This thorough analysis of the data will ensure that no information in the Raman spectra is overlooked.

### 2.7.2 Peak fittings of *E. coli*

Many of the bands in the Raman spectra of *E. coli* are convoluted, and fittings of the bands must be performed to deconvolve the bands. This is common for the Raman spectra of biological samples due to the complexity of the cells. For example, a paper which studied human mammary epithelial cells deconvolved all bands in the Raman spectra using individual Lorentzian fits to obtain the position and linewidth of the bands [191]. Little work has been done in the literature to optimise fittings of the bands in the Raman spectra of biological samples, and many papers do not include details of which models were used for the fitting of bands. For example,

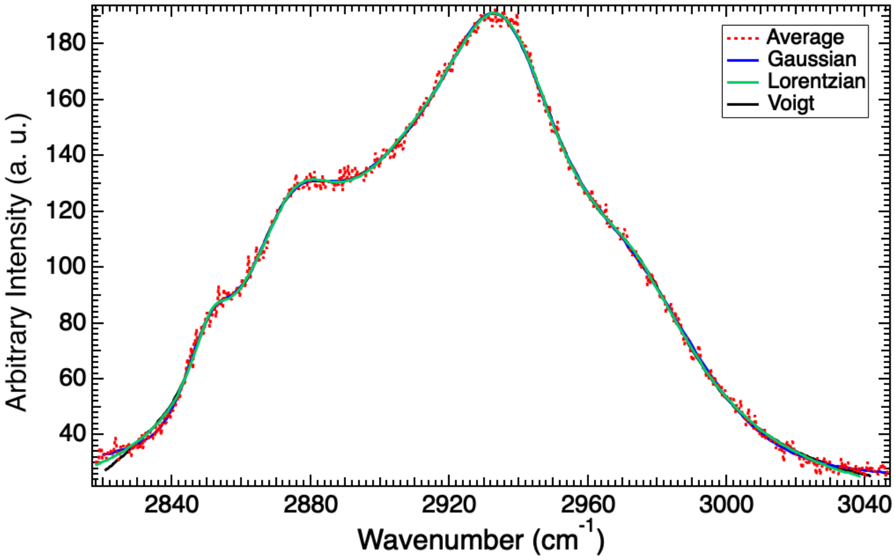

**Figure 2.22:** Fittings of the high wavenumber region of the average Raman spectrum of *E. coli*, which is one of three biological replicates. The fittings are performed using different models for determination of the best fit, Lorentzian, Gaussian and Voigt models. Each profile produce equally optimal fits, thus overlay each other.

Zu *et al.* performs peak intensity ratio analysis of the bands in the Raman spectra of *E. coli* before and after being exposed to alcohol 1-Butanol, however, no details are provided on the type of fittings used for the bands to extract the necessary information [121]. Here, the residuals will be compared for fittings performed using different models to determine the best fit for the data, as is not often done within literature.

As a sample region in the Raman spectra of *E. coli*, the high wavenumber region will be used to demonstrate the fitting and deconvolution of the bands using different models. This region will be used as it is most complex, thus provides the most stringent test for the optimisation of fitting types.

The fittings of the high wavenumber region of the average *E. coli* spectrum with Lorentzian, Gaussian and Voigt models are shown in Figure 2.22. Each of the models provide equally optimal fittings, thus overlay each other. The corresponding residuals are shown in Figure 2.23. The residuals each have a similar magnitude for all fitting types, confirming that the fitting of the different models are comparable in quality. Different fitting types are used on biological samples throughout literature.

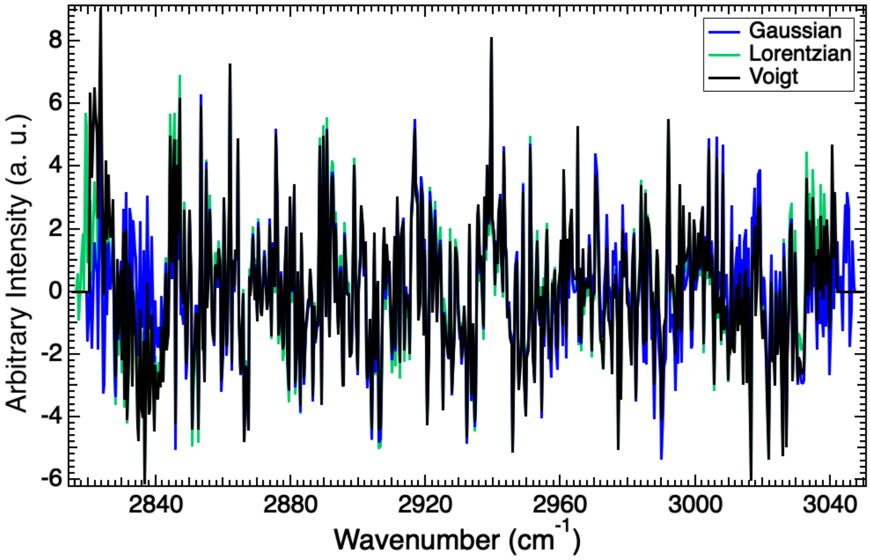

**Figure 2.23:** Residuals of the fittings of the high wavenumber region of the average Raman spectrum of *E. coli*, which is one of three biological replicates. The fittings are performed using different models for determination of the best fit, Lorentzian, Gaussian and Voigt models. Each profile produce equally optimal fits, thus the residuals overlay each other.

Ghiata *et al.* fitted the bands in the Raman spectra of biological tissues with a Gaussian profile in work which analysed the changes in the Raman spectra when the tissues underwent heat treatment [192]. Thus, given the equally optimal fit produced by the Gaussian fit, this model will be used throughout this work for the fitting of each of the bands in the Raman spectra of *E. coli*. The deconvolution of the bands in the high wavenumber region of the average Raman spectrum of *E. coli* is shown in Figure 2.24.

The criteria for band fitting in the Raman spectra of *E. coli* was to achieve the best possible fit with the minimum number of bands feasible. This criteria was followed for all fittings to ensure the bands were not over-fitted.

### 2.7.3 Peak Intensity ratios

Peak intensity ratios (PIRs) are found by dividing the amplitude of one band by the amplitude of another. That is, the peak intensity ratio I of the two bands A, with an intensity $I_A$ and B, with an intensity $I_B$ is given by $I = I_A / I_B$. The amplitudes are obtained from the fittings of the bands.

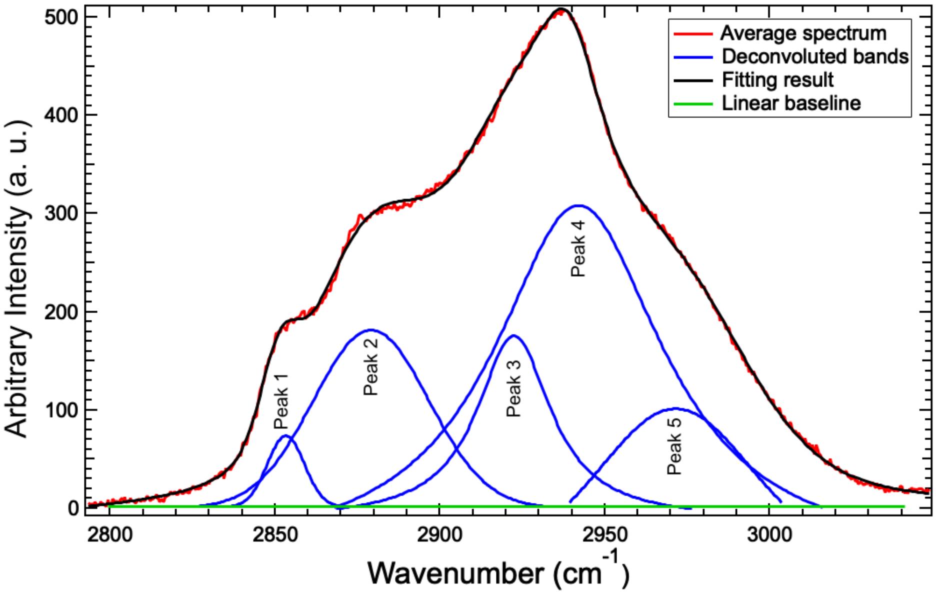

**Figure 2.24:** Deconvolution of the bands in the high wavenumber region of the average Raman spectrum of *E. coli*. The bands are fitted with Gaussian profiles as this was shown to be the most optimal fitting type.

### 2.7.4 Error Analysis

To determine the standard error of the mean of the quantities obtained from peak fittings, location, amplitude and FWHM of the bands in the Raman spectra, the standard error (SE) wave of the average spectrum is used. The average + SE wave and the average - SE wave is representative of the SE envelope, included on all graphs through this work. This can be seen on the average Raman spectrum in Figure 2.9. To obtain SE values for the quantities obtained from fittings the SE envelope is fitted. This involves fitting the average + SE and the average - SE, which produces two SE values for location, amplitude and FWHM of each band. The value which has the larger magnitude is used for the SE value for the given quantity. This is done for the location, amplitude and FWHM for all bands in Raman spectra discussed throughout this thesis.

The error of the associated PIR, I, of bands A and B with intensities $I_A$ and $I_B$ respectively is calculated using the equation

$$\Delta I = I\sqrt{\left(\left(\frac{\Delta I_A}{I_A}\right)^2 + \left(\frac{\Delta I_B}{I_B}\right)^2\right)} \tag{2.13}$$

where $\Delta$ represents the error of each corresponding quantity.

## 2.8 Principal Component Analysis

Principal component analysis (PCA) is a multivariate statistical tool that reduces the dimensionality of a data set, while retaining most of the information in order to determine similarities or differences within the data. PCA reduces the data to fewer dimensions by geometrically projecting the data onto lower dimensions, known as principal components (PCs), in order to represent the data using a limited number of PCs. The PCs represent the variability of all of the variables in the original data set. Let $X_1, X_2, ...X_p$ be a set of $p$ variables, where $p = 0, 1, ....$ PCA defines a new set of variables $Y_1, ....Y_K$, where $k = 0, 1, ....$ and $k < p$. The Y variables are made up of linear combinations of the X variables, i.e.,

$$Y_i = a_{i1}X_1 + .... + a_{ip}X_p \tag{2.14}$$

These are the PCs of the data. The first PC $Y_1 = a_{11}X_1 + ... + a_{1p}X_p = \mathbf{a_1'X}$ is defined such that it is the linear combination which encapsulates the largest amount of variance of the original data set. The second PC $Y_2 = a_{21}X_1 + ... + a_{2p}X_p = \mathbf{a_2'X}$ represents the next largest amount of variance in the data set, subject to $\mathbf{a_2'a_2} = 1$ and $\mathbf{a_2'a_1} = 0$, and so on for the remaining PCs. Each of the PCs are independent of one another, or in the geometrical interpretation they can be thought of as being orthogonal to one another. This condition means that the number of PCs is limited to either the number of samples, or the number of features, whichever of the two is smaller. It also means that no information is duplicated in the PCs.

The coefficients $\mathbf{a_1'X} = a_{11}, a_{12}, .....a_{1p}$ of the first PC are known as the component loadings. Similarly for the second and subsequent PCs. The loading can be used to interpret the components and provides information on the variables which are significant for the given PC.

Plots of the PCs in three dimensional PCA space are used to distinguish if the PCs are related to one another. The positioning of the loadings in PCA space provides information on how each of the components correlate to one another. Separation of the data demonstrates a lack of correlation across the PCs, i.e., the samples vary. When PCA is performed on Raman spectra the loadings appear as a spectral wave, therefore, the bands which differ between samples can be found through examination of the loading vectors.

Prior to PCA being performed in R Studio, the data must be preprocessed. Firstly the spectra are cut so that all data are within the same range, in order to ensure that separation did not occur due to differing lengths of waves across and within samples. Following this, the data is then linearly baseline subtracted, to subtract any fluorescence from the data. The spectra are also interpolated which creates a common x-wave and number of channels for all data in the set, across experimental days and samples. If all data do not have the same x wave and number of points it is not possible to perform PCA.

Only relative intensities are considered in Raman spectra and so all spectra are normalised prior to PCA. The spectra are normalised to the total area of the spectra. Many different kinds of normalisation are performed on Raman spectra in published works, here total spectrum area has been used as it allows for comparison of all spectra collected across different days and conditions. Sapers *et al.* performed normalisation to the band at $\sim$1460 cm$^{-1}$ in the Raman spectrum of *E. coli* [193], however, normalisation to a band is not appropriate in this work as some bands may disappear as a result of cell interaction with graphene.

Smoothing is also performed on the spectra using a cubic spline so that the noise and cosmic spikes do not interfere with the results of the PCA. Cosmic spikes are common in Raman spectra and arise from cosmic rays hitting the detector in the Raman spectrometer [194]. Due to the number of spectra collected in this work, the noise is reduced in the spectral average, however, PCA considers single spectra, thus, noise can also interfere with the analysis of Raman spectra, specifically for biological samples due to the low intensity of bands in the Raman spectra [194].

These preprocessing steps are performed to ensure that any discrimination is a result of the characteristics of the spectra. PCA is commonly used for the investigation of biological samples using Raman spectroscopy. For example, Hamasha *et al.* utilised PCA to discriminate between different strains of *E. coli* [195]. Separation was achieved in PCA space indicating the ability of Raman spectroscopy to discriminate between strains of bacteria. Similarly to the treatment of the spectra performed on the spectra in this work prior to PCA, Hamasha *et al.* also performed normalisation and baseline subtraction before PCA [195]. Normalisation to the maximum intensity of the band was utilised. Cubic and quadratic smoothing was also performed on the spectra, similarly to this work which used cubic smoothing [195].

When performing PCA any outliers in the dataset were identified and checked. If any of the outliers were deemed to be abnormal, for instance any spectral data with a low signal to noise ratio, they were removed from the dataset so as not to interfere with the analysis and skew the corresponding results.

## 2.9 Convergence Tests

In this work, the standard error (SE) and second order standard deviation (2SD) of the data are analysed to determine if enough data has been collected that the spectral average is sufficiently representative of the sample. These so-called convergence tests involve plotting of the SE and 2SD waves for increasing numbers of spectra in the average spectrum. Specifically, the average waves for increasing numbers of spectra in the average spectrum are produced, along with the corresponding SE and 2SD waves. For example, the spectral average for ten random spectra is produced, with the corresponding SE and 2SD graphs. Then an average of 20 random Raman spectra is made, again with the associated errors graphs. This is then done for increasing numbers of spectra, until the SE and 2SD graphs converge to a point such that the quantities cannot be reduced any further. At this point convergence has been achieved and the sample has been properly characterised. Example convergence tests for the 2SD of graphene are shown in Figure 2.25b.

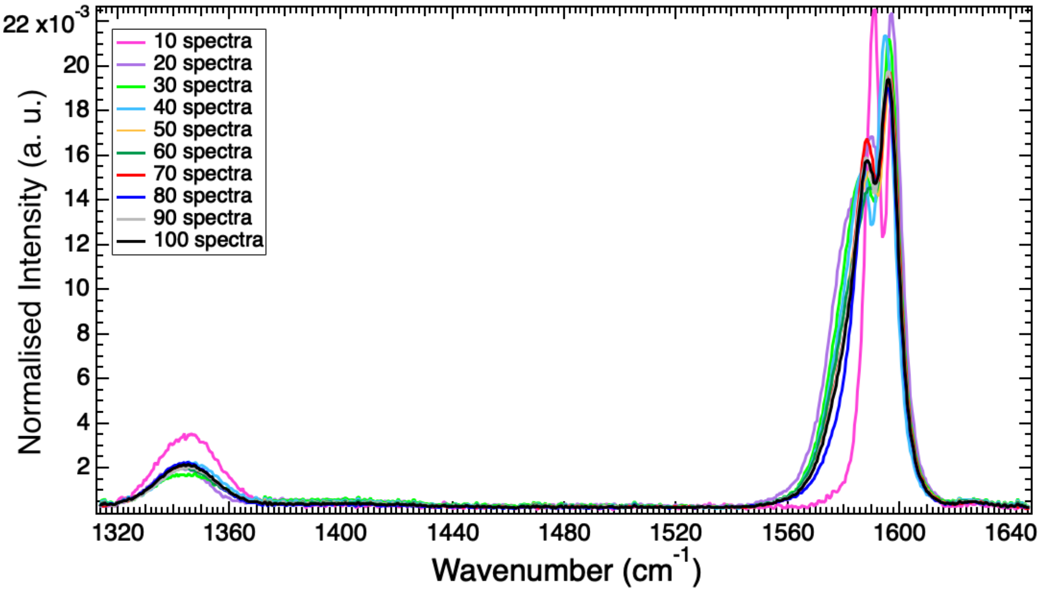

**(a)** Second order standard deviation convergence graphs for the normalised graphene spectra for increasing number of spectra in the average spectrum.

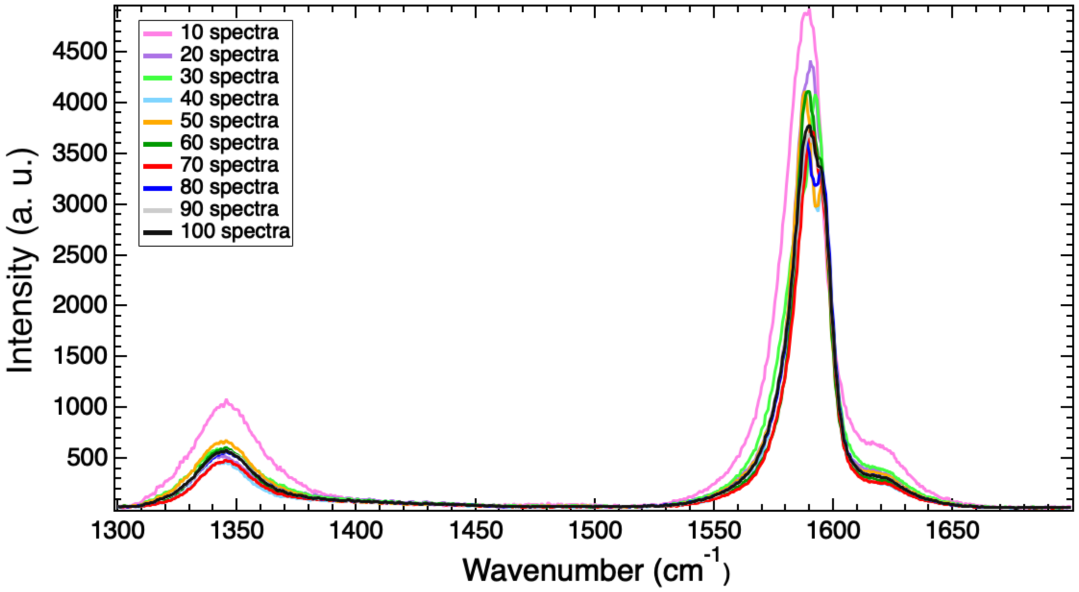

**(b)** Second order standard deviation convergence graphs for the non-normalised graphene spectra for increasing number of spectra in the average spectrum.

**Figure 2.25:** Convergence tests of the Raman spectra of graphene showing the second order standard deviation for increasing number of spectra in the average spectrum for normalised and non-normalised data.

## 2.10 Convergence Rates

The method for obtaining a convergence rate is similar to the method used in the convergence tests (Section 2.9), and involves analysis of the SE of the spectral data for increasing numbers of spectra in the average. This method involves computation of the absolute or percentage SE value for a given quantity, such as the location of a band in the Raman spectra, for increasing numbers of spectra in the average. For example, for investigation into the rate of convergence of the level of defect of a given graphene sample, the relative intensity of the D-band could be studied. The SE value for the relative intensity of the D-band would be computed for two spectra in the average spectra, then for three spectra in the average, then four spectra in the average and so on, until the maximum number of spectra is reached. The SE values decrease with increasing numbers of spectra in the average spectrum, which, when plotted with respect to the number of spectra in the average can be fitted to produce a convergence rate. The convergence rate for each sample, in this example, would be indicative of the level of defect of the sample. These graphs are produced using a manual code in Igor Pro.

The graphs are fitted with the model:

$$f(N) = 1/\sqrt{N}$$

where $N$ is the number of spectra. The rate of change was found by finding the gradient of the curve at various points. This produces a convergence rate, $\lambda$, for each graph and, thus, for each associated quantity. This convergence rate can be used for analysis of the level of heterogeneity of the quantity analysed, such as the heterogeneity of a specific biomolecule in a biological sample.

The convergence rates are performed on the mean of normalised bands or PIRs of bands in the Raman spectra, i.e., on relative intensities of bands. A higher decay rate indicates a more rapid decay of the SE, thus correlating to a more homogeneous sample or quantity. Lower decay rates indicate higher levels of heterogeneity.

**Table 2.4:** Table of peak fittings and peak intensity ratios for normalised and non-normalised graphene data. The analysis was performed on averages consisting of 100 individual Raman spectra. The uncertainties are from the fitting of the ± SE envelope.

| | **Normalised** | | | | **Non-normalised** | | | |
|---|---|---|---|---|---|---|---|---|
| **Band** | **Location** | **± SE** | **FWHM** | **± SE** | **Location** | **± SE** | **FWHM** | **± SE** |
| **D-band** | 1342.2 | 0.1 | 26.8 | 0.7 | 1342.5 | 0.5 | 27 | 2 |
| **$G_1$-band** | 1579.0 | 0.1 | 18.2 | 0.5 | 1579.2 | 0.2 | 18.8 | 0.1 |
| **$G_2$-band** | 1585.7 | 0.1 | 13.3 | 0.1 | 1585.8 | 0.1 | 13.5 | 0.1 |
| **D′-band** | 1621.8 | 0.1 | 11.3 | 0.8 | 1622.1 | 0.2 | 12.8 | 0.8 |
| $I_D/I_{G2}$ | 0.17 ± 0.03 | | | | 0.17 ± 0.2 | | | |
| $I_{D'}/I_{G2}$ | 0.031 ± 0.003 | | | | 0.035 ± 0.005 | | | |

## 2.11 Normalised vs non-normalised data

The data were checked for the effect of normalisation on the analysis. This involved performing fittings and PIR analysis for investigation of any differences between the results. This was tested on the Raman spectra of graphene between the wavenumbers 1300 - 1800 cm$^{-1}$. The fittings results and corresponding PIRs are shown in Table 2.4. Both fitting results and PIR values are within error of each other. Therefore, both normalised and non-normalised data analysis produces the same results for the analysis of Raman spectra.

The convergence tests were also checked to establish whether normalisation resulted in faster convergence of the sample. The results are shown in Figure 2.25, which displays the convergence tests of normalised and non-normalised Raman spectra of a graphene sample. Both convergence tests achieve convergence of the data at a similar rate, and to the same level, thus, indicating that normalisation of the data has little affect on the 2SD convergence due to the high levels of characterisation achieved in this work.

As the normalised and non-normalised convergences produce similar results it was decided that the convergence tests performed on the spectra would be done so on the non-normalised data, as this offers a more robust test. Thus, for consistency across data analysis procedures, the non-normalised data is used for data analysis.

Furthermore, as only relative intensities of bands in the Raman spectra are considered, specifically through the calculation of PIRs, normalisation of the data is not necessary. The exception is the use of normalised Raman spectra in the convergence rate graphs, as this is performed on singular bands, thus, in order for consideration of relative intensities the bands are normalised prior to analysis.

# 3

# Characterisation of CVD Graphene using Raman Spectroscopy

Raman spectroscopy is the gold standard for characterisation of graphene, due to its ability to provide information on the number of layers, doping level and defects of the sample [64]. Much work has been done on the investigation into graphene samples using Raman spectroscopy, and the wealth of information provided in the spectra [64, 67]. The work presented in this chapter draws from published works and goes beyond the literature to analyse of the heterogeneity of graphene samples formed via chemical vapour deposition (CVD). Principal component analysis (PCA) and peak intensity ratios (PIRs) are used, as well as novel methods of analysis for investigation of the heterogeneity of the samples.

The level of heterogeneity of the graphene studied in this work is reflected through significant changes in the Raman spectra, such as extreme band shifts of up to 28 $\mathrm{cm}^{-1}$ across samples. These levels of heterogeneity are likely to be attributable to defects in CVD graphene samples. These defects arise from the formation process, such as rip and tears in the graphene sample from the transfer process, and grain boundaries which introduces compressive strain into the graphene sample due to limited domain size, governed by the temperature used in graphene growth [52, 196, 197, 198].

The interactions of graphene with *Escherichia coli* (*E. coli*) are studied in this thesis (Chapter 5), and the level of heterogeneity of the graphene samples uncovered in this work could have repercussions for the interactions of the graphene with such biological samples [57]. For instance, it has been reported that simulations of heterogeneously oxidative graphene demonstrated the ability to cause cell membrane rupture when interacting with cells, while homogeneously oxidised graphene caused no damage to the cells, indicating that it was the heterogeneity which caused cell damage [199]. Therefore, it is essential that the graphene samples are characterised to a high level, in order to understand the sample properties prior to interaction with cells. This includes collection of sufficient Raman data for characterisation of graphene using Raman spectroscopy. A method of characterisation is proposed in this chapter, which involves convergence of the standard error (SE) and second order standard deviation (2SD) of the average spectrum for increasing numbers of spectra. Such a method is necessary to ensure reliability of data throughout published works.

## 3.1 Raman Spectroscopy of Graphene

The average Raman spectra of the four graphene samples studied in this work can be seen in Figure 3.1. Each average spectrum comprises one hundred random point spectra. The prominent bands in the Raman spectra of graphene are the D-band located at 1342.9 ± 0.3 $\mathrm{cm}^{-1}$, the G-band at 1586.2 ± 0.2 $\mathrm{cm}^{-1}$, the D′-band arising at 1623.3 ± 0.2 $\mathrm{cm}^{-1}$ and the G′-band, also known as the 2D-band, at 2680.0 ± 0.1 $\mathrm{cm}^{-1}$. The uncertainties arise from fitting of the SE envelope, as described in Chapter 2: Section 2.7.4.

The average band locations of the four samples are in agreement with the loca-

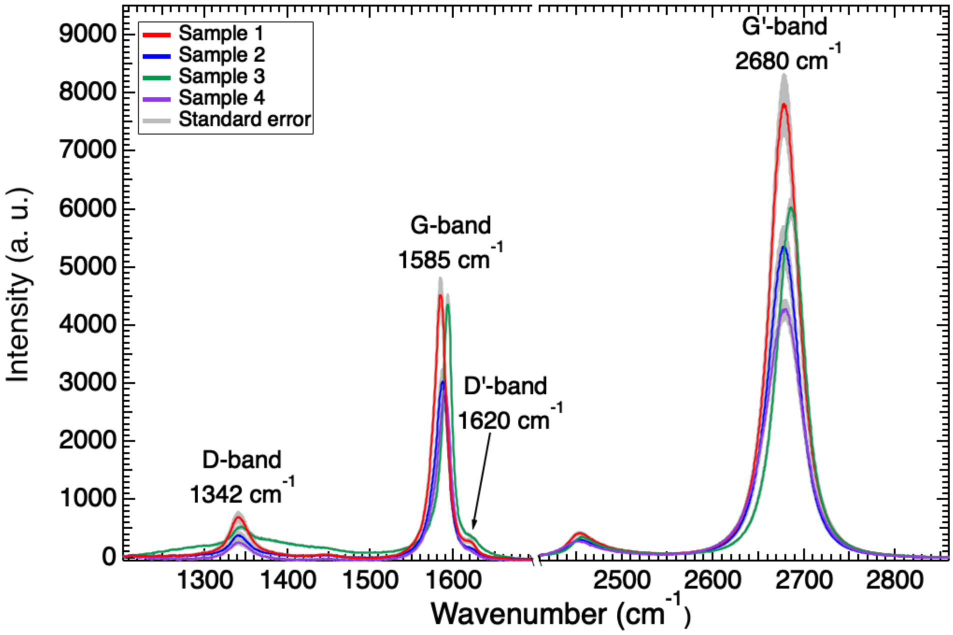

**Figure 3.1:** The average spectra of four CVD graphene samples. Each spectrum comprises 100 individual Raman spectra, collected from random points all across the sample. The grey envelope represents the standard error of the mean (SE) of the averaged spectrum. The main bands in the Raman spectrum have been labelled. These non-normalised averages have been lineally baseline subtracted.

tions reported in literature for these bands. Specifically, for single layer graphene (SLG) formed via CVD on an Si/SiO$_2$ substrate the G-band has been found to arise between 1580 cm$^{-1}$ and 1590 cm$^{-1}$ [58, 161, 169, 174], the G$'$-band between 2676 cm$^{-1}$ to 2693 cm$^{-1}$, the D-band at 1346 - 1350 cm$^{-1}$ and the D$'$-band at $\sim$ 1610 cm$^{-1}$ [161, 165, 174]. The D- and G$'$-bands are dispersive, meaning the band locations are dependent on the laser wavelength, originating from the double resonance (DR) Raman process [200, 201]. Thus, band locations will be compared against Raman spectra acquired using a 532 nm wavelength, as was used in this work. The individual band locations for the four samples studied in this work are in Table 3.1. Average band locations reported in literature for CVD and micromechanically exfoliated (ME) samples have also been included for comparison.

The G-band in the Raman spectrum of graphene (Fig. 3.1) at 1586.2 ± 0.2 cm$^{-1}$ arises due to in-plane LO and TO phonon modes which belong to the E$_{2G}$ representation at the Γ point [36, 203, 204, 205]. These phonon modes are degenerate

**Table 3.1:** Table of peak locations obtained from fittings of the bands in the Raman spectra of four CVD graphene samples. The G′-band has been fitted with a Voigt and a double Lorentzian profile, the results of both are included. The standard error values (SE) for each measurement are included, as obtained from fitting of the SE envelope. The maximum instrumentation error is 3 cm$^{-1}$. Average peak locations reported in literature are included for samples formed via CVD and mechanical exfoliation (ME) [58, 67, 161, 166, 174]. S1, S2, S3 and S4 are graphene samples one, two, three and four respectively.

| **Band** | **Fitting type** | **Sub-band** | **Location (cm$^{-1}$)** | | | | | | | | **Lit. ref** | |
|---|---|---|---|---|---|---|---|---|---|---|---|---|
| | | | **S1** | **SE** | **S2** | **SE** | **S3** | **SE** | **S4** | **SE** | **CVD** | **ME** |
| **D-band** | **Lorentzian** | - | 1342.5 | 0.5 | 1342.13 | 0.01 | 1344.5 | 0.1 | 1342.3 | 0.4 | 1349 | - |
| **G-band** | **Double Lorentzian** | G1 -band | 1579.2 | 0.2 | 1581.4 | 0.3 | 1589.5 | 0.2 | 1582.1 | 0.4 | 1587 | 1580 |
| | | G2-band | 1585.8 | 0.1 | 1588.3 | 0.1 | 1592.7 | 0.03 | 1590.3 | 0.1 | | |
| **D′-band** | **Gaussian** | - | 1622.1 | 0.2 | 1623.1 | 0.1 | 1624.7 | 0.3 | 0 | 0 | - | - |
| **G′-band** | **Voigt** | - | 2679.5 | 0.2 | 2678.0 | 0.1 | 2684.9 | 0.1 | 2677.8 | 0.1 | 2687 | 2690 |
| | **Double Lorentzian** | G1-band | 2673.0 | 0.2 | 2670.8 | 0.3 | 2678.6 | 0.3 | 2670.3 | 0.3 | | |
| | | G2-band | 2686.0 | 0.2 | 2684.8 | 0.5 | 2690.5 | 0.1 | 2686.0 | 0.1 | | |

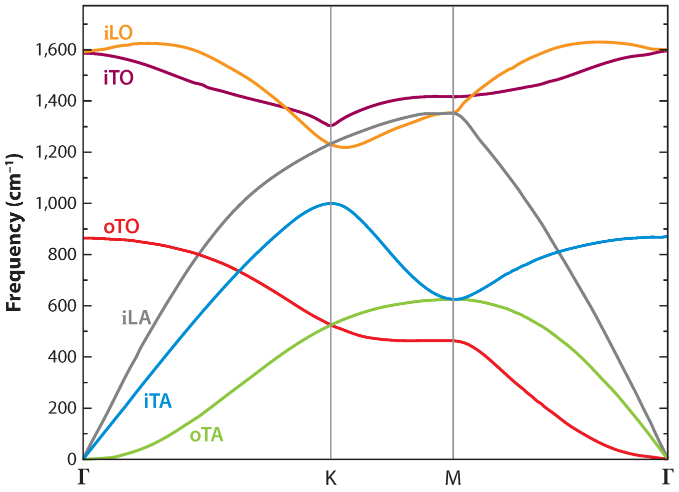

**Figure 3.2:** Phonon dispersion relation of single layer graphene [202]. The i and o represent in-plane and out-of-plane vibrations respectively. L and T correspond to longitudinal and transverse phonon modes, corresponding to whether the phonon vibration is parallel with that of the nearest carbon-carbon bond or if it is perpendicular to it respectively. Finally the O represents optical phonons, while the A acoustic phonon modes.

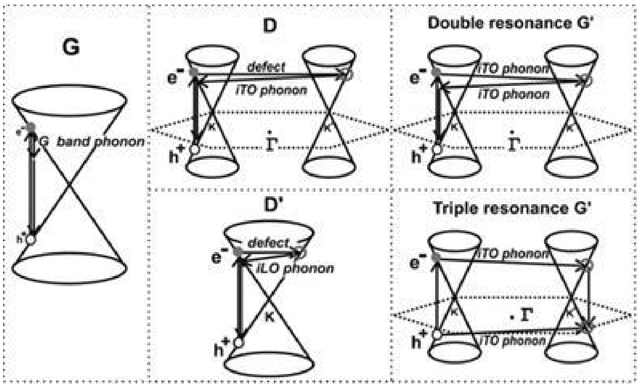

**Figure 3.3:** Raman scattering in graphene. (Left) First order Raman scattering process which gives rise to the G-band in the Raman spectrum of graphene. (Top center) Second-order double resonance (DR) single phonon intervalley process involving a defect and an iTO phonon which results in the D-band. (Top right) Second-order DR two phonon scattering process which gives rise to the G′-band. (Bottom right) Second-order triple resonance two phonon scattering process which also results in the G′-band. (Bottom center) Intervalley one-phonon second-order DR process involving a defect and an iLO phonon resulting in the D′-band in the Raman spectra of graphene. Figure obtained from [36].

at the Γ point, as shown in Figure 3.2, corresponding to vibrations of sublattice A against neighbouring sublattice B, thus it is a characteristic band in the Raman spectra of $sp^2$ hybridised carbon allotropes [36, 206].

The scattering process involves the excitation of an electron-hole pair by an incident photon, following which the electron or the hole are scattered by an iTO or an iLO phonon at the Γ point (Fig. 3.3). The electron-hole pair then recombines, emitting a photon in the process which is red-shifted by the amount of energy transmitted to the zone centre phonon [36, 204]. The momentum of the photon is equal to the momentum difference between the incident and scattered light.

The G-bands in the Raman spectra presented in this work are asymmetric in shape, thus have been fitted with a double Lorentzian model giving rise to the so-called $G_1$-band and $G_2$-band. The asymmetric contributions to the G-band may be attributable to unintentional p-doping of the sample from the Si/SiO$_2$ substrate [59, 143, 144, 189]. The doping of the sample may also be due to localized charge inhomogeneity within the laser probe area, as reported by Casiraghi *et al.* to be the cause of asymmetric tendencies of the G-band when investigating charged impurities in graphene [59, 189]. Furthermore, the G′-band is fitted with both a double

Lorentzian model and a Voigt profile, producing two sets of results for the band. The Voigt model was found to be the most optimal fit for two of the four samples studied, while two samples obtained optimal fittings with a double Lorentzian profile (Chapter 2: Section 2.7.1). The optimal fitting of the G′-band with a double Lorentzian may be representative of band splitting, which has been found to occur for additional strain in graphene samples [207]. The deconvolution of both bands can be seen in Appendix Figures A.2a and A.2b for the G- and G′-band respectively.

Unlike the G-band, the G′-band arises due to a DR process. The G′-band originates from inelastic scattering events of two iTO phonons near the K-point (Fig. 3.3) [36]. This band is also referred to as the 2D-band due to its location ($\sim$ 2680 cm$^{-1}$) in the Raman spectrum of graphene being approximately twice that of the D-band ($\sim$ 1340 cm$^{-1}$). The stretching mode of the carbon atoms which gives rise to the G′-band is known as ring breathing of the graphene honeycomb lattices [66]. This process is always allowed, as the second scattering is an inelastic scattering from a second phonon [208]. The G′-band in graphene is due to two phonons with opposite momentum in the highest optical branch near the K point ($A_{01}$ symmetry at K) [64].

The D-band originates from DR process involving an iTO phonon and a defect near the K-point (Fig. 3.3) and has been attributed to the ring breathing of the iTO phonon modes [206]. This process is only allowed when the second scattering by the defect occurs, thus is only present in the Raman spectra when the sample contains defects [206, 209].

Similarly, the D′-band is only present in the Raman spectra of graphene samples which contains defects (Fig. 3.1) [36, 68]. The D′-band arises at 1623 ± 0.2 cm$^{-1}$, due to an intravalley scattering process (Fig 3.3). Similarly to the D-band, it is a second order process which gives rise to the D′-band involving the scattering of a charge carrier by a defect in the sample, however, the second scattering process results from an iLO phonon [36].

As mentioned previously, the band locations found in this work are in agreement with those reported in literature for CVD graphene (Table 3.1) [58, 161, 174]. For ME graphene samples, also considered as pristine graphene due to its high quality, low defect nature, the G-band has been found to appear at $\sim$ 1580 cm$^{-1}$ [67]. This is comparable to the values obtained for the G$_1$-bands of samples one, two and four, however, the G$_2$-bands for these samples arises at 5 - 12 cm$^{-1}$ higher than this. Both the G$_1$-band and G$_2$-band for sample three are out of error of the $\sim$ 1580 cm$^{-1}$ location reported in literature for ME graphene, with the G$_2$-band arising at 7 - 10 cm$^{-1}$ higher than the other samples [67].

These band shifts may be due to residual strain in CVD graphene samples compared with pristine ME graphene [207, 210]. The bands in the Raman spectra are sensitive to residual strain in the samples, and shifts of up to 57 cm$^{-1}$ have been reported for the G-band due to the application of biaxial strain strain to graphene samples [207, 211, 212, 213]. Thus, strain may be responsible for the band shifts seen in the spectra in this work.

Furthermore, band splitting has also been reported for strain applied to samples, for instance in the work by Mohiuddin *et al.* splitting of the G-band into the G$_1$- and G$_2$-bands was reported for applied uniaxial strain to the ME graphene sample [207]. This band splitting was attributed to the splitting of the E$_{2G}$ mode into two distinct components, one polarised along the plane and one perpendicular to it. Thus, the emergence of the G$_1$- and G$_2$-bands in this work, in addition to G-band shifts is consistent with strain being present in the sample [207, 211, 212, 213]. Strain of between 0.5 % and 0.61 % produces a G-band similar to the band obtained in the Raman spectra in this work, thus, it is possible the graphene samples studied in this work possess comparable levels of strain [207].

Strain is known to affect CVD graphene samples due to the use of photoresists on the sample during the formation process [214, 215]. Photoresists are polymers used to protect the graphene, such as PMMA, when transferring the graphene onto the desired substrate [214, 215]. PMMA is used during the fabrication of the graphene samples used in this work [49]. It is put onto the graphene after its formation at extremely high temperatures ($\sim$ 1000 °C), following which both are then allowed to cool in order to undergo the transfer process [49]. Graphene has a negative thermal expansion coefficient ($\sim$-8.0$\times10^{-6}$/°C), whereas PMMA has a large positive thermal expansion coefficient ($\sim$5$\times10^{-5}$/°C to 10$\times10^{-5}$/°C). This results in the graphene expanding while the PMMA shrinks after fabrication, inducing compressive strain into the sample [59, 215]. Thus, it is likely that the graphene samples studied in this work possess additional residual strain compared with pristine graphene, due to the use of PMMA during the growth process [49, 215].

Furthermore, it has also been reported that residual PMMA may remain on the graphene surface following fabrication [216, 217]. Figure 3.4b shows an optical image of the graphene studied in this work, indicating potential residual PMMA islands on the graphene surface [218, 219]. The additional band shifts experienced by graphene sample three indicate that the level of strain is not homogeneous across the three graphene samples, despite being produced under the same conditions, and may be due to spectra being collected from such PMMA islands [49].

The locations of the G′-band are down-shifted compared with the locations for ME graphene as reported in literature (Table 3.1) [67]. Again, the use of photoresist, PMMA can result in band shifts of the G′-band [59]. For instance, Matsubayashi reported blue shifts of 4 $\text{cm}^{-1}$ to the position of the G′-band due to compressive stress in the sample when investigating the effect of photoresists such as polymethyl methacrylate (PMMA) on the graphene sample [59]. Thus, the band shifts of the G′-band reported in this work could be due to compressive strain in the sample [59].

In order to quantify the level of defect due to residual PMMA in the graphene samples, and other defects arising from the formation process, such as holes and rips due to the transfer from the Cu catalyst on the Si/$\text{SiO}_2$ substrate, peak intensity ratio (PIR) analysis of the bands in the Raman spectra can be used [197, 198]. Optical images of such potential holes and rips are shown in Figure 3.4 for the graphene studied in this work.

### 3.1.1 Peak intensity ratio analysis of the Raman spectra of CVD graphene

The relative intensity of the D- and D′-bands increase with the amount of defect in the sample, while the G-band intensity is said to be independent of defects [220]. Therefore, the amount of defect in a sample can be quantified by calculating the PIR of the D-band to the G-band ($\text{I}_D/\text{I}_G$), as shown in Figure 3.5 [68, 204, 221]. This

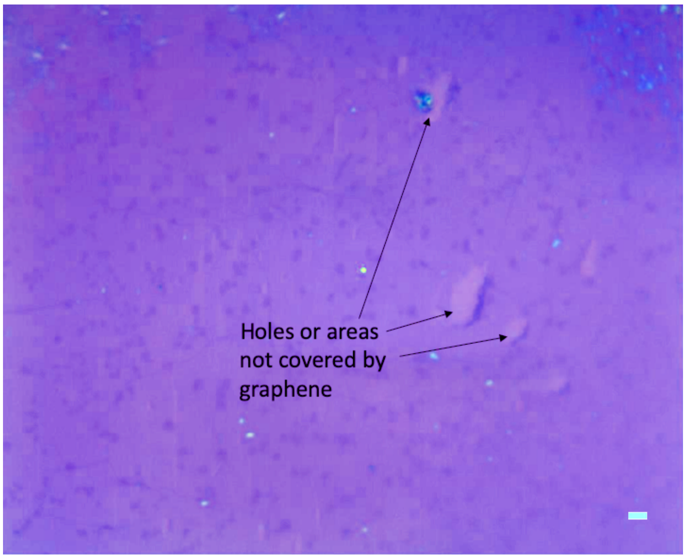

**(a)** Optical image of the CVD graphene sample studied in this work showing holes and rips in the sample, indicated by the arrows. Such rips and holes can arise in the graphene due to the transfer process [197, 198]. The scale bar is 2 $\mu$m.

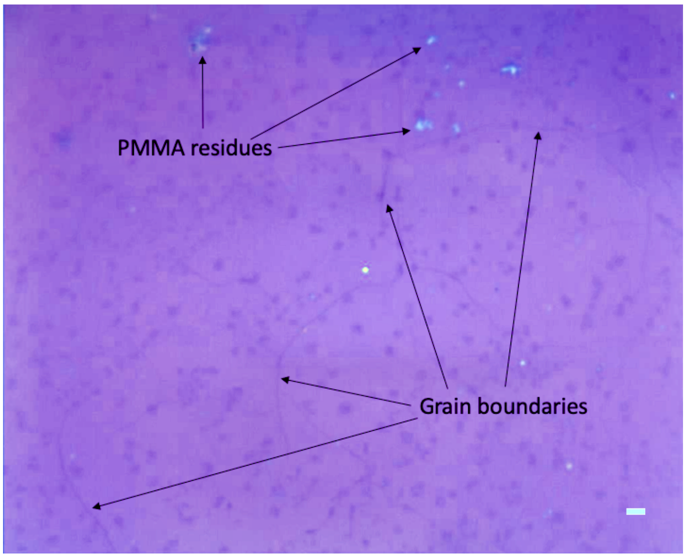

**(b)** Optical image of the CVD graphene sample studied in this work showing residual PMMA on the graphene sample and grain boundaries in the sample, indicated by the arrows [218, 219]. PMMA is used during the formation process to protect the graphene sample during the transfer process [59, 207, 210, 216, 217]. Grain boundaries are due to the coalescence of domains in the graphene sample [52, 196]. The scale bar is 2 $\mu$m.

**Figure 3.4:** Optical images showing the potential types of defects present in the CVD graphene samples studied in this work.

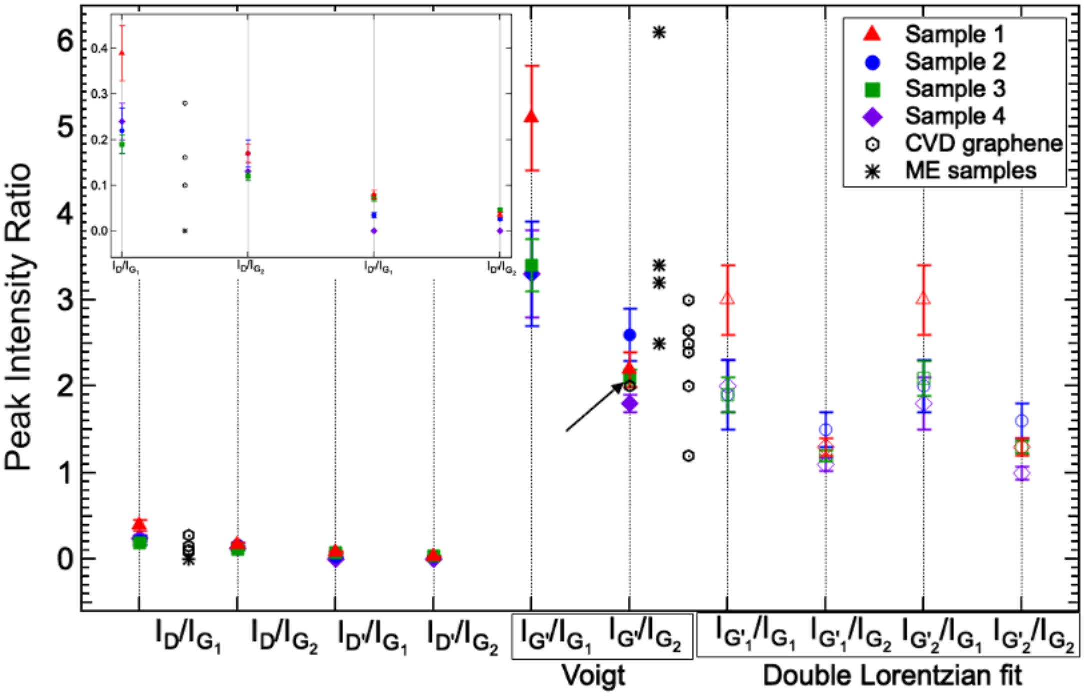

**Figure 3.5:** Peak intensity ratio (PIR) analysis for the four CVD graphene samples studied in this work. The PIRs are shown for the G′-band fitted with both a Voigt model (filled marker) and a double Lorentzian (unfilled marker), the corresponding fitting type is labelled below the graph. The micromechanically exfoliated (ME) and chemical vapour depositions (CVD) samples refers the $I_{G'}/I_G$ PIR values reported in literature for these sample types [36, 58, 59, 67, 161, 162, 164, 166, 167, 169, 174, 175, 188, 222]. All literature values are PIRs from the Raman spectra of graphene on a substrate. Only one paper has fitted the G-band with a double Lorentzian, as done in this work, the $I_{G'}/I_{G2}$ PIR is referenced on the graph with an arrow [59]. All other literature values have fitted the bands with single peaks. The inset shows a close up of the defect PIRs: $I_D/I_{G_1}$, $I_D/I_{G_2}$, $I_{D'}/I_{G_1}$ and $I_{D'}/I_{G_2}$.

graph also includes the PIRs reported in literature for $I_D/I_G$ for graphene samples formed using CVD and ME [36, 58, 59, 67, 161, 162, 164, 166, 167, 169, 174, 188, 222].

The inset of Figure 3.5 shows a zoom in of the defect induced PIRs, specifically the $I_D/I_{G_1}$, $I_D/I_{G_2}$, $I_{D'}/I_{G_1}$ and $I_{D'}/I_{G_2}$, which have values in the range 0 - 0.4. As can be seen from the graph, these values are within error of those reported in literature for CVD graphene [36, 58, 59, 161, 174, 175]. Highly defected graphene, has been reported to have a value of $I_D/I_G \sim 2.2$ - 2.9, therefore, the PIR values obtained in this work indicate the level of defect of the samples are low [66, 223].

The defect-induced PIR values obtained are, however, higher than those reported for pristine SLG in published works (Fig. 3.5) [67, 206, 209]. The increase in the PIR values for CVD graphene compared with ME graphene is due to CVD samples possessing increased levels of defect due to the way they are formed, compared with ME samples [224]. For example, CVD graphene has reported to have smaller domain sizes in comparison to ME graphene [141, 225]. Coalescence of two graphene domains results in a grain boundary, introducing a level of defect into the sample from disruption of the honeycomb lattice structure [52, 196]. An optical image demonstrating the potential presence of grain boundaries for the graphene samples studied in this work is shown in Figure 3.4b [52, 196]. Kalbac *et al.* reported a PIR $I_D/I_G = 0.28$ due to small domain size when investigating CVD graphene, comparable to the PIRs obtained in this work (Fig. 3.5) [174]. Thus, the presence of additional grain boundaries in the polycrystalline CVD graphene may be attributable to the increase in defect-induced PIRs in this work, compared with pristine ME graphene [224, 225].

The defect-induced PIRs are outside of error of one another across the four samples, for instance, for the $I_{D'}/I_{G_1}$ ratio only sample one and three are in agreement (Fig. 3.5), with the D′-band not being present in graphene sample four. This indicates heterogeneity in the level of defect in each of the samples. This is likely to be due to variation in the amount of micro-structural defects in the graphene sample, such as holes and rips due to the transfer process of the graphene onto the $Si/SiO_2$ substrate (Fig. 3.4) [197, 198, 219, 226].

PIRs of the bands in the Raman spectra of graphene can also be used for determination of the number of layers in a graphene sample [64]. The intensity of the G-band is reported to be unchanged when comparing SLG and bulk graphene or graphite, whereas the intensity of the G′-band decreases and broadens for increasing numbers of layers in the graphene sample, due to splitting of the electronic band structure near the Fermi energy [64]. Therefore the computation of the ratio $I_{G'}/I_G$ is often used as a marker to determine the number of layers in the sample. The values of the PIRs obtained in this work are in Figure 3.5. The fittings of the G′-band with a Voigt and double Lorentzian produces multiple PIRs, all of which are included on Figure 3.5 for consideration. PIR values from published works are also included.

The PIRs obtained in this work for the band fittings with a Voigt model are in agreement with literature values reported for SLG formed via ME and CVD (Fig. 3.5) [58, 59, 67, 161, 162, 166, 167, 168, 169, 170, 174, 175, 185, 187, 188, 222, 227, 228, 229]. All PIRs are within error of one another, expect the $I_{G'}/I_{G_1}$ for graphene sample one which produces a larger PIR than the other samples. Changes in $I_{G'}/I_{G_1}$ have been reported due to variation in the doping levels of a sample [230]. For instance, Das *et al.* showed that for undoped graphene the PIR $I_{G'}/I_G \sim 3.2$, which decreased to a value of $I_{G'}/I_G < 1.5$ when the electron hole doping of the sample was increased two fold [230]. Therefore, the increase in the PIR found for graphene sample one in this work (Fig. 3.5) may be due to inhomogeneous doping of the graphene samples [230].

The PIRs obtained for the fittings with a double Lorentzian (Fig. 3.5) are comparable to the value found by Das *et al.* of $I_{G'}/I_G < 1.5$ for the doped graphene samples [230]. The PIRs are also in agreement with the values reported by Zhao *et al.*, who found $I_{G'}/I_G = 1.2$ when investigating CVD SLG [164]. These PIR values are low compared with other reports for the PIRs of SLG formed via CVD, and has been attributed to unintentional doping of the graphene sample from the substrate [164]. Therefore, the PIR values obtained for the graphene samples in this work for the double Lorentzian fittings may be reduced due to the p-doping of the sample from the Si/SiO$_2$ substrate [164].

The PIR values obtained in this work are confirmatory that the graphene samples studied in this work are SLG, when compared against literature results for CVD SLG [36, 58, 59, 161, 162, 164, 169, 174, 175]. However, the PIRs for both Voigt and double Lorentzian fittings are on average lower than literature value for ME SLG (Fig. 3.5) [67, 166, 167, 188, 222]. Particularly for the PIRs of the double Lorentzian fittings, only sample one is within error of the published results for ME graphene. Similarly, the literature results for the PIRs for CVD SLG are also lower than the reported results for ME SLG. For instance for the values included on the graph, the PIRs for the ME samples fell within the range 2.5 - 6.1 ± 0.2, while the values for CVD graphene were between 1.2 - 3 [36, 58, 59, 67, 161, 162, 164, 166,

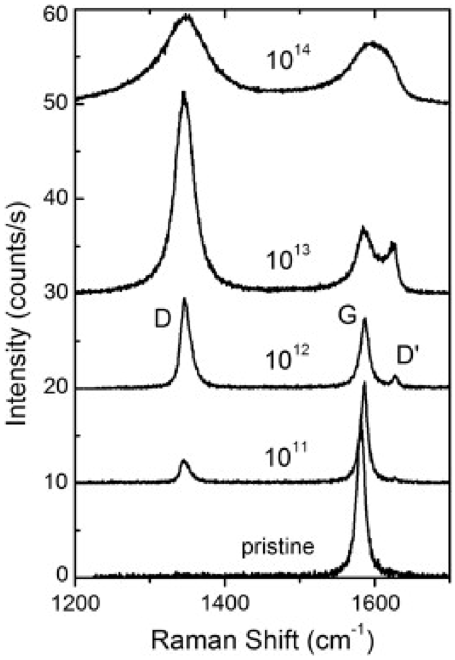

**Figure 3.6:** Figure from the work by Lucchese *et al.* which analysed the evolution of the first-order Raman spectra of a single layer graphene sample deposited on an $SiO_2$ substrate following different levels of ion bombardment of the sample [231]. The ion doses are indicated next to the respective spectrum in units of $Ar^+$ / $cm^2$. The spectra are displaced vertically for clarity. A laser wavelength of 514 nm was used for collection of the spectra. The pristine spectra, and the spectra following ion bombarment of the sample with $10^{12}$ $Ar^+$ / $cm^2$ and $10^{13}$ $Ar^+$ / $cm^2$ are analogous to the Raman spectra collected in this work showing different levels of defect in the graphene sample.

167, 169, 174, 175, 188, 222].

This decrease in the PIRs of CVD graphene reported in this work and in literature may be due to the inherent defects in CVD graphene, which cause relative decreases in intensity of the bands in the Raman spectra of graphene [231]. For instance, Lucchese *et al.* reported that for heavily defected graphene the G-band underwent significant decreases in intensity with respect to the D-band, which correspondingly increased in relative intensity, demonstrated in Figure 3.6 [231]. Unfortunately, the effects of the ion-induced defects on the G′-band is not investigated in the work by Lucchese *et al.* [231]. Thus, defects in the sample, such as strain from the residual PMMA on the graphene and grain boundaries (Fig. 3.4), may explain the difference between the values obtained in this work for CVD graphene and those reported in literature for ME SLG in literature for the PIR $I_{G'}/I_G$ [67]. These relative decreases in the G- and G′-bands in the Raman spectra due to doping and defects in the sample

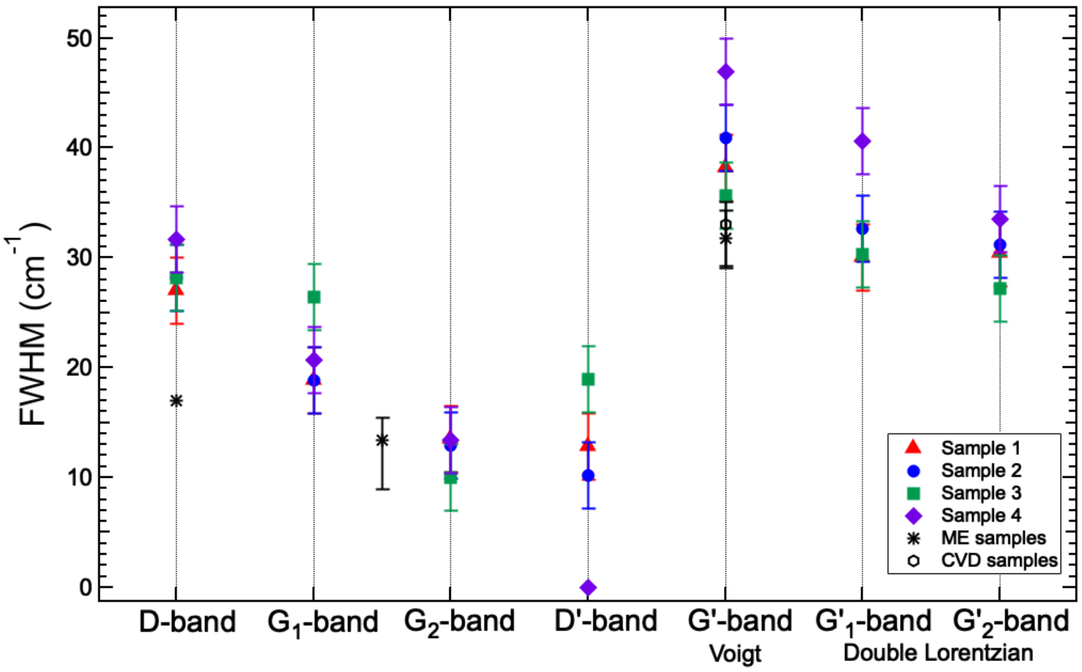

**Figure 3.7:** FWHM of the bands in the Raman spectra of four CVD graphene samples. The G′-band is fitted with both a Voigt model (filled marker) and a double Lorentzian (unfilled marker), the corresponding fitting type is labelled below the graph. The micromechanically exfoliated (ME) and chemical vapour deposition (CVD) samples refers to the average FWHM values reported in the literature [58, 161, 166, 169, 174, 188, 227, 229]. The bars on the literature values represent the range of values reported in literature, the error bars on the values from this work correspond to the maximum uncertainties. All literature values refer to graphene samples on an Si/SiO$_2$ substrate, the same as the samples that have been studied here, and represent fittings of the bands with a single peak. Any papers which performed fits with double peaks failed to provide FWHM values for the bands [59].

bring into question the reliability of this PIR for determination of the number of layers [232, 233].

Another method for evaluation of the number of layers in a graphene sample using Raman spectroscopy is use of the FWHM values of the bands [67]. Figure 3.7 shows the results obtained for the FWHM of the bands in the Raman spectra. The results from literature are also presented on this graph for SLG formed via CVD and ME [58, 161, 169, 170, 174, 175, 229].

The D-band shows significant broadening compared with the literature values of for ME SLG reported in literature (Fig. 3.7) [67]. Similarly the FWHM of the G$_1$-

band is outside of error of the values reported in literature for this quantity in ME graphene, while the $G_2$-band is within error of the literature values [166, 188, 227, 229]. The FWHM of the G-band for CVD graphene samples is not often provided within literature, and many of the papers discussed here have not provided this quantitative measurement for comparison [36, 161, 162, 164, 165, 168, 174, 175]. For instance, Roscher *et al.* studied the broadening of the G-band for the Raman spectrum of graphene compared with graphite, however, did not provide quantitative FWHM values, rather the broadening was determined using an $R^2$ goodness of fit test, which is incompatible with non-linear models, such as Raman bands [168]. In this thesis all FWHM values are included for comparison across samples.

The source of the broadening of the G-band in this work compared with the values reported in literature may be due to the inhomogeneous and unintentional doping of the sample from the substrate [187]. Doping due to the laser has also been reported within literature (Fig. 3.7) [230, 234]. Furthermore, asymmetric G-band tendencies were also reported in these works due to unintentional doping of the sample [230, 234]. Broadening and asymmetric perturbations of the G-band were both found in this work, thus, this may be due to unintentional doping of the samples from the laser and the p-doping of the sample from the substrate [230, 234].

The FWHM of the G′-band fitted with a double Lorentzian model is within error of the values reported in published works for this measurement for both ME and CVD samples [58, 161, 166, 169, 174, 188, 227, 229]. However, the G′-band fitted with a Voigt model is outside of error of these literature values, also suggestive of band broadening. It has been reported that doping can result in an increase in the FWHM of the G′-band of between 5 - 15 $cm^{-1}$ [187]. Therefore, the broadening of the G′-band seen in this work may also be due to additional inhomogeneous doping of the graphene sample from the $Si/SiO_2$ substrate on which the sample is deposited [187].

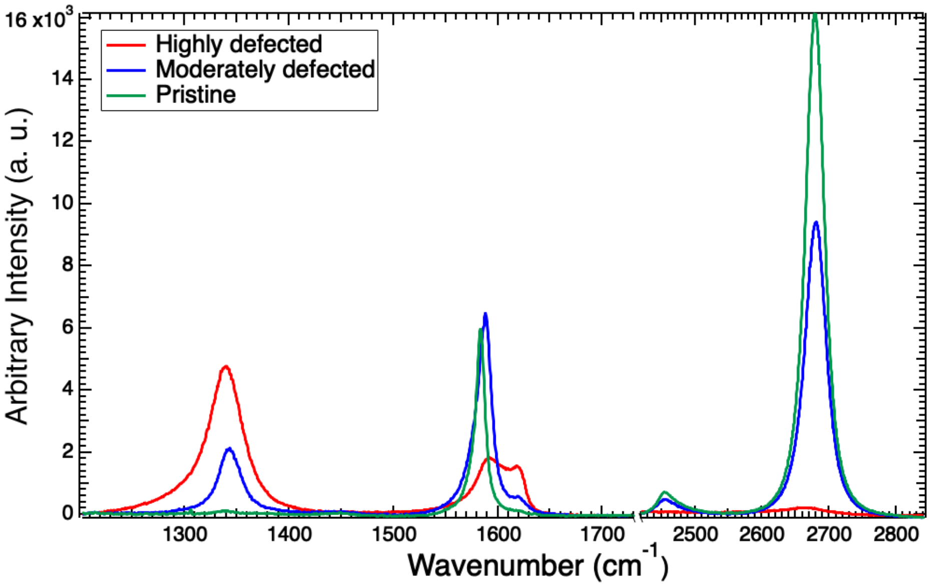

**Figure 3.8:** Three point Raman spectra of graphene obtained from the same sample showing different levels of defect. One spectrum shows an area of pristine graphene (green), the D-band has low intensity relative to the other bands in the spectrum and the both G- and G′-bands appear as intense, symmetric spectral features. The spectrum from the slightly defected area of graphene (blue) contains a relatively intense D-band to the G- and G′-bands. The spectrum obtained from the highly defected area of the sample (red) shows an intense D-band and splitting of the G-band. The G′-band in this spectrum has decreased in relative intensity. These non-normalised spectra are linearly baseline subtracted. All spectra were collected using the same parameters.

## 3.2 Analysis of point Raman spectra to investigate the heterogeneity of CVD graphene samples

In order to investigate the differing levels of defect and heterogeneity within a graphene sample, three point Raman spectra of varying levels of defect, collected from the same sample, are presented and analysed here (Fig. 3.8). One spectrum represents a pristine area of graphene, one from a moderately defected area and the third is a spectrum representative of a highly defected area of graphene. The levels of heterogeneity shown here are significant, and does not appear to have been reported before for spectra collected from the same graphene sample.

Spectra similar to those shown in Figure 3.8 have been produced by Lucchese *et al.* in work studying ion induced defects in graphene samples (Fig. 3.6) [231]. The evolution of these spectra following different levels of ion-bombardment is analogous to the spectra in Figure 3.8, confirming the changes in the spectra shown here are characteristic of increasing amount of defect in the sample. Unfortunately, Lucchese *et al.* does not analyse the affect of these defects on the G′-band [231], as has been done here.

To quantify the level of defect in the different areas of the sample represented by the Raman spectra (Fig. 3.8), the $I_D/I_G$ and $I_{D'}/I_{G'}$ ratios have been calculated for each spectrum (Table 3.2). The corresponding $I_{G'}/I_G$ PIR have also been computed to demonstrate how this affects the relative intensities of the G- and G′-bands. The PIR values are obtained against the $G_2$-band as this is the prominent band of the G-bands and is in line with what has been done in literature [59].

As expected, the $I_D/I_{G2}$ and $I_{D'}/I_{G2}$ PIRs increase with increasing level of defect in the spectrum. The PIR values for $I_D/I_{G2}$ are in agreement literature values for pristine, moderately defected and highly defected graphene reported to be $I_D/I_G = 0$, $I_D/I_G \sim 0.3$ and $I_D/I_G > 3$ respectively [67, 174, 235]. This provides further evidence of the increasing level of defect of the spectra.

The relative decreases in the G′-band with increasing defects are clear from the spectra (Fig. 3.8), and this is quantified from the PIR values obtained (Table

**Table 3.2:** Table showing the peak intensity ratios (PIRs) for three Raman spectra of different levels of defect. Pristine, moderately defected and highly defected spectra collected from the same sample. The defect-related PIRs confirm the increasing levels of defect of the spectra. The level of defect in these spectra is shown to have a direct impact on the results of the $I_{G'}/I_G$ PIR. The PIR values are obtained against the $G_2$-band as this is the prominent of the G-bands and is in line with what has been done in literature [59].

| | **Peak intensity ratios** | | |
|---|---|---|---|
| **Area of graphene** | $\mathbf{I}_D/\mathbf{I}_{G2}$ | $\mathbf{I}_{D'}/\mathbf{I}_{G2}$ | $\mathbf{I}_{G'}/\mathbf{I}_{G2}$ |
| **Pristine** | 0.0167 ± 0.0008 | 0.013 ± 0.002 | 3 ± 0.02 |
| **Moderately defected** | 0.409 ± 0.008 | 0.054 ± 0.002 | 1.8 ± 0.7 |
| **Highly defected** | 8.2 ± 0.6 | 1.8 ± 0.1 | 0.36 ± 0.02 |

3.2). $I_{G'}/I_G = 3 \pm 0.02$ for the pristine spectrum is comparable to the PIR values reported in literature for pristine SLG, $I_{G'}/I_G = 2.5$ to 6.1 [67, 166, 188, 222]. The value obtained for the moderately defected spectrum is similar to the PIR values for the CVD graphene samples studied in this work (Fig. 3.5), and is in agreement with the expected value for CVD graphene reported in literature to be $I_{G'}/I_G > 2$ [161, 174, 175]. Thus, this indicates that this spectrum represents moderately defected graphene, similar to CVD graphene [161]. The PIR for the spectrum collected from the highly defected area of graphene shows a large decrease in the relative intensity of the G′-band as a result of the defects in the sample. This PIR value is closer to that obtained for bilayer graphene, reported to be $I_{G'}/I_G = 0.8$ [169]. This shows the misconceptions that could arise for use of this PIR for determination of the number of layers in the graphene when defects are present in the sample.

It is evident from the variation in PIRs (Table 3.2) that the level of defect in a graphene sample can have a consequential effect on the value of $I_{G'}/I_G$. This analysis demonstrates the issues with the use of the marker $I_{G'}/I_G$ for determination of the number of layers in the graphene sample. This may be particularly problematic for use on CVD graphene samples due to the defects present in graphene formed in this way, such as wrinkles, holes and grain boundaries, as is the case for the graphene studied in this work (Fig. 3.4) [59, 207, 210, 216, 217]. The reduction in the PIRs seen here is consistent with the lower PIR values obtained for the graphene samples studied in this work compared with ME graphene (Fig. 3.5). Therefore, the relative intensities of the bands in the Raman spectra may be affected by the inherent defects in the samples.

Analysis of this kind does not appear to have been performed before for spectra collected from the same graphene sample. For instance, most works examining the levels of defect in graphene samples are investigations of defects induced into the graphene sample. For example, the work by Lucchese *et al.* which investigated ion-induced defects in the graphene samples (Fig. 3.6) [231]. The analysis presented in this chapter demonstrates the importance of random point sampling from all across the graphene sample, something which is not always done within literature. Some works focus only on small areas of the samples, collecting maps of spectra from specific points on the graphene, which is not representative of the entire sample [169]. In this work, spectra are collected from all across the sample for characterisation.

The significant levels of heterogeneity presented here could also have repercussions for the interaction of graphene with biological samples, such as *E. coli* as is done in this work (Chapter 5). For example, CVD graphene has been reported to be biocompatible [236], however, it has also been shown using simulations that defects in a graphene sample could result in the interactions with biological samples to change. Gu *et al.* studied the chicken villin headpiece subdomain (HP35), a protein found in the cytoskeleton of eukaryotic cells, interfaced with graphene [57]. It was reported that interfacing with graphene had no affect on HP35, however, when interfaced with defected graphene severe protein denaturation was observed, due to the attraction of the charged polar residues of the HP35 to the defects [57]. Simulations predicted that the residues would become anchored to the defects by strong interaction. The movement of the protein around this anchored point created an effective centripetal force resulting in local unfolding near the defect, exposing the core hydrophobic and aromatic elements of the protein which eventually unfolds due to hydrophobic interactions [57].

Unfortunately the effect of graphene defects on bacteria does not appear to have yet been studied, however, this demonstrates that the level of defect and heterogeneity could seriously impact how graphene interacts with cells. This is extremely concerning for the application of graphene, such as in wearable biomedical devices, as has been proposed [45]. Thus, this further reiterates the importance of proper characterisation of graphene samples prior to use.

## 3.3 Convergence Tests

Given the heterogeneity that is encapsulated in collection of the random point Raman spectra from the graphene samples, it is essential to ensure that proper characterisation is performed on graphene samples. The proper characterisation of graphene relies on sufficient data being collected to fully represent the sample. This section demonstrates the method used to ensure that sufficient data has been collected for each graphene sample, which involves investigation of the standard error (SE) and second order standard deviation (2SD) waves, of the average spectrum, for increasing numbers of spectra, to determine when the sample is characterised, such that the SE and 2SD is sufficiently converged. Only when these quantities have been converged within a reasonable margin can the sample be deemed to be characterised to a sufficiently high standard. This test allows for determination of how well characterised a sample is with a given number of spectra.

In this work a total of 100 spectra were collected from random points all across each sample. The corresponding SE convergence graphs for graphene sample one are shown in Figures 3.9a and 3.9b and the 2SD convergence graphs in Figures 3.10a and 3.10b for range one and two respectively. These waves are generated for increasing numbers of spectra in the spectral average up to 100 spectra, in increments of 10 spectra. The inset of the figures show a close up of the convergence of each of the peaks. The aim of the SE graphs is for each of the bands in the Raman spectra to converge to a point. The SE for increasing numbers of spectra in the average continually lowers until the SE is at a minimum which cannot be reduced further, i.e. the SE associated with the natural heterogeneity of the sample, coupled with the error of the instrument.

The SE could potentially be converged to a slightly lower value for more spectra in this work (Fig. 3.9a & 3.9b), however, due to time limitations within this work 100

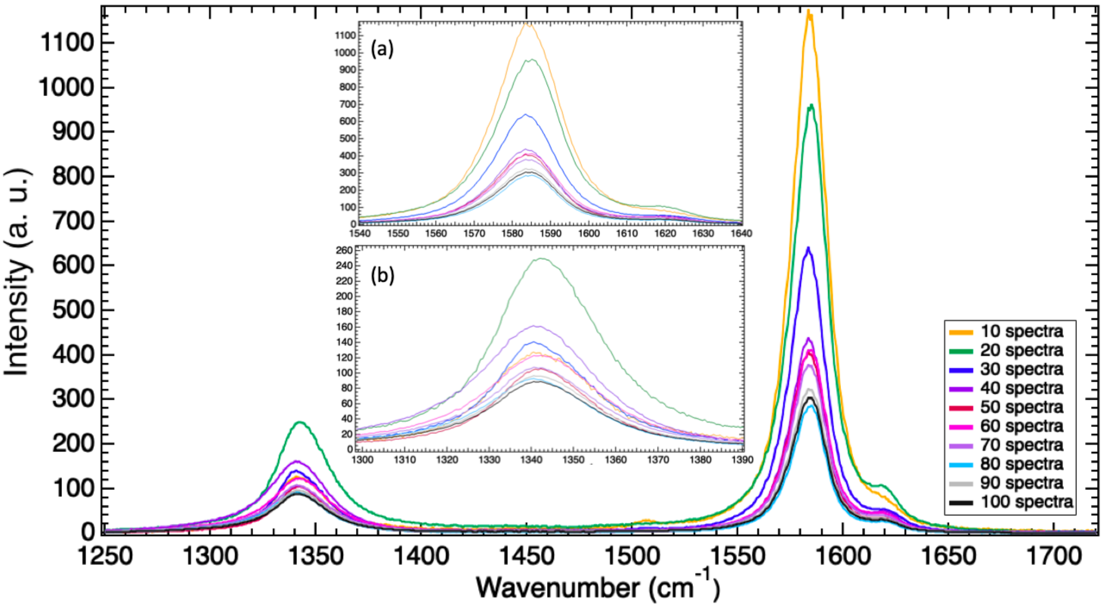

**(a)** SE convergence graphs of graphene sample one for the bands in the Raman spectra between the wavenumbers 1200 cm$^{-1}$ to 1800 cm$^{-1}$. The inset images are (a) a zoom in of the SE convergence of the G- and D′-bands and (b) a zoom in of the SE convergence of the D-band for increasing numbers of spectra in the average.

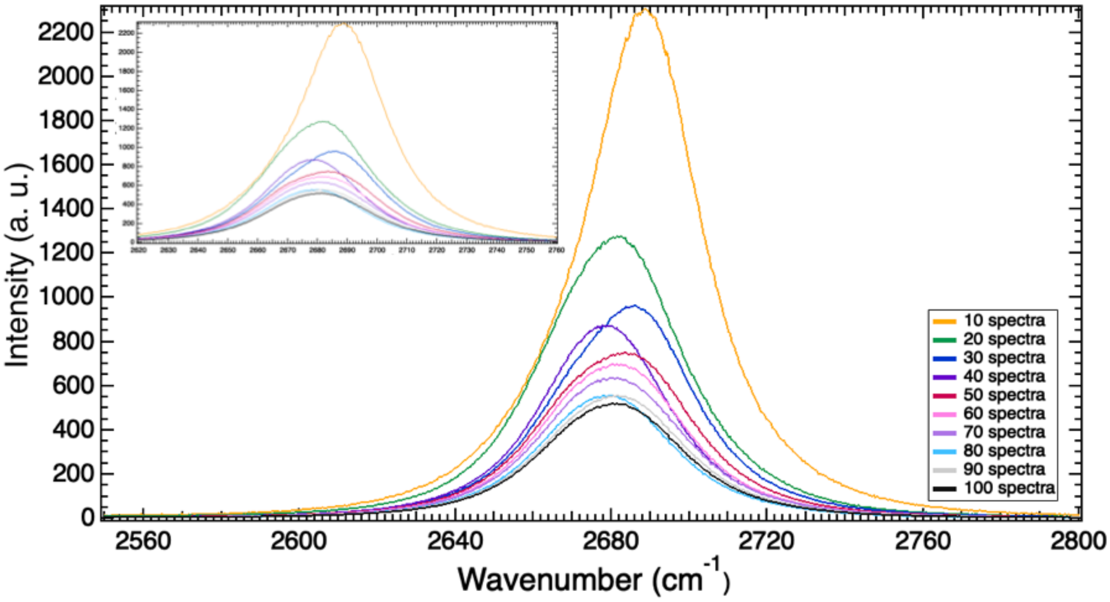

**(b)** SE convergence graphs of graphene sample one for the bands in the Raman spectra between the wavenumbers 2400 cm$^{-1}$ to 2800 cm$^{-1}$. The inset image is a zoom in of the SE convergence graphs of the G′-band.

**Figure 3.9:** Standard error (SE) graphs for the Raman spectra of graphene. The SE graphs are computed for increasing numbers of spectra in the spectral average.

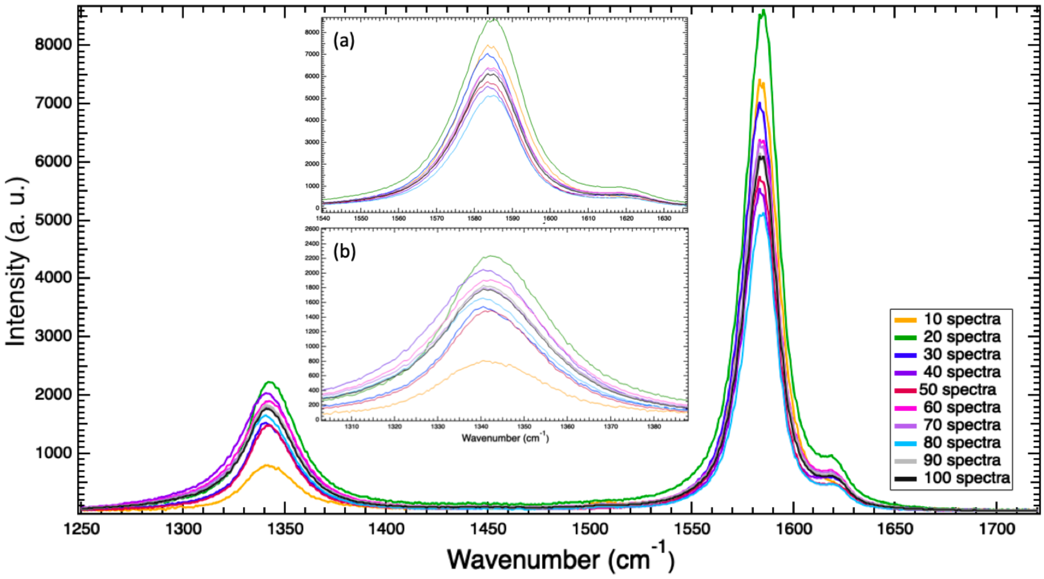

**(a)** 2SD convergence graphs of graphene sample one for the bands in the Raman spectra between the wavenumbers 1200 cm$^{-1}$ to 1800 cm$^{-1}$. The 2SD graphs are computed for increasing numbers of spectra in the spectral average. The inset images are (a) a zoom in of the 2SD convergence of the G- and D′-bands and (b) a zoom in of the 2SD convergence of the D-band for increasing numbers of spectra in the average.

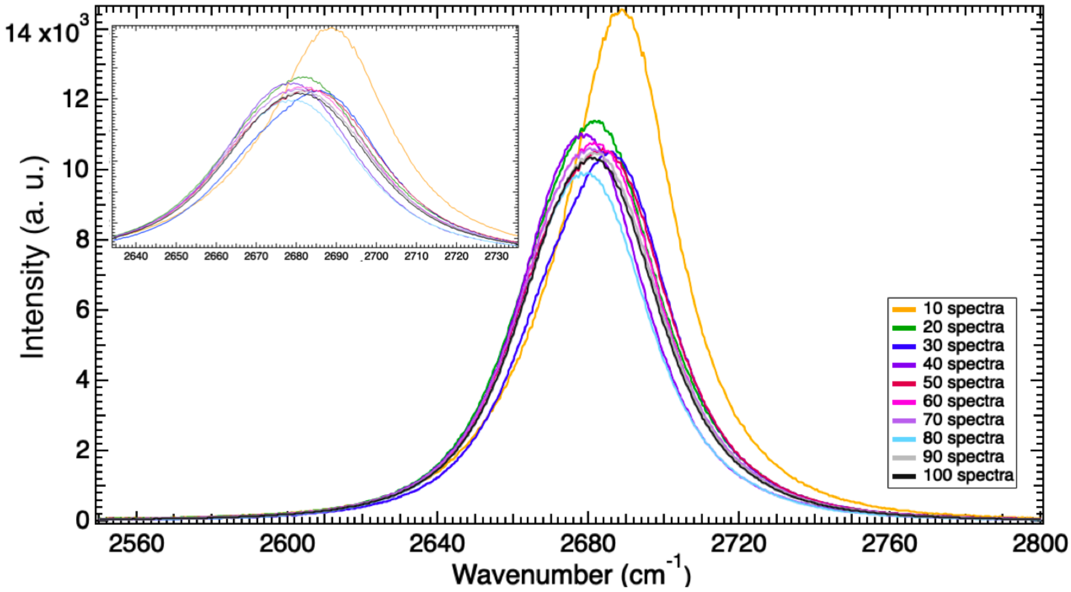

**(b)** 2SD convergence graphs of graphene sample one for the bands in the Raman spectra between the wavenumbers 2400 cm$^{-1}$ to 2800 cm$^{-1}$. The 2SD graphs are computed for increasing numbers of spectra in the spectral average. The inset image is a zoom in of the 2SD convergence graphs of the G′-band.

**Figure 3.10:** Second order standard deviation (2SD) graphs for the Raman spectra of graphene. The graphs are computed for increasing numbers of spectra in the spectral average.

spectra was decided to bring the SE and 2SD to a sufficiently low value to conclude that the level of characterisation to be representative of the sample. The SE of the converged waves represent the SE envelope displayed on average graphs throughout. The same is done for 2SD graphs (Fig. 3.10a & 3.10b). The SE and 2SD waves were brought to a value of $< 5$ % before being deemed sufficiently characterised. Future work in this project will involve collection of additional spectra for analysis of when complete convergence will be achieved. The convergence tests for the other samples are shown in the Appendix: Figures A.3a to A.8b.

Often little to no form of analysis is performed on the graphene spectra in published works to ensure proper characterisation is achieved, resulting in insufficient data being collected to characterise the sample. For instance Wu *et al.* collected only ten Raman spectra to characterise a graphene sample [58]. However, just one spectrum was shown in the paper to represent the entire sample, with corresponding analysis such as peak locations and PIRs pertaining to the single spectrum [58]. Similarly Matsubayashi *et al.* collected only 11 spectra from a graphene sample to represent the various changes in the Raman spectra from four different stages of the formation process, resulting in large uncertainties [59]. For instance, PIR uncertainties were large relative to the data, such as the PIR $I_D/I_G = 0.13 \pm 0.2$ [59]. This large uncertainty makes the data unreliable and inconclusive. In this thesis, much smaller uncertainties were obtained on PIRs (Fig. 3.5) due more thorough characterisation of the samples.

Many papers do not provide the number of spectra collected within the work, suggesting that it is not yet understood the level of variation that is captured in the Raman spectra of graphene, and how that can affect the associated SE and 2SD quantities [36, 161, 162, 164, 174, 175, 213]. For example, when investigating the growth of CVD graphene samples, Tu *et al.* used Raman as a tool for characterisation, however, no information on the number of spectra collected was included in the work [161]. Thus, it is unknown the level of characterisation achieved in the work, and the spectra could be unrepresentative of the entire graphene sample [161]. It does not appear that any other work has converged the statistical uncertainties associated with the data to ensure proper characterisation of the sample, as has

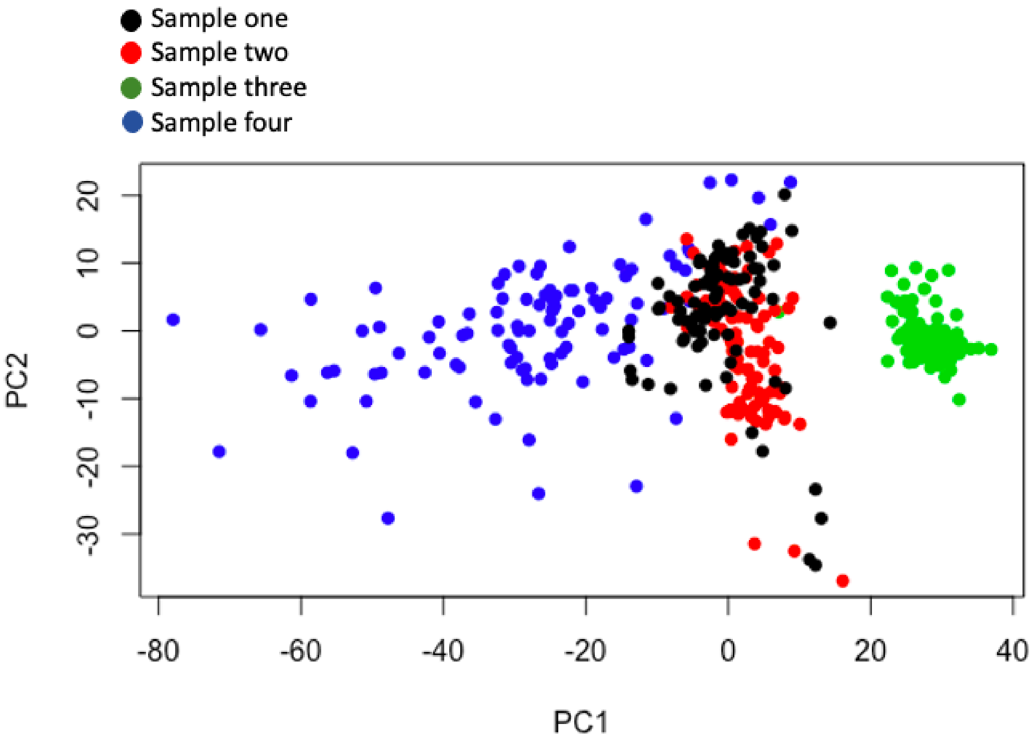

**Figure 3.11:** PCA comparing the Raman spectra of four different graphene samples for the wavenumbers between 1200 cm$^{-1}$ to 1800 cm$^{-1}$. There is separation along PC1 which accounts for 55% of the total variation.

been presented here.

## 3.4 Investigation of the heterogeneity of CVD graphene samples using principal component analysis

Given the level of characterisation performed in this work, the analysis of the spectra across the four graphene samples will be presented, to determine the heterogeneity between the samples. This is done using PCA, and will give an indication into the reproducibility of the graphene samples studied in this work, which were fabricated under the same conditions [49].

The results from the PCA performed on the spectra between the wavenumbers 1300 cm$^{-1}$ and 1800 cm$^{-1}$ are shown in Figure 3.11. There is separation of graphene samples three and four with samples one and two along principal component (PC1), which represents 55.0 % of the total variance of the data. The data did not sepa-

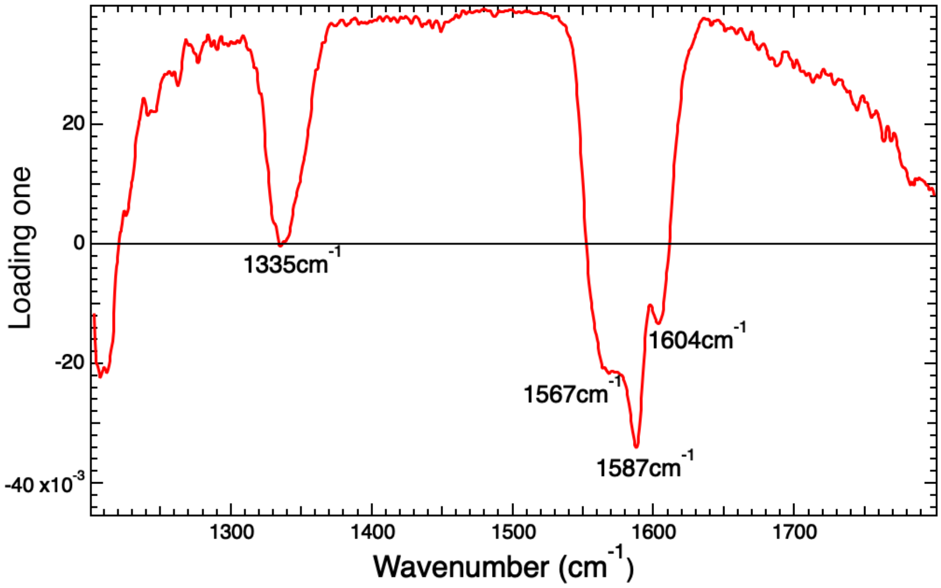

**Figure 3.12:** PC1 loading results for the PCA performed on the graphene spectra between the wavenumbers 1200 cm$^{-1}$ to 1800 cm$^{-1}$ for four graphene samples which showed separation along PC1 with a variation of 55%. The main differences in the Raman spectra which resulted in the separation along PC1 are labelled on the graph.

rate along any other PC. The separation along PC1, which exemplifies the largest variance compared with the other PCs, represents that there is intrinsic differences between samples three and four, compared with samples one and two.

In order to determine specifically what is causing the separation of the graphene samples in PCA space, the corresponding loading has been plotted (Fig. 3.12), on which the spectral components are labelled. For clarity, the points found by the loadings to be the cause of separation in PCA space have also been labelled on the average spectral graphs for the four graphene samples (Fig. 3.13).

It is evident from the average spectra (Fig. 3.13) that there is significant variation in the spectra at the wavenumbers found by PCA to be the main points of difference between the four samples (Fig. 3.12). This is particularly evident at the location 1587 cm$^{-1}$, due to the shifts in the average position of the G-band for each sample. This is the reason for the spectral locations 1567 cm$^{-1}$, 1587 cm$^{-1}$ and 1604 cm$^{-1}$ causing separation in PCA space.

The G-band in the Raman spectra is extremely sensitive to additional strain being applied to the sample [207, 210]. For instance, red shifts of 10 cm$^{-1}$ were

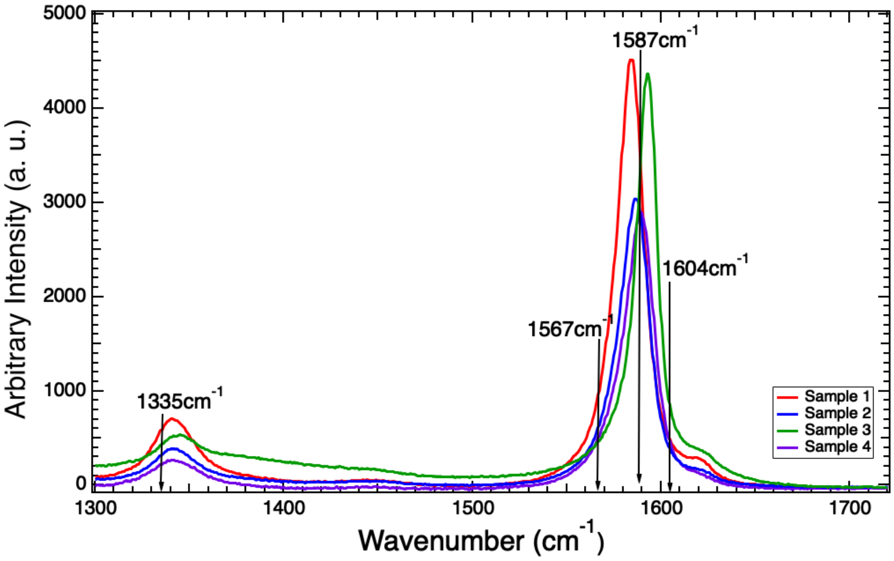

**Figure 3.13:** Average Raman spectra of graphene between the wavenumbers 1300 cm$^{-1}$ and 1800 cm$^{-1}$ with the main spectral components which caused separation of the spectra along PC1 in PCA space labelled. Graphene samples three (green) and four (purple) were found to separate from samples one (red) and two (blue) in PCA space.

reported by Ni *et al.* when investigating uniaxial strain applied to graphene [213]. Therefore, the band shifts reported in the PCA for the graphene samples may be due to residual strain in the sample [59, 207, 210, 215, 216, 217].

These shifts in the G-band of the spectra collected from the different graphene samples is more significant when considering the raw data which comprises these averages. There are large shifts in locations of all bands in the Raman spectra across samples. The largest difference in locations of D-bands in the raw Raman spectra of graphene are the bands located at 1340 cm$^{-1}$ and 1348 cm$^{-1}$, pertaining to a shift of 8 cm$^{-1}$. This is 2 cm$^{-1}$ outside of the maximum possible value of instrumentation error (± 3 cm$^{-1}$ on each measurement).

The G-band displayed even more variation in band positions across samples, the most extreme blue shifted G-band location found to be at 1577 cm$^{-1}$, while the most extreme red shifted G-band location at 1597 cm$^{-1}$ when comparing all the raw data collected across the samples, correlating to a shift of 20 cm$^{-1}$. These spectra which displayed the largest variation are shown in Figure 3.14, the spectral components causing separation in PCA space (Fig. 3.12) have also been marked on the graph for reference. Within samples the band locations also displayed significant shifts, with the G-band positions varying between 1578 $cm^{-1}$ and 1593 $cm^{-1}$, a difference of 15 $cm^{-1}$ being the maximum difference found. A plot of all the raw data collected across the four samples can be seen in the Appendix: Figure A.9. This significant variation in the band locations in the Raman spectra is likely to contribute to the separation in PCA space (Fig. 3.13).

The shifts in the G-band in the Raman spectra (Fig. 3.14) may be due to residual PMMA on the graphene sample due to the difficulty in removing the polymer from the surface [216, 217]. Ahn *et al.* reported that in order to remove the PMMA completely from the graphene surface it was necessary to use high temperatures to break the backbone bond of the polymer, requiring temperatures of 300 – 400 °C [217]. This can, however, result in amorphous carbon in the graphene sample and so is generally not used [217]. The optical image Figure 3.4b of the samples studied

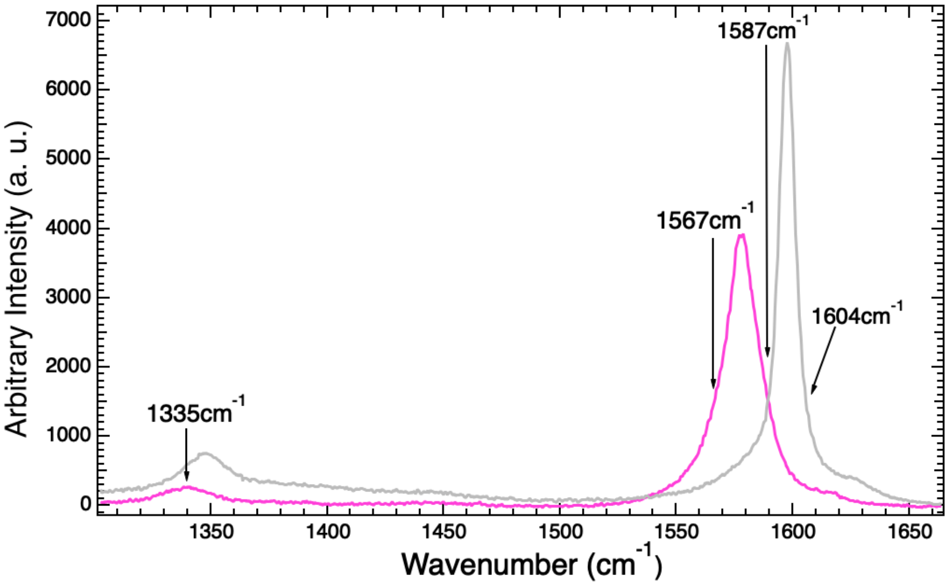

**Figure 3.14:** Peak shifts of the bands in the Raman spectra of graphene across different samples between the wavenumbers 1300 $cm^{-1}$ and 1800 $cm^{-1}$. The labels on the graph correspond to the spectral components highlighted by PCA to be the main points of difference in the Raman spectra of graphene across four different samples. The pink spectrum is from graphene sample three and the grey spectrum is from graphene sample one. There is a difference of 20 $cm^{-1}$ between the positions of the G-band and a difference of $\sim$ 8 $cm^{-1}$ for the D-band when comparing the two spectra.

in this work may demonstrate the presence of the PMMA islands remaining on the graphene surface.

Residual PMMA can apply strain levels of up to 0.15 % in the sample [216]. Mohiuddin *et al.* reported that for 0.11 % strain applied to a graphene samples, the G-band underwent a shift of up to 5 $\text{cm}^{-1}$ [207]. However, the maximum band shift reported in this work within a single graphene sample is 15 $\text{cm}^{-1}$, indicating higher levels of strain in the sample. According to the work of Mohiuddin *et al.* strain of approximately 0.5 to 0.6 % causes shifts of this magnitude [207]. Thus, this analysis is suggestive of levels of strain of 0.5 to 0.6 % being present in the graphene sample, causing shifts of the G-band in the Raman spectra, likely as a result of PMMA use and residual PMMA on the graphene following use in the fabrication process [207, 215, 216, 217].

PCA was also performed on the second range of the graphene spectra from 2400 to 2900 $\text{cm}^{-1}$ (Figure 3.15). There is separation of the samples along PC3, which represents 10.5 % of the variance for the data set. This is the only PC along which the data separated. The corresponding loading for the PCA is shown in Figure 3.16 which indicates there is one main spectral difference between the samples at 2679 $\text{cm}^{-1}$. To demonstrate the variation of the spectral averages about this point, this location is shown on the average graph for the G′-band of the four graphene samples (Figure 3.17).

The location found to cause variation of the graphene samples (2679 $\text{cm}^{-1}$) falls at around the peak centre of samples one, two and four, however, there is a noticeable shift in the peak center for graphene sample three. This shift may contribute to the separation of the samples in PCA space. Sample four is also separated from the others in PCA space, however, there appears to be no significant differences between the average spectrum for graphene sample four compared with one and two, therefore, to further investigate the cause of this separation the raw data must be considered for clarity.

Across the four samples, there are significant shifts in the G′-band of the individual point Raman spectra, with the most blue and red-shifted bands in the spectra located at 2664 $\text{cm}^{-1}$ and 2692 $\text{cm}^{-1}$ respectively, pertaining to a location differ-

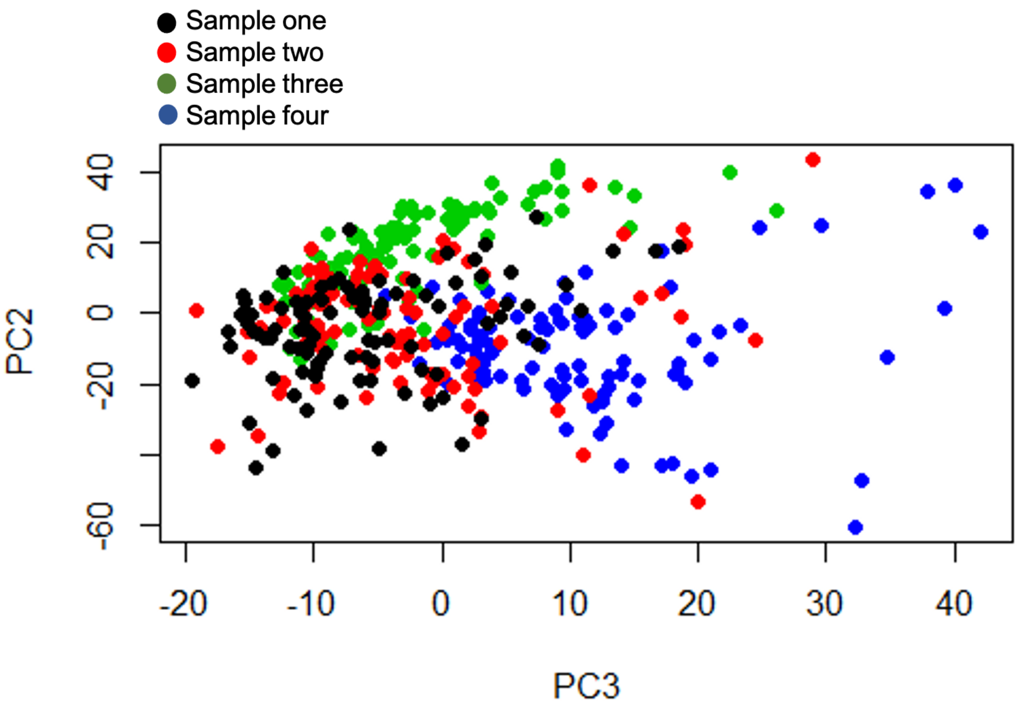

**Figure 3.15:** PCA comparing the Raman spectra of four different graphene samples for the wavenumbers between 2400 cm$^{-1}$ to 2900 cm$^{-1}$. There is separation along PC3 which accounts for 10.5 % of the total variation of the data set.

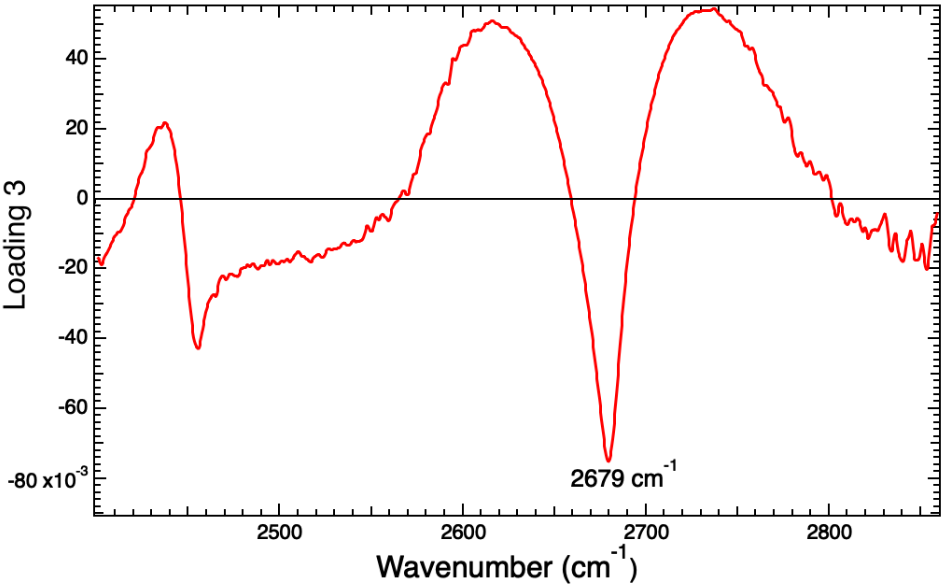

**Figure 3.16:** PC3 loading results for the PCA performed on the graphene spectra between the wavenumbers 2400 cm$^{-1}$ to 2900 cm$^{-1}$ for four graphene samples which showed separation along PC3 with a variation of 10.5 %. The main difference in the Raman spectra which resulted in the separation along PC3 are labelled on the graph.

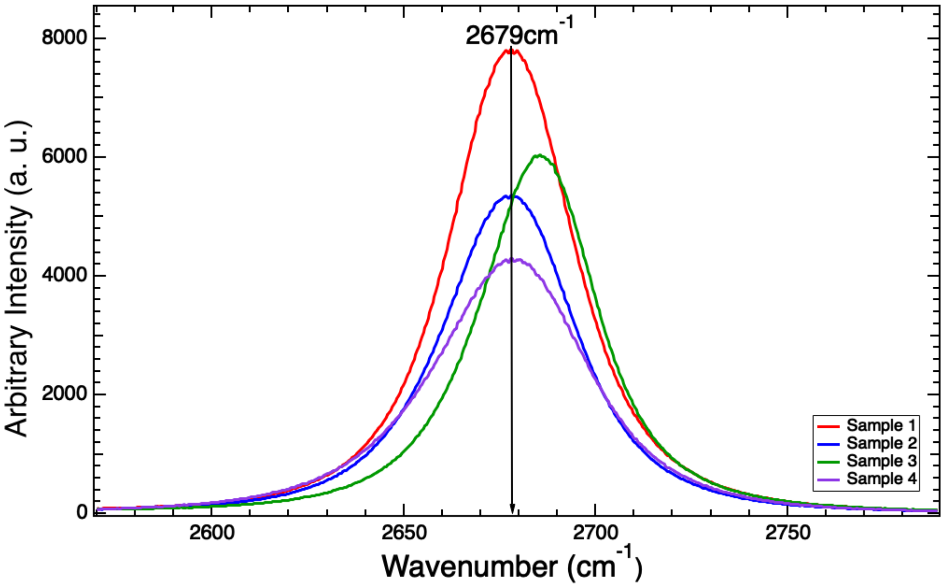

**Figure 3.17:** Average Raman spectra of graphene between the wavenumbers 2400 cm$^{-1}$ and 2900 cm$^{-1}$ with the main spectral components which caused separation of the spectra along PC3 in PCA space labelled. Graphene samples three (green) and four (purple) were found to separate from samples one (red) and two (blue) in PCA space.

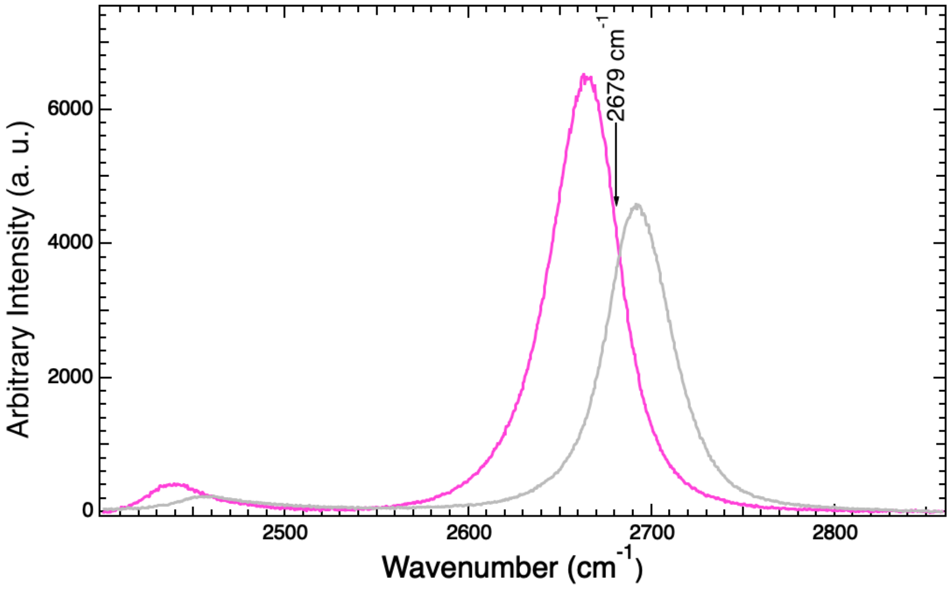

**Figure 3.18:** Peak shifts of the bands in the Raman spectra of graphene across different samples between the wavenumbers 2400 cm$^{-1}$ and 2900 cm$^{-1}$. The label on the graph correspond to the spectral component highlighted by PCA to be the main point of difference in the Raman spectra of graphene across four different samples. The pink spectrum is from graphene sample four with a G′-band located at 2664 cm$^{-1}$. The grey spectrum is from graphene sample two with the G′-band at 2692 cm$^{-1}$. There is a difference of 28 cm$^{-1}$ between the positions of the two G′-bands.

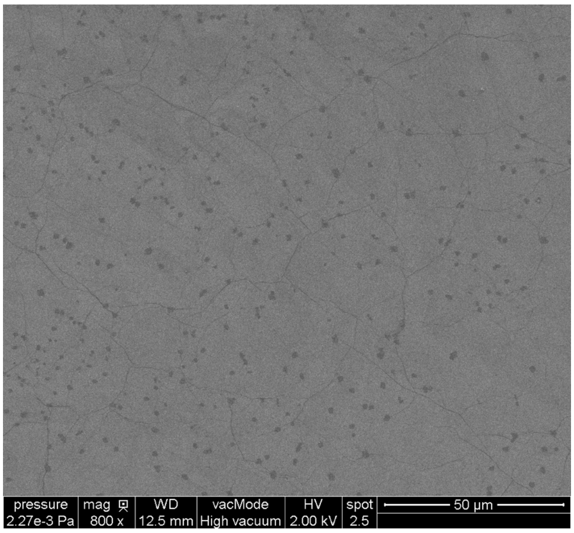

**Figure 3.19:** SEM image obtained from Graphenea [49]. This image is included online for consideration when purchasing the CVD graphene samples used in this work. The dark patches in the graphene sample have been reported in the literature to be bilayer graphene islands [198]. The lines in the samples have been reported to be cracks, wrinkles and grain boundaries [198, 237]. None of these features are referred to or discussed by Graphenea.

ence of 28 cm$^{-1}$. For ease, only the most extreme shifts have been shown here, to demonstrate the level of heterogeneity of the graphene sample (Fig. 3.18). A plot of all the raw data collected across the four samples can be seen in the Appendix: Figure A.10. These shifts in the G′-band may be due to the presence of bilayer islands in the graphene sample [161]. Blue shifting of the G′-band from 2699 to 2686 cm$^{-1}$ when collecting spectra from monolayer and bilayer graphene respectively for CVD graphene samples has been reported by Tu *et al.* when investigating graphene growth by CVD [161]. Tu *et al.* does not include information on the laser wavelength used within this study, thus this work cannot be directly compared with the exact wavenumbers obtained due to the dispersive nature of the G′-band [64, 161]. However, the magnitude of the blue shifting of the band is highly suggestive that bilayer areas could be present in the samples studied in this work.

A scanning electron microscopy (SEM) image obtained from Graphenea, the manufacturer of the graphene studied in this work, is shown in Figure 3.19 [49]. The image is from graphene samples fabricated under the same conditions as studied here. There are many noticeable dark patches on the sample, which other papers have referenced as bilayer graphene [198, 238, 239]. There is no reference by Graphenea that bilayers areas are present in the graphene sample, however, this optical image is evidence that they may be present in the sample [49, 198]. Furthermore, the blue shifting of the band reported here also suggests the presence of bilayer graphene in the sample [161].

The presence of bilayer islands in the graphene sample would also be in agreement with the PIR analysis (Fig. 3.5). PIRs for the graphene studied in this work were found to be low for SLG, which is commonly reported as being $\mathrm{I}_{G'}/\mathrm{I}_G > 2$ (Fig. 3.5) [58, 59, 67, 161, 162, 166, 167, 168, 169, 170, 174, 175, 185, 187, 188, 222, 227, 228, 229]. While the PIRs for the bands fitted with a double Lorentzian in this work are in agreement with the PIR value reported by Zhao *et al.* for doped SLG $\mathrm{I}_{G'}/\mathrm{I}_G = 1.2$ [164], however, the PIRs are also within error of the PIR value obtained by Tu *et al.* for bilayer graphene, found to be $\mathrm{I}_{G'}/\mathrm{I}_G = 1.1$ [161]. Thus, this is further suggestion of bilayer graphene being present in the sample [161]. However, this reduction in PIR $\mathrm{I}_{G'}/\mathrm{I}_G$ may also be due to doping and defects in the samples (Table 3.2) [164].

The G′-band location shifts were also investigated within samples, the largest differences were bands located at 2664 $\mathrm{cm}^{-1}$ for the most down shifted and 2691 $\mathrm{cm}^{-1}$ for the most up-shifted band, resulting in a band location difference of 27 $\mathrm{cm}^{-1}$ found for graphene sample four. This level of heterogeneity within the graphene sample is more than was displayed by any other sample, and may be the cause of the separation of this sample in PCA space (Fig. 3.15).

These significant G- and G′-band shifts found for the graphene samples in this work may be due to defects in the graphene sample [240]. For instance, grain boundaries which result from limited domain size in CVD graphene samples contributes to the level of defect in the graphene sample [51, 52, 196, 212]. The grain boundaries introduce compressive strain into the sample, which can cause a red shift in the G-band and a blue shift in the G′-band [212]. Specifically, Chong *et al.* reported shifts of up to 6 $\mathrm{cm}^{-1}$ and 24 $\mathrm{cm}^{-1}$ for the bands respectively [212]. Thus, it may be the presence of grain boundaries in the graphene sample causing shifts of the bands [212]. Grain boundaries are currently unavoidable in the fabrication process of CVD graphene, and the samples in this work have domain sizes of up to 20 $\mu$m, suggestive of the presence of grain boundaries at the interface of the domains [49].

An optical image of the graphene sample studied in this work highlights a potential grain boundary in the samples (Fig. 3.4b).

The levels of heterogeneity shown here within a graphene sample with no modifications following growth have not been reported within the literature to our knowledge. For instance, the heterogeneity of graphene following defects or strain being applied to the sample has been investigated, however, such significant levels of variation in the spectra of unperturbed graphene does appear to have been reported and investigated as thoroughly, using multiple forms of analysis, as has been done in this work [211, 231].

It is evident that the samples studied in this work are not homogeneous [49]. Furthermore, it is also indicative each sample displays differing levels of defects such as strain and grain boundaries, reflected through the significant variation in the band locations in the Raman spectra (Fig. 3.14 and 3.18). In the next section a novel method for analysis of the heterogeneity of the graphene samples is applied to the samples, to determine the rate of convergence, and thus the rate of heterogeneity of the samples.

## 3.5 Statistical Convergence Rates of CVD Graphene samples

A novel method for investigation of the level of heterogeneity of a given sample is proposed here. This analysis involves performing fittings on a given normalised band in Raman spectrum of graphene for an average of one spectrum, then two spectra, three spectra etc. up to the maximum number of spectra, in this case 100 spectra. The corresponding SE value of the normalised intensity of the band is then plotted, which decreases for increasing numbers of spectra in the average, as also demonstrated by the SE and 2SD convergence tests (Section 3.3). This produces a decay graph, termed a convergence rate graph. This graph can be fitted with a $1/\sqrt{N}$ function producing a convergence rate $\lambda$ for each graphene sample. The amount of heterogeneity in a graphene sample results in varying decay rates. A larger value of $\lambda$ indicates a more rapid decay of the SE meaning the sample is more

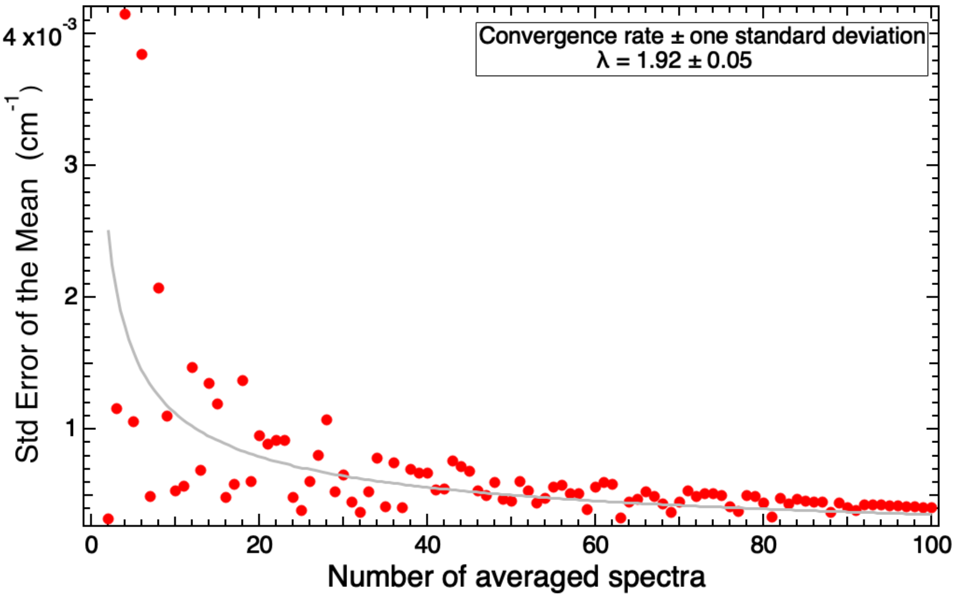

**Figure 3.20:** Image showing the convergence of the standard error of the mean of the normalised amplitude of the D-band for increasing numbers of spectra in the spectral average for graphene sample one. $\lambda$ represents the rate of convergence, which provides information about the heterogeneity of the defects in the sample.

homogeneous, while smaller $\lambda$ values are representative of a slower decay and a more heterogeneous samples.

Here, the analysis has been performed on the normalised intensity of the D-band in the Raman spectra for increasing number in the average. The decay rates obtained for these convergence graphs will give insight into the level of defect and heterogeneity of the samples. These convergence rates can also be performed on other quantities, for instance, a convergence rate could be obtained for the location of the G-band in the Raman spectra in order to investigate the level of heterogeneity of the sample due to the variation in G-band location, which may be a result of residual strain in the sample [211].

A convergence test of the standard error of the mean (SE) of the normalised D-band intensity for increasing numbers of spectra in the averaged Raman spectrum of graphene sample one can be seen in Figure 3.20. The SE for this data converges to a value of $\sim 0.00040$, for around 95 to 100 individual point Raman spectra in the spectral average. The fitting of this convergence graph produces a rate of change of $\lambda = 1.92 \pm 0.05$.

**Table 3.3:** Convergence rates, $\lambda$, of the standard error of the mean of the normalised intensity of the D-band in the Raman spectra for four CVD graphene samples. The convergence rate indicates the level of heterogeneity of the sample, with a large convergence correlating to a more homogeneous sample.

| | **Convergence rate** $\lambda$ | **± SE** |
|---|---|---|
| **Sample one** | 1.92 | 0.05 |
| **Sample two** | 0.89 | 0.02 |
| **Sample three** | 0.48 | 0.1 |
| **Sample four** | 0.57 | 0.2 |

The convergence rates for the other samples can be seen in Table 3.3, the corresponding convergence rate graphs are included in the Appendix (Figures A.11, A.12 and A.13 for samples two, three and four respectively). Graphene sample two achieves the next highest rate of convergence after sample one. This indicates that when comparing graphene sample one with the other samples, graphene sample two possesses the most comparable levels of heterogeneity and defect. This is in agreement with the PCA results which found graphene samples one and two not to vary, indicated by the lack of separation of the samples in PCA space (Fig. 3.11). The univariate analysis is also in agreement, with the PIR $I_D/I_{G2} = 0.17 \pm 0.03$ for both samples (Fig. 3.5). However, the $I_D/I_{G1}$ PIR is in disagreement, with the values falling just outside of error of one another, indicating slight variation in the defect levels of the sample which may be the cause of the difference in convergence rates (Table 3.3). Overall, the majority of analysis demonstrates that graphene sample one differs significantly when compared with samples three and four and is most comparable with graphene sample two. Graphene samples one and two produce the largest convergence rates, indicating they are the least defected of the samples.

The convergence rate achieved for graphene sample three is much lower compared with graphene samples one and two, indicating a more heterogeneous sample (Table 3.3), and suggestive that the level and types of defects in sample three are less homogeneous. This is also true for the SE and 2SD convergence tests for graphene sample three (Appendix: Figures A.5a & A.5b and Figures A.6a & A.6b for the SE and 2SD convergences respectively). When compared with the other graphene samples, graphene sample three is not as converged as the other samples when the average of 100 Raman spectra is reached, indicating that the level of heterogeneity and defect of this sample is larger than the other CVD graphene samples studied here.

The heterogeneity of graphene sample three differing from the other samples was also demonstrated through PCA (Fig. 3.11). Sample three separated from all other samples, also suggestive of variation of the sample. This is, however, not in agreement with the PIRs obtained for graphene sample three: $I_D/I_{G1} = 0.19 \pm 0.06$ and $I_D/I_{G1} = 0.12 \pm 0.06$, both of which are comparable with the results for the other samples (Fig. 3.5), and the latter of which is in fact the lowest of this PIR for all samples, indicating the lowest level of defect of the samples. This highlights the importance of performing more than one type of analysis on the Raman spectra.

Graphene sample four produces a lower convergence rate than graphene samples one and two and a higher rate than that obtained for graphene sample three (Table 3.3). This suggests that sample four has an average amount of heterogeneity and defect when compared with samples one, two and three. Again, this is in agreement with the SE and 2SD convergence tests performed on the data showing increased convergence compared with sample three and decreased compared with samples one and two (Appendix: Figures A.7a & A.7b and Figures A.8a & A.8b for the SE and 2SD convergences respectively). This is also in line the PCA findings, which showed sample four separating from all other samples (Fig. 3.11), with the most amount of scatter indicating increased levels of variation in the sample.

Overall, the analysis indicates that graphene sample three is the most heterogeneous of the samples, likely to be a result of more varying defects compared with the other samples, thus resulting in the lowest convergence rate (Table 3.3). This tool could aid in the determination of the level of characterisation required for a given sample. It acts as an excellent complementary tool alongside the univariate PIR analysis and multivariate PCA performed in this work, as an efficient tool to determine the level of heterogeneity of a given sample. This could be significant for determining if graphene samples are of a sufficiency high quality to be used within applications, as a tool for quality control.

A statistical analysis tool like the one proposed here could also be extremely beneficial for understanding the differing levels of defects of samples. It is important that differences between samples which are produced under the same conditions are investigated. These convergence tests rely only on the changes in the normalised D-band intensity, and so are not influenced by changes in the spectra resulting from unintentional doping or the sensitivity of the G-band to perturbations in the sample. There is currently a need for a test like this given the lack of reliability of the use of PIRs and the need for further analysis into the heterogeneity of graphene samples in literature. In future work, this protocol would work best alongside determination of the types of defects in graphene samples and how they affect the rate of convergence. Eventually, alterations in the rate of convergence for certain bands could be linked to a specific type of defect in the Raman spectra.

The level of analysis of the CVD graphene samples performed in this chapter is necessary for complete and proper characterisation. Furthermore, for graphene to be utilised in biomedical devices, and for interaction with biological samples, analysis of this level is necessary to understand the fundamental properties and defects of the sample [57].

## 3.6 Conclusion

Many methods of analysis have been performed within this chapter on the Raman spectra of graphene, some of which are well established of methods of characterisation and some novel methods which investigate the samples in ways which not been done previously. This work has achieved a thorough level of characterisation which does not appear to have been accomplished before.

The perturbations of the Raman spectra studied in this work compared with pristine graphene are significant. The FWHM of $G_1$-band was found to be between 19 - 30 $cm^{-1}$, indicating band broadening compared with ME SLG, whereas the FWHM of the $G_2$-band had a value of 11 - 14 $cm^{-1}$, in agreement with the expected value for pristine graphene [67, 166, 185, 187, 188, 222, 227, 228, 229]. The G′-band produced FWHM values of between 35 $cm^{-1}$ - 46 $cm^{-1}$, larger than expected for SLG [166, 188, 227, 229]. The asymmetric nature and broadening of bands in this work indicates that there is unintentional inhomogeneous doping of the graphene sample, likely to be resultant from the Si/$SiO_2$ substrate [59, 189]. Phonon softening resulting from strained or stressed samples may also have contributed to the increases in the width of the bands in the Raman spectra seen here [211, 230].

An average PIR of $I_{G'}/I_{G2} = 2.2 \pm 0.2$ was achieved for fitting of the G′-band with a Voigt model in this work. This is in agreement with the values in literature for CVD SLG, which is generally found to be $\sim 2$ [161, 174, 175]. However, this PIR analysis was found to unreliable when performed on spectra representing different levels of defect in the graphene sample. The $I_{G'}/I_{G2}$ value was found to change considerably for varying levels of defect in the sample. The PIR for the Raman spectra representing pristine graphene was found to be $I_{G'}/I_G = 3 \pm 0.02$, for moderately defected $I_{G'}/I_G = 1.8 \pm 0.7$, and for the highly defected Raman spectrum of graphene $I_{G'}/I_G = 0.36 \pm 0.02$ across samples. This analysis demonstrates the impact of defects in CVD graphene has on this Raman marker, and indicates why it is unreliable for determination of the number of layers in the graphene samples.

The different types of defect in the graphene sample, for example, the residual strain from the use of PMMA during the fabrication process, contributes to the extreme levels of heterogeneity found in the samples studied within this work [215]. PCA performed on the Raman spectra found all samples, except samples one and two, to separate for the wavenumbers 1300 - 1800 $cm^{-1}$ and 2400 - 2900 $cm^{-1}$ in PCA space. The lower wavenumbers were found to separate along PC1, representing 55 % of the variance of the data set. The higher wavenumbers separated along PC3 representing 10.5 % of the total variance. The reason for the separation of these samples in PCA space is due to significant shifts in the bands in the Raman spectra. Examination of the raw data found that there were band shifts of up to 8 $cm^{-1}$ for the location of the D-band, shifts of up to 20 $cm^{-1}$ for the position of the G-band and of up to 28 $cm^{-1}$ for the G′-band in the Raman spectra. These band shifts may be due to the residual strain from the use of PMMA on the sample, as well as smaller domain size compared with ME graphene, and cracks and holes from the transfer of the graphene onto the substrate, which contribute to the heterogeneity levels of the samples studied in this work [52, 196, 214, 241].

A novel method for determination of the level of heterogeneity of the graphene samples was also proposed and performed on the spectra. This involved plotting the SE of the normalised intensity of the D-band in the Raman spectra in a convergence rate graph, to obtain a convergence rate for each sample. Samples one and two achieved the same convergence rate of 1.92 ± 0.05 and 0.89 ± 0.02 respectively. The convergence rate for graphene sample three was 0.48 ± 0.1, while graphene sample four obtained a convergence rate of 0.57 ± 0.2. Therefore, this analysis confirmed that graphene sample three was the most heterogeneous of the samples. Graphene sample four obtained the average convergence rate compared with the other samples and graphene samples one and two were the most homogeneous samples. No other method of analysis allows for determination of the heterogeneity in a graphene sample in such a way.

The number of spectra collected to represent each graphene sample has also proven to be significant, alongside random point sampling. Given the level of heterogeneity found within this work, it is essential that enough spectral data are collected from each sample, that it is properly characterised. Within this work statistical tests were performed involving convergence of the SE and 2SD of the Raman spectra for increasing numbers of spectra in the average. These convergence tests ensure that sufficient data are collected to be statistically representative of the entire sample. To our knowledge, no other test like this has been performed before, and often insufficient numbers of data are collected for the characterisation of CVD graphene samples, as little as ten spectra per sample, with many works not providing information on the number of spectra collected [58, 67, 169]. Consideration of the SE and 2SD convergence tests presented in this work indicates that a minimum of 100 individual Raman spectra collected from all points in the graphene sample is necessary for proper and thorough sample characterisation.

A thorough level of characterisation is performed in this chapter, with full investigation into the changes in the Raman spectra being explored. No other work has performed analysis to this extent or performed such extensive analysis on the spectra, to our knowledge. This may be the reason why such levels of heterogeneity do not appear to have been reported before within literature. This heterogeneity of the graphene samples could have serious implications for the application of this type of graphene. Particularly, in wearable graphene devices, and such applications which entail close proximity of graphene with human cells, it is not known what effect these high levels of heterogeneity will have on the interactions of the graphene with the cells [45]. In future it is necessary that both the specific defects which are contributing to this inhomogeneity and how this affects the properties of the graphene sample is understood.

Future work for this project would involve performing Raman mapping of the graphene samples. The work presented within this chapter laid the basis for future work involving more extensive Raman measurements. It has provided good understanding of the samples which could be further expanded with Raman mapping.

# 4

# Characterisation of *E. coli* using Raman Spectroscopy

The use of Raman spectroscopy for analysis of *Escherichia coli* (*E. coli*) has previously been studied within literature for characterisation and identification of the bacterium [154, 242]. The ability for Raman spectroscopy to be utilised as a tool for characterisation is, however, hindered by the heterogeneity of the bacterial sample causing variation in the Raman spectra, which could result in misclassification of bacteria [108]. For example, Kastanos *et al.* investigated the classification of bacteria for urinary tract infection (UTI) diagnosis and reported that Raman was able to classify the majority of bacteria causing infection, however, two of seventeen samples were misclassified as incorrect bacteria types [243]. This poses a potential issue for the use of Raman spectroscopy for identification of bacteria in clinical settings [155]. Thus, it is important that sufficient data are collected, to ensure that a given bacterial sample is properly characterised and the average Raman spectrum is representative of the heterogeneity of the entire sample. No protocol currently exists within the literature pertaining to the level of characterisation necessary for bacterial samples using Raman spectroscopy, and many papers collect insufficient numbers of spectra to be representative of the wealth of information contained in the Raman spectra [151, 153]. There are works within literature which have collected as few as ten or less spectra for characterisation of a bacterial sample [120, 151, 153, 159].

The work in this chapter investigates the number of spectra necessary to properly represent an *E. coli* sample across three biological replicates, and proposes a standardised procedure which can be used across systems to ensure proper characterisation of the sample [87]. Papers have called for standardised procedures due to the ambiguity surrounding the level of characterisation needed [108, 244, 245, 246]. Schie *et al.* proposed a procedure for Raman characterisation of biological samples, specifically looking at lymphocytes, to determine the number of spectra required to characterise the sample [246]. However, the standardised procedure proposed is system-specific to large biological cells, as it investigates the heterogeneity of spectra collected at different points on the same cell, not applicable to *E. coli* due to the small size of the cells [246]. Furthermore, the work by Schie *et al.* [246] does not ensure convergence of the statistical quantities such as standard error of the mean (SE) and second order standard deviation (2SD) for the number of spectra collected, as was done in this thesis.

Evidence will be presented in this chapter to show that the protocols used in this work go beyond proposed protocols of characterisation in literature. Furthermore, the procedure for the determination of the number of spectra required to ensure proper characterisation presented in this chapter can be applied to any system, as was done with graphene (Chapter 3). The heterogeneity of the *E. coli* samples are also investigated using PCA and peak intensity ratio (PIR) analysis, as well novel methods of analysis which allow investigation into heterogeneous biomarkers in the Raman spectra of *E. coli*.

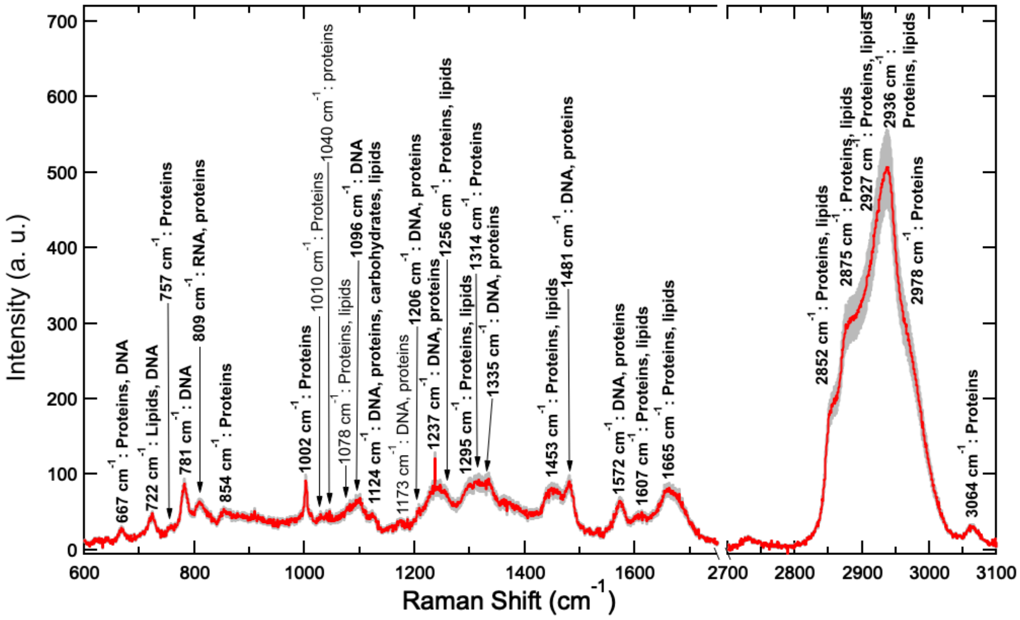

**Figure 4.1:** Average Raman spectrum of *E. coli* comprising 55 individual Raman spectra. The grey envelope represents the standard error of the mean (SE) of the averaged spectrum. The band locations are labelled, with the corresponding biomolecular assignments included on the graph [77, 120, 124, 136, 153, 155, 156, 247]. The peaks in bold are common to all three *E. coli* replicates studied. The spectra which make up this non-normalised average have been linearly baseline subtracted.

## 4.1 Raman Spectroscopy of *E. coli*

An average Raman spectrum of *E. coli*, strain MG1655, is shown in Figure 4.1. It is an average of 55 individual Raman spectra collected from random points across the sample on $CaF_2$ (Fig. 4.2), and represents one of the three biological replicates presented in this chapter. The grey envelope represents the SE envelope for the given sample, this was converged across the three replicates, as will be discussed in Section 4.2. The bands in the averaged *E. coli* Raman spectrum, labelled on the graph, are representative of the biomolecules of the cells, i.e., lipids, proteins and DNA (Table 4.1)[124].

The bands arise from the Raman-active modes of the biomolecules in the cell, such as stretching, bending, rocking or twisting of bonds (Table 4.1) [124]. For example, Figure 4.3 shows O-P-O$^-$ symmetric and $PO_2^-$ asymmetric stretching of the phosphate bonds in the DNA backbone which contribute to the bands at 1096

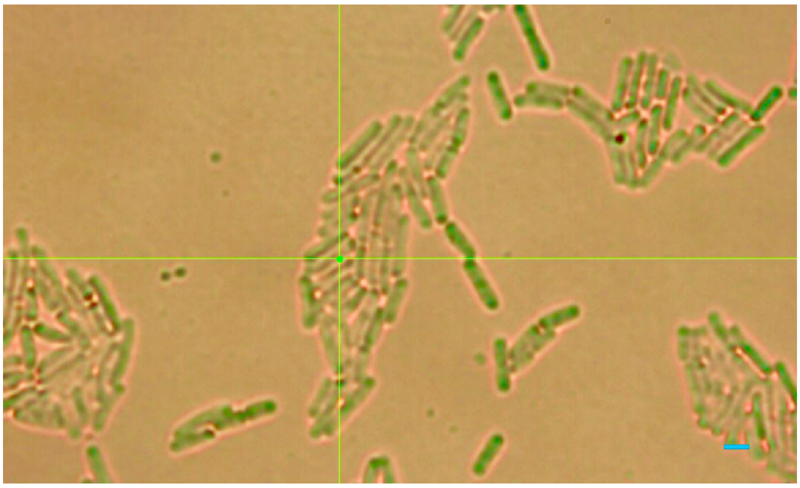

**(a)** Optical image of an *E. coli* sample studied in this work. The *E. coli* cells are dried onto a $CaF_2$ disc. The green dot represents the position of the Raman laser. The scale bar is 2 $\mu$m.

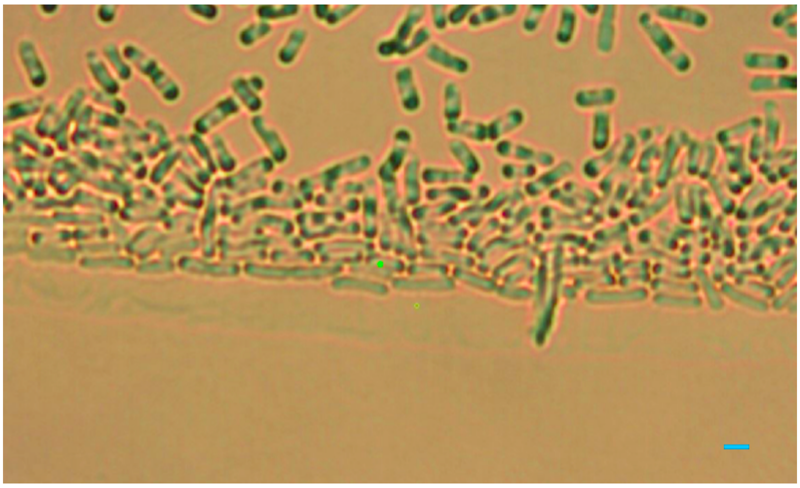

**(b)** Optical image of an *E. coli* sample studied in this work. The *E. coli* cells are dried onto a $CaF_2$ disc. The green dot represents the position of the Raman laser. The scale bar is 2 $\mu$m.

**Figure 4.2:** Optical images of an *E. coli* sample dried on $CaF_2$ which was characterised using Raman spectroscopy in this work. Both images are from different points in the same sample.

**Table 4.1:** Table showing the band locations for the average Raman spectra of the three *E. coli* samples studied in this work. Band locations from literature are included for comparison as well as the corresponding biomolecular assignment. Most bands in the Raman spectra of *E. coli* are convolved, representing more than one biomolecule. The maximum error of the band locations is instrumentation error of 3 cm$^{-1}$. The stated uncertainties are obtained from the fitting of the SE envelope. S1, S2 and S3 refer to *E. coli* samples one, two and three. The nucleobases are adenine (A), cytosine (C), guanine (G), thymine (T) and uracil (U). The units are cm$^{-1}$.

| **Location (cm$^{-1}$)** | | | **Literature location (cm$^{-1}$)** | **Peak Assignment** | **Bond** | **Reference** |
|---|---|---|---|---|---|---|
| **S1** | **S2** | **S3** | | | | |
| 667.9 ± 0.1 | 667.29 ± 0.04 | 666.0 ± 0.2 | 665 - 668 | **DNA:**<br>G, T, C | C-S stretching | [77, 124, 136] |
| 722.4 ± 0.1 | 722.6 ± 0.1 | 721.0 ± 0.2 | 720 - 730 | **Phospholipids**<br>**DNA:** A | CH$_2$ rocking | [77, 123, 124, 136, 156] |
| 755.9 ± 0.1 | 758.8 ± 0.3 | 755.22 ± 0.06 | 759 | **Proteins:**<br>Tryptophan | - | [77, 124] |
| 782.03 ± 0.03 | 781.49 ± 0.01 | 780.43 ± 0.02 | 783 | **DNA:**<br>U, T, C | C=O, C-N<br>Ring deformation | [77, 120, 124, 153, 155, 156] |
| 809.4 ± 0.1 | 809.2 ± 0.2 | 809.35 ± 0.07 | 811 - 813 | **RNA**<br>**Proteins:** Tyrosine | C-O-P-O-C of DNA backbone<br>C-C stretching | [77, 124, 136, 155, 156] |
| 854.25 ± 0.05 | 854.1 ± 0.5 | 853.5 ± 0.3 | 857 | **Proteins:** Tyrosine<br>Skletal mode of alpha-anomers | C-C stretching<br>C-O-C stretching<br>1,4 glycosidic link | [77, 124, 155, 156] |
| 1002.33 ± 0.02 | 1002.15 ± 0.03 | 1000.90 ± 0.03 | 1000 - 1005 | **Proteins:**<br>Phenylalanine | C-C stretching of aromatic ring | [77, 124, 136, 153, 155, 156, 247] |
| - | 1010.3 ± 0.2 | - | 1008 | **Proteins:**<br>Phenylalanine | - | [124] |
| 1040.7 ± 0.7 | - | - | 1035 | **Proteins** | - | [124] |
| 1078.1 ± 0.4 | 1078.2 ± 0.8 | 1076.9 ± 0.1 | 1080 | **Proteins:** Alkane<br>**Phospholipids** | C-C stretch<br>Phosphate vibrations | [77, 124, 156] |
| - | 1093.1 ± 0.5 | - | 1095 - 1100 | **DNA:** DNA backbone vibration | O-P-O- symmetric stretching | [77, 136, 155, 156] |
| 1098.3 ± 0.2 | 1099 ± 1 | 1096.96 ± 0.06 | 1095 - 1100 | **DNA:** DNA backbone vibration | O-P-O- symmetric stretching<br>C-N | [77, 124, 136, 155, 156] |
| 1124.6 ± 0.2 | 1124.4 ± 0.2 | 1123.6 ± 0.1 | 1126 | **DNA:** C, T<br>**Proteins**<br>**Carbohydrates**<br>**Lipids** | C-C<br>C-N stretching<br>C-O stretching | [77, 124, 156] |
| - | 1173.1 ± 0.2 | 1172.6 ± 0.1 | 1170 - 1175 | **Proteins:** Tyrosine<br>Phenylalanine<br>**DNA** C, G | C-H in-plane bending mode<br>C-H | [77, 124, 136] |

**Table 4.1 continued.**

| Location ($cm^{-1}$) | | | Literature location | Peak Assignment | Bond | Reference |
|---|---|---|---|---|---|---|
| S1 | S2 | S3 | | | | |
| 1205.8 ± 0.1 | 1206.2 ± 0.3 | 1205.9 ± 0.1 | 1208 | **Proteins:** Tryptophan, Phenylalanine<br>**DNA:** A, T | $C-C_5H_6$ | [77, 124] |
| 1237.2 ± 0.3 | 1237.3 ± 0.1 | 1236.06 ± 0.04 | 1242 - 1250 | **Proteins:** Amide III<br>**DNA:** U | C-H bend<br>C-N, N-H | [77, 120, 124, 153] |
| 1255.9 ± 0.1 | 1256.4 ± 0.1 | 1255.78 ± 0.06 | 1256 | **Proteins:** Amide III<br>**DNA:** T<br>**Lipids** | - | [115, 124] |
| 1294.0 ± 0.3 | 1295 ± 1 | 1295 ± 2 | 1300 | **Lipids**<br>**Proteins** | $CH_3$ and $CH_2$ twisting or bending | [77, 120, 136] |
| 1314.0 ± 0.5 | 1314.8 ± 0.4 | 1314 ± 1 | 1314 | **Proteins** | $CH_3$ and $CH_2$ twisting mode | [124] |
| 1335.6 ± 0.3 | 1335.3 ± 0.9 | 1334.2 ± 0.8 | 1336 | **Proteins**<br>**DNA:** G | $CH_3$ and $CH_2$ deformation<br>CH deformation | [77, 124] |
| 1453.64 ± 0.07 | 1452.49 ± 0.05 | 1453.4 ± 0.2 | 1453 | **Protein deformation**<br>**Lipids** | $CH_2$ deformation | [120, 121, 124, 155, 156] |
| 1481.13 ± 0.01 | 1481.2 ± 0.1 | 1480.1 ± 0.1 | 1481 - 1486 | **Proteins:** Amide II<br>**DNA:** A, G | - | [77, 124, 247] |
| 1572.2 ± 0.3 | 1572.5 ± 0.3 | 1572.2 ± 0.5 | 1574 - 1578 | **DNA:** A, G<br>**Proteins:** Amide II | Ring breathing modes<br>NH deformation<br>CN stretching | [77, 115, 124, 153, 155, 156] |
| 1606.4 ± 0.1 | 1606.10 ± 0.08 | 1607.9 ± 0.3 | 1605 - 1607 | **Proteins:** Tyrosine<br>Phenylalanine<br>**Unsaturated lipids** | C=C | [77, 121] |
| 1665.8 ± 0.3 | 1665.1 ± 0.4 | 1663.8 ± 0.4 | 1660 | **Lipids**<br>Unsaturated fatty acids<br>**Proteins:** Amide I | C=C<br>Phenyl ring vibration | [77, 153, 155, 156] |
| 2852.73 ± 0.02 | 2851.86 ± 0.03 | 2851.65 ± 0.03 | 2855 | **Fatty acids**<br>**Lipids** | $CH_2$ symmetric stretch | [124, 153] |
| 2875.7 ± 0.5 | 2874.28 ± 0.02 | 2873.89 ± 0.07 | 2875 | **Lipids**<br>**Proteins** | $CH_2$ asymmetric stretch | [124] |
| 2929.5 ± 0.1 | 2924.7 ± 0.4 | 2926 ± 1 | 2929 | **Lipids**<br>**Proteins** | $CH_2$ assymmetric and $CH_3$ symmetric stretch, | [153] |
| 2936.65 ± 0.02 | 2936.84 ± 0.01 | 2935.80 ± 0.08 | 2935 | **Lipids**<br>**Proteins** | Chain end $CH_3$ stretch | [124] |
| 2978.3 ± 0.02 | 2979.16 ± 0.01 | 2976.1 ± 0.6 | 2973 | **Proteins** | Asymmetric $CH_3$ stretch | [124] |
| 3062.6 ± 0.5 | 3065 ± 2 | 3065 ± 2 | 3067 | **Proteins** | - | [248] |

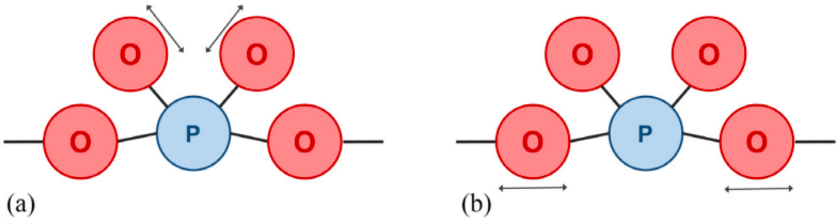

**Figure 4.3:** Vibrational modes of the backbone of DNA (a) $PO_2^-$ symmetric stretching responsible for the band at 1096 cm$^{-1}$ (b) O-P-O bond stretching which gives rise to the band at 781 cm$^{-1}$ in the Raman spectra. Figure obtained from [249].

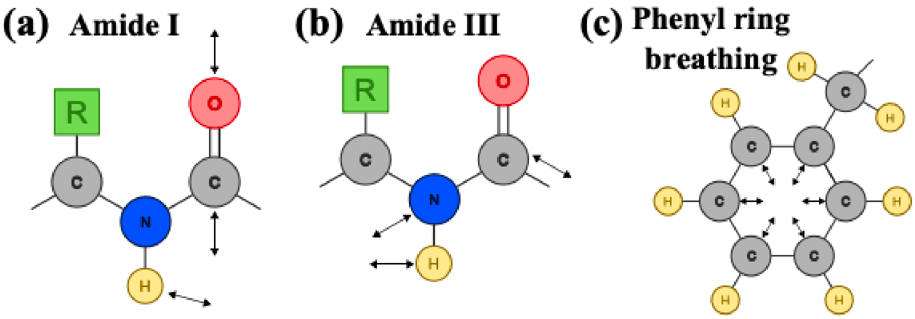

**Figure 4.4:** Vibrational modes for the bands in the Raman spectra representative of proteins (a) carbonyl C=O stretching with a small contribution from in-plane N-H bending (b) the Amide III mode arising at 1256 cm$^{-1}$ in the Raman spectra with the largest contribution from the N-H bending mode and lesser so from the C=O stretching (c) phenyl ring breathing mode giving rise to the intense band at 1002 cm$^{-1}$ representing phenylalanine. Figure obtained from [249].

cm$^{-1}$ and 781 cm$^{-1}$ respectively [249]. More complicated vibrational modes for bands associated with proteins, such as the band at 1665 cm$^{-1}$ representing Amide I, the sharp intense band at 1002 cm$^{-1}$ for amino acid phenylalanine and the band at 1256 cm$^{-1}$ indicative of Amide III can be seen in Figure 4.4 [249]. These bands are labelled on the average *E. coli* spectrum (Fig. 4.1).

The three *E. coli* samples discussed in this chapter correspond to three biological replicates, the averages of which are shown in the Appendix: Figure A.14. The band locations, as labelled on the average spectrum (Fig. 4.1), were obtained from peak fittings and are an average of the locations across the three *E. coli* samples studied in this work. The separate band locations of the three *E. coli* samples are in Table 4.1, along with the corresponding molecular vibration and cellular component which gives rise to this band, as obtained from literature [77, 115, 119, 120, 121, 123, 124, 136, 153, 155, 156, 247]. Many of the bands in the *E. coli* Raman spectra (Fig. 4.1) are convolved, i.e., each band is generally representative of at least one, often more, biomolecules due to the complexity of the *E. coli* cells [250].

This work attempts to achieve a spectral average of the samples which is fully representative of the heterogeneity which they encompass. The levels of characterisation achieved in this work will first be presented, followed by an investigation of the heterogeneity of the spectra using principal component analysis (PCA) and peak intensity ratios (PIRs).

## 4.2 Standard error and second order standard deviation convergence tests

In this section, the number of spectra collected have been analysed for investigation into the level of characterisation achieved across the three *E. coli* samples. This will involve examination of the standard error (SE) and second order standard deviation (2SD) waves, to determine the amount of spectra necessary to converge these quantities so that the average is fully representative of the analyte. This convergence allows for determination of how well characterised a sample is with a given number of spectra.

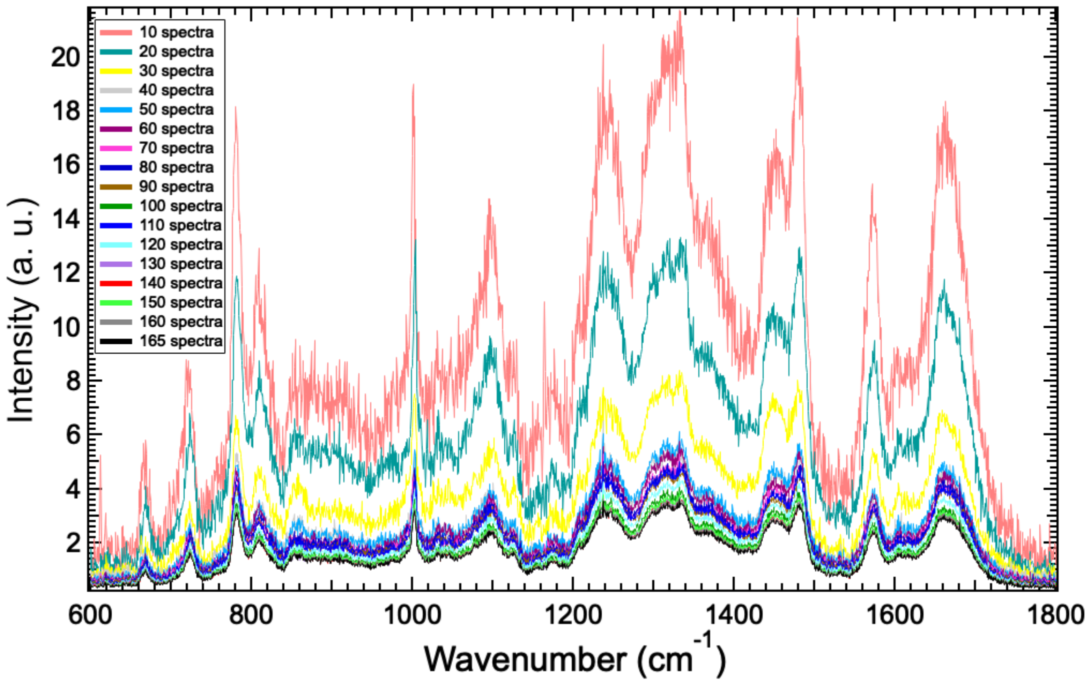

**(a)** SE convergence graphs for the fingerprint region (600 - 1800 cm$^{-1}$) in the Raman spectra across three *E. coli* samples.

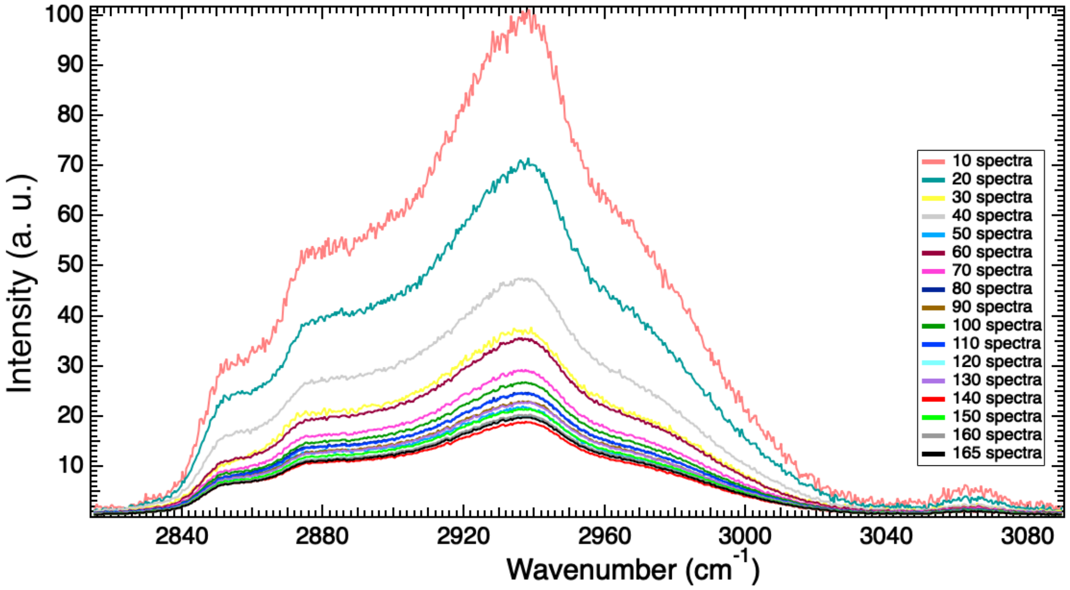

**(b)** SE convergence graphs for the high wavenumber (2800 - 3100 cm$^{-1}$) region in the Raman spectra across three *E. coli* samples.

**Figure 4.5:** Convergences of the standard error (SE) waves for the fingerprint and high wavenumber region of the Raman spectra of *E. coli* for increasing numbers of spectra in the average spectrum, up to the maximum 165 spectra collected in this work, with each replicate represented by 55 Raman spectra. The non-normalised spectra have been linearly baseline subtracted.

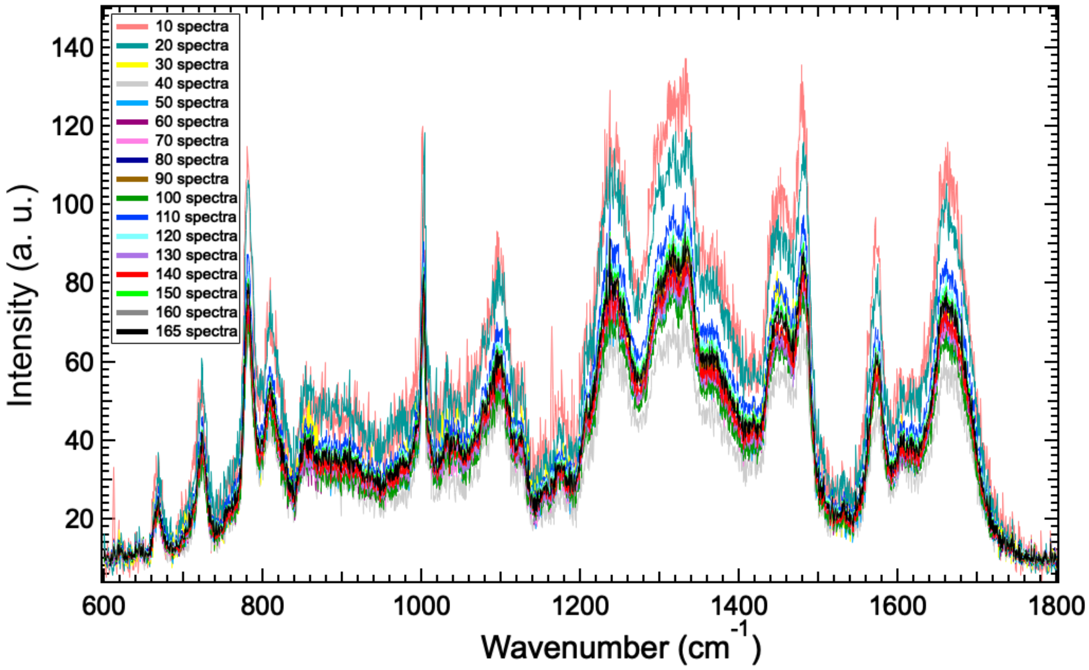

**(a)** 2SD convergence graphs for the fingerprint region (600 - 1800 cm$^{-1}$) in the Raman spectra across three *E. coli* samples.

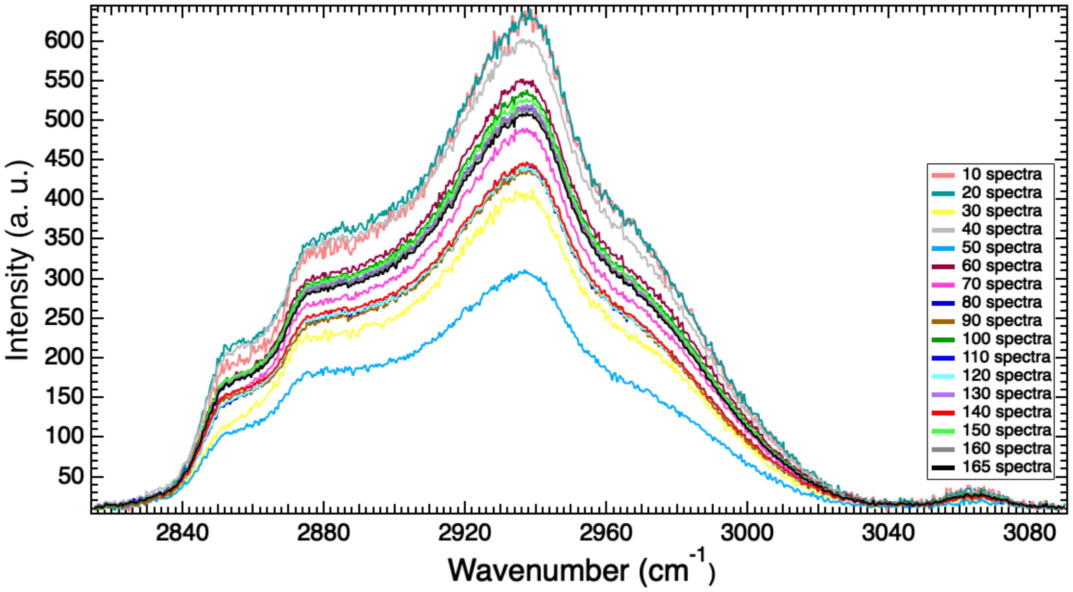

**(b)** 2SD convergence graphs for the high wavenumber (2800 - 3100 cm$^{-1}$) region in the Raman spectra across three *E. coli* samples.

**Figure 4.6:** Convergences of the second order standard deviation (2SD) waves for the fingerprint and high wavenumber region of the Raman spectra of *E. coli* for increasing numbers of spectra in the average spectrum, up to the maximum 165 spectra collected in this work, with each replicate represented by 55 Raman spectra. The non-normalised spectra have been linearly baseline subtracted.

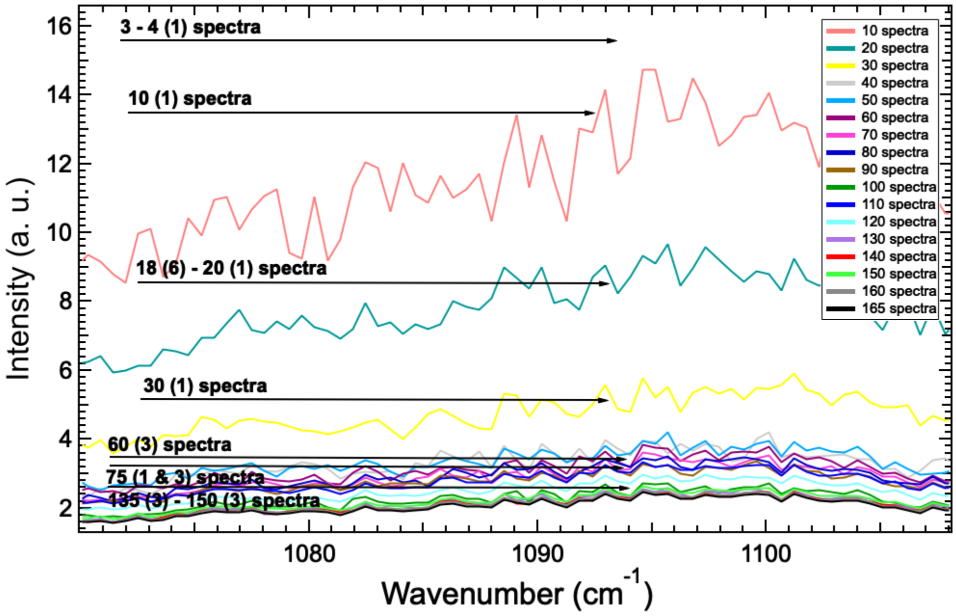

**(a)** Zoom in of the SE convergence waves for the *E. coli* spectra across three replicates in this work. The number of spectra collected for characterisation of bacteria samples in the literature are labelled on the graph [77, 108, 120, 121, 136, 151, 152, 153, 154, 155, 159].

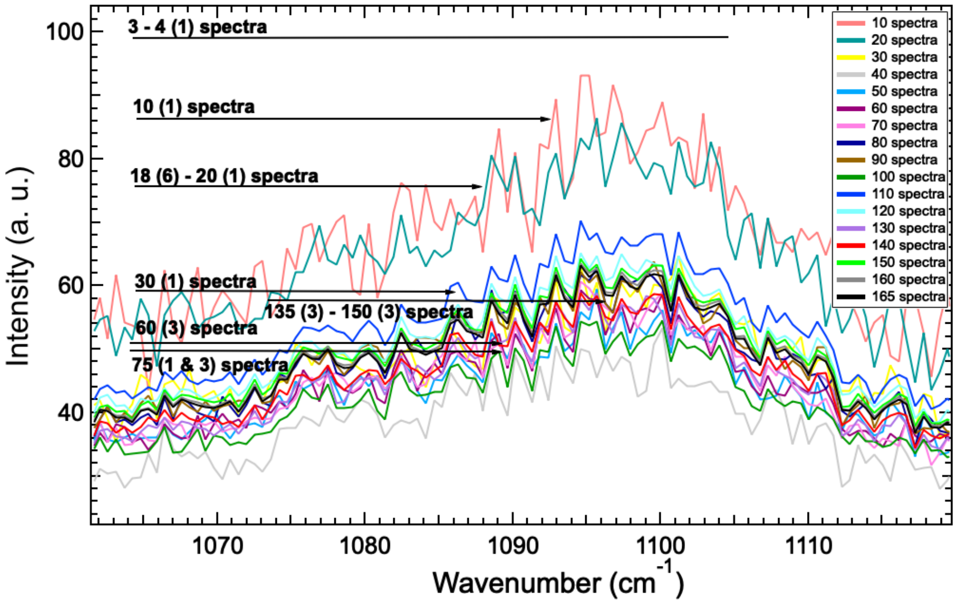

**(b)** Zoom in of the 2SD convergence waves for the *E. coli* spectra across three replicates in this work. The number of spectra collected for characterisation of bacteria samples in the literature are labelled on the graphs [77, 108, 120, 121, 136, 151, 152, 153, 154, 155, 159].

**Figure 4.7:** Zoomed in areas of the SE and 2SD convergence graphs with the total number of spectra collected in the literature studies of Raman spectroscopy for characterisation of bacteria samples. The number in brackets is the number of replicates over which these spectra were collected.

The convergence of the SE and 2SD is performed on 165 spectra across the three *E. coli* samples, with each sample represented by 55 point Raman spectra. Figures 4.5a and 4.5b shows the convergence of the SE of the mean for the fingerprint and high wavenumber regions respectively. The SE graphs decrease in magnitude for increasing numbers of spectra in the average, until such a point where the SE cannot be decreased any further, i.e., convergence is achieved, as demonstrated for the 165 spectra across the three *E. coli* samples. Figures 4.6a and 4.6b shows the convergence of the 2SD for the fingerprint and high wavenumber region respectively for increasing numbers of spectra in the average. Similarly the 2SD waves demonstrate convergence to a point for increasing numbers of spectra in the average.

The convergence tests for a single replicate is included in the Appendix: Figures A.15 and A.16 for consideration. While the data achieves reasonable convergence across one sample, the data are not completely converged. Full convergence could not be achieved within one biological replicate due to the amount of time required for spectral collection.

Figures 4.7a and 4.7b show a zoomed in section of the SE and 2SD convergence graphs (from Figures 4.5a & 4.6a respectively). This allows for closer examination of the level of convergence achieved. The SE and 2SD waves are within $< 1$ % error of each other, indicating sufficiently low levels of SE and 2SD, thus the samples are converged. Additionally, the total number of spectra collected for the characterisation of bacteria in the literature are labelled on the graph, in order to highlight the level of characterisation achieved in this work compared with previous studies of Raman on bacteria [77, 108, 120, 121, 136, 151, 152, 153, 154, 155, 159]. The number of spectra represents the total number of spectra collected across the number of replicates performed in the work, which is included in brackets. Table 4.2 also shows the number of Raman spectra collected from bacterial samples in literature, and includes the number of biological replicates performed. It is evident there is no standard to determine the minimum number of spectra necessary for characterisation, thus bringing into question the reliability of data.Often insufficient spectra are collected from a given sample resulting in the sample being under-represented by the spectral average. It can be seen from the SE and 2SD convergence graphs

**Table 4.2:** Table of experimental details from literature for the collection of Raman spectra from bacterial samples, including the number of spectra collected for characterisation. This includes whether the spectra are from single cells or colonies, the laser wavelength and the spectral resolution of the data. Whether the sample is dried or in media is also included. The number of spectra collected for within each work and the number of biological replicates performed is also shown.

| **Number of spectra** | **Replicates** | **Bacteria** | **Colony or single cell** | **Dried or in media** | **Spectral resolution (cm$^{-1}$)** | **Laser (nm)** | Ref. |
|---|---|---|---|---|---|---|---|
| 30 | 1 | *S. epidermidis*<br>*E. coli* | Colonies | In agar | - | 785 | [154] |
| 25 | 3 | *S. aureus*<br>*S. epidermidis*<br>*E. coli*<br>*E. faecium* | Colonies | Media | 8 | 830 | [155] |
| 10 | 1 | *E. coli*<br>*S. aureus*<br>*S. epidermidis*<br>*Candida albicans* | Colonies | - | - | 785 | [159] |
| 3 to 4 | 1 | *E. coli* | Clusters | Dried | 1 - 2 | 514 | [151] |
| 75 | - | *E. coli* | Single optically trapped cells | - | - | 785 | [152] |
| 45 | 3 | *E. coli* | - | Dried | 7 | 785 | [136] |
| 3 | 6 | *E. coli* | Single cell | Dried | - | 532 | [153] |
| 20 | - | *E. coli* | Single cell | Media | - | 633 | [156] |
| 10 | 1 | *S. epidermidis*<br>*E. coli* | - | Dried | 6 | 532 | [120] |
| 50 | 3 | *E. coli* | - | Dried | 9 - 15 | 532 | [121] |
| 20 | 3 | *E. coli* | Single cell | Dried | 1 | 532 | [77] |

(Figure 4.5 and Figure 4.6 respectively) that for as little as ten spectra the SE and 2SD have large magnitudes, and are at unsatisfactory levels for a complete data set. Specifically, for the 2SD convergences in this work, the percentage difference between the 2SD for ten spectra and the maximum 165 spectra was found to be 37 %. Therefore, utilising ten or less spectra or characterisation would result in large uncertainties for the data, and thus may bring the reliability of results into question.

Moritz *et al.* collected 75 spectra from a cell sample, more than in any other published study [152]. While this does not compute to a statistically converged data set the resultant spectral average is statistically more representative, however, only one biological replicate was performed, thus reproducibility has not been determined [152]. Three biological replicates were performed in this work.

Zu *et al.* and Bittel *et al.* achieve similar levels of characterisation compared with this work, with collection of 50 and 45 spectra respectively per sample, also performing three biological replicates (Table 4.2) [121, 136]. However, both works had large spectral resolutions, specifically 9 - 15 cm$^{-1}$ for the spectra collected in the work by Zu *et al.* and 7 cm$^{-1}$ in the work by Bittel *et al.*. A much lower spectral resolution of 3 cm$^{-1}$ was achieved in this work, resulting in more accurate data [121, 136].

The level of analysis of the number of spectra performed here is necessary for proper characterisation of the biological sample. Despite the fact that some papers have reported the need for standardised levels of characterisation, no standardised procedure is currently applied in literature to deal with the issue [155]. The method of convergence of the SE and 2SD presented in this section provides an easy and efficient method of determination of the number of spectra required to properly characterise a biological sample, and is applicable to other systems (as was done with graphene spectra in Chapter 3). It ensures that the natural heterogeneity of samples is not overlooked, and is properly represented by spectral averages. The implementation of this method for published studies would ensure reliability of data across the board.

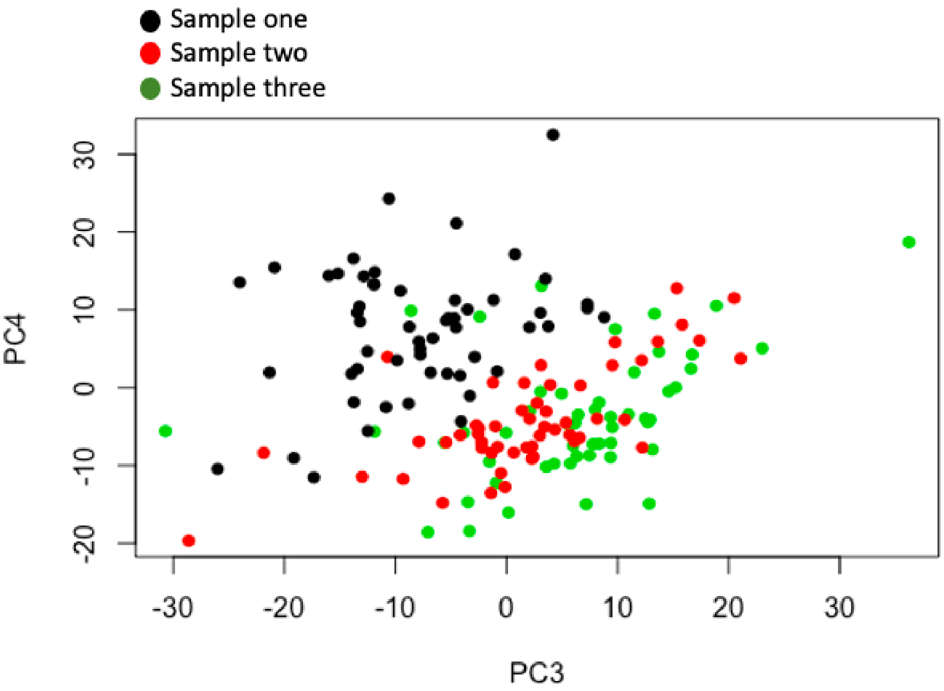

**Figure 4.8:** PCA results for comparison of the fingerprint region of the three *E. coli* samples (600 - 1800 cm$^{-1}$). The graph shows separation along PC3 which represents 5.35 % variance of the entire data set.

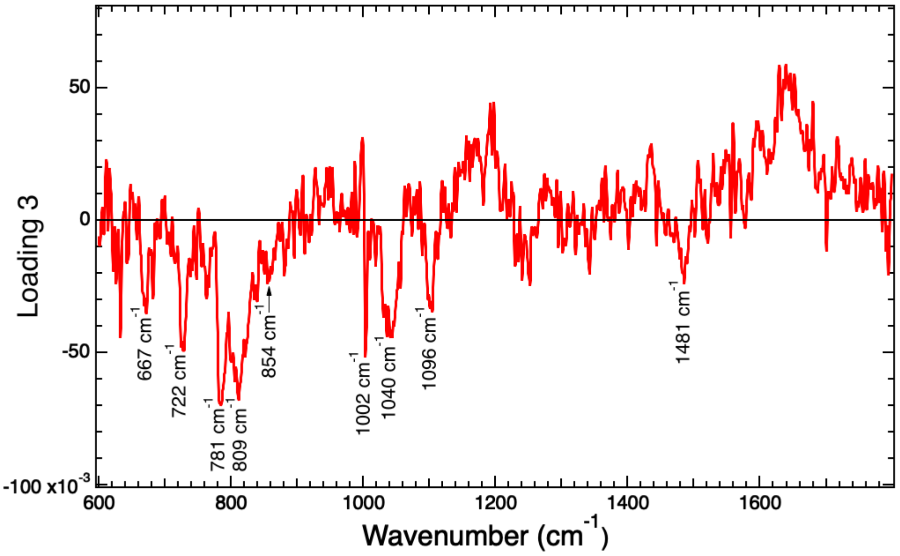

**Figure 4.9:** The loading for PC3, along which there was separation in the PCA results for the spectra of three *E. coli* samples between the wavenumbers 600 to 1800 cm$^{-1}$. PC3 represents 5.35 % of the total variance for the data set. The main spectral components of the loading are labelled, indicating the bands which are causing variation between the samples.

## 4.3 Analysis of heterogeneity across *E. coli* samples

### 4.3.1 Principal component analysis of the Raman spectra

The heterogeneity will now be assessed at a population level across all spectra collected from each *E. coli* sample, using PCA. The result of the PCA performed on the fingerprint region of the spectra (600 - 1800 cm$^{-1}$) is shown in Figure 4.8. There is separation along PC3 which encapsulates 5.35 % of the total variance of the data set. The corresponding loading shows the spectral features causing the separation along PC3 (Figure 4.9). The band assignments for these peaks can be found in Table 4.1.

PCA was also performed on the high wavenumber region of the spectra of *E. coli* (2800 - 3100 cm$^{-1}$), the results of which can be seen in Figure 4.10. There is separation along PC4 which represents 3.13 % of the total variance of the data set. The corresponding loading (Fig. 4.11) indicates that only two spectral features in the high wavenumber are causing the separation in PCA space, specifically the convolved lipid - protein bands band at 2875 cm$^{-1}$ and 2936 cm$^{-1}$ [124].

The separation in PCA space indicates phenotypic differences of the samples at a population level. For instance, the band at 1040 cm$^{-1}$, representative of proteins, noted in the loading to represent one of the spectral features causing separation of the three *E. coli* samples in PCA space (Fig. 4.9) was found to appear only in the average spectrum for *E. coli* sample one, and was not present in the other samples (Fig. 4.1). The presence of this band in the Raman spectrum of *E. coli* sample one is suggestive of increased metabolic processes of proteins in comparison with the other samples [121, 124]. Additionally, the absence of this band in two of the three biological replicates may be attributable to inhibition of protein synthesis during cell death, which has been found to cause a decrease in the relative intensity of this band [77]. For the high wavenumber region the band at 2936 cm$^{-1}$ was found to cause separation (Fig. 4.11). It is a protein-dominant band (Fig. 4.12), thus, the variation of this band is further evidence of the protein heterogeneity across the three samples

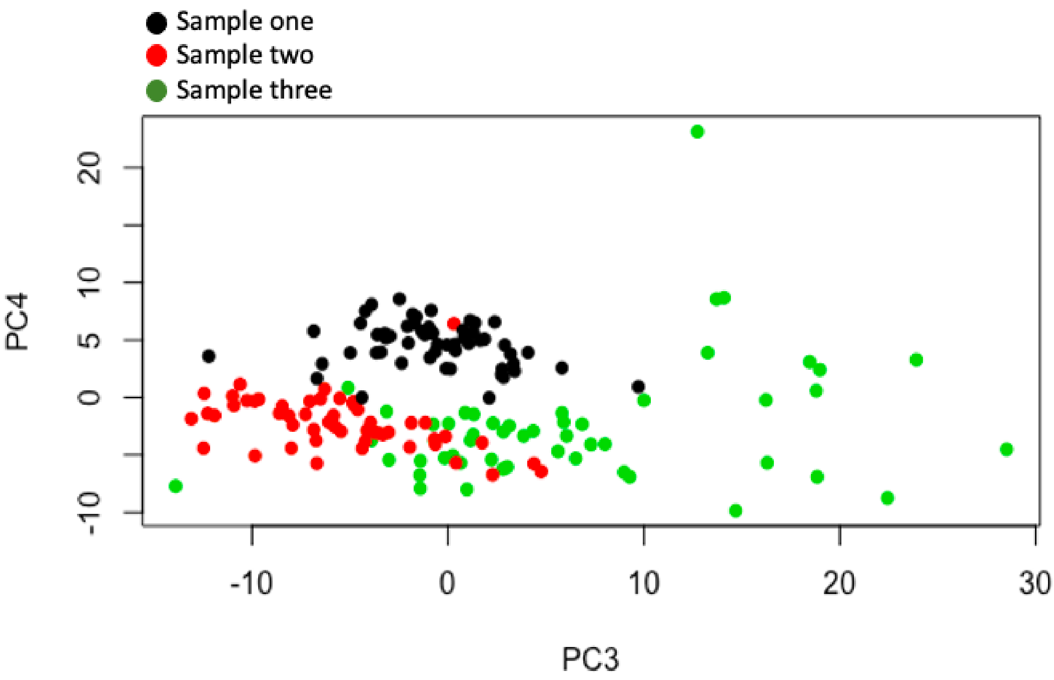

**Figure 4.10:** PCA results for comparison of the high wavenumber region of the three *E. coli* samples (2800 - 3100 cm$^{-1}$). The graph shows separation along PC4 which represents 3.13 % variance of the entire data set.

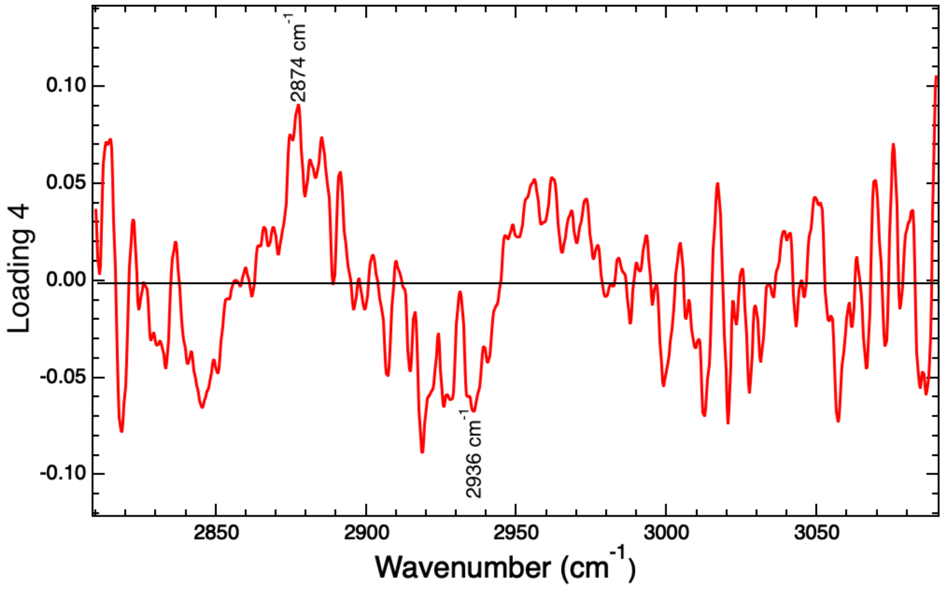

**Figure 4.11:** The loading for PC4, along which there was separation for the three *E. coli* samples between the wavenumbers 2800 to 3100 cm$^{-1}$. PC4 represents 3.13 % of the total variance for the data set. The main spectral components of the loading are labelled, indicating the bands which are causing variation between the samples.

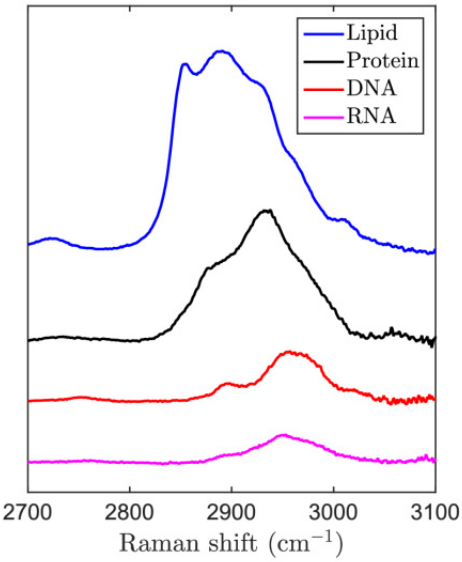

**Figure 4.12:** Raman signature of biochemical components of cells in the high wavenumber region of the Raman spectra (2800 - 3100 cm$^{-1}$), specifically showing lipids, proteins, RNA and DNA spectra, collected using a laser wavelength of 785 nm. The spectra are normalised using total area normalisation. Figure obtained from [249].

[249, 251]. This heterogeneity demonstrates the importance of performing at least three biological replicates, something which is not always done within literature (Table 4.2) [120, 151, 154, 159], and is consistent with different toxicity processes and defences employed by bacterial samples under toxic conditions [109].

It is not unusual for different cells within a population to respond differently to toxic conditions, and within literature it has been found that cells within a population can evolve to avoid cell death by toxic substances. For instance, Bigger *et al.* found that sub-populations of a genetically homogeneous culture of *S. aureus* did not die following prolonged doses of penicillin which caused the death of the majority of cells in the population [109]. These cells, termed persister cells, are genetically identical to the non-resistant cells in the same population and do not require proximity to antibiotics to develop resistance [252]. In other words, sub populations of cells can respond differently to stressful environments, thus, the separation in PCA space may be due to different toxicity responses, which could also explain the presence of the band at 1040 cm$^{-1}$ in the Raman spectrum of only one sample [109].

The RNA/ DNA bands at 667 cm$^{-1}$, 722 cm$^{-1}$, 781 cm$^{-1}$, 1096 cm$^{-1}$ and 1481 cm$^{-1}$ were also found to change according to PCA results (Fig. 4.9) [77, 124, 136, 155, 156]. This may be due to natural heterogeneity of RNA/ DNA across samples due to variation in growth stages of the cells [253]. The RNA/ DNA is known to vary with the stage at which the cell is at in its growth. For example, Manoharan *et al.* reported relative intensity increases of RNA bands in the Raman spectra for bacteria entering the logarithmic phase [253]. Thus, the changes in the RNA/DNA bands Raman spectra may be indicative of variation of growth rates across samples [253].

Alterations in the DNA in Gram negative bacteria has been found to occur as a result of toxic perturbations to the cells [119, 121]. For example, Xie *et al.* reported changes in the band at 781 cm$^{-1}$ due to degradation of DNA following heat treatment. Thus, the changes in the RNA/ DNA according to PCA results (Fig. 4.9) could be suggestive of heterogeneous DNA degradation during the desiccation process [119, 121].

The changes in the band at 722 cm$^{-1}$ (lipids and DNA), according to the PCA results (Fig. 4.9), may be due to a toxicity response from lack of nutrients, i.e., cell starvation [77, 120, 123, 124, 136, 156]. Specifically, the changes in this band may be representative of a stress response, attributable to alterations in lipid composition of cells due to cell starvation [254]. For example, it has been found that more varieties of phospholipids are present in growing cells compared with starving cells [254]. Thus, this variation of the 722 cm$^{-1}$ band may be attributable to slowing of cellular processes from lack of nutrients and dessication [254].

The lipid-protein band at 2875 cm$^{-1}$ in the high wavenumber region, prominent in pure lipid signatures (Fig. 4.12), was also found to vary from the PCA results (Fig. 4.11) [249]. This is further indication of heterogeneity in the lipids between the three samples. Lipid perturbations are crucial for *E. coli* cell response to toxicity and stress and may be representative of different toxicity responses of the samples [255]. The variation in the lipid signatures seen here may also be natural variation in lipid conformation across the samples [254, 255].

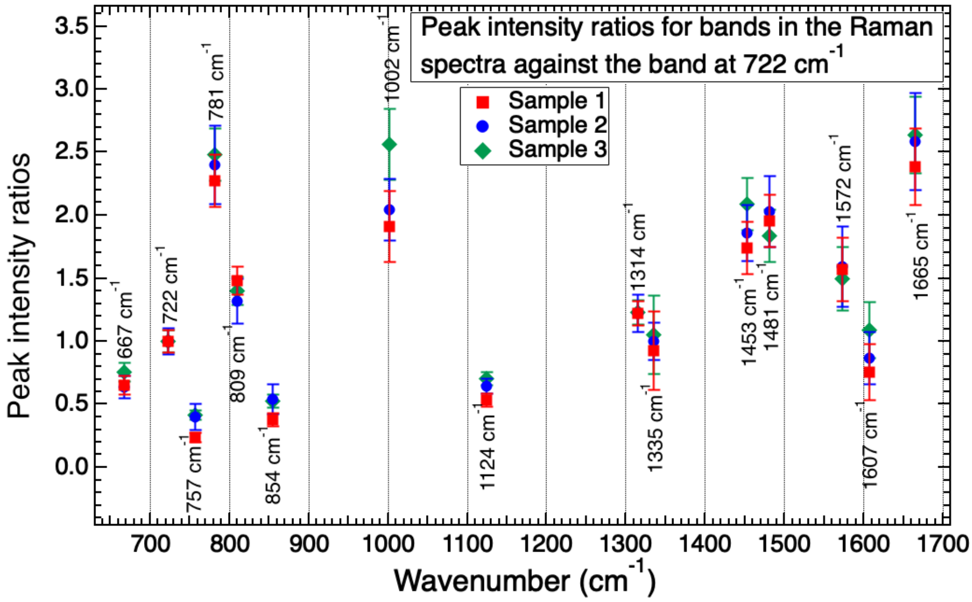

**Figure 4.13:** Peak intensity ratios for bands in the Raman spectrum of *E. coli* against the band at 722 cm$^{-1}$ representing lipids and DNA [77, 123, 124, 136, 156]. This band was determined to vary between the three samples according to PCA results.

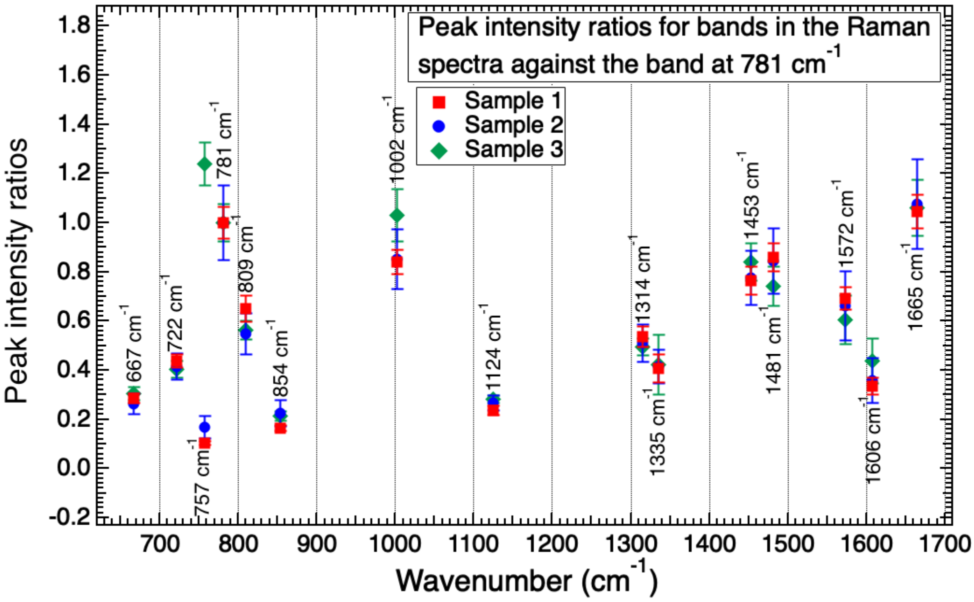

**Figure 4.14:** Peak intensity ratios for bands in the Raman spectrum of *E. coli* against the band at 781 cm$^{-1}$ representing DNA [77, 120, 124, 153, 155, 156]. This band was determined to vary between the three samples according to PCA results.

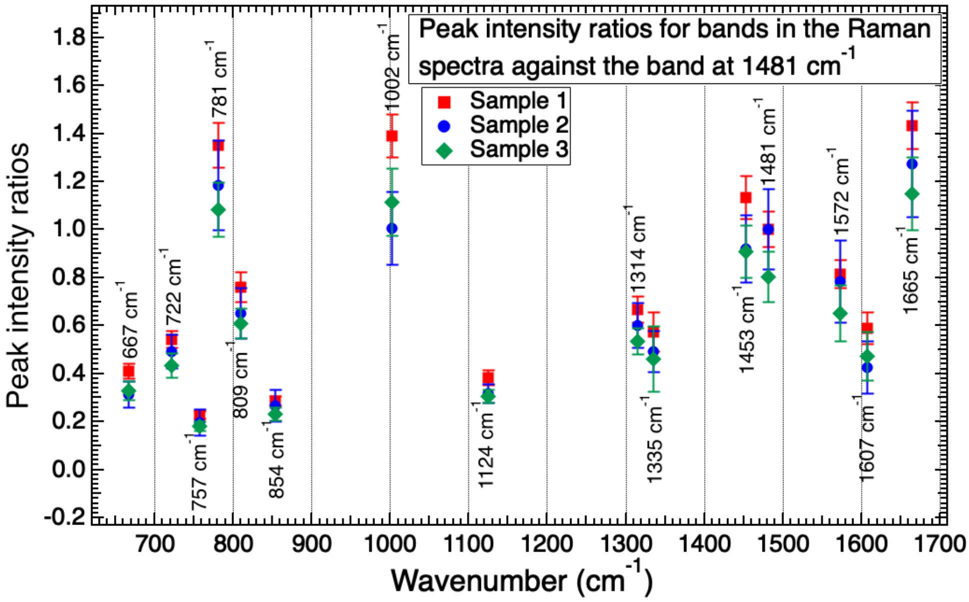

**Figure 4.15:** Peak intensity ratios for bands in the Raman spectrum of *E. coli* against the band at 1481 cm$^{-1}$ representing proteins and DNA [77, 124, 247]. This band is being analysed to determine the heterogeneity between the three *E. coli* samples as it was found by PCA to be the cause of heterogeneity between the samples (Fig. 4.8). Separation of the PIRs indicates heterogeneity of the biomolecule between the *E. coli* samples.

## 4.3.2 Peak intensity ratio analysis of the Raman spectra

In order to analyse the heterogeneity of the spectral averages PIR analysis has been performed on the bands noted to change from PCA (Fig. 4.9). PIRs against the bands at 722 cm$^{-1}$ (lipids / DNA), 781 cm$^{-1}$ (DNA) and 1481 cm$^{-1}$ (protein/ DNA) are shown in Figures 4.13, 4.14 and 4.15 respectively, to investigate the heterogeneity of different biomolecules in the average.

The PIRs against the band at 722 cm$^{-1}$ which is a lipid-dominant band, convoluted with DNA signatures shows no separation for any of the bands in the average Raman spectra across three *E. coli* replicates (Fig. 4.13) [77, 123, 124, 136, 156]. This is indicative that the variation found for this band by the PCA results (Fig. 4.8 & 4.9), present at a single spectrum level, is not present in the spectral average. This may be due to the phenotypic differences in this band being representative of natural heterogeneity of lipids in the sample [254, 255], which is not significant enough to cause separation at a spectral average level. The lack of separation across these PIRs also demonstrates a high level of reproducibility across the replicates.

The PIRs against the band at 781 $\mathrm{cm}^{-1}$ (DNA) displays variation of the samples for only two of the bands in the Raman spectra, those at 757 $\mathrm{cm}^{-1}$ and 1002 $\mathrm{cm}^{-1}$, representative of tyrosine and phenylalanine respectively (Fig. 4.14) [77, 124, 136, 153, 155, 156, 247]. This indicates that the heterogeneity of the DNA in the cells is dependent on protein variation. The relative changes in the DNA and protein bands may be due to the slowing growth of the cell as a result of inhibited protein synthesis from the desiccation process, subsequently resulting in DNA variation [77, 251]. The other PIRs against the band at 781 $\mathrm{cm}^{-1}$ are all within error of one another, thus, the bands which demonstrate separation may be biomarkers for heterogeneity, sensitive to variation in the sample and changes due to cell death.

The PIRs against the band at 1481 $\mathrm{cm}^{-1}$ (proteins and DNA) show separation for the bands at 667 $\mathrm{cm}^{-1}$ representative of DNA and proteins and the band at 1002 $\mathrm{cm}^{-1}$ for phenylalanine (Fig. 4.15), both of which were also found to vary according to PCA (Fig. 4.9) [77, 124, 136, 153, 155, 156, 247]. This further reiterates that the relative changes of the bands seen in the spectra are primarily resultant from heterogeneous alterations in DNA and proteins, which may be due to variations in the toxicity response of the *E. coli* samples from desiccation and lack of nutrients [77, 251]. Again, the other PIRs show reproducibility across the samples, thus, the bands at 667 $\mathrm{cm}^{-1}$ and 1002 $\mathrm{cm}^{-1}$ could be considered as heterogeneity biomarkers.

The link between protein and DNA heterogeneity could be a specific cellular response due to desiccation, resulting in associated variation of the biomolecules. It has been predicted using cell modelling that heterogeneity in protein expression in *E. coli* can cause metabolic variability, i.e., can result in variation in the growth rates of cells within the same population [251]. As a result, modelled populations of bacteria were shown to contain sub-populations with different growth rates, resultant in bacterial heterogeneity in the culture as a whole [251]. Therefore, this variation in the rate of growth due to the protein heterogeneity may explain the changes of the protein bands at 667 $\mathrm{cm}^{-1}$, 757 $\mathrm{cm}^{-1}$ and 1002 $\mathrm{cm}^{-1}$ with respect to the DNA PIRs [77, 124, 136, 153, 155, 156, 247, 251]

The band at 1002 $\mathrm{cm}^{-1}$ in particular was found to vary for both PIRs $I_{1002}/I_{1481}$

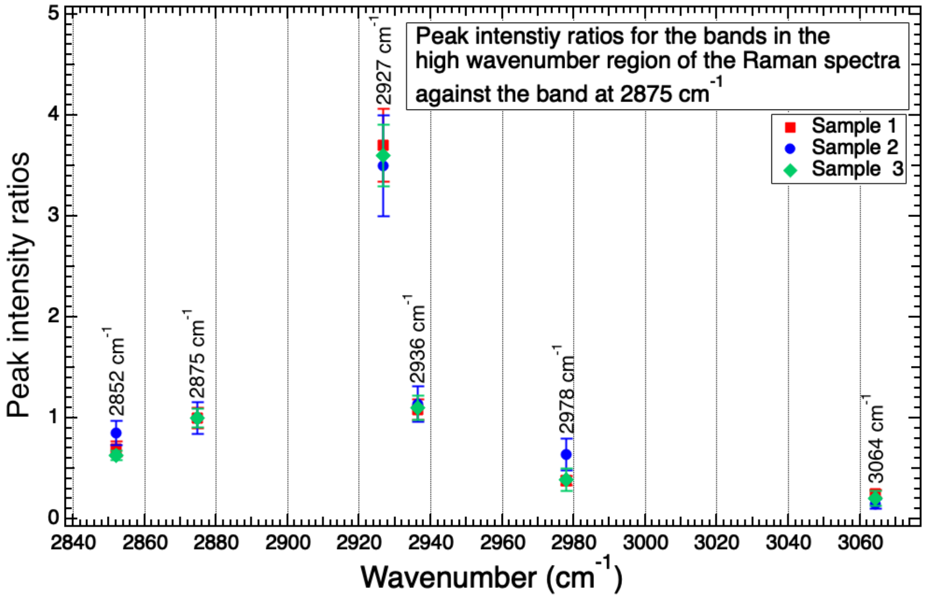

**Figure 4.16:** Peak intensity ratios for bands in the Raman spectrum of *E. coli* against the band at 2875 cm$^{-1}$ representing lipids and proteins [124]. This band is being analysed to determine heterogeneity between the three *E. coli* samples as it was found by PCA to be the cause of variation between the samples (Fig. 4.10). Separation of the PIRs indicates heterogeneity of the corresponding biomolecules. The band assignments can be found in Table 4.1.

and $I_{1002}/I_{781}$ (Fig. 4.14 & 4.15). This band was also reported in the PCA loadings for differing across the three samples (Fig. 4.9), and so may be a sensitive biomarker for heterogeneity across samples. This band arises due to phenylalanine, and so it may be indicative of variation of proteins across the samples [77, 124, 136, 153, 155, 156, 247, 251]. Proteins lose their shape and integrity with the loss of water, thus, this variation may be due to the different conformational changes of the proteins across samples due to the dessication process [256].

In the high wavenumber region, the heterogeneity of the bands at 2875 cm$^{-1}$ and 2936 cm$^{-1}$ is analysed using PIR analysis, shown in Figure 4.16 and 4.17 respectively, both of which were found to cause separation in PCA space (Fig. 4.11). The PIRs have been compared for the bands in the high wavenumber region (2800 cm$^{-1}$ - 3200 cm$^{-1}$) for the three samples. There is no separation for any of the PIRs against either of the bands. This suggests that the heterogeneity of these bands, which caused separation in PCA space, was due to natural variation of the cells across the samples, which is fully represented across all three samples in the corresponding

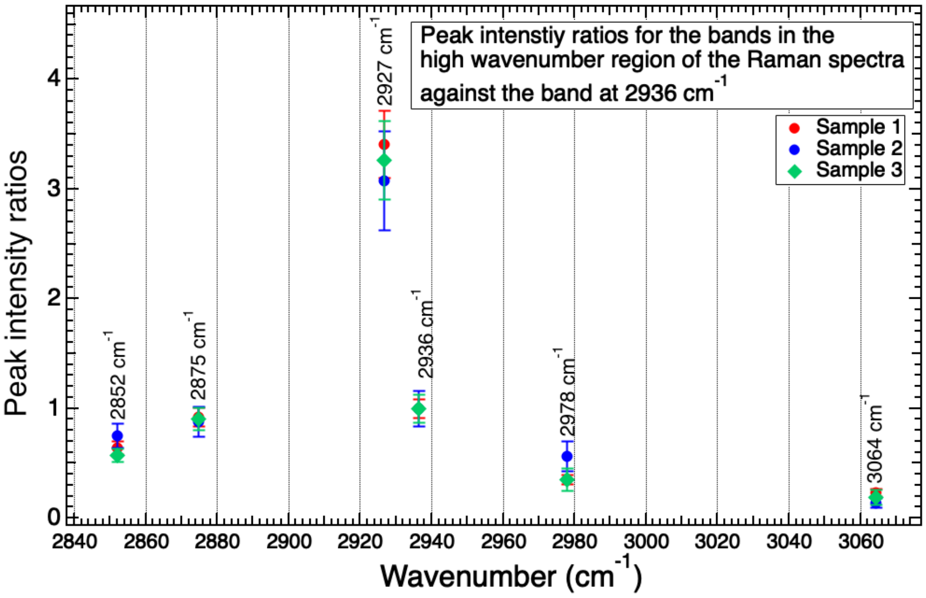

**Figure 4.17:** Peak intensity ratios for bands in the Raman spectrum of *E. coli* against the band at 2936 cm$^{-1}$ representing proteins and lipids [124]. This band was determined to vary between the three samples according to PCA results.

spectral average.

### 4.3.3 Convergence rate tests of the peak intensity ratio biomarkers

To further investigate the heterogeneity of PIR biomarkers, convergence rates have been obtained for the change in the percent standard error of the mean (pSE) of the PIR for increasing numbers of spectra in the average spectrum, which will be compared across the three samples. The convergence rate of the band at 1453 cm$^{-1}$ (proteins) against the band at 781 cm$^{-1}$ (DNA) is shown in Figure 4.18 [120, 121, 124, 155, 156]. Each point on the graph represents the pSE for the PIR $I_{1453}/I_{781}$ for increasing numbers of spectra in the spectral average, which produces a convergence rate graph. This is then fitted to produce a convergence rate ($\lambda$) for each graph. More homogeneous samples produce a faster convergence, thus, a larger convergence rate $\lambda$. The convergence rates for each sample are also investigated for the PIR $I_{1453}/I_{1481}$.

The band at 1453 cm$^{-1}$ has been reported to change due to altered metabolic

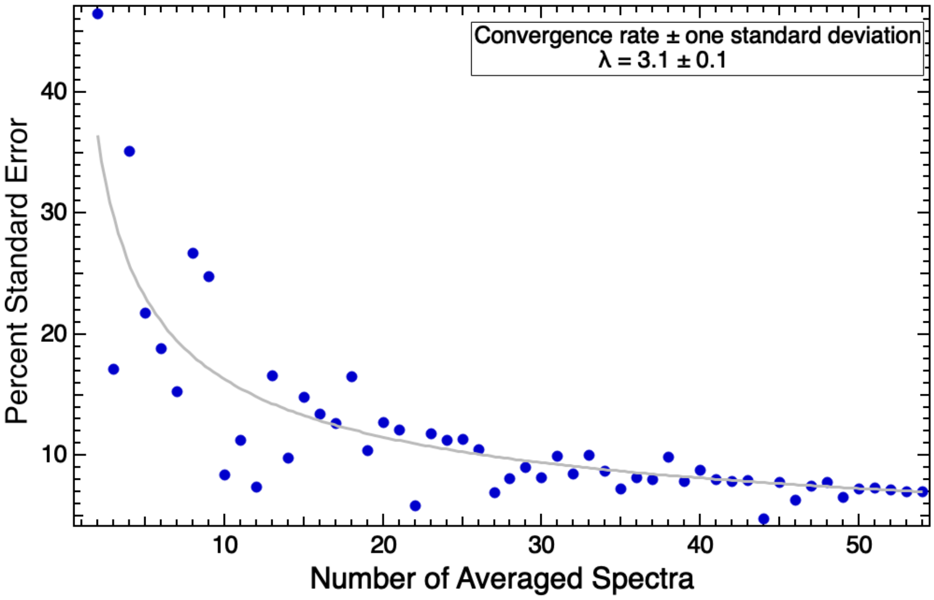

**Figure 4.18:** Convergence of the percent standard error of the mean of the PIR biomarker $I_{1453}/I_{781}$ for increasing numbers of spectra in the average spectrum. The band at 781 $cm^{-1}$ was found to vary across three *E. coli* samples using PCA. The band at 1453 $cm^{-1}$ has been noted to change due to altered metabolic processes in *E. coli* as a result of lethal conditions and cell death [77, 121]. $\lambda$ is the rate of convergence.

**Table 4.3:** PIR biomarker convergence rates of bands in the Raman spectra of *E. coli.* The rate of convergence determines the heterogeneity of a sample, with a larger convergence rate indicative of a more homogeneous sample. The bands at 781 $cm^{-1}$ and 1481 $cm^{-1}$ were found to vary across the three samples according to PCA. The band at 1453 $cm^{-1}$ has been found to change due to altered metabolic processes in *E. coli* as a result of lethal conditions and cell death [77, 121].

| | **Convergence rates** | |
|---|---|---|
| | **$I_{1453}/I_{781}$** | **$I_{1453}/I_{1481}$** |
| **Sample 1** | 3.1 ± 0.1 | 3.4 ± 0.1 |
| **Sample 2** | 6.9 ± 0.2 | 6.3 ± 0.2 |
| **Sample 3** | 5.2 ± 0.1 | 5.2 ± 0.1 |

processes in *E. coli* as a result of lethal conditions and cell death within literature [77, 121]. This band was found not to differ across three *E. coli* samples, according to PIR analysis (Fig. 4.13, 4.14 & 4.15) and PCA (Fig. 4.9), thus indicating similar metabolic responses to cell death across the samples [77, 121]. Analysis of the heterogeneity rate of the PIRs for each sample will give an insight into the variation of the metabolic responses of the cells studied within each sample, with respect to the bands at 781 $cm^{-1}$ (DNA) and 1481 $cm^{-1}$ (proteins and DNA) [77, 120, 124, 153, 155, 156, 247]. The bands at 781 $cm^{-1}$ and 1481 $cm^{-1}$ were chosen for the analysis as they were found to change according to PCA results (Fig. 4.9). Thus, the convergence rates of the PIRs will give an indication into the level of heterogeneity of the metabolic state for the biomolecules DNA and protein within samples, and will also be comparable across samples [77, 121].

The convergence of PIR biomarker $I_{1453}/I_{781}$, shown in Figure 4.18, achieves a rate of $\lambda = 3.1 \pm 0.1$ for *E. coli* sample one. The convergence rates of the PIR $I_{1453}/I_{781}$ for the other samples (Table 4.3) are not within error of one another for the three samples, indicating heterogeneity of the biomarker between the samples. This PIR did not vary across the three spectral averages (Fig. 4.14), however, the band at 781 $cm^{-1}$ (DNA) did vary according to PCA results (Fig. 4.9). Thus, in agreement with the PCA results, the convergence rates suggest heterogeneity which may be due to altered metabolic processes in *E. coli* cells [77, 121]. Sample two achieved the highest convergence rate, suggestive that the metabolic processes of DNA in that sample are most homogeneous, while sample one the lowest rate, thus, the most heterogeneous sample.

The convergence rates for the PIR biomarker $I_{1453}/I_{1481}$ are also included in Table 4.3, with the corresponding graphs in the Appendix: Figures A.17 to A.21. The rates for the three samples are outside of error of one another, indicating differing levels of heterogeneity across the samples. Sample one gave the lowest convergence rate compared with the other samples. Therefore, it is indicative that *E. coli* sample one possesses high levels of heterogeneity for the biomarker $I_{1453}/I_{1481}$. The band at 1481 $cm^{-1}$ was found to change according to PCA results (Fig. 4.9). Thus, the heterogeneity in *E. coli* sample one could be the primary contributor to the separation in PCA space. The convergence rate of $I_{1453}/I_{1481}$ is indicative of more heterogeneous metabolic responses of the cells due to the dessication and cell death process for *E. coli* sample one, also reflected through separation in PCA space partly due to the band at 1481 $cm^{-1}$ [77, 121]. In agreement with the $I_{1453}/I_{781}$ biomarker, the PIR $I_{1453}/I_{1481}$ found sample two to have the largest convergence rate, thus reflecting least variation in the sample (Table 4.3).

This analysis allows for investigation into the heterogeneity of the biomarkers in the Raman spectra of *E. coli* across different biological samples, in a way which has not previously been analysed within literature. These convergence rates could allow for future work to compare the heterogeneity of biomarkers during different cellular processes, such as cell growth or death.

Furthermore, the level of analysis into the heterogeneity of the samples performed in this section is more than what is commonly done within literature. For example, Hermelink *et al.* studied the phenotypic differences of *Legionella bozemanii* and *Bacillus cereus* using Raman spectroscopy, however, the results presented in this thesis demonstrated more thorough analysis of the Raman spectra [172]. Hermelink *et al.* discussed the changes of the relative intensities of the bands with no quantitative analysis performed, comparatively in this work, the relative intensities were quantified using PIR analysis, PCA was performed on the spectra and a novel method for analysis of the heterogeneity of PIR biomarkers was utilised [172]. Furthermore, similar convergence tests will also be applied to the individual bands to investigate the heterogeneity of biomolecules within the sample.

Given the level of heterogeneity which has been demonstrated across all spectra collected using PCA, PIRs and convergence rates, the heterogeneity of single spectra will now be investigated to show how much variation can be present within a single sample, through analysis of single spectra collected from different points in the sample. This will further reiterate the need for collection of sufficient numbers of spectra for characterisation of bacterial samples.

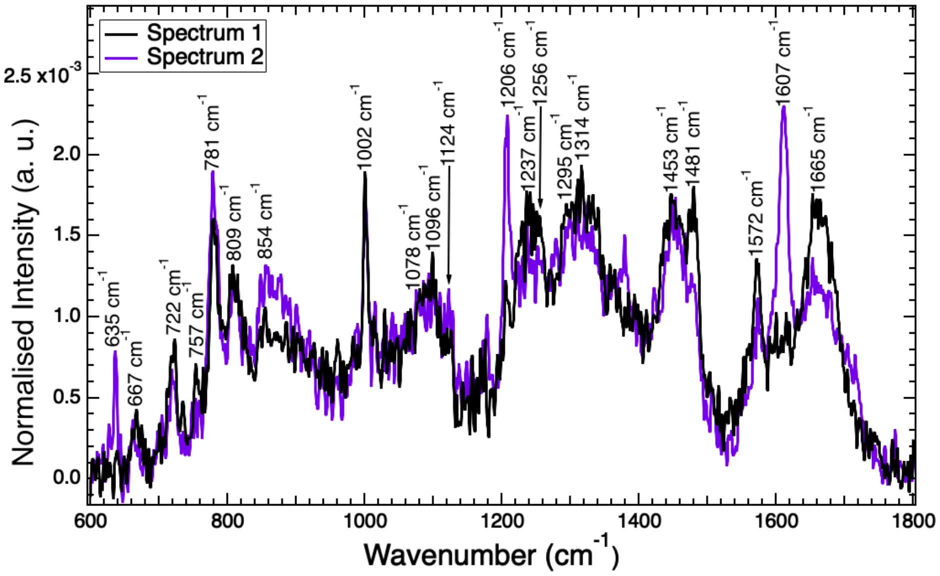

**(a)** Two Raman spectra collected from different cells in the same *E. coli* sample. Both spectra have been normalised and smoothed for ease of comparison.

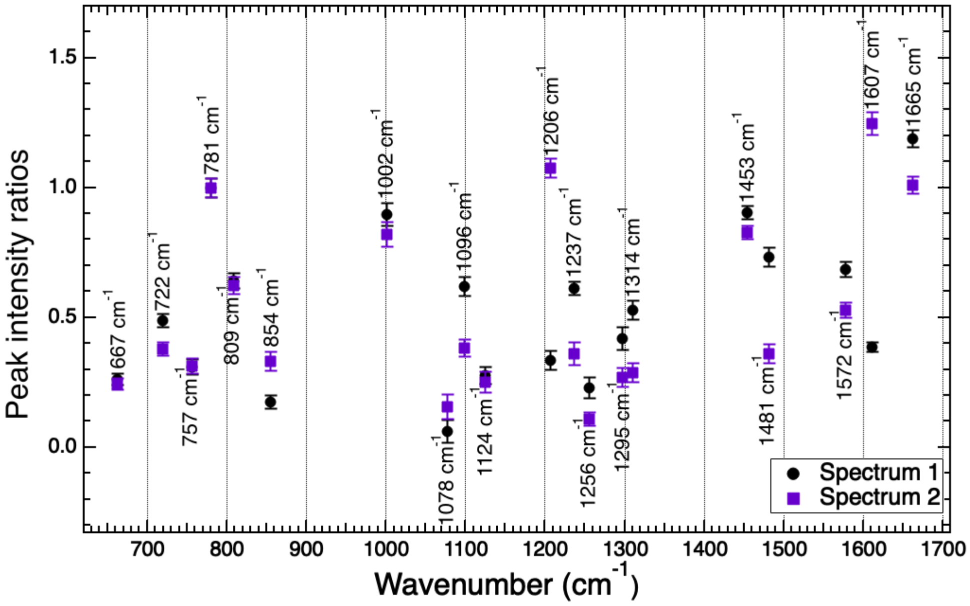

**(b)** Peak intensity ratios (PIRs) for the two Raman spectra collected from the same bacterial sample. The peak intensity ratios are computed against the band at 781 cm$^{-1}$ representing RNA/ DNA [77, 120, 153, 156], as it had the same relative intensity for the two spectra. The error bars represent fitting uncertainties.

**Figure 4.19:** The fingerprint region of two Raman spectra collected from different cells in the same *E. coli* sample and the corresponding PIRs, which demonstrate the level of heterogeneity of spectra collected from different cells in a biological sample. The PIRs are computed against the band at 781 cm$^{-1}$ as it was found to vary across the three samples according to PCA and was also used for PIR for the spectra averages.

## 4.4 Heterogeneity of single spectra of *E. coli*

Figure 4.19a shows two Raman spectra collected from different cells in the same *E. coli* sample (the corresponding optical images are in Fig. 4.2). These spectra have been normalised and smoothed for ease of comparison, the band locations have been labelled on the graph. There are clear differences in the spectra, such as the relative intensities of the bands.

The heterogeneity of the spectra from the same sample shown in Figure 4.19a has been suggested to be a result of cells in the same culture stochastically transitioning among different phenotypes in order to enhance the overall fitness of the cell population [111]. Cell variation can be detected in genetically identical colonies due to the bacteria adapting to survive in alternating and unpredictable environments, i.e., to prepare against any attacks from toxic substances or conditions [110, 111]. However, quantification of such heterogeneity does not appear to have been performed using Raman spectroscopy and specific variation of biomolecules has not been investigated to the level presented in this chapter.

For instance, García-Timermans *et al.* investigated the phenotypic heterogeneity of *E. coli* using Raman spectroscopy and flow cytometry, however, only the fingerprint region is considered in the work, with the high wavenumber region not collected in the Raman spectra [257]. Furthermore, following growth, the *E. coli* cells were stored at 4 °C and analysed using Raman spectroscopy within a week, however, it was shown in another paper published by the same group that the length of time left in storage can cause changes in the Raman spectra [108]. Specifically, it was found that the bands at 781 $cm^{-1}$, 1395 $cm^{-1}$, 1572 $cm^{-1}$ and 1581 $cm^{-1}$ displayed significant changes following storage of 5 and 12 days according to Random forest analysis [108, 257]. Therefore, the collection of the Raman spectra one week following growth could cause variation in the Raman spectra [108, 257]. For the spectra collected in this work, fresh samples were used for each experiment, i.e., samples were prepared the same day Raman analysis was performed.

In order to quantify the difference in relative intensity of the bands in the Raman spectra shown in Figure 4.19a peak intensity ratios (PIRs) for each spectrum were computed against the band at 781 $cm^{-1}$ representing RNA/ DNA (Table 4.1)

[77, 120, 153, 156]. This band was chosen as it had the same relative intensity for both spectra, indicating homogeneity. This band has also been used for determination the metabolic functions being undertaken by *E. coli* cells following exposure to alcohol in literature [121]. Furthermore, it has been used in this work for determination of heterogeneity between samples when studying the spectral averages for each sample (Fig. 4.14). The PIRs for the two spectra are shown in Figure 4.19b. Band assignments are in Table 4.1.

The PIRs for the bands representative of DNA/ RNA at 722 cm$^{-1}$, 1096 cm$^{-1}$, 1237 cm$^{-1}$, 1256 cm$^{-1}$ and 1572 cm$^{-1}$ [77, 115, 120, 123, 124, 136, 153, 155, 156] show separation for the two spectra (Fig. 4.19b). These changes in the RNA/ DNA associated bands may be due to the physical distortions of DNA within dehydrating cells [258]. This deformation of the DNA would particularly be in agreement with the changes seen in the band representing the DNA backbone at 1096 cm$^{-1}$ [77, 124, 136, 155, 156]. The variation in the RNA/ DNA shown here could give an indication into the different changes the cells underwent due to the dehydration process [259]. The bands at 722 cm$^{-1}$ and 1096 cm$^{-1}$ were also found to change according to PCA, indicating that the variation in these bands is significant at a population level (Fig. 4.9). As the 1096 cm$^{-1}$ band also varies in PCA results (Fig. 4.9), it is possible that the potential DNA deformation occurred both within and across samples, suggesting significant levels of heterogeneity could be introduced into an *E. coli* sample due to the dessication process.

The PIRs for the high wavenumber region (Fig. 4.20a) of the spectra are shown in Figure 4.20b. The PIRs are computed against the protein and lipid band at 2927 cm$^{-1}$ (Fig. 4.20b) as this has previously been used to monitor cell death and membrane fluidity [121]. This band was also used for PIR analysis of the spectral averages for determination of heterogeneity between samples.

The PIRs show separation for the bands at 2852 cm$^{-1}$ (fatty acids and proteins), 2875 cm$^{-1}$ (lipids and proteins) and 3064 cm$^{-1}$ (proteins) for the two Raman spectra (Fig. 4.20b) [124]. The band at 2875 cm$^{-1}$ was also found to vary according to PCA results performed on all spectra across the three replicates (Fig. 4.11).

The changes in the lipid-predominant bands in the fingerprint region at 722 cm$^{-1}$,

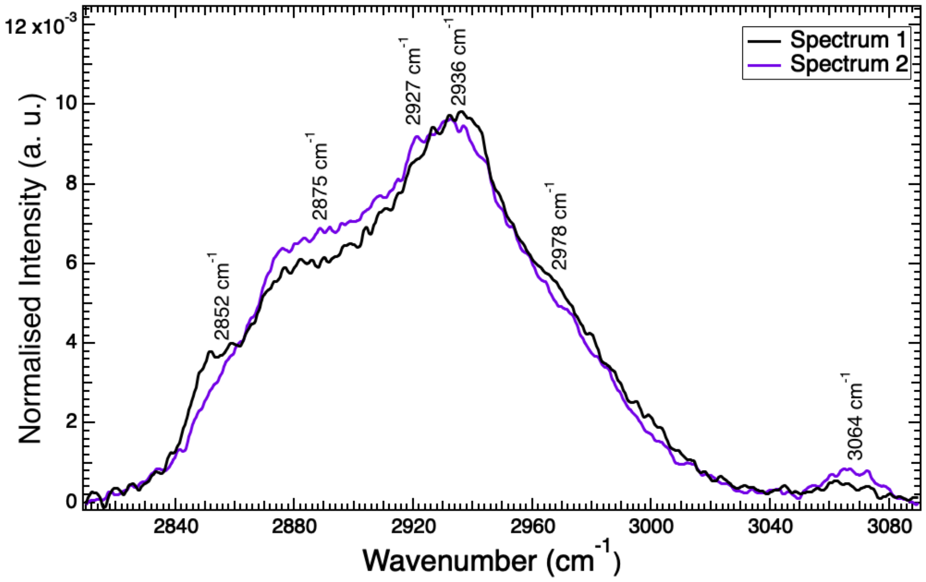

**(a)** The high wavenumber regions of two Raman spectra collected from the same *E. coli* sample. Both spectra have been normalised and smoothed for ease of comparison.

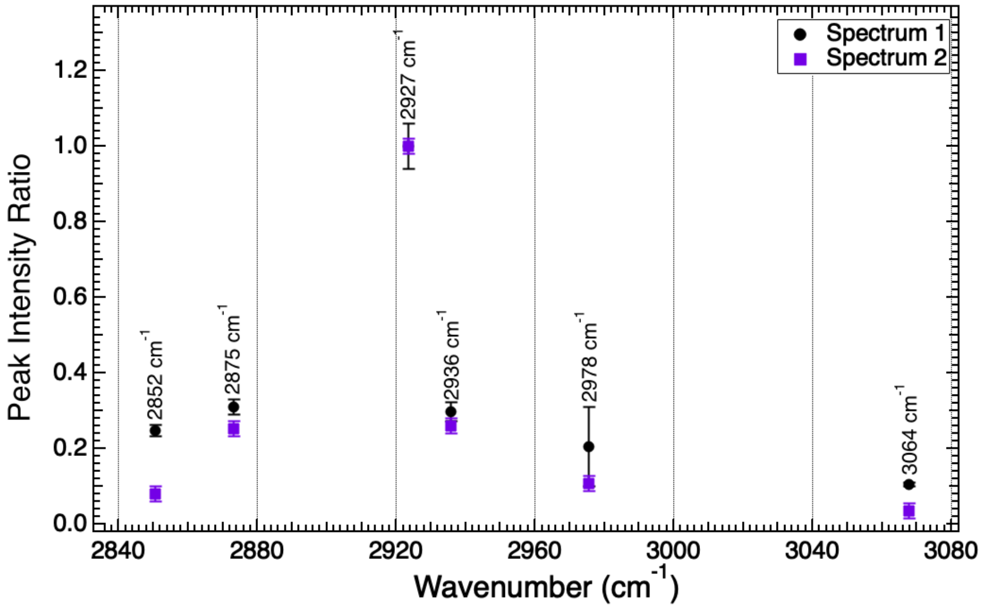

**(b)** Peak intensity ratios (PIRs) for the two Raman spectra collected from the same sample. The PIRs are computed against the band at 2927 cm$^{-1}$ representing lipids and proteins [124], which has previously been used to assess membrane fluidity [121]. The error bars represent fitting uncertainties.

**Figure 4.20:** The high wavenumber region of two Raman spectra collected from different cells in the same *E. coli* sample and the corresponding PIRs, which demonstrate the level of heterogeneity of spectra collected from different cells in a biological sample. The PIRs are computed against the band at 2927 cm$^{-1}$, found not to vary according to PCA and PIRs of all spectra.

1078 cm$^{-1}$, 1295 cm$^{-1}$, 1453 cm$^{-1}$ and 1665 cm$^{-1}$ and the high wavenumber region at 2852 cm$^{-1}$ and 2875 cm$^{-1}$ (Fig. 4.19b and 4.20b) [77, 120, 121, 123, 124, 136, 153, 155, 156] may be due to natural heterogeneity of lipopolysaccharides (LPS) as has been reported in the literature, which could explain the differences in the PIR values obtained for the two spectra [103].

Proteins are one of the biomolecules represented by nine of the thirteen bands in the fingerprint region (Fig. 4.19) and all of the bands in the high wavenumber region (Fig. 4.20) which display separation for the PIR values obtained for the two spectra, those being the bands at 854 cm$^{-1}$, 1078 cm$^{-1}$, 1206 cm$^{-1}$, 1237 cm$^{-1}$, 1295 cm$^{-1}$, 1453 cm$^{-1}$, 1481 cm$^{-1}$, 1607 cm$^{-1}$, 1665 cm$^{-1}$, 2852 cm$^{-1}$, 2875 cm$^{-1}$ and 3064 cm$^{-1}$ [77, 120, 121, 124, 136, 153, 155, 156]. The heterogeneity of these protein bands may be due to the cellular processes which take place due to cell desiccation [260]. As the cells undergo dehydration the proteins can lose their shape and integrity [256]. However, according to work by Nystrom *et al.* this is not the case for all proteins in the bacterial cells, in fact during desiccation of 12 hours the bacteria cell was found to attempt to protect the proteins from oxidative modifications, which often occurs during dehydration due to the formation of reactive oxygen species (ROS) [261]. The differences in the Raman spectra shown here are indicative of these heterogeneous protein modifications resultant from cell desiccation. The bands at 854 cm$^{-1}$, 1481 cm$^{-1}$ and 2875 cm$^{-1}$ were also found to change according to PCA results, indicating that these modifications may be causing variation at a population level also, suggesting significant levels of variation of proteins [256, 260]

This analysis of the Raman spectra goes beyond previous investigations, through its ability to identify specific proteins and amino acids. For example, significant differences were found for the PIR of the protein-dominant band at 1206 cm$^{-1}$, representative of phenylalanine and tryptophan (Fig. 4.19b) [77, 124]. This indicates that these proteins and amino acids may be altered due to cell dehydration, and could act a marker for the cell undergoing different metabolic processes during desiccation. Papers are generally published focusing on the variation of one specific biomolecule, such as proteins [256, 261], however, published work on the heterogeneity of specific proteins and amino acids in a bacteria population has proved difficult

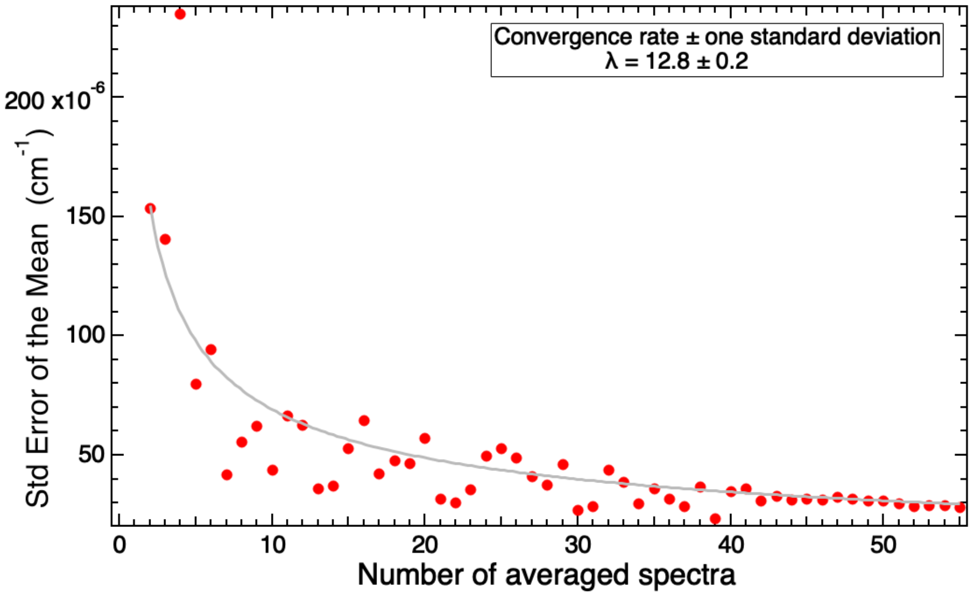

**Figure 4.21:** Convergence of the standard error of the mean of the normalised intensity of the band at 1002 cm$^{-1}$, representative of phenylalanine [77, 124, 136, 153, 155, 156, 247]. This band was found to vary across the three samples, according to PCA results and PIRs against the bands at 781 cm$^{-1}$ and 1481 cm$^{-1}$. $\lambda$ is the rate of convergence.

to find following extensive literature searches.

This analysis of the single spectra presented here goes beyond what has been done for analysis of bacterial samples using Raman spectroscopy. For instance, Schuster *et al.* investigated the heterogeneity of *Clostridia* using Raman spectroscopy, however, no quantitative analysis was performed on the four spectra collected from the same sample, rather relative intensity were discussed from visual observation [160].

The levels of heterogeneity presented here show the necessity to collect sufficient spectra from a given bacteria sample to ensure the sample is properly characterised.

## 4.5 Heterogeneity of biomolecules in *E. coli*

In addition to analysis of the heterogeneity of the PIR biomarkers for biological systems, and to further investigate the heterogeneity of specific biomolecules in samples, convergence rates can also be obtained for individual bands in the Raman spectra. This test determines the absolute standard error of the mean (SE) of the normalised intensity of the bands in the Raman spectra of *E. coli* for increasing

**Table 4.4:** Convergence rates for bands in the Raman spectra of *E. coli* samples. The rate of convergence corresponds to the heterogeneity of the biomolecule(s) that the band represents. A larger convergence rate indicates increased homogeneity. The band assignments are included.

| **Location** | **Convergence rates** | | | **Band** | **Ref.** |
|---|---|---|---|---|---|
| **(cm$^{-1}$)** | **S1** | **S2** | **S3** | **assignment** | |
| 667 | 5.65 ± 0.09 | 5.91 ± 0.09 | 7.7 ± 0.2 | DNA | [77, 124, 136] |
| 722 | 3.82 ± 0.08 | 7.1 ± 0.1 | 10.5 ± 0.2 | Lipids, DNA | [77, 123, 124, 136, 156] |
| 781 | 8.6 ± 0.1 | 10.0 ± 0.2 | 11.0 ± 0.2 | DNA | [77, 120, 124, 153, 155, 156] |
| 809 | 7.2 ± 0.1 | 7.1 ± 0.2 | 14.8 ± 0.2 | RNA, Proteins | [77, 124, 136, 155, 156] |
| 1002 | 12.8 ± 0.2 | 15.3 ± 0.4 | 23.8 ± 0.4 | Proteins | [77, 124, 136, 153, 155, 156, 247] |
| 1453 | 8.9 ± 0.2 | 8.2 ± 0.2 | 12.5 ± 0.2 | Proteins, lipids | [120, 121, 124, 155, 156] |
| 1481 | 6.3 ± 0.1 | 10.7 ± 0.2 | 15.2 ± 0.3 | Proteins, DNA | [77, 124, 247] |
| 1572 | 5.74 ± 0.09 | 5.27 ± 0.08 | 9.9 ± 0.2 | Proteins, DNA | [77, 115, 124, 153, 155, 156] |
| 1607 | 3.07 ± 0.05 | 5.44 ± 0.09 | 13.8 ± 0.3 | Proteins, lipids | [77, 121] |
| 1665 | 4.69 ± 0.08 | 5.54 ± 0.09 | 11.2 ± 0.2 | Proteins, lipids | [77, 153, 155, 156] |
| 2852 | 11.8 ± 0.2 | 15.5 ± 0.3 | 3.83 ± 0.06 | Lipids | [124, 153] |
| 2875 | 27.1 ± 0.5 | 62.6 ± 1 | 6.1 ± 0.1 | Proteins, lipids | [124] |

numbers of spectra in the average spectrum. When plotted against the number of spectra in the average spectrum, this produces a convergence rate graph, the same as those seen for analysis of the heterogeneity of graphene (Chapter 3), thus, allowing for analysis of the heterogeneity of band-specific biomolecules. For example, the convergence rate for the band at 1002 cm$^{-1}$ is shown in Figure 4.21. This band is representative of phenylalanine which was found to vary across three samples from PCA (Fig. 4.8), as well as for the PIRs against the bands at 781 cm$^{-1}$ (Fig. 4.14) and 1481 cm$^{-1}$ (Fig. 4.15). For the sample shown here, the SE was converged to 2.81 x $10^{-5}$ at a rate of $\lambda = 12.8 \pm 0.2$ (Fig. 4.21).

The convergence rates for the 1002 cm$^{-1}$ band for the other samples are in Table 4.4. Sample three achieves a higher convergence rate compared with the other two replicates. This indicates that phenylalanine in *E. coli* sample three is more homogeneous than the other samples. Sample one produced the lowest convergence rate for the band at 1002 cm$^{-1}$, indicating higher levels of heterogeneity. This band was also found to vary in the PCA results (Fig. 4.9), thus, according to the convergence rates seen here, the heterogeneity of this band mainly stems from sample one,

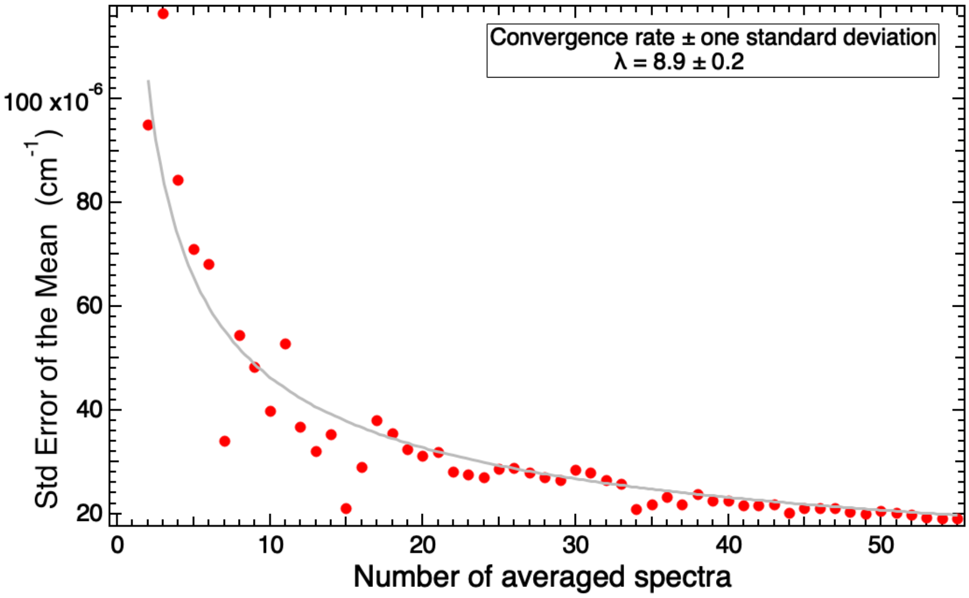

**Figure 4.22:** Convergence of the standard error of the mean of the normalised intensity of the band at 1453 cm$^{-1}$, representative of lipids and proteins [120, 121, 124, 155, 156]. This band was found to vary across the three samples, according to PCA results and PIRs against the bands at 781 cm$^{-1}$ and 1481 cm$^{-1}$. $\lambda$ is the rate of convergence.

which gave the lowest convergence rate. The variation of this band may be due to different toxicity response of the cells due to cell death, or the amino acids undergoing different conformational changes due to the dessication process [256]. Sample one being the most heterogeneous of the samples is not in agreement with the PIR results against the band at 781 cm$^{-1}$, which shows separation for the PIR $I_{1002}/I_{781}$ for sample three only (Fig. 4.14), found to be the most homogeneous sample in this analysis. Thus, the separation of the PIR may be a result of heterogeneity of the 781 cm$^{-1}$ biomarker.

Comparatively, the band at 1453 cm$^{-1}$ obtained a lower convergence rate than the band at 1002 cm$^{-1}$, indicating decreased homogeneity of this biomarker. The 1453 cm$^{-1}$ band (lipids and proteins) converged to 1.90 x 10$^{-5}$ at a rate of $\lambda$ = 8.9 ± 0.2 (Fig. 4.22) [120, 121, 124, 155, 156]. The convergence rates of the 1453 cm$^{-1}$ band for the other samples (Table 4.4) were all lower than the corresponding convergence rates for the band at 1002 cm$^{-1}$. However, the values obtained for the 1002 cm$^{-1}$ band vary significantly across values, whilst for the 1453 cm$^{-1}$ the variation is less significant. This increased variation in the values obtained for the

1002 cm$^{-1}$ are in agreement with both PCA and PIR analysis, which found the band at 1002 cm$^{-1}$ to be heterogeneous, while showing the 1453 cm$^{-1}$ peak not to vary across the three samples (Fig. 4.9). This can allow the conclusion that the 1453 cm$^{-1}$ is more heterogeneous within samples, while the 1002 cm$^{-1}$ band displays greater heterogeneity across samples.

The largest variation in the convergence rates for the band at 1453 cm$^{-1}$ was seen for sample 3 which had a value of 12.5 ± 0.2 compared with 8.9 ± 0.2 and 8.2 ± 0.2 for samples one and two respectively (Table 4.4). All three results were outside of error of one another. Similar results were obtained for the convergence of the PIR biomakers $I_{1453}/I_{781}$ and $I_{1453}/I_{1481}$, which demonstrated heterogeneity across the three samples (Table 4.3). This band has been previously used for determination of changes in the metabolic processes of bacteria due to toxic conditions and substances [77, 121]. Thus the variation of convergence rates of this band is indicative of significant variation of the metabolic processes of the cells across the population [77, 121]. This heterogeneity may only be observable at a single spectrum level, and may not be significant at a population level, hence, the lack of separation in PCA and PIR analysis.

For the convergence rates of the band at 781 cm$^{-1}$ (DNA), all samples are outside of error of one another (Table 4.4). This is in agreement with PCA results (Fig. 4.9), which found this band to vary across the samples. Variation in bands associated with DNA can occur due to cells or samples being at different stages in their growth cycle, causing natural heterogeneity of the DNA in the cells [253]. The heterogeneity may also be a result of changes in the DNA due to the cell death process [253].

The convergence rates of other bands in the three *E. coli* spectra are in Table 4.4. In general *E. coli* sample one achieves lowest convergence rates, meaning it is the most heterogeneous of the three replicates. This heterogeneity can also be seen in the PCA results (Fig. 4.8), with *E. coli* sample one displaying separation from the other samples.

Sample three has the largest convergence rates, however, the rates for this sample vary most significantly when compared with the other samples, suggesting that this sample was undergoing different cellular processes compared with the other samples, despite being most homogeneous within the sample. This heterogeneity can also be seen in the PCA results (Fig. 4.10), with *E. coli* sample three displaying separation from the other samples.

Some of the bands which are representative of the same biomolecule produce different convergence rates, for instance, for the bands at 667 $\text{cm}^{-1}$ and 781 $\text{cm}^{-1}$ produce different rates for *E. coli* sample three (Table 4.4), despite both being representative of RNA/ DNA. This may be due to the fact that the band at 667 $\text{cm}^{-1}$ is representative of nucleic acids guanine, thymine and cytosine, while the 781 $\text{cm}^{-1}$ of uracil, thymine and cytosine [77, 120, 124, 136, 153, 155, 156]. Thus, it is likely that the variation in the guanine is causing the decrease in convergence rates for the 667 $\text{cm}^{-1}$ band.

These convergence rates offer an insight into the heterogeneity of specific biomolecules across *E. coli* samples in a way which has not previously been done. The ability of Raman spectroscopy to detect changes in metabolic states of cells has previously been investigated, and this analysis could aid future investigations in an attempt to show the variation of biomolecules due to cellular alterations [77]. For future work, this analysis could allow an interesting look into how heterogeneous these changes are across biological samples following specific cellular changes or perturbations, such as cell interaction with graphene.

## 4.6 Conclusion

The level of characterisation achieved in this chapter goes beyond what has previously been done before within literature to our knowledge, in order to ensure full representation of the heterogeneity of the *E. coli* sample within the spectral average. The number of spectra required for characterisation of the *E. coli* samples in the work was determined through convergence of the SE and 2SD. It was found that convergence of the data was achieved for the 55 individual point Raman spectra across three *E. coli* replicates, i.e., for a total of 165 spectra. This level of characterisation goes beyond what has been done within literature to our knowledge, with some papers collecting ten or less spectra for representation of an entire cell population

[120, 151, 153, 159], or only performing one biological replicate for characterisation purposes [120, 151, 152, 154, 159].

Characterisation to the level performed in this chapter is necessary due to the significant levels of inter- and intra-sample heterogeneity for the three *E. coli* replicates investigated in this work. In order to investigate this inter-sample heterogeneity two random point spectra collected from the same *E. coli* sample were analysed. These spectra displayed significant variation, which was analysed using PIR analysis. These PIRs uncovered relative intensity differences of many of the bands representing RNA/ DNA, specifically those at 722 $cm^{-1}$, 1096 $cm^{-1}$, 1237 $cm^{-1}$, 1256 $cm^{-1}$ and 1572 $cm^{-1}$ [77, 115, 120, 123, 124, 136, 153, 155, 156]. These changes are likely due to cells in the same sample being at different growth stages, a natural occurrence in bacterial samples [253].

The cell variation within samples also caused changes in the bands representative of proteins, such as the bands at 854 $cm^{-1}$, 1078 $cm^{-1}$, 1206 $cm^{-1}$, 1237 $cm^{-1}$, 1295 $cm^{-1}$, 1453 $cm^{-1}$, 1481 $cm^{-1}$, 1607 $cm^{-1}$, 1665 $cm^{-1}$, 2852 $cm^{-1}$, 2875 $cm^{-1}$ and 3064 $cm^{-1}$ [77, 120, 121, 124, 136, 153, 155, 156]. This protein variation in the Raman spectra of the two cells may be representative of protein modifications resultant from cell dessication [256, 260].

The heterogeneity of all Raman spectra were also compared across the three samples, to determine heterogeneity across the replicates, using PCA and PIR analysis of the spectral averages. The lipid bands at 722 $cm^{-1}$ and 2875 $cm^{-1}$ were found to vary across the three samples according to the PCA results, however, the PIR analysis showed no separation, indicating that the heterogeneity may be natural variation of lipids across the samples [77, 123, 124, 136, 156, 254, 255].

The PIR analysis uncovered that the RNA/ DNA heterogeneity was heavily linked with the variation in the protein bands. For instance, the PIRs against the band at 781 $cm^{-1}$ representative of DNA only showed separation for the protein-related bands at 757 $cm^{-1}$ and 1002 $cm^{-1}$ [77, 120, 124, 153, 155, 156]. This associated variation is due to heterogeneity of proteins in the sample causing retardation of cell growth, thus resulting in differences in DNA signatures across the sample [251]. The variation in the protein bands may be due to heterogeneous inhibited protein synthesis from the dessication process [77, 251].

Novel methods for determination of the heterogeneity in the PIR biomarkers and individual bands in the Raman spectra were then utilised. These so-called convergence rates were obtained for the PIRs $I_{1453}/I_{781}$ and $I_{1453}/I_{1481}$, the former of which showed separation in the PIR analysis, whereas the latter displayed no differences across the three samples. Irrespective of this, the $I_{1453}/I_{781}$ PIR achieved an average convergence rate of $5.1 \pm 0.1$, and the $I_{1453}/I_{1481}$ PIR biomarker an average convergence of $5.0 \pm 0.1$. Thus, despite the $I_{1453}/I_{781}$ biomaker being more heterogeneous between samples than the $I_{1453}/I_{1481}$ PIR, this analysis suggest both biomarkers have similar levels of homogeneity across samples.

The investigation of the PIR biomarkers provides a new method for analysis of heterogeneity of the metabolic processes of the cell. For instance, the relative intensity of the band at 1453 $\text{cm}^{-1}$ can be used to monitor cell viability [77, 121]. Thus, the variation of the PIRs $I_{1453}/I_{781}$ and $I_{1453}/I_{1481}$ is reflective of the heterogeneity of the metabolic processes of the cells in the sample with respect to changes in DNA and proteins respectively [77, 121]. Therefore, future work could involve utilising this method for analysis of the heterogeneity of the metabolic processes of bacterial samples following cellular changes, for example, different methods of cell death.

Analysis of the heterogeneity of individual bands was also performed to gain a more specific insight into the alterations of particular biomolecules using convergence rates of the SE of the normalised intensity of the bands. For instance, it was found that on average pure DNA bands achieved lower convergence rates than lipid or protein bands. For example, the band at 781 $\text{cm}^{-1}$ (DNA) has an average convergence rate of $\lambda = 9.9 \pm 0.2$ across the three samples, whereas the proteins band at 1002 $\text{cm}^{-1}$ and the lipid band at 2852 $\text{cm}^{-1}$ have higher convergence of $\lambda = 17.3 \pm 0.4$ and $\lambda = 10.4 \pm 0.5$ respectively. This indicates increased heterogeneity for DNA compared with other biomolecules in the samples.

The rates of convergence of the biomolecules of *E. coli* sample one were lower than the other samples, indicating this sample is the most heterogeneous of the three replicates.

The level of analysis performed in this chapter is more than has been done within literature. For example, it is common for works to visually compare the relative intensity changes of bands in the Raman spectra without quantification [123], however, in this work both PCA and PIR analysis were performed. The methods proposed within this chapter ensure full and proper characterisation of biological samples using Raman spectroscopy. The convergence of the SE and 2SD is a suitable method for determination of the level of characterisation achieved, and is an appropriate protocol for application across literature to ensure reliability of data.

# 5

# Analysis of Graphene's Antibacterial Properties Using Raman Spectroscopy

The ability of graphene to kill microbes is something which has been previously investigated, and proven, within literature [71, 73, 74, 75]. For example, Akhavan *et al.* found the percentage of viable bacteria to decrease by 70 % following the interaction of *E. coli* with graphene nanowalls for 60 minutes [75]. The biomolecular mechanism via which graphene causes the death of bacteria is, however, not something which is currently understood. This is because it is often the morphology of the cells which is examined following the interfacing of graphene and bacteria, such as the use of scanning electron microscopy (SEM) by Li *et al.* to show the morphological changes, specifically membrane damage and cytoplasm leakage, due to cell death by CVD graphene [71]. Li *et al.* thus hypothesised that graphene kills cells by cell membrane destruction, however, no specific cellular changes, i.e., changes of biomolecules such as proteins, lipids or RNA/ DNA, are shown or discussed [71].

The counting of colony forming units (CFUs) is commonly utilised within the literature to determine the viability of cells following interaction with graphene [71, 74, 75]. The ability of the cells to form colonies can be used as a measure of cellular viability. Thus, counting the number of colonies before and after interfacing with graphene can allow determination of loss of cell viability. For example, Akhavan *et al.* used the method of counting CFUs and measurements of the concentration of RNA to evaluate the efflux of cytoplasmic materials when assessing the antibacterial properties of graphene and graphene oxide (GO) nanowalls [75]. The counting of CFUs showed a decrease in the number of viable *E. coli* cells of over 50 % following interaction with graphene nanowalls. However, the work by Akhavan *et al.* was limited only to investigation of the change in RNA, and no information on changes in other biomolecules were considered [75]. By utilising Raman spectroscopy this work aims to investigate the composition of various biomolecules following interaction with graphene such as proteins, lipids and RNA/ DNA, and will look to gain an understanding into the biomolecular interactions between graphene and *E. coli*.

Raman spectroscopy has significant potential to investigate the changes in the cells following interaction with graphene. It has previously been used to investigate the changes in chemical composition of bacterial cells following death by different lethal conditions [77]. For instance, Teng *et al.* found that cell death by antibiotic ampicillin caused changes in lipid related bands at 957 cm$^{-1}$, 1302 cm$^{-1}$, 1445 cm$^{-1}$ and 1660 cm$^{-1}$ in the Raman spectra [77]. This is consistent with inhibition of cell wall synthesis, the process via which ampicillin has been found to cause cell death [77, 262]. Whereas, it has been reported that death by heat treatment changed protein-related bands at 1250 cm$^{-1}$, 1610 cm$^{-1}$ and 1670 cm$^{-1}$ representative of protein denaturing at high temperatures [120]. Raman has also been used to investigate the antimicrobial properties of GO, a study which found changes in the bands at 729 cm$^{-1}$ (adenine), 490 cm$^{-1}$ (proteins) and 610 cm$^{-1}$ (Amide IV), for which cell death was attributed to cell membrane degradation [123]. However, there was no quantitative analysis performed on the Raman spectra and only visual observation of changes in band intensities are discussed. In this thesis, both principal component analysis (PCA) and peak intensity ratio (PIR) analysis are performed on the spectra to determine what changes the cell undergoes due to cell death by graphene.

Specifically, the aforementioned investigations will involve determining the relative intensities of the bands in the Raman spectra prior to and after being interfaced with graphene [121]. PCA and PIR analyses will be utilised to determine changes in the Raman spectra due to interaction with graphene. Zu *et al.* used PIRs in the high wavenumber region of the Raman spectra to investigate *E. coli* cell death by alcohol [121]. Changes in the PIR of the bands at 2852 $\mathrm{cm^{-1}}$ (FAs and lipids) and 2924 $\mathrm{cm^{-1}}$ (lipids and proteins), i.e., the PIR $I_{2852}/I_{2924}$, were used to assess changes in membrane fluidity after cell death by alcohol [121, 124, 127, 153]. Similar analysis will be performed in this work, which will aim to determine the biomolecular changes in the cell following interfacing with graphene. No published work has studied the changes in *E. coli* cells following interaction with CVD graphene using Raman spectroscopy, thus to the best of our knowledge, the findings in this thesis will be the first report of such investigations.

Many hypotheses have been proposed for the ability of graphene to cause cell death. For instance, Li *et al.* suggested that the bacterial cells lose electrons due to the negative resting potential of the bacterial cell membrane forming a circuit with CVD graphene on a conductor or semiconductor substrate, specifically Cu and Ge [71]. Furthermore, graphene on $Si/SiO_2$ showed little reduction in cell viability, thus, it was hypothesised that graphene on $Si/SiO_2$ has no antimicrobial properties due to the substrate being an insulator, unable to form the proposed circuit [71]. The work by Li *et al.* has however, been criticised for use of antibacterial Cu interfering with the results [71, 74].

It has been suggested that the size and shape of the graphene can affect its antimicrobial properties [263]. For instance, it has been shown using fluorescence microscopy that the shape of graphene quantum dots (GQDs), which are carbon nanosheets of $< 20$ nm in lateral dimension, affects its ability to disrupt the cell membrane [263]. GQDs which were curved in shape displayed higher levels of toxicity to *S. aureus* compared with flat GQDs [263]. It has also been shown that the size of GO can affect its ability to cause cell death [264]. Specifically, the antimicrobial efficiency was shown to be four times greater for a reduction in sheet size from 0.65 $\mu$m$^2$ to 0.01 $\mu$m$^2$ [264]. This was attributed to high defect density of smaller graphene sheets, causing higher oxidative stress [264]. This work will investigate large area graphene, specifically samples of 1 cm$^2$.

The most common hypothesis to be proposed for the ability of graphene to kill microbial cells is the extraction of lipids from the lipid bilayer of the cell by graphene [73, 75, 123]. This hypothesis is based on the idea that nanographene acts as a knife, cutting into the membrane, extracting the lipids from the lipid bilayer [73]. However, as nanographene is not being studied within this work, rather it is large area graphene (1 cm$^2$) on a substrate, it is unlikely that this method of cell inhibition would be possible. The graphene will be unable to act as a nanoscale knife cutting into the cell membrane due to the increased size of the samples, which is $10^7$ orders of magnitude larger than nanographene.

The antimicrobial properties of large area CVD graphene have been investigated less than graphene formed via other methods [71, 265]. For instance, for the published works explored in this chapter almost 60 % of those examined graphene nanosheets, while around 25 % were investigating CVD graphene [71, 73, 74, 75, 123, 264, 266]. Some works have even claimed the CVD graphene possesses no antimicrobial properties [74]. However, the work presented in this thesis shows significant changes in the Raman spectra of the cells following interaction with CVD graphene. For example, the emergence of new bands in the high wavenumber region of the spectra such as the band at 3000 cm$^{-1}$, or the splitting of peaks, for instance the band at 722 cm$^{-1}$ into the bands at 717 cm$^{-1}$ and 727 cm$^{-1}$, suggestive of conformational changes of the cell following interaction with graphene.

The work in this chapter aims to investigate the biomoleular interactions of graphene and *E. coli* using Raman spectroscopy, to gain an understanding into the mechanism of cell death. Two experimental designs are presented in this chapter to investigate the toxicity response of the *E. coli* cells after being interfaced and cultured with graphene.

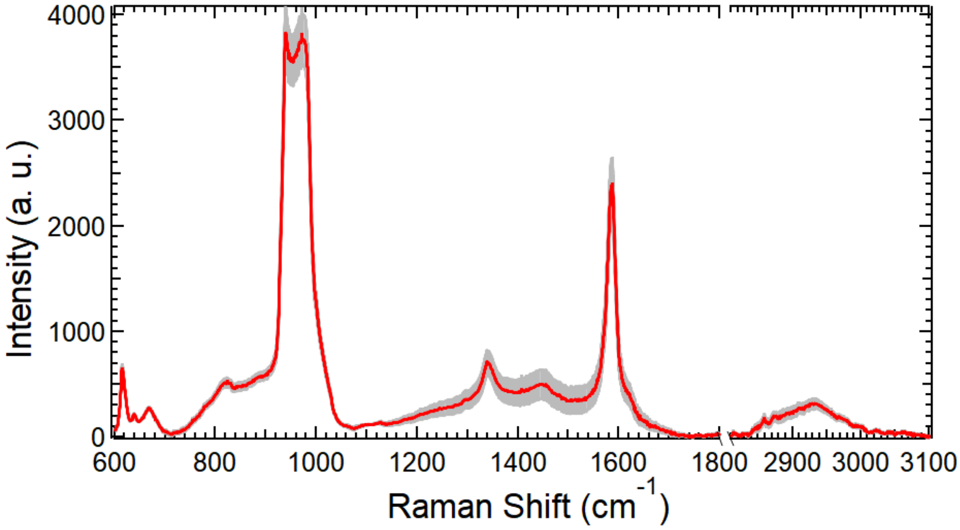

**(a)** Average spectrum of *E. coli* on CVD graphene. Intense graphene and Si/SiO$_2$ signatures in the fingerprint region (600 - 1800 cm$^{-1}$) effectively obstruct the Raman signals of *E. coli*. The grey represents the SE of the mean of the averaged spectrum.

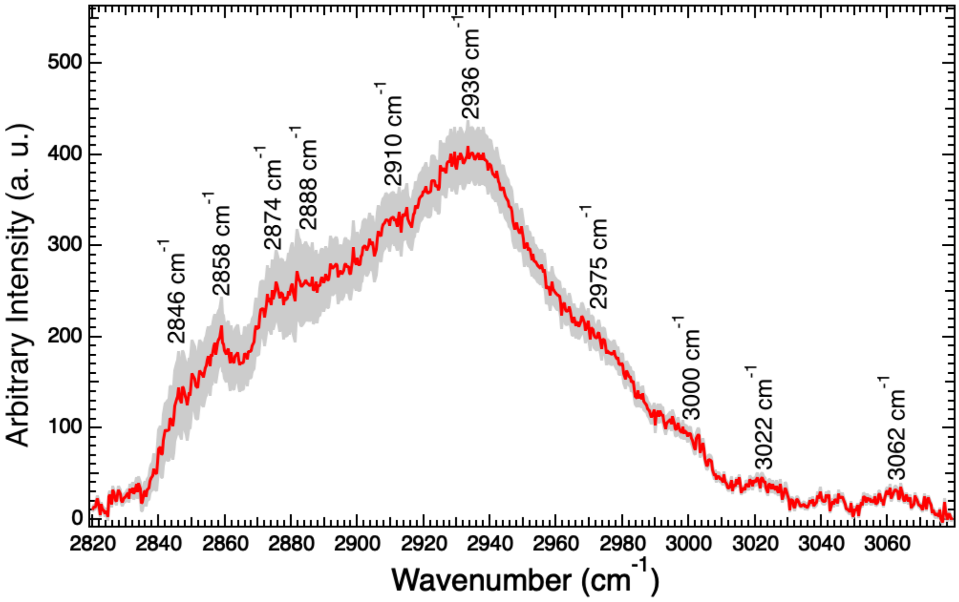

**(b)** The high wavenumber region (2800 - 3100 cm$^{-1}$) of the average spectrum of *E. coli* on CVD graphene. The grey represents the SE of the mean of the averaged spectrum.

**Figure 5.1:** Average spectrum of *E. coli* on CVD graphene showing (a) the full average spectrum and (b) the high wavenumber region. The cells were placed onto the CVD graphene surface following growth to interface. The Raman spectra were collected from *E. coli* cells on the graphene. The averaged spectrum is an average of 55 individual non-normalised Raman spectra collected from random points across the sample for one biological replicate.

## 5.1 *E. coli* Interfaced with Graphene

For the work presented in this section, the *E. coli* cells were interfaced with graphene following growth. The cells were washed to ensure the removal of all media, and were re-suspended in sterile water. The cells were pipetted onto the graphene in 5 $\mu l$ droplets, in the same way that was done for the characterisation of *E. coli* on $CaF_2$ (Chapter 2: Section 2.5.1). The cells dried onto the graphene surface during interfacing with the sample, and the Raman spectra were collected from these dried cells on the graphene surface.

An average Raman spectrum is shown in Figure 5.1a. It is an average of 55 individual Raman spectra collected from a single biological replicate of this experiment. Unfortunately, due to the intense graphene and $Si/SiO_2$ signatures in the fingerprint region (600 - 1800 $cm^{-1}$), the Raman spectrum of *E. coli* was obstructed (Fig. 5.1a). Background subtraction of these data were attempted in order to remove the graphene signals from the spectra. However, due to the low intensity of the bands in the Raman spectra of *E. coli* this introduced ambiguity as to whether peaks arising in the spectra were Raman signals of *E. coli* or due to leftover signal from subtraction of the intense graphene and $Si/SiO_2$ background noise. An example of such residual signal from background subtraction is shown in the Appendix: Figure A.22. The fitting of the bands in the average spectrum are shown in the Appendix along with the corresponding residuals (Fig. A.24).

As a result, the focus in this chapter will be on the high wavenumber region (2800 - 3100 $cm^{-1}$) of the Raman spectra, which was unimpeded by the graphene and substrate signatures (Fig. 5.1b). The high wavenumber region is particularly significant as it primarily constitutes lipids and proteins (Table 5.1), the main biomolecules in the *E. coli* cell membrane. Therefore, investigation of this region will give an insight into the hypothesis that graphene's antimicrobial properties are due to its ability to extract the lipids from the lipid bilayer of the cell [73, 75, 123].

The average spectrum of the high wavenumber region of one of the three biological replicates can be seen in Figure 5.1b. It is an average of 55 individual Raman spectra collected from random cells all across the sample. The three replicate averages are included in the Appendix (Figure A.23). The peak locations of the three

**Table 5.1:** The locations of the bands in the high wavenumber region of the Raman spectra for three replicates of *E. coli* interfaced with graphene sample, referred to as interfaced S1, S2 and S3. The *E. coli* band locations correlate to the bands in the high wavenumber region of the Raman spectrum, averaged across three biological replicates. The units of all locations are $cm^{-1}$. The maximum instrument error is 3 $cm^{-1}$ on each measurement. The stated errors are obtained from the fitting of the standard error envelope (as described in Chapter 2). Fatty acids has been abbreviated to FAs.

| **Interfaced band locations** | | | ***E. coli* band locations** | **Literature location** | **Band Assignment** | **Bond** | **Ref.** |
|---|---|---|---|---|---|---|---|
| **S1** | **S2** | **S3** | | | | | |
| 2847 ± 3 | 2845.7 ± 0.2 | 2846.8 ± 0.8 | 2852 ± 1 | 2846 | FAs<br>Lipids | Symmetrical stretching vibrations of $CH_2$ and $CH_3$ | [121, 124, 127] |
| 2857 ± 3 | 2858.1 ± 0.1 | 2857.8 ± 0.2 | | 2855 | FAs<br>Lipids | $CH_2$, $CH_3$ symmetric stretch | [121, 124, 153] |
| 2875 ± 2 | 2872.0 ± 0.3 | 2872.8 ± 0.1 | 2877 ± 2 | 2875 | Lipids<br>Proteins | $CH_2$ asymmetric stretch | [124, 155] |
| 2882.2 ± 0.1 | 2887 ± 2 | 2896 ± 3 | - | 2882 - 2895 | Unsaturated lipids<br>Proteins | $CH_2$ asymmetric stretching of lipids and proteins | [124, 127] |
| 2910.3 ± 3 | 2908.5 ± 0.7 | 2909.61 ± 0.05 | - | 2910 | Lipids | CH, $CH_3$ stretch | [124, 127] |
| - | - | - | 2927 ± 3 | 2929 | Lipids<br>Proteins | $CH_2$ asymmetric stretch, symmetric $CH_3$ stretch | [124, 153] |
| 2936.7 ± 0.2 | 2932.3 ± 0.8 | 2938 ± 1 | 2936 ± 1 | 2935 | Lipids<br>Proteins | Symmetrical $CH_2$ and $CH_3$ stretch | [124, 127, 267] |
| 2972 ± 2 | 2977.4 ± 0.5 | 2975.5 ± 0.7 | 2978 ± 1 | 2973 | Proteins | Asymmetric $CH_3$ stretch | [124, 267] |
| 3000.45 ± 0.01 | 2999.5 ± 0.3 | 3000.09 ± 0.05 | - | 3000 | Lipids<br>Unsaturated FAs | CH stretching | [124, 127] |
| 3021.3 ± 0.5 | 3022.3 ± 0.2 | 3021.1 ± 0.5 | - | 3015 | Lipids | C–H stretching | [124] |
| 3062.8 ± 0.8 | 3061 ± 2 | 3063.2 ± 0.2 | 3064.25 ± 0.06 | 3067 | Proteins | C=C-H aromatic stretch | [248, 267] |

samples, with corresponding biomolecular assignments and bonds which give rise to the bands are shown in Table 5.1. The Raman spectra of *E. coli* after being interfaced with graphene will be compared against the spectra collected from the three *E. coli* samples dried onto $CaF_2$, as presented in Chapter 4, which will be used as a control. The locations of the peaks in the averaged *E. coli* spectrum, are included in the table for comparison of band shifts as a result of cell death by graphene (Table 5.1). The *E. coli* band locations were obtained from fittings of the averaged spectra across three biological replicates.

There is significant variation of the band locations in the averaged *E. coli* spectrum compared with the Raman spectra of *E. coli* interfaced with graphene (Table 5.1). The first of these differences is the potential splitting of the band at 2852 $cm^{-1}$ into two bands at 2846 $cm^{-1}$ and 2858 $cm^{-1}$, representative of lipids and fatty acids (FAs) [121, 124, 127]. It is uncommon for two bands to appear in this region in the Raman spectra of FAs or lipids. Czamara *et al.* studied 35 different lipids using Raman spectroscopy, and found only a single band was present between $\sim$ 2832 $cm^{-1}$ to 2862 $cm^{-1}$ in the Raman spectra of each lipid, that is, in no spectrum were there two bands between these wavenumbers as found in this work for the bands at 2846 $cm^{-1}$ and 2858 $cm^{-1}$, which are representative of symmetric $CH_2$ and $CH_3$ stretching vibrations of FAs and lipids [124, 127]. This suggests that the two bands are present due to the splitting of the band at 2852 $cm^{-1}$ as a result interfacing with graphene. Following literature searches, no reports of such splitting of this band were found. Therefore, this suggests the band splitting is a unique toxicity response of the cells due to being in contact with graphene. These bands arise due to FAs and lipids, therefore, the changes in these bands suggest significant perturbations of these biomolecules, and is indicative of lipid bilayer perturbation [121, 124, 127, 153].

There are additional bands present in the Raman spectra of *E. coli* interfaced with graphene compared with the *E. coli* spectrum, specifically the lipid bands at 2910 $cm^{-1}$, 3000 $cm^{-1}$ and 3022 $cm^{-1}$ [124, 268]. These bands are prominent in the Raman spectra of FAs [126, 268]. In particular, the band at 2910 $cm^{-1}$ is especially prominent in the Raman spectra of saturated FAs myristic acid, palmitic acid, and arachidic acid [268]. The 3022 $cm^{-1}$ band is also due to the presence of saturated FAs [126], while the band at 3000 cm$^{-1}$ is a prominent band in the spectrum of palmitoleic acid, a monounsaturated FA [268]. Therefore, the arisal of the bands at 2910 cm$^{-1}$, 3000 cm$^{-1}$ and 3022 cm$^{-1}$ in the Raman spectra of *E. coli*, representative of C-H stretching of lipids and FAs, following interfacing with graphene may be further indication of perturbations to the FAs and lipids in the cell [124, 127]. Specifically it is suggestive of conformational changes due to cell disruption as a result of being interfaced with graphene. This is in agreement with papers which have hypothesised that graphene kills bacterial cells by disrupting the lipid bilayer of the cell [73, 75, 123].

Investigation of the changes in the Raman spectra across the three samples will be performed, which analyses the heterogeneity of the *E. coli* samples due to cell death by graphene.

## 5.2 Analysis of the heterogeneity of the Raman spectra of *E. coli* following interaction with CVD graphene

PCA was performed on the three replicates for analysis of the different mechanisms employed during cell death by graphene within the samples. The data separated along PC1, representative of 19.0 % of the variance of the data set (Fig. 5.2). The corresponding loading showing the features which caused separation in PCA space is shown in Figure 5.3. The data did not separate along any other PC.

Two of the spectral features noted to change according to the PCA results (Fig. 5.2 & 5.3) are the bands at 2888 cm$^{-1}$ and 2895 cm$^{-1}$. Comparison of the band locations for the three *E. coli* interfaced with graphene samples (Table 5.1) indicates a noticeable shift in the location of the band at 2888 cm$^{-1}$ for samples one and two, to a location of 2895 cm$^{-1}$ for sample three. A similar shift is reported by Czamara *et al.*, who found that the protein-lipid $CH_2$ asymmetric stretching vibration at 2885 cm$^{-1}$ in the Raman spectra of HMEC-1 cells cultured for a six hour period, shifted to 2895 cm$^{-1}$ in the Raman spectra collected after 24 hours of incubation [127].

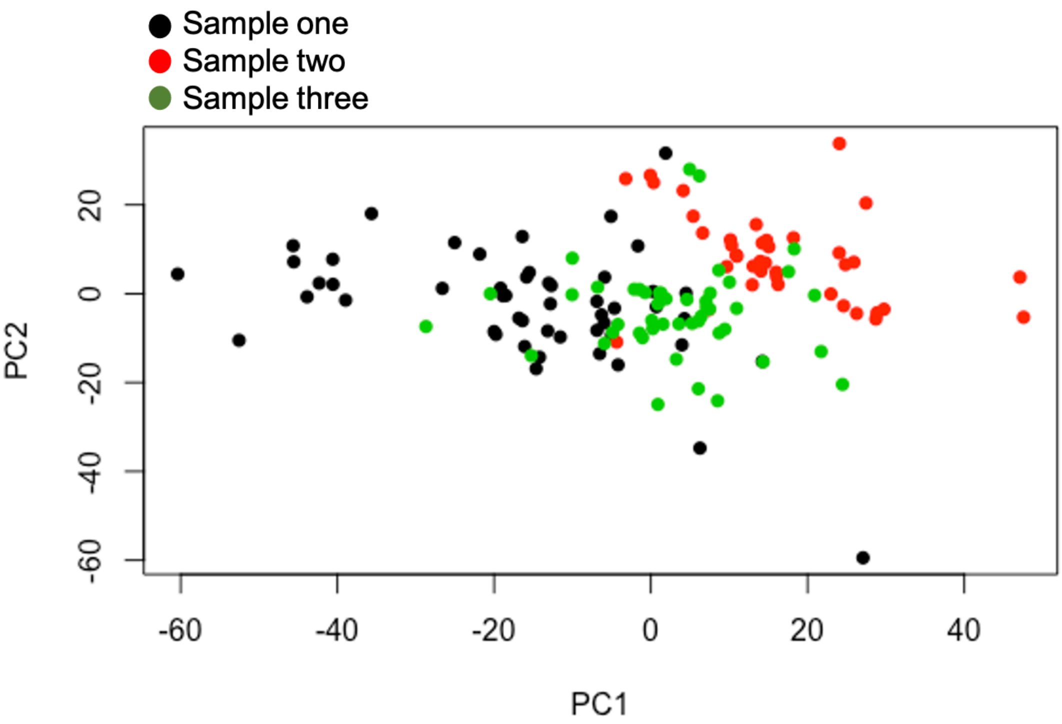

**Figure 5.2:** PCA results for the high wavenumber region (2800 - 3100 $cm^{-1}$) in the Raman spectra of three samples of *E. coli* interfaced with graphene, showing PC1 against PC2. There is separation along PC1 which represents 19.0 % of the total variance of the data.

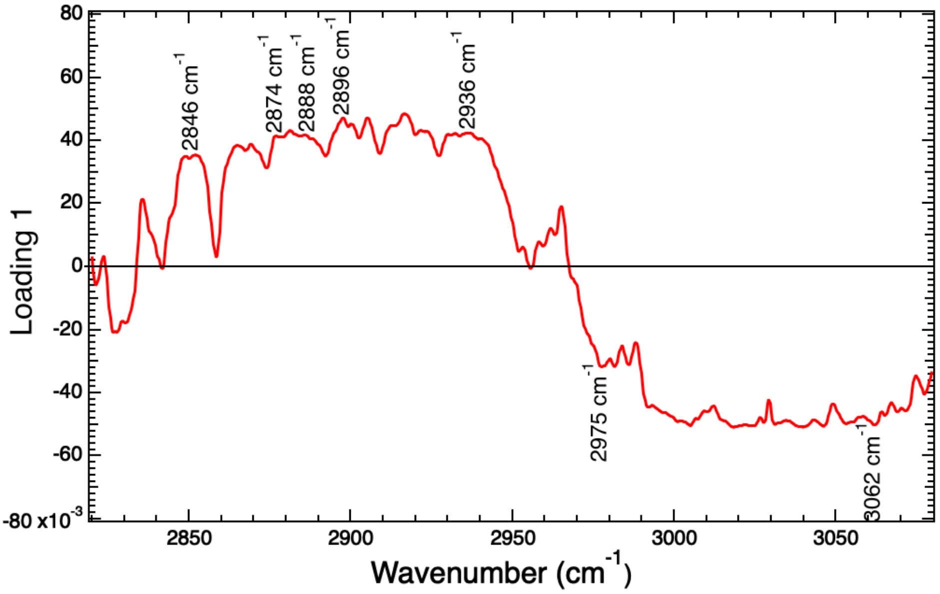

**Figure 5.3:** Loading one for the PCA results of the Raman spectra of the three *E. coli* interfaced with graphene samples. There is separation along PC1 representative of 19.0 % of the total variance of the data set. The main spectral features causing separation are labelled.

The reason for this band shift is not explained, however, the bands arise due to the same bonds and biomolecules, thus, the differences may be due to variation in the growth stages of the *E. coli* samples, which has been reported to cause changes in the cellular proteins and lipids [253, 269, 270]. The *E. coli* samples in this work were grown to the same optical density ($OD_{600} = 0.4$ - $0.6$) and so if this band shift is a result of variation in growth phases this is due to natural growth variation in the bacterial samples.

The change in band locations from 2888 $cm^{-1}$ to 2895 $cm^{-1}$, and the separation of the samples in PCA space, may be reflective of changes in FA composition reflective of different toxicity responses across samples. Sample three of the *E. coli* interfaced with graphene replicates was interfaced with graphene sample three, which according to the novel convergence rate tests presented in Chapter 3 is the most heterogeneously defected of the samples used for these experiments (Section 3.5). Thus, the interactions between the graphene and the bacteria may differ as a result. It has been shown that heterogeneity of graphene can cause different interactions with cells [199]. For instance, pristine graphene and homogeneously oxidative graphene were found to cause no damage to bacterial cells according to cryo-electron microscopy (Cyro-EM) and simulations of the interactions [199]. Comparatively simulations of heterogeneously oxidative graphene resulted in cell membrane rupture [199]. Therefore, the shift of the band from 2888 $cm^{-1}$ to 2895 $cm^{-1}$ and the separation of the samples in PCA space may be due to different interactions of the *E. coli* cells with the heterogeneously defected graphene samples.

Four of the bands found to change across the three samples are lipid-related bands, specifically those at 2846 $cm^{-1}$, 2874 $cm^{-1}$, 2888 $cm^{-1}$ and 2936 $cm^{-1}$ [121, 124, 127, 155]. Lipids and FA composition has been found to naturally vary dependent on the stage at which the cells are at in their growth cycles, as determined using mass spectrometry [271]. The changes in these bands may also be reflective of different toxicity responses of the samples [252]. As discussed in Chapter 4, cells can stochastically transition in order to prepare for unexpected lethal attacks which could result in cell death [109, 252]. These so-called persister cells can alter themselves to avoid cell death, to ensure a sub-population of cells will survive any stress conditions. For example, a sub-population of cells within a population were shown not to die following prolonged dosages of penicillin which would of eradicated a homogeneous cell population [109, 252]. Therefore, it is possible that the differences in the Raman spectra seen here for the different samples may be due to the cells reacting in a different way to the harmful interaction with graphene [109, 252]. This may also be due to different interactions of the lipids in the cells with the differing levels of defects of the graphene samples.

The interactions of the bacterial cells and lipids with the defects could be further investigated using Raman spectroscopy by identifying or inducing specific types of defects in the graphene sample. This would allow investigation of how different defects affect bacterial cell death, and could be further examined by interfacing pure lipids with these defects to monitor the changes. This type of study could be significant in determining if increased level of defect in graphene promotes the loss of cell viability, as hypothesised within this work, allowing graphene to be utilised in a more targeted manner.

In order to further investigate the changes in the Raman spectra of *E. coli* interfaced with graphene compared with the control *E. coli* samples, PCA results performed on the two data sets comprising the three biological replicates of each experiment will now be investigated.

## 5.3 Analysis of the Raman spectra of *E. coli* interfaced with CVD graphene

The PCA results of *E. coli* and *E. coli* interfaced with graphene are shown in Figure 5.4. This figure shows the separation of the data set along PC3 and PC7 which represent 7.39 % and 0.94 % of the total variance respectively. The corresponding loadings can be seen in Figures 5.5 and 5.6 respectively, with the spectral features causing separation in PCA space labelled.

Loading three (Fig. 5.5) of the PCA results, representative of the bands causing separation along PC3 (Fig. 5.4), indicates the band at 3000 cm$^{-1}$ as a spectral component which varies between the *E. coli* spectra compared with *E. coli* inter-

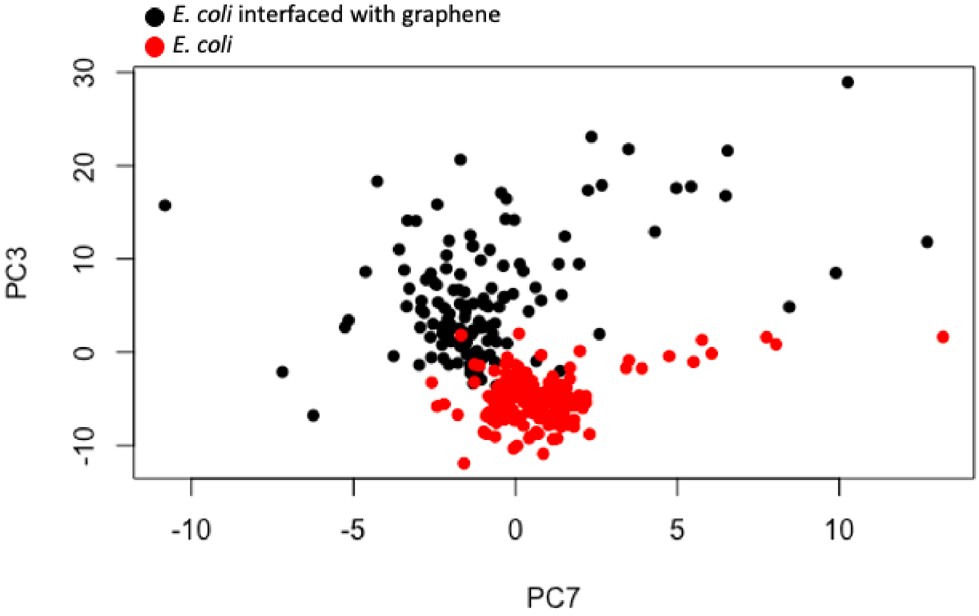

**Figure 5.4:** PCA results for the high wavenumber region (2800 - 3100 cm$^{-1}$) in the Raman spectra of *E. coli* (black) and *E. coli* interfaced with graphene (red). There is separation along PC3 and PC7 which represent 7.39 % and 0.94 % of the total variance of the data set respectively. The separation represents different cellular changes due to cell death by graphene.

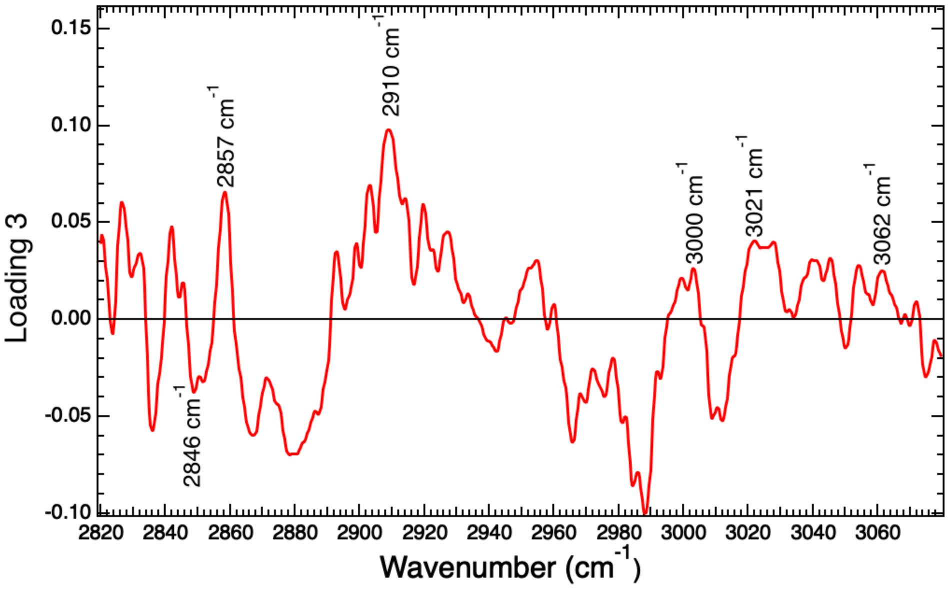

**Figure 5.5:** Loading three for the PCA results of *E. coli* compared with *E. coli* interfaced with graphene. There was separation along PC3 representative of 7.39 % of the total variance of the data set. The main spectral features causing separation are labelled on the loading.

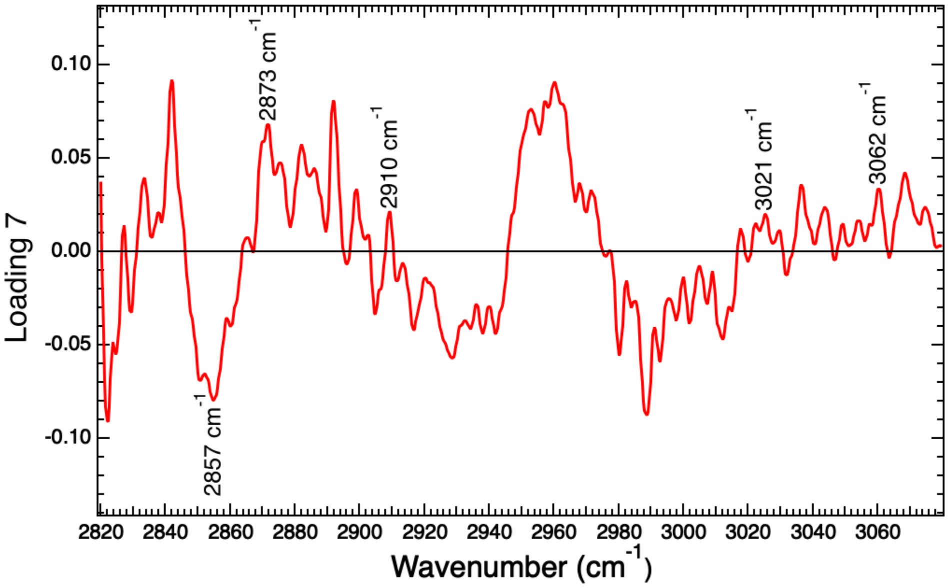

**Figure 5.6:** Loading seven for the PCA results of *E. coli* compared with *E. coli* interfaced with graphene. There was separation along PC7 representative of 0.94 % of the total variance of the data set. The main spectral features causing separation are labelled on the loading.

faced with graphene. This band arises only in the *E. coli* interfaced with graphene spectra (Table 5.1). The band at 3000 cm$^{-1}$ has been reported to only appear as an additional feature in the Raman spectra due to stretching modes of additional =C-H bonds of unsaturated FAs [268]. Therefore, this suggests relative changes in the FA composition, pertaining specifically to variation in the unsaturated FAs in the cells, and may be due to changes in the level of saturation of the FA composition of the *E. coli* [127].

The lipid band at 3022 cm$^{-1}$ was found to vary between the *E. coli* and *E. coli* interfaced with graphene spectra, according to both loading three and loading seven of the PCA results (Fig. 5.5 & 5.6). This is again due to the band being present only in the *E. coli* interfaced with graphene spectra (Table 5.1). This band has been found to arise due to saturated FAs being present in the sample, and diminishes for increasing levels of unsaturation in the sample [126]. That is, the presence of the band at 3022 cm$^{-1}$ in the *E. coli* interfaced with graphene spectra suggests alterations of the FA composition, specifically additional saturated FAs which are not present in the *E. coli* sample [126].

The separation along PC7 also uncovered changes in the band at 2874 cm$^{-1}$

(Loading 5.6), which arises due to proteins and lipids [124, 155]. Changes in this band have been reported to be representative of the preservation of saturated FAs in the cells as a toxicity response to lethal conditions [121]. Furthermore, this band was found by Zu *et al.* to change as a result of alteration of membrane fluidity of cells representative of a toxicity response to alcohols, following *E. coli* cell growth with alcohol for one hour [121]. Thus, the changes in the band at 2874 $\mathrm{cm}^{-1}$ may be reflective of changes in the saturation of the membrane due to altered membrane fluidity from cellular stress by graphene [121]. These changes in lipid and FA composition, which may be causing a change in the membrane fluidity, could be further investigated using mass spectroscopy as a complementary tool to Raman spectroscopy, which has previously been used to monitor changes of FAs and lipids in cells [271].

Raman spectroscopy can determine relative changes in the metabolic state of the cells and provide insight into changes in the chemical composition of the cells [160]. For *E. coli* interfaced with graphene results presented here, the variation of each of these bands are suggestive of relative changes in the level of saturation in the *E. coli* samples due to being interfaced with graphene [121, 126, 127]. Specifically, the spectra displayed additional bands correlating to an increase in the bonds related to saturated FAs, such as the emergence of the band at 3022 $\mathrm{cm}^{-1}$, and changes in the band at 2874 $\mathrm{cm}^{-1}$ also demonstrated preservation of saturated FAs in the cells [121, 126].

Further work could be performed using Raman spectroscopy to more thoroughly investigate the cause of these changes, specifically pure lipids could be interfaced with the graphene samples and the changes in the Raman spectra monitored. This would allow monitoring of the exact variation in lipid bands, particularly if this was performed for specific lipids and FAs present in *E. coli* which are hypothesised to change in this work, such as myristic acid and palmitic acid [268].

To further investigate the interactions of *E. coli* with graphene the second experimental design of graphene cultured with *E. coli* will now be presented.

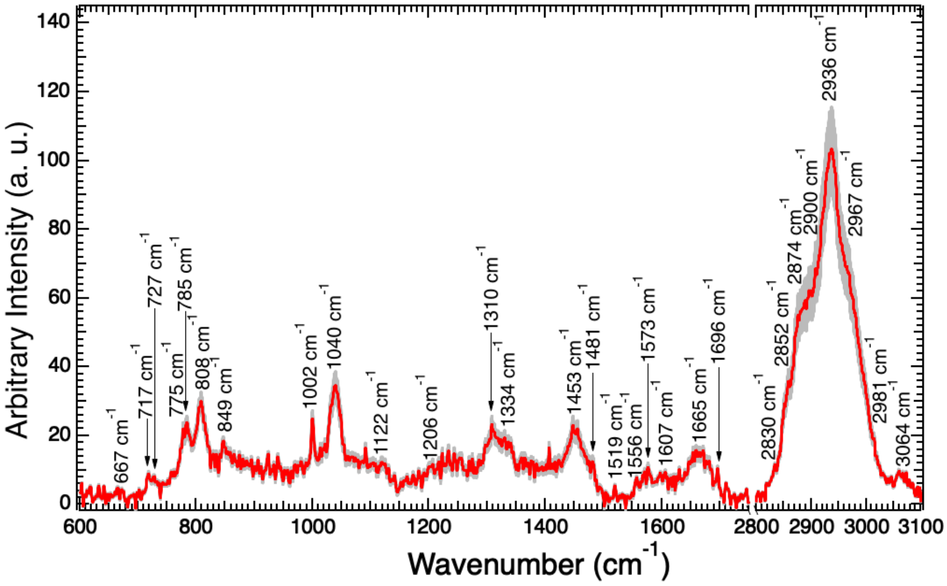

**Figure 5.7:** Average spectrum of *E. coli* after being spun down onto CVD graphene and left to interface for 1.5 hours. The cells were washed and air-dried onto a $CaF_2$ disc following which the Raman spectra were collected. This spectrum is an average of 55 individual smoothed Raman spectra collected from random points across the sample. The grey represents the SE of the mean of the averaged spectrum.

## 5.4 *E. coli* cultured onto Graphene

In order to further investigate the antimicrobial properties of graphene, an experiment was performed to analyse the interactions of *E. coli* and CVD graphene when it was cultured on the antimicrobial material. Following overnight growth of the *E. coli*, the cells were diluted into fresh media and spun down onto the graphene in a 24 well plate using a swing out centrifuge. The cells were incubated with the graphene in media for 1.5 hours at 37 °C. Following which the cells were washed from the graphene and placed onto a $CaF_2$ disc for Raman analysis. This allowed for collection of Raman spectra of *E. coli* which had been cultured on CVD graphene, and which is free of background graphene and $Si/SiO_2$ signatures.

The average Raman spectrum is shown in Figure 5.7. It is an average of 55 individual Raman spectra collected from random points across the sample. The spectra have been smoothed due to increased levels of noise, likely to a result of additional artefacts in the sample from cell culturing with graphene. The raw spectrum is shown in Figure A.25. Dead cell spectra have been shown to have additional noise compared with live cell spectra, thus the additional toxicity perturbations of cells due to interaction with graphene may be the cause of the additional noise [272]. Due to time restraints within the PhD, only one biological replicate of the experiment has been performed.

The locations and corresponding assignments are shown in Table 5.2. As with the *E. coli* interfaced with graphene, the Raman spectra of *E. coli* dried onto $CaF_2$ will be used as a control. Thus, Table 5.2 also includes the *E. coli* band locations for comparison of band shifts or additional peaks in the *E. coli* interfaced with graphene spectra.

There is significant variation in the bands in the Raman spectrum of *E. coli* compared with *E. coli* cultured with graphene (Table 5.2). For instance the band appearing at 722 $cm^{-1}$ in the Raman spectrum of *E. coli* appears to have split into two bands at 717 $cm^{-1}$ and 727 $cm^{-1}$ both representative of DNA and lipids [77, 123, 124, 136, 156]. This band was also observed to vary in a literature study following exposure of *E. coli* cells with penicillin for 4.5 hours [152]. Penicillin is has been found to cause cell death by inhibition of cell wall synthesis [274, 275]. Thus, the splitting of the 722 $cm^{-1}$ bands into the DNA, lipid convoluted bands at 717 $cm^{-1}$ and 727 $cm^{-1}$ may be due to inhibition of the cell wall synthesis, and thus, reflective of slowing of the cellular processes as a result [276]. The 722 $cm^{-1}$ band in the Raman spectrum of *E. coli* has also been found to change due to cell death by GO, as reported by Nanda *et al.* [123]. However, no reason is stipulated as to why this change occurs.

In order to further investigate if the alterations of these bands is a result of the inhibition of the cell wall, this mechanism could be monitored using metabolic fluorescent staining [277]. This method has previously been utilised to determine the specific mode of action of cell-wall-inhibiting antibiotics, such as ramoplanin, and vancomycin [277]. Thus, fluorescence staining could be utilised in this case in a similar manner, alongside Raman spectroscopy, to determine alterations in bacterial cell wall synthesis due to interaction with graphene.

There are also noticeable changes in bands associated with proteins. For instance,

**Table 5.2:** Table of band locations and assignments for peaks in the average Raman spectrum of *E. coli* cultured with graphene. The bands in the average Raman spectrum of *E. coli* are included for comparison. The units on all locations are cm$^{-1}$. The maximum instrument error is 3 cm$^{-1}$ on each measurement. The stated uncertainties are obtained from the fitting of the standard error envelope. Fatty acids is abbreviated to FAs and phenylalanine to phe. C, A, G, T, U are the nucleic acids cytosine, adenine, guanine, thymine and uracil.

| **Interfaced location** | **E. coli locations** | **Literature location** | **Peak Assignment** | **Bond** | **Reference** |
|---|---|---|---|---|---|
| 666.1 ± 0.6 | 667.1 ± 0.1 | 665-668 | **DNA:** G, T<br>**Protein:** cystine | C-S stretching | [77, 124, 136] |
| 717.49 ± 0.03 | - | 718-720 | **Membrane phospholipid head**<br>**DNA** | C-N | [124] |
| 727.0 ± 0.2 | 722.0 ± 0.2 | 720-730 | **DNA:** A<br>**Phospholipids** | CH$_2$ rocking | [77, 123, 124, 136, 156] |
| - | 756.6 ± 0.2 | 759 | **Proteins:** Tryptophan | - | [77, 124] |
| 775 ± 2 | - | | **Lipids:** Phosphatidylinositol | - | [124] |
| 785 ± 2 | 781.32 ± 0.02 | 783 | **RNA/ DNA:** U, C, T | C=O, C-N ring deformation | [77, 120, 124, 153, 155, 156] |
| 807.9 ± 0.3 | 809.3 ± 0.1 | 811 - 813 | **Proteins:** tyrosine<br>**RNA** | C-C stretching<br>C-O-P-O-C in A-RNA backbone | [77, 124, 136, 155, 156] |
| 848.9 ± 0.3 | 854.0 ± 0.3 | 857 | **Proteins:** tyrosine | CC stretching<br>COC | [77, 124, 155, 156] |
| 1000.2 ± 0.1 | 1001.79 ± 0.03 | 1000-1005 | **Proteins:** Phe | CC stretching | [77, 124, 136, 153, 155, 156, 247] |
| 1038.7 ± 0.7 | 1040.7 ± 0.7 | 1035 | **Proteins** | - | [124] |
| - | 1077.5 ± 0.3 | 1080 | **Proteins**<br>**Lipids** | Phosphate vibrations<br>C-C stretch | [77, 124, 156] |
| - | 1098.2 ± 0.5 | 1095 - 1100 | **DNA** | PO2-, CC stretching<br>COC stretching, C-N | [77, 124, 136, 155, 156] |
| 1121.9 ± 0.6 | 1124.2 ± 0.2 | 1126 | **DNA:** C, T<br>**Proteins**<br>**Carbohydrates**<br>**Lipids** | C-N stretching, C-C<br>C-O stretching | [77, 124, 156] |
| - | 1172.8 ± 0.2 | 1170- 1175 | **Proteins:** Tyrosine, Phenylalanine<br>**DNA:** C, G | C-H in-plane bending mode | [77, 124, 136] |
| 1202.8 ± 0.3 | 1206.0 ± 0.2 | 1208 | **Proteins:** tryptophan, phenylalanine<br>**RNA/ DNA:** A, T | C-C$_5$H$_6$ | [77, 124] |
| - | 1236.8 ± 0.1 | 1242-1250 | **Proteins:** Amide III<br>**RNA:** U | C-N, N-H | [77, 120, 124, 153] |
| - | 1256.0 ± 0.1 | 1256 | **Proteins:** Amide III<br>**Lipids**, **DNA:** T | | [115, 124] |

**Table 5.2 continued**

| **Interfaced location** | ***E. coli* locations** | **Literature location** | **Peak Assignment** | **Bond** | **Reference** |
|---|---|---|---|---|---|
| - | 1294.7 ± 0.9 | 1300 | **Lipids** | $CH_2$/ $CH_3$ twisting or bending | [77, 120, 136] |
| 1309.73 ± 0.05 | 1314.4 ± 0.7 | 1314 | **Proteins** | $CH_3$, $CH_2$ twisting mode | [124] |
| 1334.4 ± 0.7 | 1335.0 ± 0.7 | 1336 | **Proteins**<br>**DNA**: G | CH, $CH_2$, $CH_3$ deformation | [77, 124] |
| 1453 ± 1 | 1453.2 ± 0.1 | 1453 | **Protein deformation**<br>**Lipids** | $CH_2$ deformation | [120, 121, 124, 155, 156] |
| 1481 ± 2 | 1480.81 ± 0.09 | 1481 - 1486 | **Proteins:** Amide II<br>**RNA/ DNA:** A, G | - | [77, 124, 247] |
| 1519.56 ± 0.01 | - | 1515 | **Proteins:**<br>Cytosine | - | [124] |
| 1556.3 ± 0.2 | - | 1554-1558 | **Proteins:** Amide II,<br>Tryptophan, Tyrosine | CN, NH, COO- | [124] |
| 1573.6 ± 0.2 | 1572.3 ± 0.4 | 1574-1578 | **RNA/ DNA:** A, G<br>**Proteins:** Amide I | NH deformation<br>CN stretching | [77, 115, 124, 153, 155, 156] |
| 1600.26 ± 0.03 | 1606.8 ± 0.2 | 1605 - 1607 | **Proteins:** Phenylalanine, tyrosine<br>**Unsaturated lipids** | C=C | [77, 121] |
| 1665.3 ± 0.4 | 1664.9 ± 0.4 | 1660 | **Lipids**<br>**Unsaturated FAs**<br>**Proteins:** Amide II, Phenylalanine | C=C<br>Ring vibration | [77, 153, 155, 156] |
| 1696.23 ± 0.01 | - | 1697 | **Proteins:**<br>Amide I | - | [124] |
| 2830 ± 1 | - | 2817–2849 | **Lipids** | $CH_2$ symmetric stretch | [124] |
| 2853.1 ± 0.1 | 2852.08 ± 0.03 | 2855 | **Lipids**<br>**FAs** | $CH_2$, $CH_3$ symmetric stretch | [121, 124, 153, 273] |
| 2874.1 ± 0.3 | 2874.6 ± 0.2 | 2870 - 2875 | **Lipids**<br>**Proteins** | $CH_2$ asymmetric stretch,<br>$CH_3$ symmetric stretch | [124, 267, 273] |
| 2900 ± 1 | - | 2900 | **Lipids**<br>**Proteins** | CH stretch | [124] |
| - | 2926.6 ± 0.7 | 2929 | **Lipids**<br>**Proteins** | $CH_2$ asymmetric stretch,<br>Symmetric $CH_3$ stretch | [124, 153] |
| 2937.42 ± 0.05 | 2936.43 ± 0.04 | 2935 | **Lipids**<br>**Proteins** | Symmetrical $CH_2$ and $CH_3$ stretch | [124, 127, 267] |
| 2966.5 ± 0.1 | - | 2970 | **Lipids**<br>**FAs** | $CH_3$ asymmetric bond | [124] |
| 2980.8 ± 0.3 | 2977.8 ± 0.2 | 2973 | **Proteins** | Asymmetric $CH_3$ stretch | [124, 267] |
| 3061.5 ± 0.4 | 3064 ± 1 | 3067 | **Proteins** | C=C-H aromatic stretch | [248, 267] |

the bands at 756 $cm^{-1}$, 1077 $cm^{-1}$, 1172 $cm^{-1}$ and 1256 $cm^{-1}$ were found not to be present in the average Raman spectrum of *E. coli* interfaced with graphene. Furthermore, the bands at 1556 $cm^{-1}$ and 1696 $cm^{-1}$ appear in the spectra of *E. coli* interfaced with graphene but are not present in the control Raman spectrum of *E. coli* (Table 5.2). The band at 1256 $cm^{-1}$ was found to significantly decrease due to denaturing of proteins in *E. coli* cells from heat treatment at 121 °C [120]. Furthermore, the band at 1556 $cm^{-1}$ was also reported by Escoriza *et al.* to appear in the Raman spectra following heat treatment of *E. coli*, which was also attributed to denaturing of proteins at high temperature [120]. As discussed previously, graphene may have the ability to cause the denaturing of proteins due to defects in the sample, which act as an anchor for the proteins, according to simulations published by Gu *et al.* [57]. Specifically it was thought that the defects attract the charged residues of the proteins resulting in the proteins becoming anchored. The movement of the protein around the anchor results in unfolding [57]. Thus, the changes in this band and the other protein-dominant bands may be due to denaturing of proteins due to interaction with the defects in CVD graphene [120].

Various methods have been employed to investigate the denaturing of proteins in bacterial cells, for example, mass spectrometry and NMR [278, 279]. Such methods could be utilised to investigate the hypothesis suggested here that graphene could cause the denaturing of proteins in bacterial cells. This could also be further examined by extracting pure proteins from the bacterial cells and monitoring their evolution after being interfaced with graphene to determine changes to specific proteins.

In order to further analyse the changes in the Raman spectra of *E. coli* cultured with graphene and the control *E. coli* sample PCA was performed on the spectra. As only one replicate of the *E. coli* cultured with graphene was performed this will be compared against one *E. coli* replicate. Each data set consists of 55 individual Raman spectra.

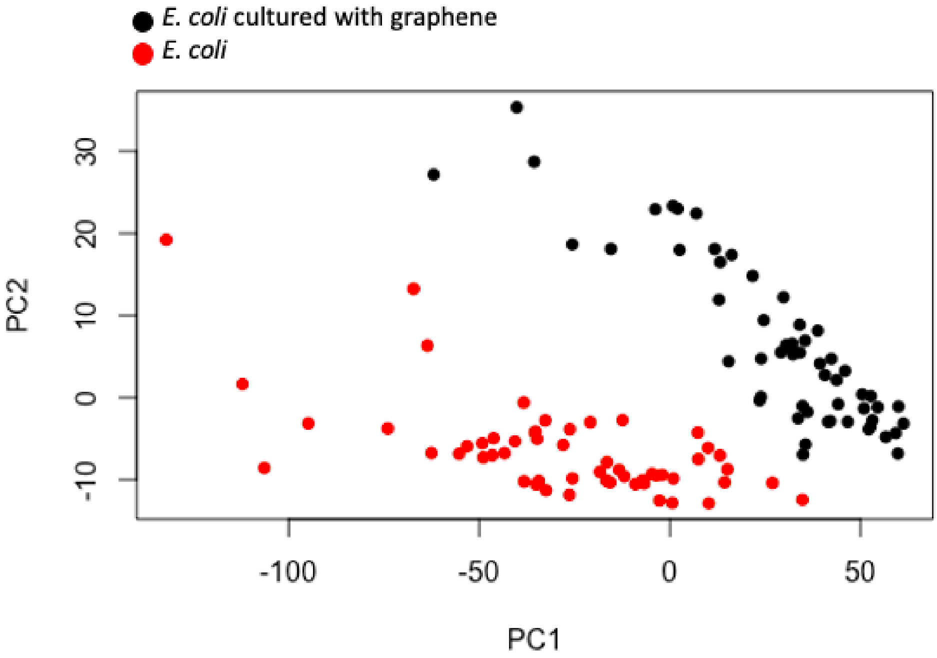

**Figure 5.8:** PCA results showing PC1 and PC2 results for *E. coli* compared with *E. coli* cultured on CVD graphene. There is separation of the two data sets along PC2 which represents 5.20 % of the total variance.

## 5.5 Analysis of the Raman spectra of *E. coli* cultured with CVD graphene

PCA was performed on the *E. coli* cultured with graphene spectra and the control of dried *E. coli* on $CaF_2$. The PCA results for the fingerprint region are shown in Figure 5.8. There is separation along PC2 which represents 5.20 % of the total variance of the data. The corresponding loading is shown Figure 5.9, the spectral features causing separation are labelled. The data did not separate along any other PC. There is noticeable scatter of the samples in PCA space, likely to be representative of the heterogeneous changes during the cell death process of the *E. coli.*

The bands representative of RNA/ DNA, located at 722 $cm^{-1}$, 808 $cm^{-1}$, 1122 $cm^{-1}$, 1237 $cm^{-1}$ and 1480 $cm^{-1}$ were found to change according to PCA results (Fig. 5.8). The changes in the RNA/ DNA are suggestive of a change in the metabolic processes of the cells [77, 120, 121]. For instance, the band at 722 $cm^{-1}$ in the Raman spectra of *E. coli* has been reported to decrease in relative intensity at the

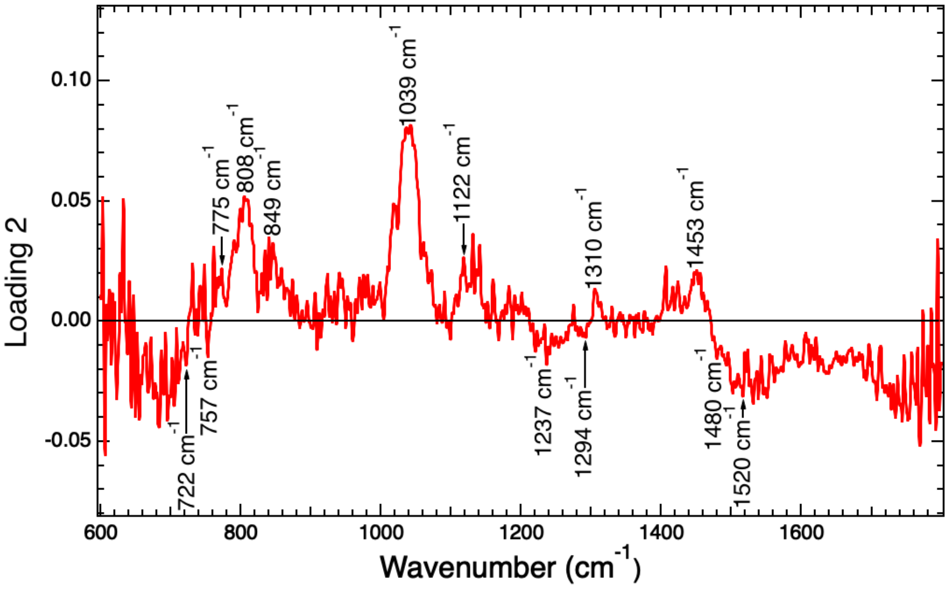

**Figure 5.9:** The corresponding loading for the PCA results of *E. coli* compared with *E. coli* cultured with CVD graphene. The data separated along PC2 which represents 5.20 % of the total variance. The spectral components found to cause separation of the data are labelled.

same rate at which the cell loses viability, thus, may be a marker for the slowing and effective inhibition of cellular processes due to lethal conditions [120]. Therefore, the changes in the RNA/ DNA bands found in this work may be due to retardation of cell growth, i.e., the slowing of metabolic processes as a result of interaction with CVD graphene [120, 280]. These changes could be further monitored in future work using methods such as counting colony forming units or using live/dead assays to determine loss of cell viability [71, 74, 75]. Such methods could be performed at specified time points to determine the time taken for the cells to cease metabolic processes following initial interaction with graphene.

The band at 785 cm$^{-1}$, which also arises due to RNA/ DNA, was not found to change in the PCA results, however, within literature it has been reported to change due to altered metabolic processes of the bacterial cells due to cell death [77, 120, 124, 153, 155, 156]. Therefore, in order to further investigate the cause of the changes in the RNA/ DNA associated bands, PIR analysis was performed on the bands in the Raman spectra of *E. coli* compared with the Raman spectra of *E. coli* cultured with graphene (Fig. 5.10). The PIRs have been computed against the band at 1453 cm$^{-1}$ (proteins and RNA/ DNA), as this band is common to both spectra

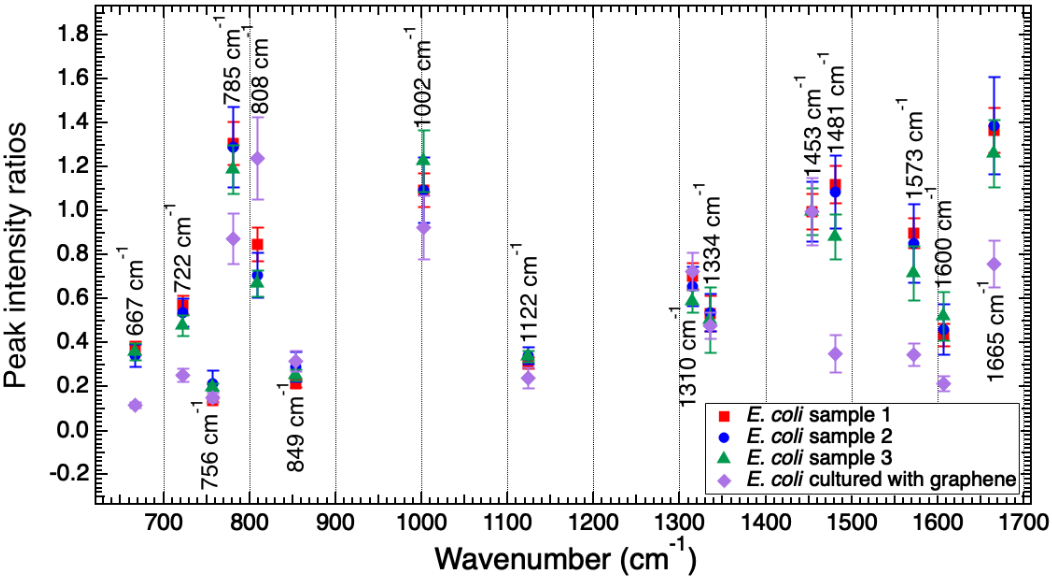

**Figure 5.10:** Peak intensity ratios (PIRs) for three *E. coli* replicates and one *E. coli* cultured on CVD graphene replicate. The PIRs have been calculated for the common bands in both spectra against the band at 1453 $\text{cm}^{-1}$ which is representative of proteins and RNA/ DNA [120, 121, 124, 155, 156]. This band has previously been used to monitor general cellular response to toxic substances and conditions in the literature [77, 119, 121].

(Table 5.2), and it has been utilised within literature to monitor general cellular response to toxic substances and conditions [77, 119, 120, 121, 124, 155, 156]. For instance, Zu *et al.* found that the relative intensity of the band increased following exposure to alcohol, 1-butanol, indicative of up-regulated metabolic process of the cell in response to the toxic conditions, [121]. In contrast, Teng *et al.* determined this band to undergo relative decreases in intensity correlating to slowing of physiological development of the cells due to interaction with ethanol [77]. Thus, changes in this band can provide insight into the overall metabolic alterations of the cells due to toxic conditions [77, 121].

The PIR graph is shown in Figure 5.10, from which it can be seen that the PIR $I_{785}/I_{1453}$ undergoes a relative decrease following interaction with graphene. This change in relative intensity is indicative of altered metabolic processes of the *E. coli* cells, and may specifically be demonstrating the slowing of cellular processes due to *E. coli* cell death by graphene [77, 120].

The PIR analysis also displays significant change for the RNA/ DNA bands in the Raman spectra. Specifically the decreases in the PIRs $I_{667}/I_{1453}$, $I_{722}/I_{1453}$, $I_{785}/I_{1453}$, $I_{1481}/I_{1453}$ and $I_{1573}/I_{1453}$, following interaction with graphene may be a result of slowing of the synthesis of nucleic acids in the cells, thus causing the slowing of cellular processes [77, 119]. The relative changes in the RNA/ DNA band at 1481 cm$^{-1}$, also found to vary according to PCA results (Fig. 5.8 & 5.9), has been reported in literature to decrease due to altered pace of cell growth resultant from toxic conditions, as reported by Teng *et al.* when investigating metabolic changes in *E. coli* due to interaction with ethanol [77].

Ethanol has been shown to cause the slowing of synthesis of nucleic acids, which results in the retardation of *E. coli* cell growth, as monitored through the incorporation of tritiated thymidine ($H^3$-TdR) into the DNA, which is widely used as tracker for DNA synthesis, and measuring the optical density [77, 281]. Thus, the relative changes in the RNA/ DNA associated bands according to the PIR analysis may be representative of slowing of cellular processes due to cell death by graphene [77, 119]. The incorporation of tritiated thymidine ($H^3$-TdR) into the DNA could also be utilised after interaction of the bacteria with graphene to track the DNA synthesis and conclude if the changes in these PIRs are in fact due to slowing of nucleic acid synthesis as hypothesised here.

The band at 1098 cm$^{-1}$, which arises due to the symmetric stretching of the phosphate bond in the DNA backbone, was also found to change according to PCA results (Fig. 5.8) [77, 124, 136, 155, 156]. This band is not present in the Raman spectra of *E. coli* cultured with graphene (Fig. 5.7). The disappearance of this band following interaction with graphene may be due to conformational changes of DNA, which has been noted to occur due to cell death [120, 123, 152]. The splitting of the bands representative of RNA/ DNA at 722 cm$^{-1}$ in the Raman spectra of *E. coli* into two bands at 717 cm$^{-1}$ and 727 cm$^{-1}$ in the spectra of *E. coli* cultured with graphene has not previously been reported on within literature, however, band splitting is further indication of conformational changes of the cells nucleic acids, and may be representative of a unique toxicity response of the cells to the antimicrobial CVD graphene [282]. Thus, the changes in these bands are suggestive of conformational changes of RNA/ DNA in the sample following interaction with graphene [120, 123, 152].

Furthermore, the bands at 808 $cm^{-1}$, 1098 $cm^{-1}$ and 1237 $cm^{-1}$ were found to vary according to PCA results due to interfacing of the cells with graphene (Fig. 5.8). Prominent changes in these DNA-associated bands have been reported in literature for the Raman spectra of bacteria due to DNA conformational changes as a result of freeze drying of bacterial cells [283]. Thus, the changes reported in this work for the DNA bands at 717 $cm^{-1}$, 727 $cm^{-1}$, 808 $cm^{-1}$, 1098 $cm^{-1}$ and 1237 $cm^{-1}$ may be due to conformational changes of the RNA/ DNA in the sample, and indicative of DNA degradation as a result of *E. coli* cell culturing with graphene [77, 119, 283]. Conformational changes of DNA has previously been investigated using AFM [284]. This could act as a complimentary tool for future work to specifically determine any conformational changes undergone by the RNA/DNA as a result of being interfaced with graphene.

According to the PCA results, ten of the twelve bands that were found to change in the Raman spectra of *E. coli* following interaction with graphene were attributable to proteins (Fig. 5.9). The changes of these bands may be due to protein inhibition, reported in published works to cause changes to the protein-related bands in the Raman spectra [77, 280]. Specifically, the bands at 1310 $cm^{-1}$ and 1480 $cm^{-1}$ have been reported to vary due to cell death by antibiotic amikacin [280]. This antibiotic is known to kill cells by inhibiting the synthesis of proteins in the cells, monitored through the fluorescence tracking [285]. Thus, the changes in the bands at 1310 $cm^{-1}$ and 1480 $cm^{-1}$ in this work due to interaction with graphene may be suggestive of inhibition of protein synthesis [280]. Such conformational changes could be confirmed by performing a similar fluorescence tracking of proteins in the bacterial cells after being interfaced with graphene, which would provide confirmation of the protein changes hypothesised in this work.

Changes in the protein bands at 808 $cm^{-1}$ and 849 $cm^{-1}$ in the Raman spectra of *E. coli* following interfacing with CVD graphene, according to PCA results (Fig. 5.9) is further suggestion of reduction in the synthesis of proteins in the *E. coli* cells [77, 286]. Variation in these bands has been previously reported within literature due to cell death by antibiotic kanamycin [77, 120], known to cause cell death by inhibition of protein synthesis by binding to the 30S ribosomal subunit of the bacteria, as analysed by nuclear magnetic resonance (NMR) [287, 288]. The PIR $I_{808}/I_{1453}$ also demonstrated significant increases in the Raman spectra of *E. coli* cultured with graphene (Fig. 5.10). Teng *et al.* specifically noted a relative increase in intensity of this band due to cell death by kanamycin [77].

Furthermore, the disappearance of the protein band at 1237 $cm^{-1}$ in the Raman spectrum of *E. coli* cultured with graphene is further suggestion of reduction in the synthesis of proteins in the *E. coli* cells [77, 286]. This band has been noted to undergo significant reduction in relative intensity due to cell death by heat treatment, as a result of conformational changes of proteins [120]. Thus the changes in the bands at 808 $cm^{-1}$ and 849 $cm^{-1}$ and the disappearance of the band at 1237 $cm^{-1}$ may be due to inhibition of protein synthesis and conformational changes due to interaction with graphene [77, 120].

To determine specifically the cause of the changes in the protein bands, additional methods could be employed, such as NMR spectroscopy for determination of conformational changes or inhibition of protein synthesis. This method was previously employed by Fourmy *et al.* when investigating such changes due to cell death by kanamycin [287], and could be utilised here in order to more definitively conclude the cause of the changes to the Raman bands of proteins reported in this work.

The lipid bands at 722 $cm^{-1}$, 775 $cm^{-1}$, 1294 $cm^{-1}$ and 1453 $cm^{-1}$ were also found to change according to PCA results (Fig. 5.9). The changes in these bands have been reported for cell death by starving, heat treatment, alcohol and antibiotics, ampicillin and penicillin [77, 120, 121, 152, 280]. The changes in these bands has been suggested to result from inhibition of the synthesis of the cell wall or alteration of the lipid bilayer of the cell [77, 120, 289]. Specifically, cell death by antibiotic ampicillin has been investigated using Raman spectroscopy and it has been found that the lipid bands at 1453 $cm^{-1}$ and 1237 $cm^{-1}$ were found to change as a result [77, 289]. The antibiotic ampicillin belongs to the beta-lactase family of antibiotics which has been reported to kill bacterial cells by inhibiting the synthesis of the cell well, according to radiolabeling and high-performance liquid chromatography (HPLC) [262]. Thus the changes in the lipid-related bands found in this work may

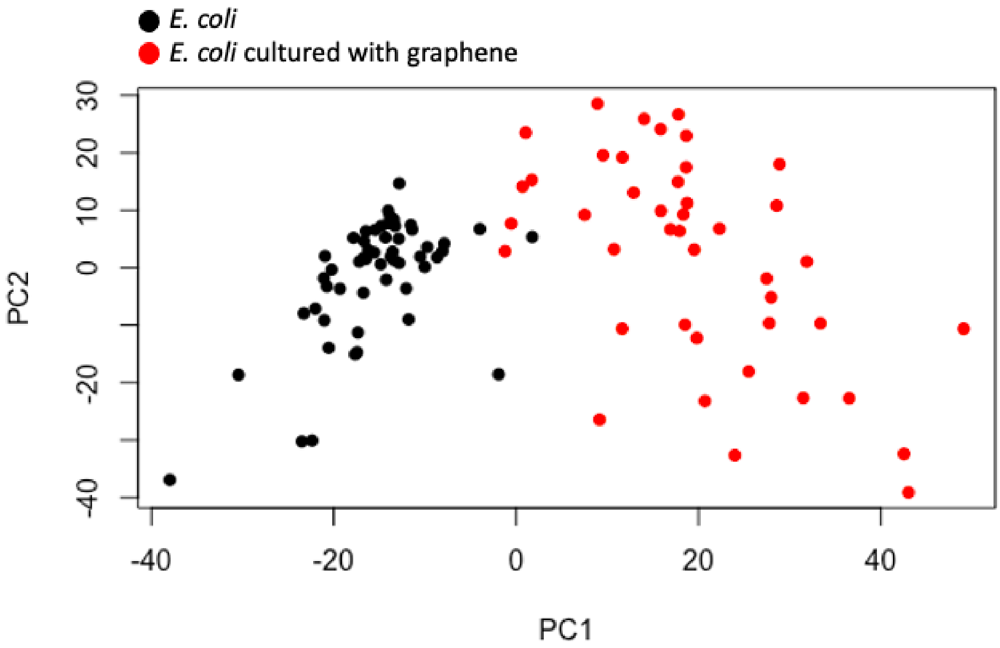

**Figure 5.11:** PCA results for the high wavenumber region (2800 $cm^{-1}$ - 3100 $cm^{-1}$) in the Raman spectra of *E. coli* compared with the Raman spectra of *E. coli* cultured with CVD graphene. The data separates along PC1 which represents 47.3 % of the variance.

be representative of inhibition of the cell wall due to interaction with graphene [77]. Radiolabeling and HPLC could also be utilised here to draw a solid conclusion into the specific cause of the alteration of the lipid bands after being in contact with graphene.

To further investigate the change in the lipids following culturing with graphene, it is essential to analyse the high wavenumber region of the Raman spectra as this is rich in lipid and protein signatures [126, 249]. The PCA results are shown in Figure 5.11, which separated along PC1. PC1 is representative of the maximum variance of the data, specifically 47.3 %. The corresponding loading is shown in Figure 5.12, with the spectral components which are causing separation labelled on the graph. All of the bands found to change in the high wavenumber region according to PCA are lipid - associated bands, suggesting significant changes in the lipid composition of the cells [121, 124, 127, 153, 267, 273].

The band at 2830 $cm^{-1}$, representative of lipids, was found to vary according to the PCA results (Fig. 5.12), it arises only in the spectra of *E. coli* cultured

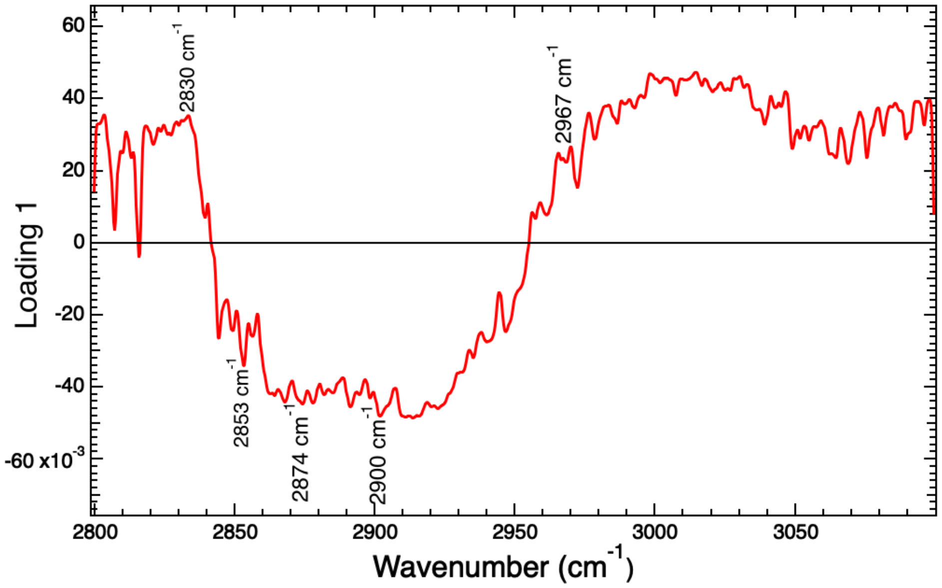

**Figure 5.12:** The corresponding loading for the PCA results of *E. coli* compared with *E. coli* cultured with CVD graphene. The data separated along PC1 which represents 47.3 % of the total variance. The spectral components found to cause separation of the data are labelled.

with graphene (Table 5.2). This band is prominent in the spectrum of saturated FA myristic acid [268]. Generally the phospholipids of *E. coli*, specifically K12 strain derivatives as studied in this work, contain only 0.5 to 2 % of myristic acid, however, increasing levels of myristic acid have been reported to be correlated to an increase in the degree of saturation of the FA composition of *E. coli* cells [178]. Therefore, the presence of the band at 2830 $\text{cm}^{-1}$ in the Raman spectra of *E. coli* cultured with graphene, may be due to increasing levels of saturation of the cells [178].

The band at 2967 $\text{cm}^{-1}$, found to change according to PCA results (Fig. 5.12), is not present in the *E. coli* spectrum and also arises only as a result of culturing with graphene (Table 5.2). Of ten different FAs investigated by Czamara *et al.* the band is present only in the spectrum of the saturated FA palmitic acid [268]. The amount of palmitic acid in *E. coli* cells has been shown to vary for different growth conditions [178, 179]. For example, the level of palmitic acid in *E. coli* was found to decrease to 16.4 % for growth at 10 °C compared with 33.1 % of the FA composition for growth at more optimal 37 °C [179]. This was due to the cells altering the level of saturation as a result of a decrease in temperature during growth [179]. Thus, the changes in the band at 2967 $\text{cm}^{-1}$, as seen by the PCA results (Fig. 5.11 &

5.12), is further indication of changing levels of saturation of the cell due to growth with CVD graphene [178, 268]. Further investigations could be performed using Raman spectroscopy to monitor these changes by interfacing the pure lipids with the graphene sample to determine the specific changes to lipids and FAs, such as palmitic acid. Additionally, the lipid and FA composition could be monitored before and after interfacing with graphene to determine specific increases in the level of saturation of the FA composition of the cell.

Both experiments of *E. coli* cultured with and interfaced with graphene have shown indications of changes in the level of saturation of the cells due to interaction with graphene. For instance, the *E. coli* interfaced with graphene spectra showed the emergence of the band at 3022 $\mathrm{cm}^{-1}$ (Table 5.1), which was suggestive of the presence of additional saturated FAs [126]. For the *E. coli* cultured with graphene the band at 2967 $\mathrm{cm}^{-1}$, also not present in the control Raman spectra of *E. coli*, may be due to changing levels of saturation of the cells [178, 268].

Alteration of cellular FA composition has previously been reported as a bacterial response to toxic conditions [290, 291]. For instance, the ratio of saturated to unsaturated FAs has been reported to decrease for the adaptation of *E. coli* to octanoic acid, which has been shown to cause *E. coli* cell death by disrupting the cell membrane [291, 292]. This change in the FA composition as a toxicity response may be due to the cellular alteration of membrane fluidity [291]. Therefore, the variation of the lipid-associated bands in the Raman spectra of *E. coli* interfaced and cultured with graphene may be indicative of a change in membrane fluidity, as a toxicity response of the cell [291]. Fluorescent membrane dyes have been shown to have the ability to assess the membrane fluidity of bacteria [293]. Such dyes could be utilised when interfacing the bacterial cells with graphene to further monitor the effect on membrane fluidity, and provide further information on the membrane changes.

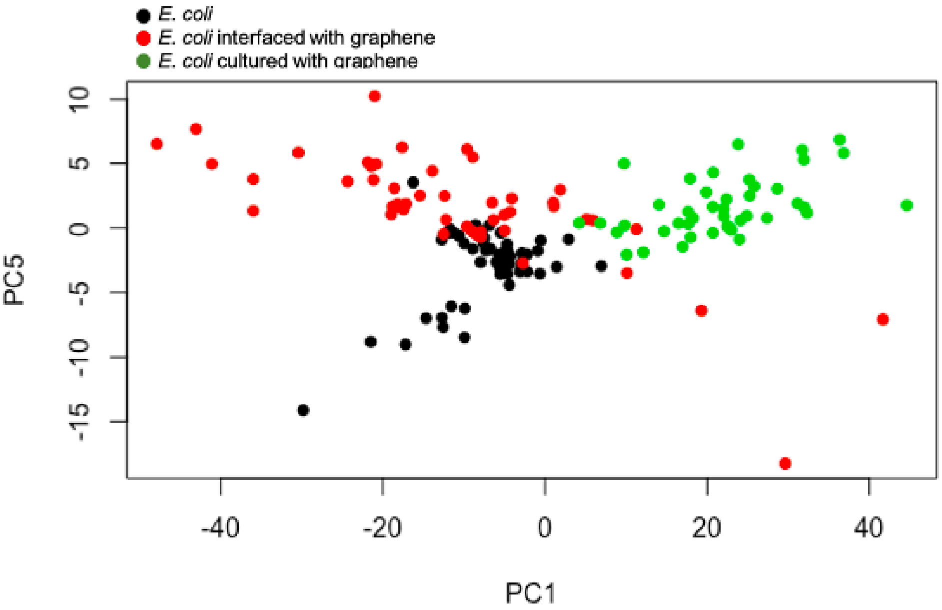

**Figure 5.13:** PCA results for the high wavenumber region (2800 cm$^{-1}$ - 3100 cm$^{-1}$) in the Raman spectra of *E. coli* compared with the Raman spectra of *E. coli* interfaced with CVD graphene and the Raman spectra of *E. coli* cultured with CVD graphene. The data separates along PC1 which represents 46.9 % of the variance. There is also separation along PC5, representative of 2.19 % of the variance.

## 5.6 Investigation of the differences between *E. coli* cultured with graphene and *E. coli* interfaced with graphene

In order to further investigate the difference between *E. coli* cultured with graphene and *E. coli* interfaced with graphene, analysis comparing the two will be presented. This is significant as it demonstrates how the cells react to the graphene in different conditions. For instance, for the cells interfaced with graphene, the *E. coli* are not in media and are undergoing the dessication process, thus the toxicity response will vary significantly compared with the *E. coli* cells cultured with graphene. The *E. coli* cultured with graphene may provide insight into whether the graphene killed the cells or simply hindered the cell processes, and eventually stopped cell growth.

PCA was performed to compare *E. coli* cultured with graphene and *E. coli* interfaced with graphene against the control *E. coli* sample. The PCA results showing

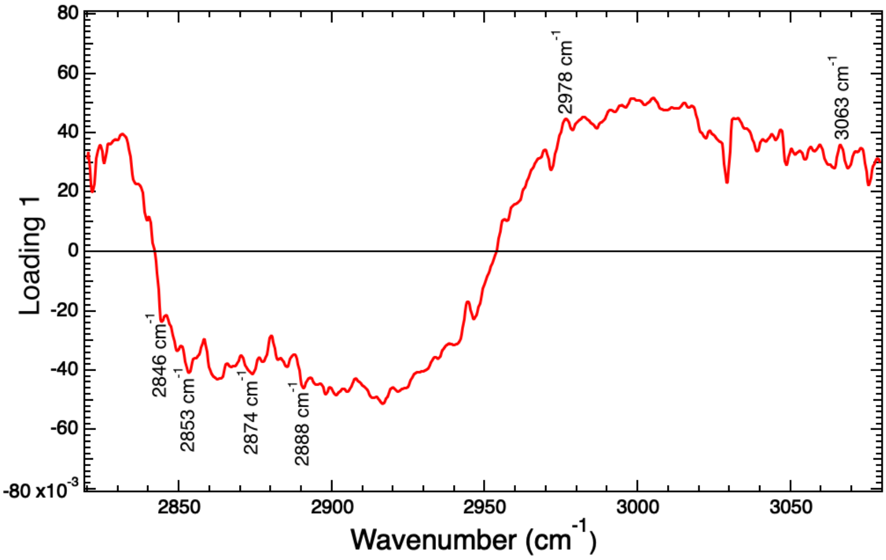

**Figure 5.14:** Loading one for the PCA results of Raman spectra of *E. coli* compared with the Raman spectra of *E. coli* interfaced with CVD graphene and the Raman spectra of *E. coli* cultured with CVD graphene. The data separates along PC1 which represents 46.9 % of the variance. The spectral components found to cause separation of the data are labelled.

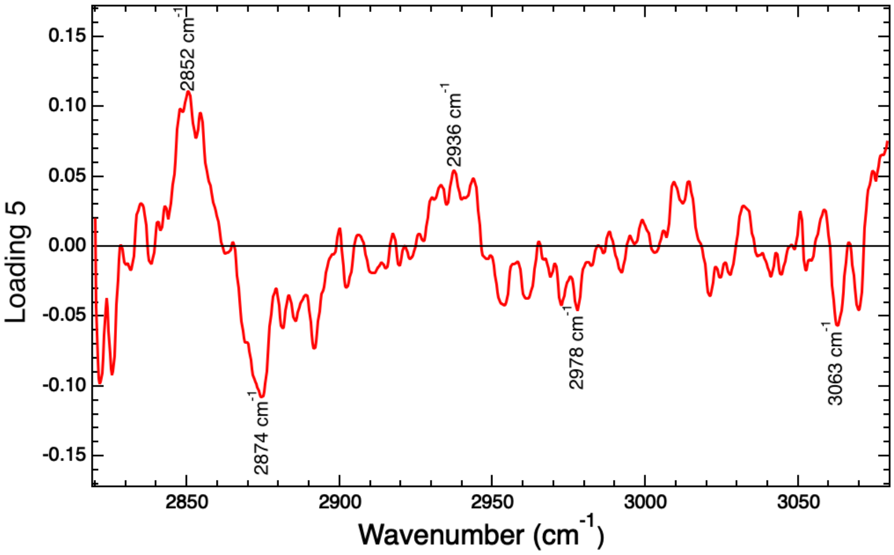

**Figure 5.15:** Loading five for the PCA results of Raman spectra of *E. coli* compared with the Raman spectra of *E. coli* interfaced with CVD graphene and the Raman spectra of *E. coli* cultured with CVD graphene. The data separates along PC5 which represents 2.19 % of the variance. The spectral components found to cause separation of the data are labelled.

PC1 against PC5 is shown in Figure 5.13. There is separation along PC1 and PC5 which represent 46.9 % and 2.19 % of the variance respectively. The corresponding loading one and loading five are shown in Figures 5.14 and 5.15 which have the spectral features resulting in separation labelled. The *E. coli* cultured with graphene appears to be most distinctly separated from the other samples, which may be indicative of more fundamental changes in the cells. Both *E. coli* cultured with and interfaced with graphene display significant amounts of scatter in the PCA plot, which may be due to increased levels of heterogeneity in the samples as the cells adapt to the toxic conditions.

The PCA results indicate a few bands which appear only in one sample, for instance, the band at 2846 $cm^{-1}$ and 2888 $cm^{-1}$ are present only in the Raman spectra of *E. coli* interfaced with graphene (Fig. 5.14). This highlights the level of variation in the bands present in each spectra, suggestive of significant conformational changes of FAs [126]. The band at 2846 $cm^{-1}$ was found to appear in the spectra of *E. coli* interfaced with graphene due to splitting of the band at 2852 $cm^{-1}$ present in the Raman spectra of *E. coli*, further indicative of cellular conformation alterations following contact with graphene.

According to PCA results the band at 2874 $cm^{-1}$ causes variance between the three samples (Fig. 5.14 & 5.15). The convoluted lipid-protein band at 2874 $cm^{-1}$, which arises due to $CH_2$ and $CH_3$ stretching, is present in the Raman spectra of the *E. coli* sample, the interfaced sample and the cultured sample (Table 5.1 & 5.2) [124, 267, 273]. This band has been reported to change due to the preservation of saturated FAs, according to a report by Zu *et al.* when examining *E. coli* cell death by 1-butanol [121]. Thus, the change in this band according to PCA results may be representative of the preserved FAs in the cell, while the changes in other bands are indicative of increases in the level of saturation of the samples, for example, the arisal of the band 3022 $cm^{-1}$ due to C-H stretching of saturated FAs [121, 126]. Overall, this is suggestive of a higher level of saturation of the FAs of the cells compared with *E. coli* spectra [121, 126]. Such findings could be further examined by interfacing specific lipids found to change in this work directly with graphene, to determine the specific changes the lipids undergo, or by utilising fluorescent dyes to

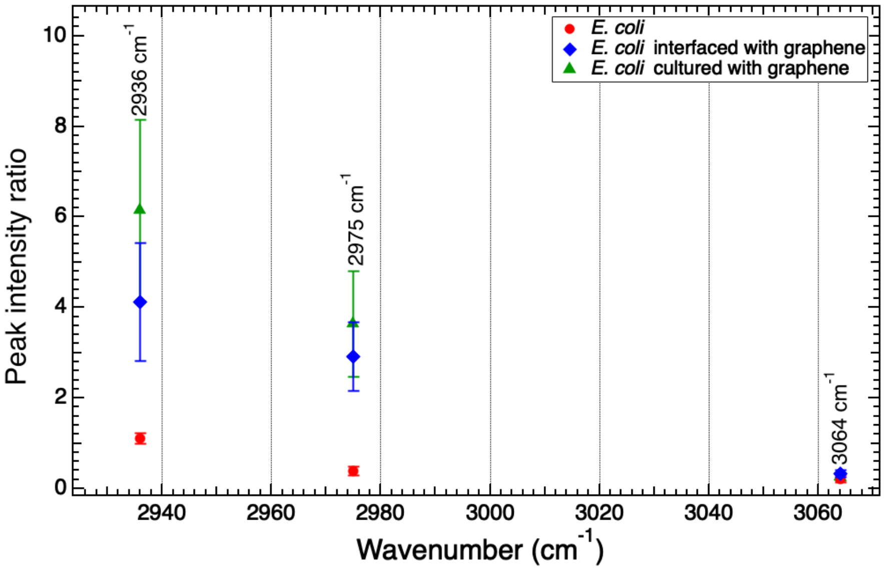

**Figure 5.16:** Peak intensity ratios for the average *E. coli* spectrum, *E. coli* interfaced with graphene spectrum and *E. coli* cultured with graphene spectrum against the band at 2874 cm$^{-1}$, representative of lipids and proteins [121, 124, 127]. Peak intensity ratios against this band have been utilised in literature for analysis of membrane fluidity of *E. coli* cells [121].

investigate changes in membrane fluidity after interaction with graphene [293].

In order to further investigate changes in the levels of saturation due to interaction with graphene, PIRs against the band at 2874 cm$^{-1}$ have been calculated for both interfaced and cultured samples. The PIR results, shown in Figure 5.16, are for the average of one biological replicate of each experiment, comprising 55 individual Raman spectra each. PIR analysis has previously been performed against the band at 2874 cm$^{-1}$ in literature to assess membrane fluidity [121, 294]. There are varying numbers of bands in the Raman spectra of each sample (Table 5.1 & 5.2), potentially due to differing conformational changes as a result of interaction with graphene, thus, only the bands common to more than one sample have been included in the PIR analysis, that is the convolved protein-lipid band at 2936 cm$^{-1}$, and the protein bands 2975 cm$^{-1}$ and 3064 cm$^{-1}$ [126].

Bands such as the protein-dominant band at 2925 cm$^{-1}$, present only in the *E. coli* spectrum, have not been considered. The reason for the disappearance in the interfaced and cultured Raman spectra of *E. coli* may be due to the inhibition of protein synthesis, something which has been found to occur for cell death by antibiotics and alcohols [77, 295]. It has also been reported that relative increases in the bands representative of lipids in the high wavenumber region could simultaneously result in significant decreases in relative protein bands, however, the reason for this connection is not understood [126]. Thus, the presence of the additional lipid bands at 2910 cm$^{-1}$, 3000 cm$^{-1}$ and 3022 cm$^{-1}$ for the *E. coli* interfaced with graphene spectra and the bands at 2900 cm$^{-1}$ and 2967 cm$^{-1}$ in the cultured Raman spectra may be causing a relative decrease in intensity of the protein-related bands, leading to the disappearance of the band at 2925 cm$^{-1}$ [126].

The PIRs for the two samples cultured and interfaced with graphene against the 2874 cm$^{-1}$ band are within error of one another, indicating similar changes in the relative intensity for bands in the high wavenumber region due to the different interactions with graphene (Fig. 5.16). This may be indicative of a specific toxicity response due to cell stress by graphene. The PIRs $I_{2936}/I_{2874}$ and $I_{2975}/I_{2874}$, however, show significant variation between the interfaced samples and the *E. coli* control sample. Despite this variation, both bands at 2936 cm$^{-1}$ and 2975 cm$^{-1}$ were not found to change in the PCA results (Fig. 5.14 & 5.15). This highlights the importance of analysis of spectral averages, in addition to individual spectra.

The band at 2975 cm$^{-1}$ arises due to asymmetric $CH_3$ stretching in proteins, while the 2936 cm$^{-1}$ band, representative of $CH_3$ stretching of proteins and symmetric $CH_2$ stretching of lipid signatures, is primarily a protein-dominant band (Chapter 4: Fig. 4.12) [249]. Therefore, the changes seen in both $I_{2936}/I_{2874}$ and $I_{2975}/I_{2874}$ suggest alterations in the cellular proteins. The band at 3064 cm$^{-1}$, also a protein band, was not found to change in the PIR analysis, however, this band was found to vary according to the PCA results comparing the three experiments (Fig. 5.14 & 5.15). The changes in these bands may be due to inhibition of proteins in the cells, a noted response of bacterial cell death [77, 295]. It may also be due to conformational changes of the proteins due to interaction with the defects of the CVD graphene sample. It has been simulated that defects in graphene can cause denaturing of proteins in eukaryotic cells, therefore, a similar process could be the cause of changes in the protein-related bands seen here [57].

In order to fully understand the changes in the proteins as a result of being interfaced with graphene and how this varies for defects in the sample, future work would entail interfacing proteins with graphene samples of various levels and types of defects. Specifically this would involve interfacing proteins with pristine graphene and comparing the changes of the same proteins with graphene samples with targeted defects, such as holes and grain boundaries. This would allow for determination of what defects are most detrimental to the proteins, and thus, the vitality of the bacteria.

The PIR $I_{2936}/I_{2874}$ demonstrated significant increases compared with the *E. coli* PIR (Fig. 5.16). The band at 2936 $cm^{-1}$ was also found to vary across the samples according to PCA (Fig. 5.15). This band has previously been found to increase as a result of variation in membrane fluidity [294]. Thus, the increase in the PIR $I_{2936}/I_{2874}$ and variation across samples according to PCA seen in this work may be attributable to changes in the fluidity of the membrane due to interaction with graphene, in agreement with the potential changes in the level of saturation of the FA composition of the cells [294]. Further work is required to understand the exact changes in the membrane composition after interaction with graphene. Specifically this could involve utilising fluorescent dyes to monitor changes in membrane fluidity and alterations in the saturation of FAs is the cells [293].

The PIR analysis and PCA presented here indicate significant changes in the lipid and FA composition of *E. coli* cells after being interfaced with graphene. Specifically, variation in the band locations in the high wavenumber region and the emergence of new bands following graphene interaction is suggestive of alteration of the level of saturation of the FA composition of the samples as a toxicity response [126]. Interestingly, differences in the bands were also seen when comparing *E. coli* interfaced with graphene and *E. coli* cultured with graphene. The changes in these spectra are indicative of differences in membrane fluidity of the cells, specifically due to different levels of saturation of the FA composition of the samples due to the stressful conditions of being in contact with graphene [126]. Such alterations in *E. coli* cells due to interfacing with graphene have not previously been investigated before using Raman spectroscopy, to the best of our knowledge. The cellular changes give an insight into the unique toxicity response of the cells to the graphene sample.

## 5.7 Conclusion

The work presented in this chapter investigates the biomolecular interactions of graphene and *E. coli* using Raman spectroscopy and presents findings which have not previously been reported within literature. Following both interfacing and culturing with CVD graphene the cells appear to undergo significant conformational changes reflected through the emergence of many new bands in the Raman spectra of both samples.

For instance, the bands at 2888 cm$^{-1}$, 2910 cm$^{-1}$ 3000 cm$^{-1}$ and 3022 cm$^{-1}$ were present as additional bands in the Raman spectra of *E. coli* interfaced with graphene compared with the control *E. coli* sample. Similarly, culturing with graphene resulted in the emergence of additional bands at 2830 cm$^{-1}$, 2900 cm$^{-1}$ and 2967 cm$^{-1}$ compared with the Raman spectra of *E. coli.* These different Raman spectra may be characteristic of conformational changes of the cells due to interaction with graphene.

Specifically, each of these additional bands in the spectra of both samples are associated with lipids and FAs, thus, this is indicative of significant perturbations to cellular lipids [124, 153, 268]. Furthermore, these differences in the Raman spectra of *E. coli* interfaced with graphene compared with *E. coli* presented here may be due to changes in the FA composition of the cell membrane as a result of the interaction with graphene. PCA results demonstrated variation in bands which may correlate to alterations in the level of saturation of the cells, representative of a toxicity response to graphene [121, 126].

For the Raman spectra of *E. coli* interfaced with graphene, the band at 3000 cm$^{-1}$ appears in the spectra, which has been reported to arise due to additional saturated FAs in the sample[268]. Furthermore, both additional bands at 2910 cm$^{-1}$ and 3022 cm$^{-1}$ are prominent bands in the Raman spectra of saturated FAs, and so are indicative of an increase in the level of saturation of the samples [126, 268].

The changes in the Raman spectra of *E. coli* cultured with graphene may also be due to increased levels of saturation of the FA composition of the cells [121, 126, 268]. The band at 2967 cm$^{-1}$ which arises only in the spectra following growth with graphene is representative of saturated FAs and is particularly prominent in the

Raman spectra of palmitic acid, which has been reported to vary in *E. coli* cells due to increasing levels of saturated FAs [178, 179].

Therefore the analysis of the lipid bands in the high wavenumber region of the Raman spectra in this work is suggestive of increases in the level of saturation of the cells due in interfacing with graphene, correlating to an increase in membrane fluidity of the cells as a result of interaction with graphene [121]. Further work could be performed to definitely determine if this is the cause of the band changes, for example, employing mass spectrometry for investigation of conformational changes of lipids and FAs in the bacterial cells.

Significant changes were also found for the protein bands in the high wavenumber region of the Raman spectra. PIR analysis showed changes in the protein dominant bands in the average Raman spectrum of *E. coli* interfaced with graphene compared with *E. coli.* The change in the PIR $I_{2936}/I_{2874}$ was suggestive of alteration of the membrane fluidity of the cells [294]. Perturbations to the protein bands in the high wavenumber were also potentially reflective of different conformational changes due to protein denaturing, which has been reported for interaction of proteins and defects in graphene in published works previously [57].

Changes were also found for the protein bands in the fingerprint region of the Raman spectra cultured with graphene. Specifically it was found that the bands at 1310 $cm^{-1}$ and 1480 $cm^{-1}$ changed due to culturing with graphene which may be attributable to inhibition of protein synthesis [280]. Further investigation of the changes of the proteins in the bands would be beneficial to determine the specific interaction of graphene and proteins in the cells.

Changes in the RNA/ DNA bands in the Raman spectra of *E. coli* cultured graphene were also found. Particularly for the band at 785 $cm^{-1}$, which displayed relative decrease in the PIR $I_{785}/I_{1453}$. This was suggestive of a slowing of the metabolic processes and growth of the cells due to culturing with graphene [77, 120]. Furthermore, the disappearance of the band at 1098 $cm^{-1}$ in the Raman spectra of *E. coli* interfaced with graphene, representative of symmetric stretching of the $PO_2$ phosphate bond in the DNA backbone, is suggestive of conformational changes of the DNA in the *E. coli* cells following interaction with graphene [120, 123, 152].

The work in this chapter provides a level of insight into the interactions of graphene and bacterial cells which has not been achieved in literature. The work presented in this chapter shows the excellent capability of Raman spectroscopy to understand the biomolecular mechanisms of cell interactions with toxic substances. With the aid of additional complementary tools to provide insight into the conformational cell changes following interaction with graphene, and further investigation of bacterial cells interfaced with graphene using Raman spectroscopy under different conditions, a full understanding into the interactions of cells with graphene. Future work would also include investigation of graphene interfaced with Gram positive bacteria to determine the difference interactions with the different bacteria.

# 6

# Conclusions and future work

This thesis successfully utilised Raman spectroscopy for analysis of the biomolecular interactions between graphene and *Escherichia coli* (*E. coli*). It was found that both culturing and interfacing of *E. coli*, may result in increased levels of saturated fatty acids (FAs) in the cells.

Specifically, the arisal of the bands at 2910 $\text{cm}^{-1}$, 3000 $\text{cm}^{-1}$ and 3022 $\text{cm}^{-1}$ in the Raman spectra of *E. coli* interfaced with graphene, which are representative of CH and $CH_3$ stretching of saturated FAs [124, 127]. In addition to the emergence of the bands at 2830 $\text{cm}^{-1}$ and 2966 $\text{cm}^{-1}$, attributable to $CH_2$ and CH stretching of lipids in the Raman spectra of *E. coli* cultured with graphene, which are particularly prominent bands in the Raman spectra of saturated FAs [178, 268]. The appearance of these bands only following interaction with CVD graphene is highly suggestive of increasing levels of saturation of the FA composition of the cells. The relative increases in the peak intensity ratio (PIR) $I_{2936}/I_{2874}$ due to contact with graphene is also suggestive of the cells altering their membrane fluidity as a toxicity response to the interaction with CVD graphene [121]. These findings are significant as they appear to be the first reports of the changes in the biochemical composition of bacterial cells due to interaction with CVD graphene.

The Raman spectra of *E. coli* cultured with graphene displays significant changes in protein-related bands, such as at 808 $\text{cm}^{-1}$ and 849 $\text{cm}^{-1}$, which may be due to inhibition of protein synthesis as a result of cell death by graphene [77]. Changes in the PIRs of the protein-related bands, specifically $\text{I}_{2936}/\text{I}_{2874}$ and $\text{I}_{2975}/\text{I}_{2874}$ may be a reflection of the denaturing of the proteins from interacting with the defects in graphene, as has been simulated within the literature [57]. Furthermore, the disappearance of the band at 1256 $\text{cm}^{-1}$ in the Raman spectra following interaction with graphene is consistent with reported denaturing of proteins after the cells underwent heat treatment [120]. Thus, this work reports conformational changes in the proteins in the *E. coli* cells in a step towards experimental understanding of the biomolecular interactions of graphene with cells.

The variation of the *E. coli* interfaced with graphene samples across the three biological replicates, as demonstrated through separation in principal component analysis (PCA), is suggestive of different toxicity responses of the cells due to the varying levels of defect of each graphene sample. The average defect induced PIRs $\text{I}_D/\text{I}_{G1} = 0.26 \pm 0.04$ and $\text{I}_D/\text{I}_{G2} = 0.15 \pm 0.02$ for the four graphene samples in this work, indicates a low level of defect in the graphene samples, likely to be due to grain boundaries, holes, rips and PMMA islands on the graphene surface from the formation process [197, 198, 218, 219]. Optical evidence also indicated the potential presence of such defects.

The defects in the samples were also shown to have a significant effect on the use of the PIR $\text{I}_{G'}/\text{I}_G$ for determination of the number of layers in a graphene sample. In this work, reduction in this PIR was found for increasing levels of defect across the samples, bringing into question the validity of the use of this marker in Raman analysis of CVD graphene. Specifically, a reduction from $\text{I}_{G'}/\text{I}_{G2} = 3 \pm 0.02$ representing an area of almost pristine graphene, to $\text{I}_{G'}/\text{I}_{G2} = 1.8 \pm 0.7$, for an area of moderately defected graphene. Further reduction to $\text{I}_{G'}/\text{I}_{G2} = 0.36 \pm 0.02$ was seen for an area of the sample representing highly defected graphene. The thorough analysis presented in this thesis demonstrates the need for system specific protocols due to the defects in the samples from the formation process.

Comparison of the CVD graphene samples in PCA space show extreme levels of heterogeneity both across and within graphene samples, with band shifts of up to 28 $\text{cm}^{-1}$ found across samples, and of up to 27 $\text{cm}^{-1}$ within samples. Such band shifts have not been reported before within a high quality graphene sample such as the CVD graphene samples investigated in this work. This shows the level of characterisation achieved in this work has unearthed serious issues with heterogeneity of the graphene samples, likely to be due to the grain boundaries, holes, rips and PMMA islands on the graphene surface, as well as potential bilayer islands in the sample [197, 198, 218, 219]. The repercussions of this for applications of graphene are unknown, and further investigation into the affect of this heterogeneity on interactions with cells is necessary. Furthermore, it is essential that similar levels of characterisation are performed across literature to ensure samples are properly represented by the spectral average. The convergence of the standard error (SE) and second order standard deviation (2SD) performed in this work acts as a robust method of determining the number of spectra necessary for proper characterisation of a sample to ensure reliability of data throughout published works.

This work also demonstrated levels of characterisation of *E. coli* samples which have not previously been achieved before within literature. The convergence of the SE and 2SD presents a novel method of determining the level of characterisation achieved for a given number of spectra from a sample. Convergence was achieved for 165 Raman spectra across three biological replicates in this work.

PCA performed on the three *E. coli* replicates displayed variation across the samples which may be due to the natural variation of the biological samples and alterations of the cells due to the desiccation process [103, 253, 254, 255]. For instance, changes in the lipid bands at 722 $\text{cm}^{-1}$, 1453 $\text{cm}^{-1}$, 1665 $\text{cm}^{-1}$, 2852 $\text{cm}^{-1}$ and 2875 $\text{cm}^{-1}$ representative of the CH stretching modes may be a result of natural variation of LPS across *E. coli* samples [103]. While changes in the protein-related bands at 809 $\text{cm}^{-1}$, 854 $\text{cm}^{-1}$, 1002 $\text{cm}^{-1}$, 1040 $\text{cm}^{-1}$, and 1481 $\text{cm}^{-1}$, 2874 $\text{cm}^{-1}$

and 2936 $\mathrm{cm}^{-1}$ may be due to inhomogeneous conformational changes of the proteins due to the desiccation process [256, 260].

The PIR analysis of the three samples demonstrated high reproducibility across the spectral averages, with separation shown for a few biomarkers, such as those at 757 $\mathrm{cm}^{-1}$ and 1002 $\mathrm{cm}^{-1}$ representative of proteins and C-C stretching of the aromatic ring of phenylalanine respectively [77, 124, 136, 153, 155, 156, 247]. These biomarkers indicate linked heterogeneity between proteins and nucleic acids in the samples, specifically due to changes in the PIRs $\mathrm{I}_{757}/\mathrm{I}_{781}$ and $\mathrm{I}_{1002}/\mathrm{I}_{781}$, where the band at 781 $\mathrm{cm}^{-1}$ arises due to RNA/ DNA [124]. No other PIRs showed separation against this band, thus, the variation in bands at 757 $\mathrm{cm}^{-1}$ and 1002 $\mathrm{cm}^{-1}$ display increased sensitivity to the heterogeneity in the sample. Thus, these bands may be specific biomarkers for monitoring the heterogeneity of biological samples. Investigation of the heterogeneity to this level does not appear to have been performed before within published works.

Overall, the levels of characterisation achieved in this work goes beyond what has previously been reported within literature. This resulted in significant levels of heterogeneity of both graphene and *E. coli* samples being uncovered. The level of analysis performed on the spectra in this thesis goes beyond other works, with multiple forms of analysis being utilised throughout, such as PCA, PIR analysis and band fittings for determination of band shifts and broadening. Furthermore, novel methods of investigation of the heterogeneity of Raman markers and bands were presented using convergence rate tests, which are a fast and definitive method of determining the heterogeneity of Raman markers. Additionally, new proposed methods for identification of the level of characterisation required for samples, in an attempt to ensure reliability of data, using convergence of the SE and 2SD were presented. These methods are applicable to different systems, and were utilised on both *E. coli* and CVD graphene. This work also appears to present the first findings of the biomolecular interactions of between CVD graphene and *E. coli*, laying the foundation for future and further analysis of the interactions of graphene and biological cells.

## 6.1 Future work

Future work will look to investigate how the levels of heterogeneity uncovered in the graphene samples in this work alter the mechanism via which the cells die. Further investigation into the heterogeneity of the graphene samples, and the potential changes in the interactions with cells is essential to fully understand the biomolecular interactions between the two. This work has provided a basis for the understanding, presenting knowledge which has not been reported before, however, more through analysis of the specific types of defect in the samples and the interactions with biological samples is necessary. This could potentially involve inducing certain types of defect into the graphene sample and investigating how the interactions vary compared with graphene samples containing different defects.

Further investigations of the changes in the bacterial cells due to interaction with graphene and the conformational changes of biomolecules which result from this, such as proteins, would provide further insight into the biomolecular interaction between the two. The changes in the bands seen in this work are suggestive of significant conformational changes of the cells, specifically proteins and lipids, and utilising Raman spectroscopy alongside other complementary tools, such as nuclear magnetic resonance, could allow further and more through investigation of these changes, specifically for investigation of the conformational alterations of the cells.

Characterisation of Gram positive bacteria should be performed using Raman spectroscopy, with an aim to compare the levels of heterogeneity of the Gram negative *E. coli* samples studied in this work, with the heterogeneity of Gram positive bacteria. It is also necessary to study the interactions of graphene and Gram positive bacteria, to fully understand the biomolecular mechanisms between graphene and bacteria. The different structure of the bacteria is likely to cause the interactions between the cells and graphene to vary accordingly, and the comparison against the changes in the Gram negative cells, as studied in this work, will give further insight into the mechanisms changing due to interaction with graphene.

It would be beneficial to perform Raman imaging to expand on the work presented in this thesis. This could be utilised to aid in the determination of the changes in the *E. coli* cells following interaction with graphene. By producing chemical images of the Raman data obtained from mapping, this could provide insight in the changes in distribution of biomolecules before and after cell death by graphene. This could give invaluable information about the heterogeneity of changes in the bacterial cells, and potentially provide insight into the biomolecules most affected by the interaction with graphene.

Raman imaging could also be applied for further anlaysis of the heterogeneity of graphene samples. Specifically, Raman imaging could be utilised to gain insight into the topography of the surface of the graphene samples. This would provide additional information about the potential presence and amount of residual PMMA on the sample surface. It would also allow thorough determination of the distribution of defects across the samples, and thus a robust comparison of the heterogeneity of the samples.

Additional future work for the characterisation of graphene will involve use of the novel convergence rate tests performed on the Raman spectra, alongside determination of the types of defects, for analysis of how different types of defect affect the heterogeneity of the samples. Consideration of other quantities within this context would allow for convergence rates to be achieved relating to certain types of defects in this sample. For instance, the application of strain to graphene samples causes significant shifts in the bands, thus, investigation of the SE of the locations of the bands in the samples using the convergence rate tests could provide insight into the resultant heterogeneity in the sample [207]. This novel method provides a potential automated tool for use in large scale characterisation and determination of the levels of heterogeneity of a sample.

The biocompatibility of graphene requires more thorough investigation, particularly due to the presence of such defects in the graphene samples and the resultant heterogeneity. Utilising Raman spectroscopy for investigation of the biomolecular interactions between graphene and mammalian cells would provide vital insight into the biocompatibility of CVD graphene. Such investigations are necessary for future applications of graphene in biomedical devices, particularly for applications which require close proximity to human cells. Thorough investigations of biocompatability will also be necessary for the application of graphene on medical equipment as proposed within this work.

# A

# Appendix

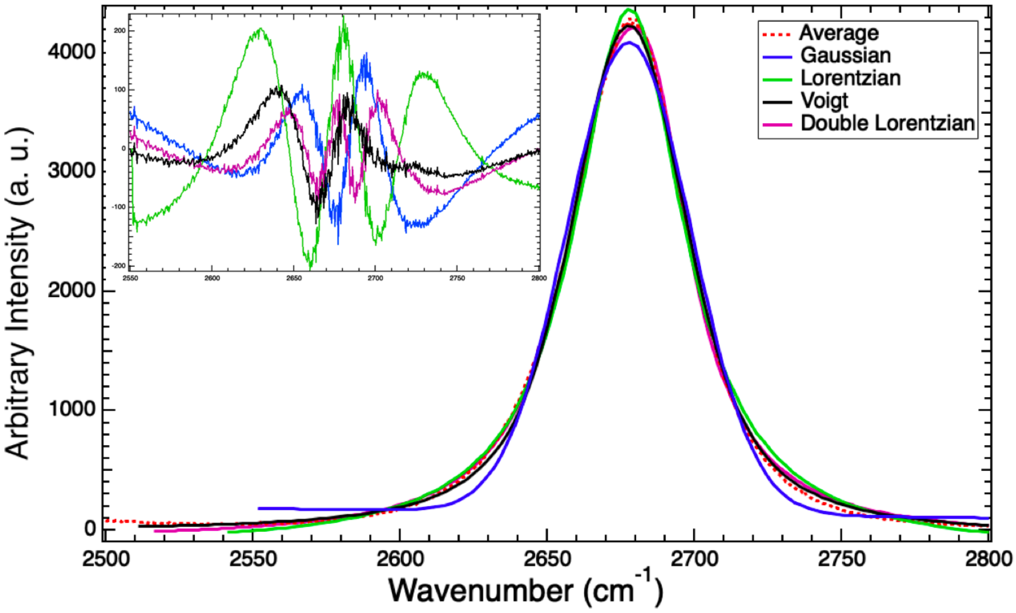

**Figure A.1:** Fittings of the G′-band in the average Raman spectrum of CVD graphene which comprises 100 individual Raman spectra. The fittings have been performed using a Gaussian, Lorentzian, Voigt and double Lorentzian model to determine which gives the most optimal fit. The inset shows the resultant residuals. In this case the double Lorentzian provides the most optimal fit for the data indicated by the smallest residual.

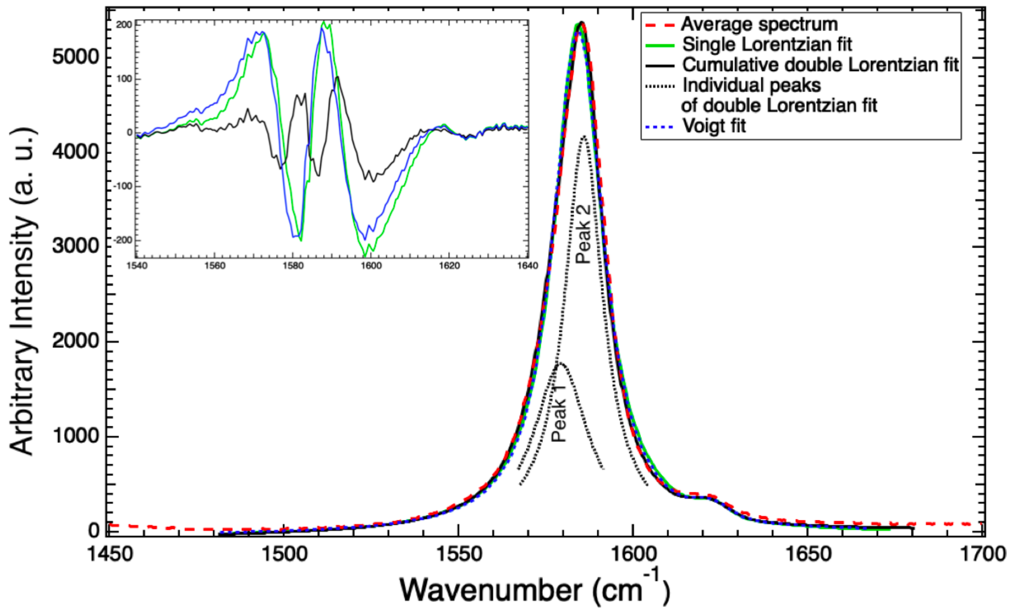

**(a)** Fittings of the G-band in the Raman spectra of CVD graphene using a single Lorentzian, a double Lorentzian and a Voigt model. Peak one and peak two are the peaks of the double Lorentzian fit corresponding to the $G_1$-band and $G_2$-band respectively, with the cumulative fit depicted using the solid black line. The inset shows the resultant residuals, the magnitude of which indicates goodness of fit.

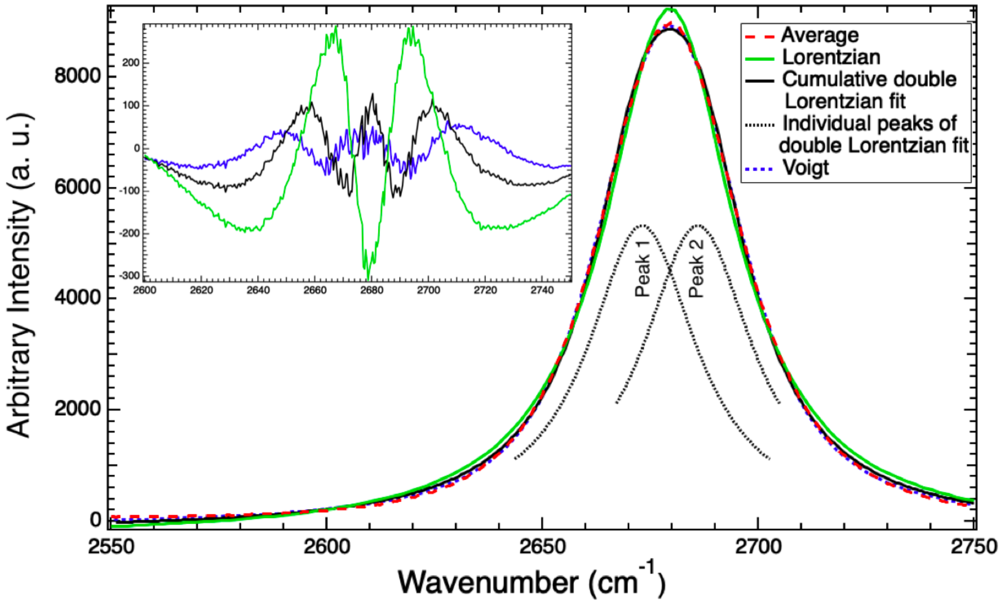

**(b)** Fittings of the G′-band in the Raman spectra of graphene using a single Lorentzian, a double Lorentzian and a Voigt model. Peak one and peak two are the peaks of the double Lorentzian fit, with the cumulative fit depicted using the solid black line. The inset shows the resultant residuals, the magnitude of which indicates goodness of fit.

**Figure A.2:** Deconvolution of the bands in the Raman spectra of graphene.

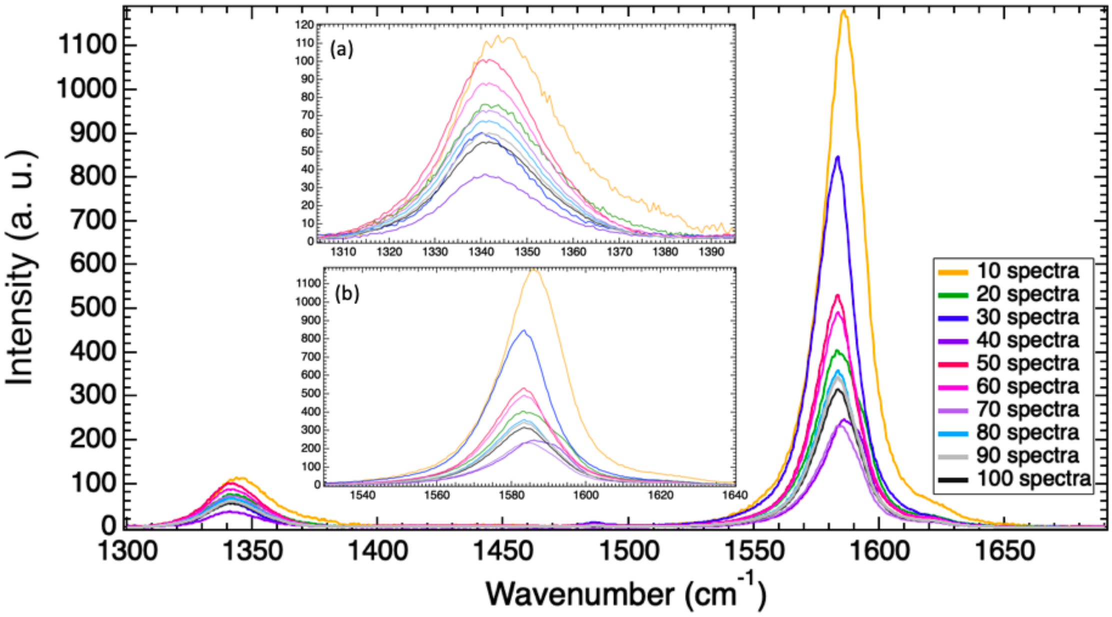

**(a)** SE convergence graphs of graphene sample two for the bands in the Raman spectra between the wavenumbers 1200 cm$^{-1}$ to 1800 cm$^{-1}$. The inset images are (a) a zoom in of the SE convergence of the D-band and (b) a zoom in of the SE convergence of the G- and D′-bands for increasing numbers of spectra in the average.

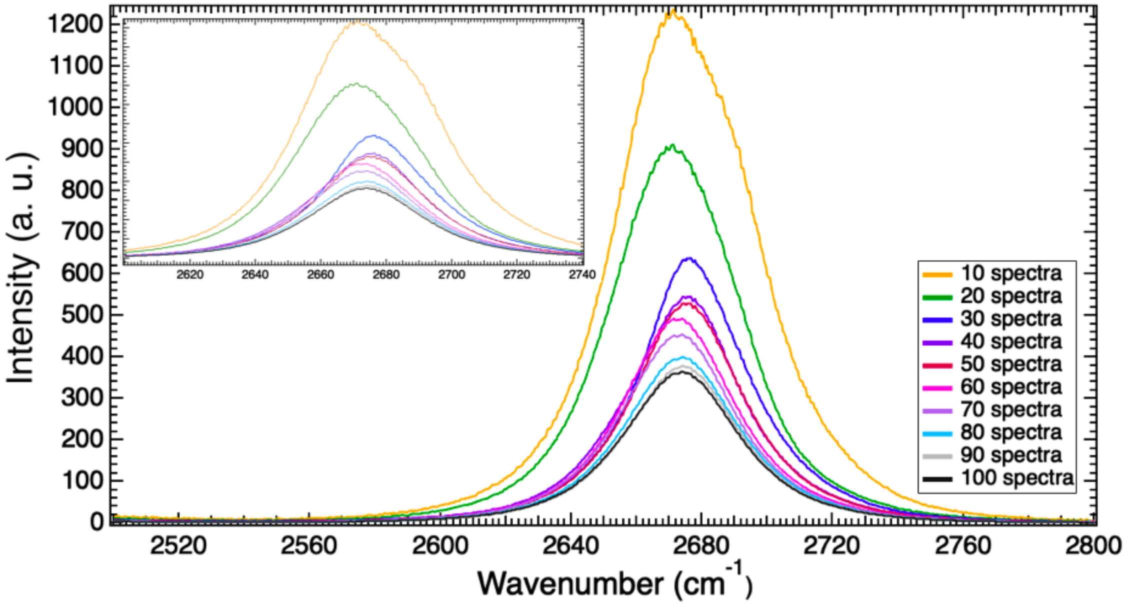

**(b)** SE convergence graphs of graphene sample two for the bands in the Raman spectra between the wavenumbers 2400 cm$^{-1}$ to 2800 cm$^{-1}$. The inset image is a zoom in of the SE convergence graphs of the G′-band.

**Figure A.3:** Standard error (SE) graphs for the Raman spectra of graphene sample two. The SE graphs are computed for increasing numbers of spectra in the spectral average.

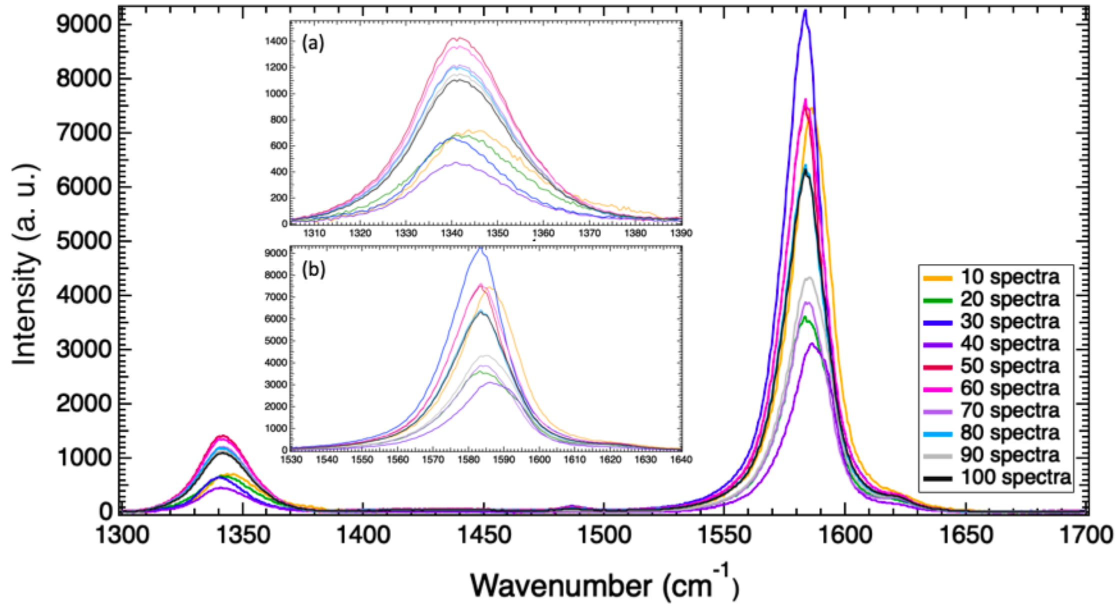

**(a)** 2SD convergence graphs of graphene sample two for the bands in the Raman spectra between the wavenumbers 1200 cm$^{-1}$ to 1800 cm$^{-1}$. The inset images are (a) a zoom in of the 2SD convergence of the D-band and (b) a zoom in of the 2SD convergence of the G- and D′-bands for increasing numbers of spectra in the average.

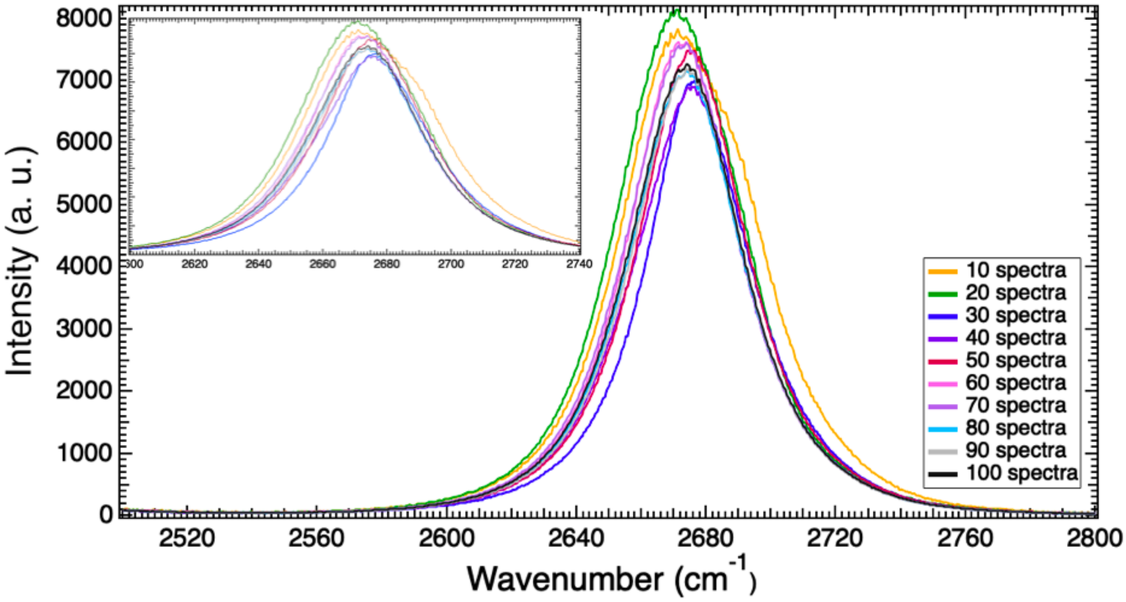

**(b)** 2SD convergence graphs of graphene sample two for the bands in the Raman spectra between the wavenumbers 2400 cm$^{-1}$ to 2800 cm$^{-1}$. The inset image is a zoom in of the 2SD convergence graphs of the G′-band.

**Figure A.4:** Second order standard deviation (2SD) graphs for the Raman spectra of graphene sample two. The 2SD graphs are computed for increasing numbers of spectra in the spectral average.

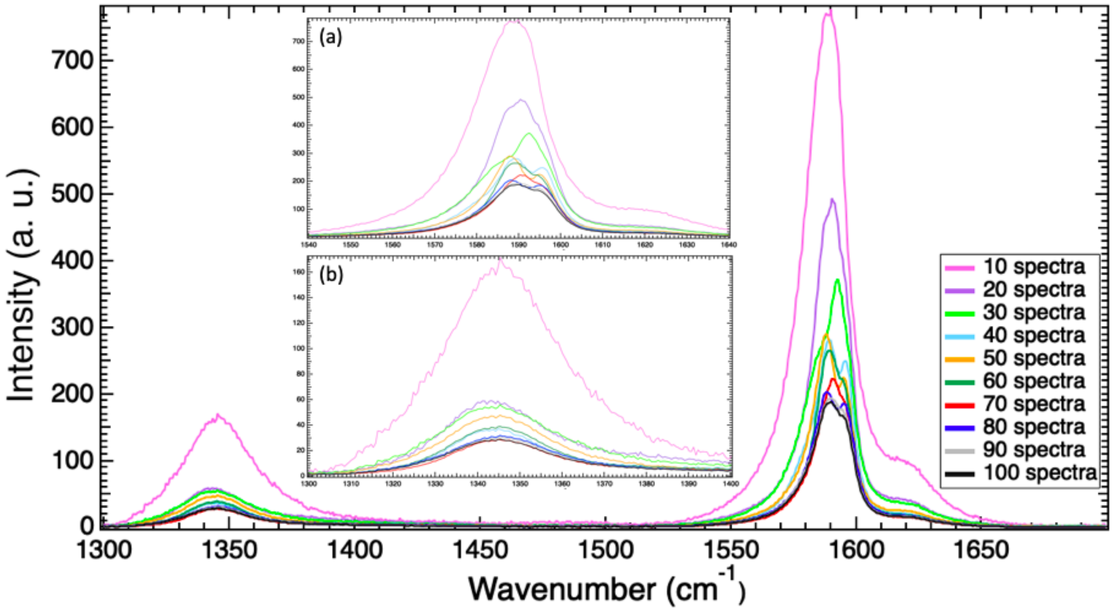

**(a)** SE convergence graphs of graphene sample three for the bands in the Raman spectra between the wavenumbers 1200 cm$^{-1}$ to 1800 cm$^{-1}$. The inset images are (a) a zoom in of the SE convergence of the G- and D′-bands and (b) a zoom in of the SE convergence of the D-band for increasing numbers of spectra in the average.

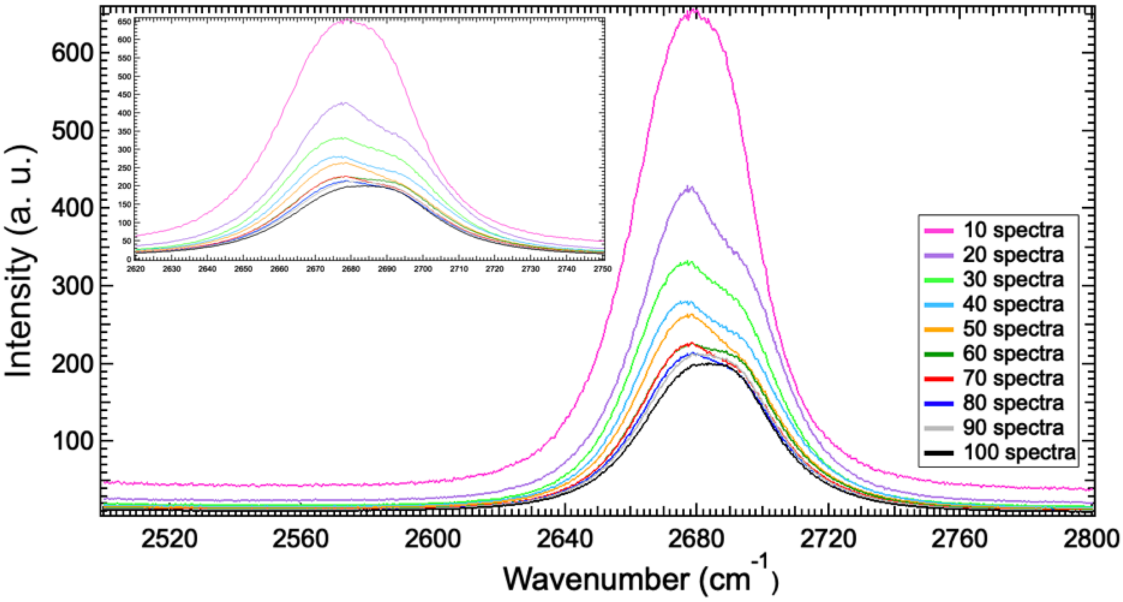

**(b)** SE convergence graphs of graphene sample three for the bands in the Raman spectra between the wavenumbers 2400 cm$^{-1}$ to 2800 cm$^{-1}$. The inset image is a zoom in of the SE convergence graphs of the G′-band.

**Figure A.5:** Standard error (SE) graphs for the Raman spectra of graphene sample three. The SE graphs are computed for increasing numbers of spectra in the spectral average.

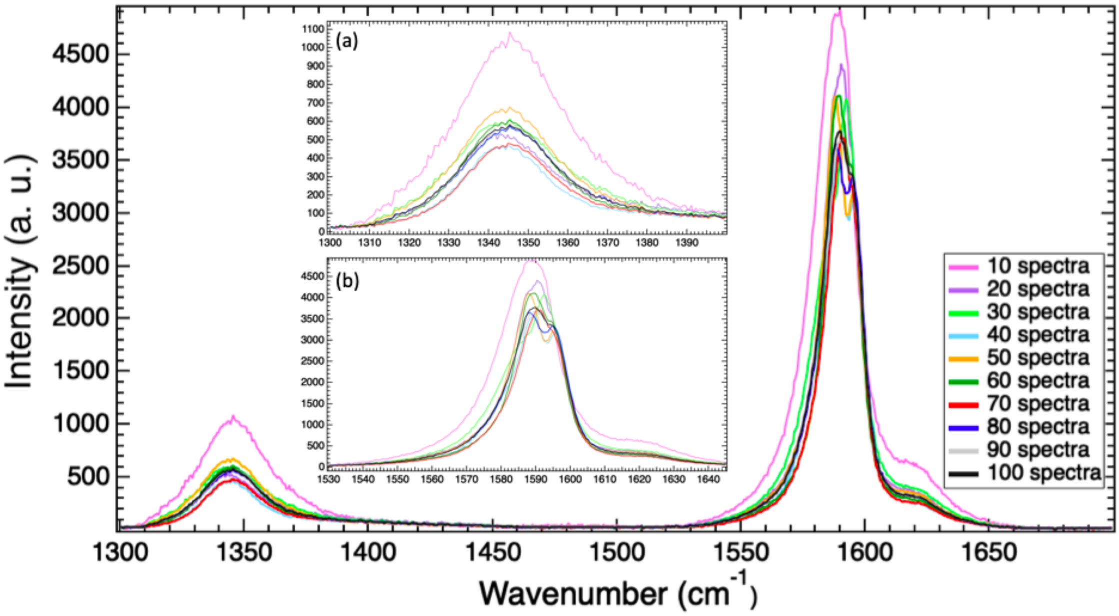

**(a)** 2SD convergence graphs of graphene sample three for the bands in the Raman spectra between the wavenumbers 1200 cm$^{-1}$ to 1800 cm$^{-1}$. The inset images are (a) a zoom in of the 2SD convergence of the D-band and (b) a zoom in of the 2SD convergence of the G- and D′-bands for increasing numbers of spectra in the average.

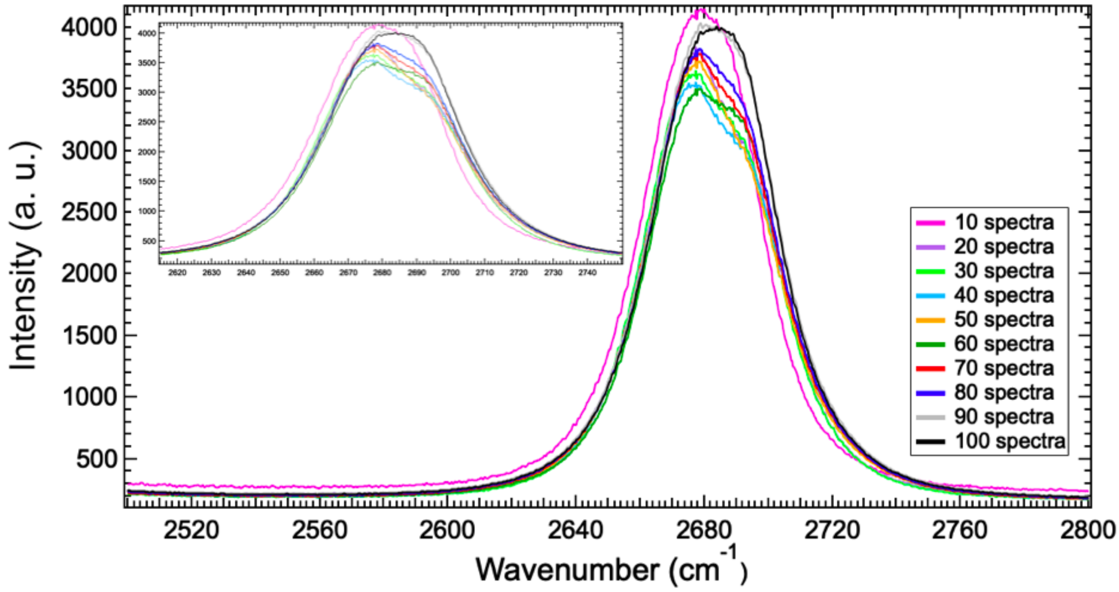

**(b)** 2SD convergence graphs of graphene sample three for the bands in the Raman spectra between the wavenumbers 2400 cm$^{-1}$ to 2800 cm$^{-1}$. The inset image is a zoom in of the 2SD convergence graphs of the G′-band.

**Figure A.6:** Second order standard deviation (2SD) graphs for the Raman spectra of graphene sample three. The 2SD graphs are computed for increasing numbers of spectra in the spectral average.

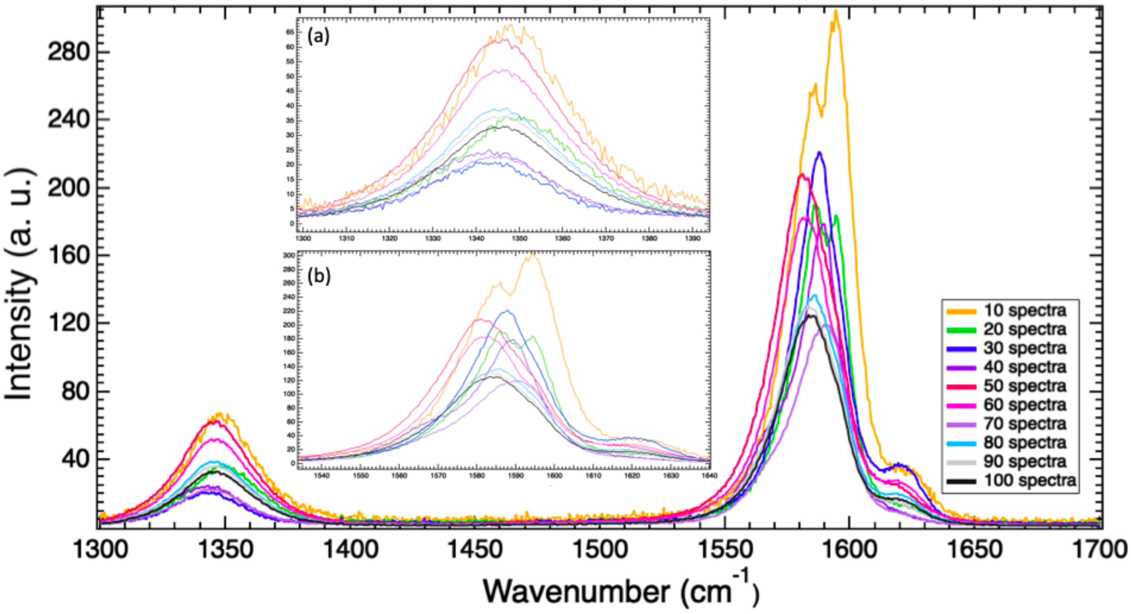

**(a)** SE convergence graphs of graphene sample four for the bands in the Raman spectra between the wavenumbers 1200 cm$^{-1}$ to 1800 cm$^{-1}$. The inset images are (a) a zoom in of the SE convergence of the D-band and (b) a zoom in of the SE convergence of the G- and D′-bands for increasing numbers of spectra in the average.

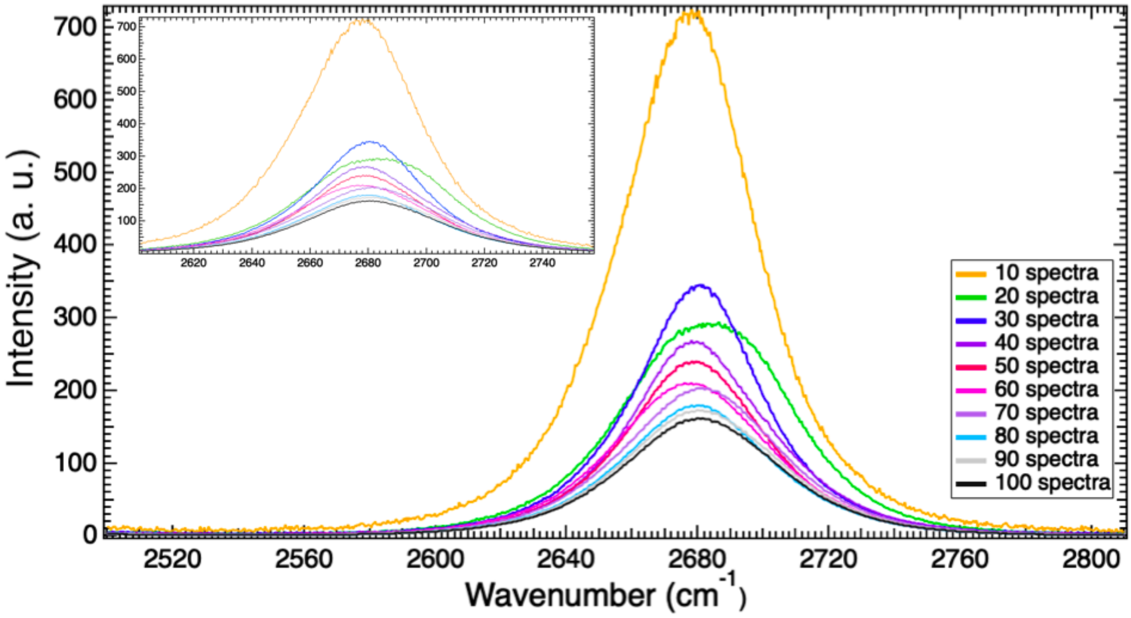

**(b)** SE convergence graphs of graphene sample four for the bands in the Raman spectra between the wavenumbers 2400 cm$^{-1}$ to 2800 cm$^{-1}$. The inset image is a zoom in of the SE convergence graphs of the G′-band.

**Figure A.7:** Standard error (SE) graphs for the Raman spectra of graphene sample four. The SE graphs are computed for increasing numbers of spectra in the spectral average.

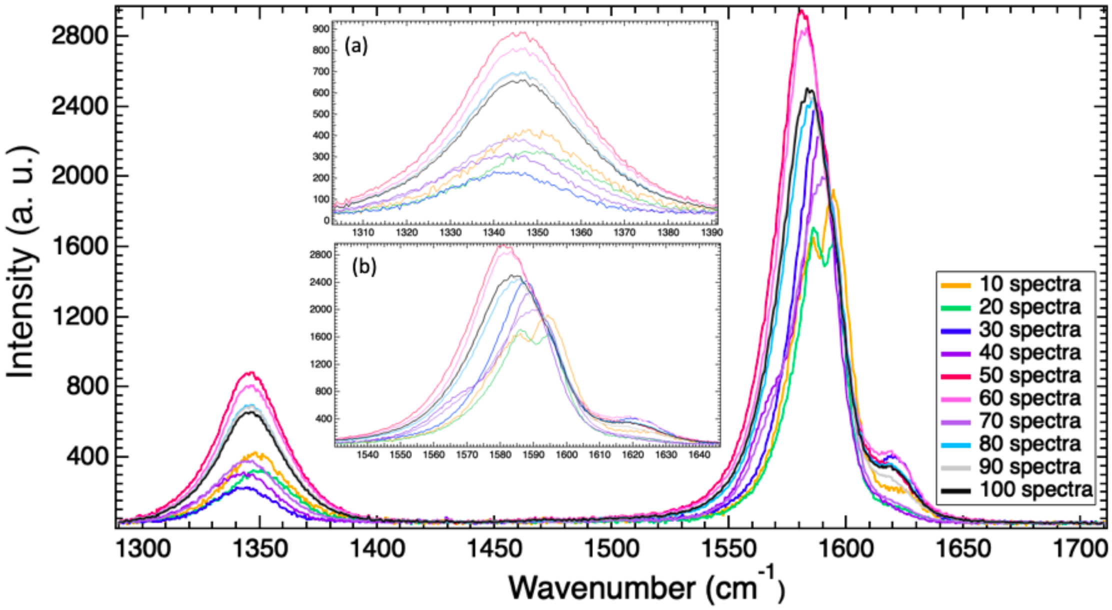

**(a)** 2SD convergence graphs of graphene sample four for the bands in the Raman spectra between the wavenumbers 1200 cm$^{-1}$ to 1800 cm$^{-1}$. The inset images are (a) a zoom in of the 2SD convergence of the D-band and (b) a zoom in of the 2SD convergence of the G- and D′-bands for increasing numbers of spectra in the average.

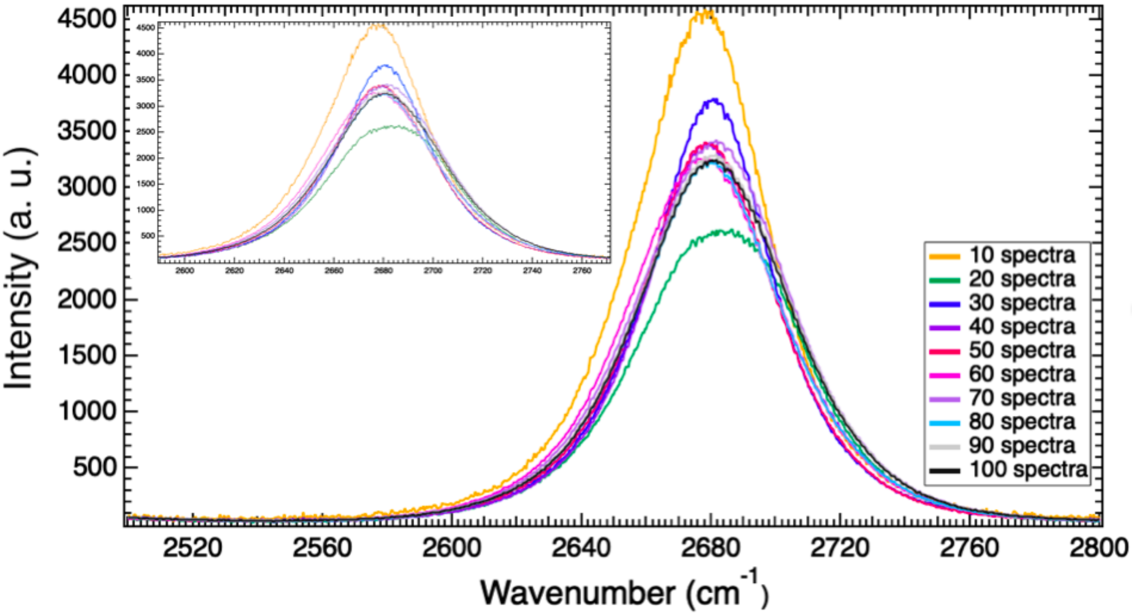

**(b)** 2SD convergence graphs of graphene sample four for the bands in the Raman spectra between the wavenumbers 2400 cm$^{-1}$ to 2800 cm$^{-1}$. The inset image is a zoom in of the 2SD convergence graphs of the G′-band.

**Figure A.8:** Second order standard deviation (2SD) graphs for the Raman spectra of graphene sample four. The 2SD graphs are computed for increasing numbers of spectra in the spectral average.

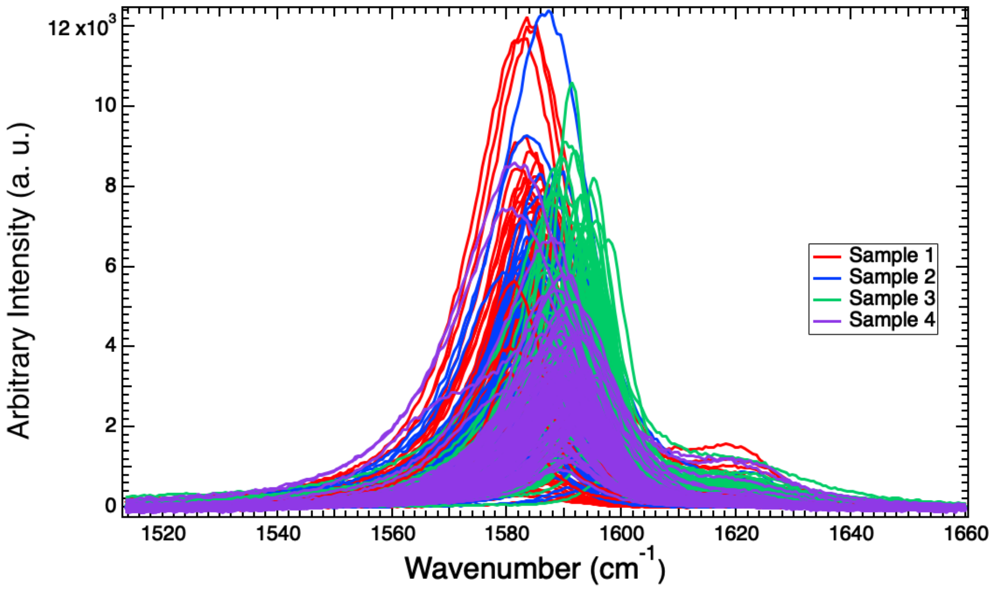

**Figure A.9:** The raw data of the G-band in the Raman spectra of graphene. All spectra collected across the four samples are included. Each sample is represented by 100 individual Raman spectra. The graph is zoomed to show the significant variation in the band locations, resulting in variation across the four graphene samples.

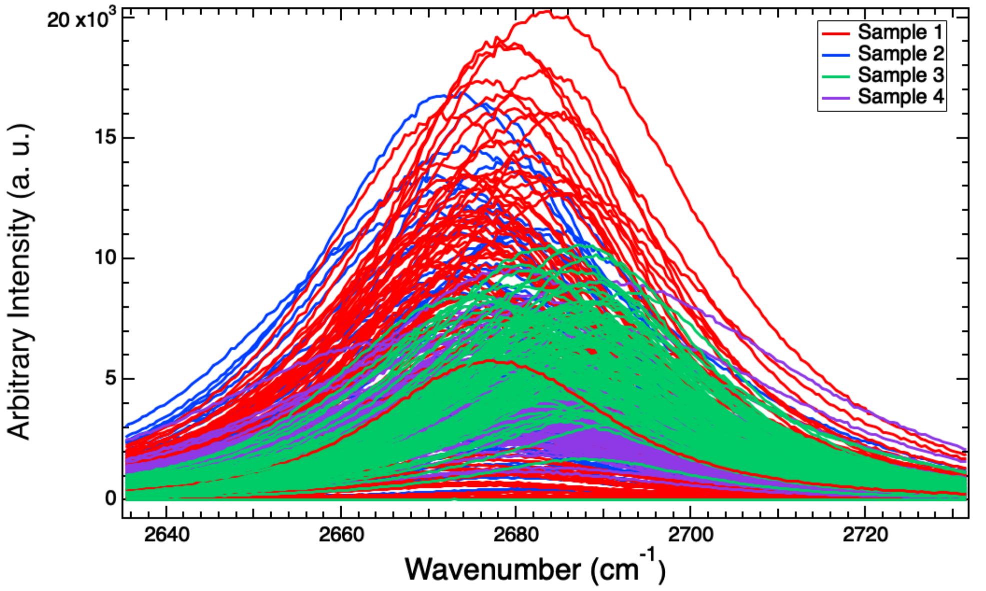

**Figure A.10:** The raw data of the G$'$-band in the Raman spectra of graphene. All spectra collected across the four samples are included. Each sample is represented by 100 individual Raman spectra. The graph is zoomed to show the significant variation in the band locations, resulting in variation across the four graphene samples.

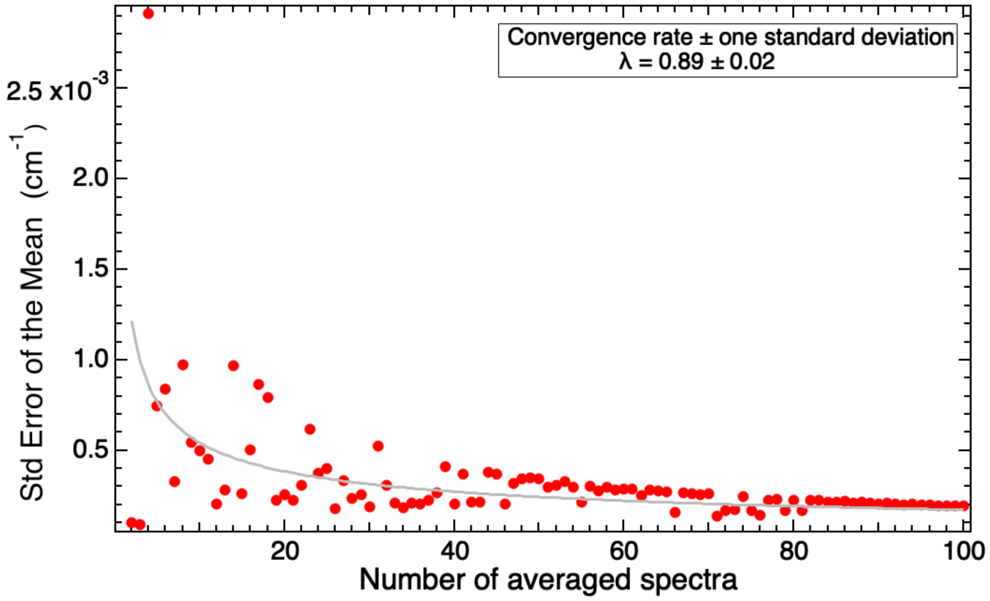

**Figure A.11:** Image showing the convergence of the standard error of the mean of the normalised amplitude of the D-band for increasing numbers of spectra in the spectral average for graphene sample 2. $\lambda$ represents the rate of convergence.

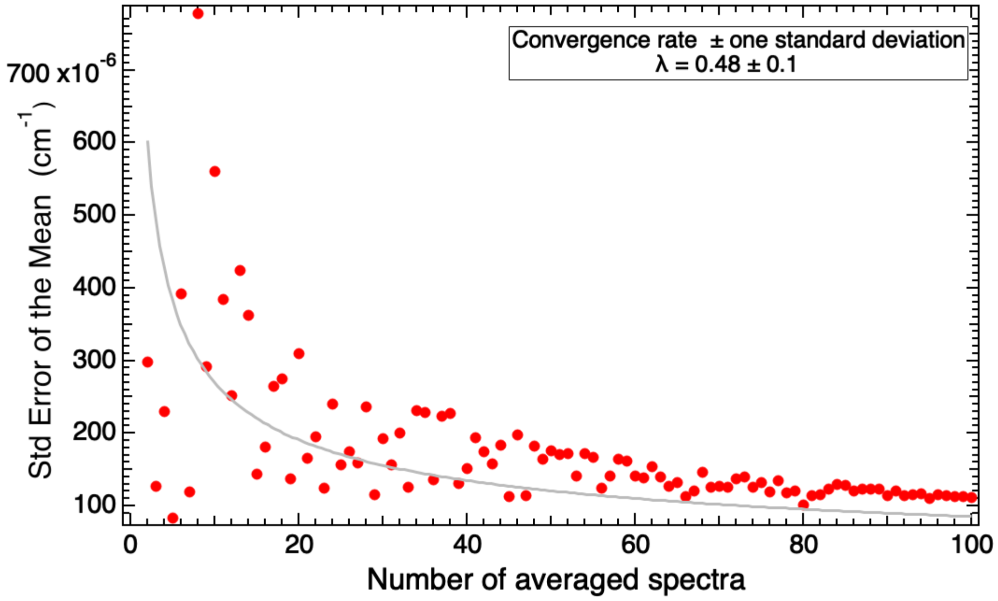

**Figure A.12:** Image showing the convergence of the standard error of the mean of the normalised amplitude of the D-band for increasing numbers of spectra in the spectral average for graphene sample 3. $\lambda$ represents the rate of convergence.

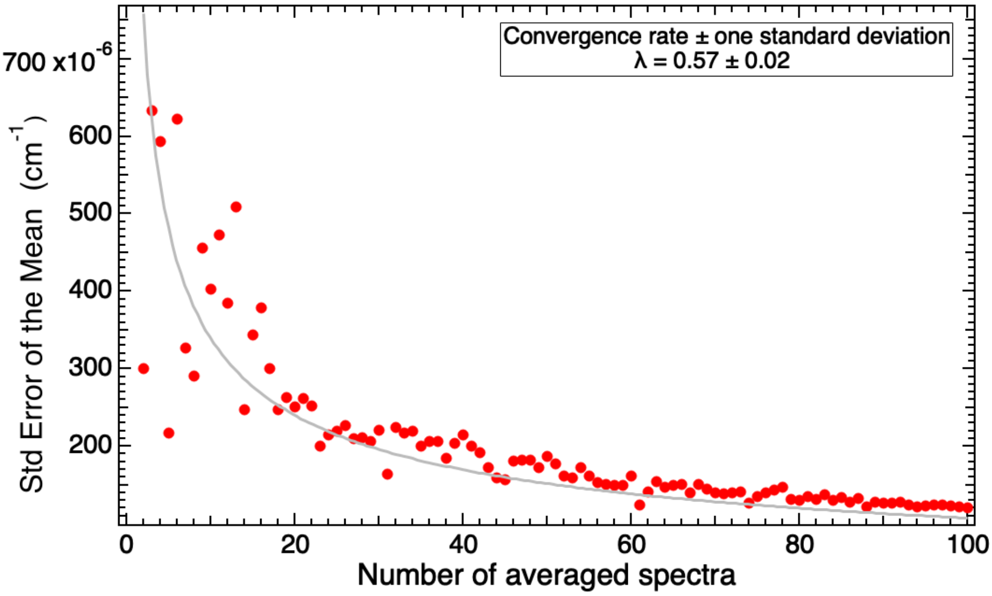

**Figure A.13:** Image showing the convergence of the standard error of the mean of the normalised amplitude of the D-band for increasing numbers of spectra in the spectral average for graphene sample 4. $\lambda$ represents the rate of convergence.

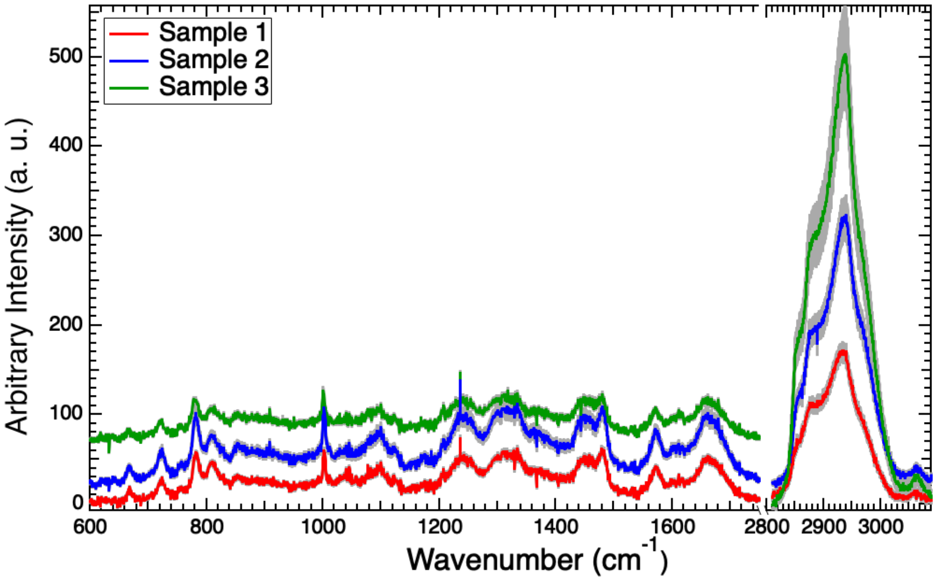

**Figure A.14:** Non-normalised averages of three *E. coli* samples corresponding to three biological replicates of the characterisation of *E. coli* using Raman spectroscopy. Each spectrum is an average of 55 individual Raman spectra collected from random points across each sample, representing both single bacterium and clumps of cells. The grey envelope is the SE of the mean. The spectra have been offset for clarity.

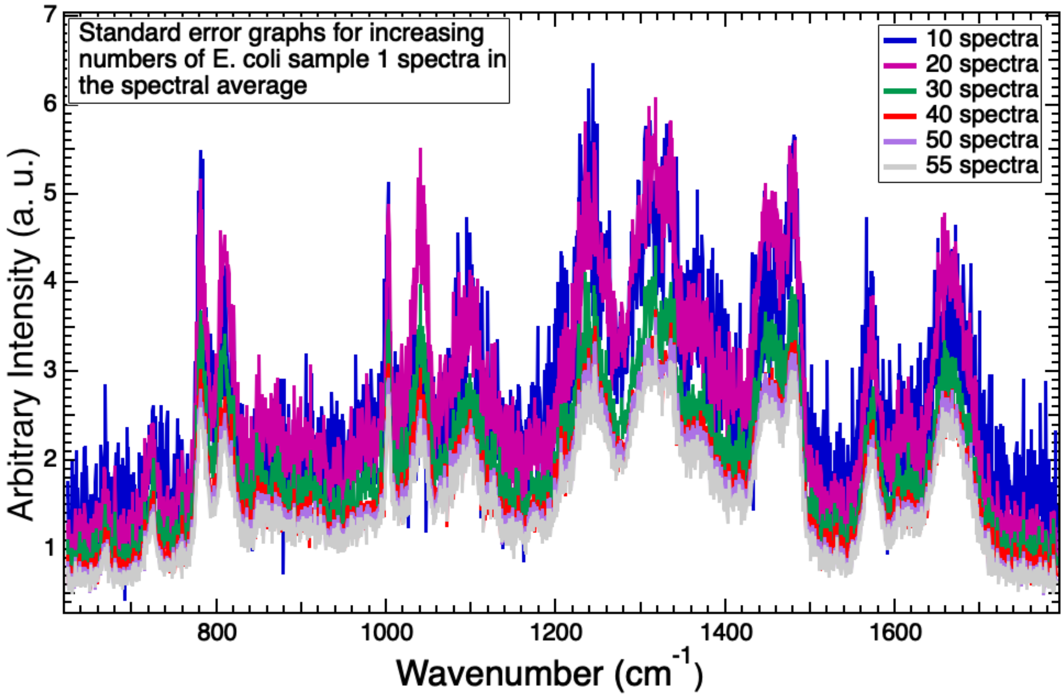

**(a)** SE convergence graphs of the Raman spectra of a single *E. coli* replicate between the wavenumbers 600 cm$^{-1}$ to 1800 cm$^{-1}$.

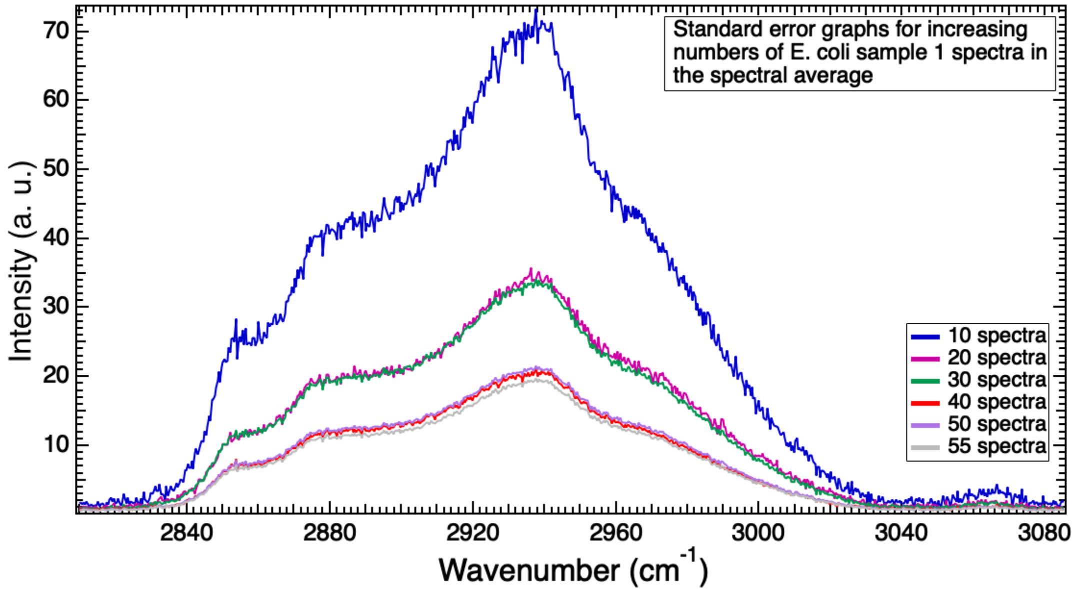

**(b)** SE convergence graphs of the Raman spectra of a single *E. coli* replicate between the wavenumbers 2800 cm$^{-1}$ to 3100 cm$^{-1}$.

**Figure A.15:** Standard error (SE) graphs for the Raman spectra of a single *E. coli* sample. The SE graphs are computed for increasing numbers of spectra in the spectral average up to the maximum 55 spectra for the data set.

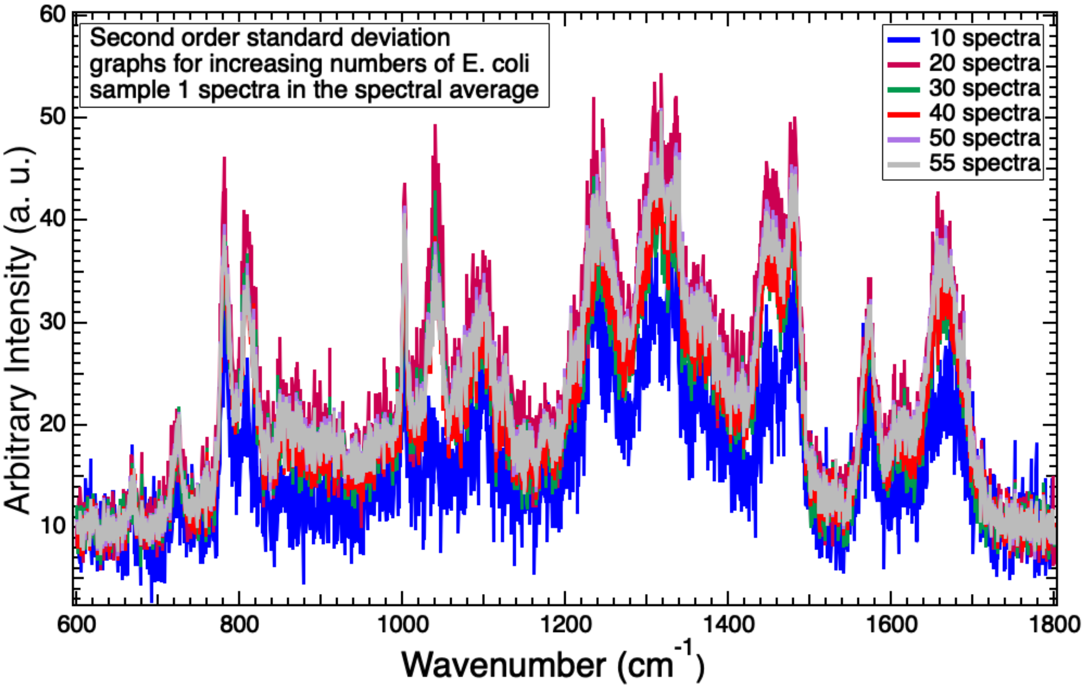

**(a)** 2SD convergence graphs of the Raman spectra of a single *E. coli* replicate between the wavenumbers 600 cm$^{-1}$ to 1800 cm$^{-1}$.

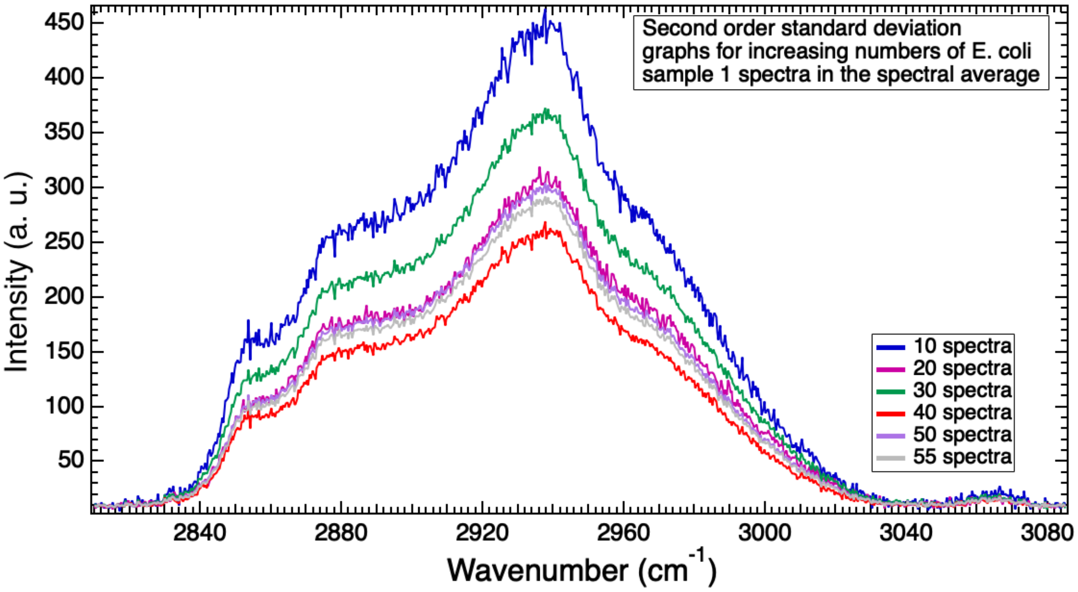

**(b)** 2SD convergence graphs of the Raman spectra of a single *E. coli* replicate between the wavenumbers 2800 cm$^{-1}$ to 3100 cm$^{-1}$.

**Figure A.16:** Second order standard deviation (2SD) graphs for the Raman spectra of a single *E. coli* sample. The 2SD graphs are computed for increasing numbers of spectra in the spectral average up to the maximum 55 spectra for the data set.

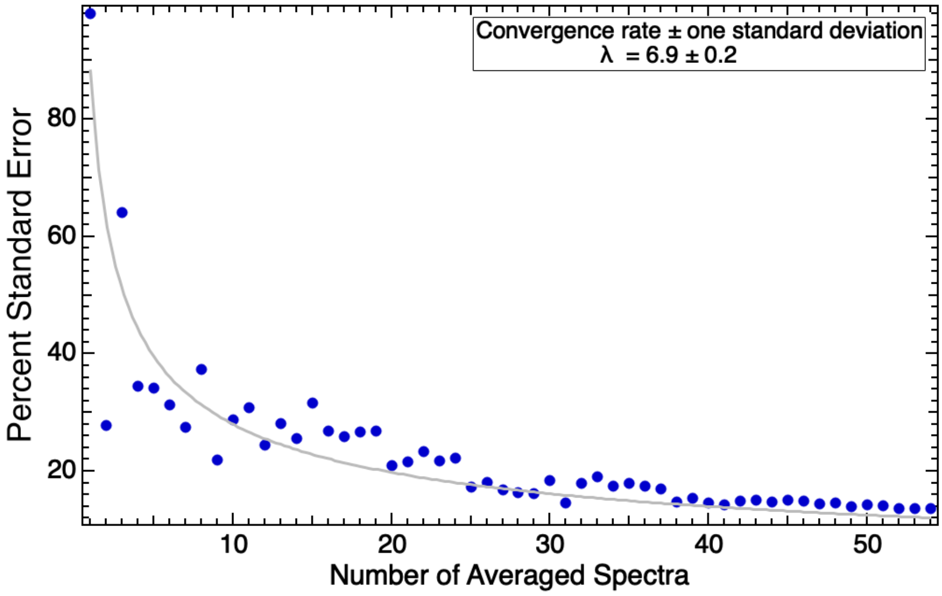

**Figure A.17:** Convergence of the percent SE of the PIR biomarker $I_{1453}/I_{781}$ for increasing numbers of spectra in the average spectrum of *E. coli* sample two. $\lambda$ is the rate of convergence which gives an indication of the level of heterogeneity of the biomarker for the sample.

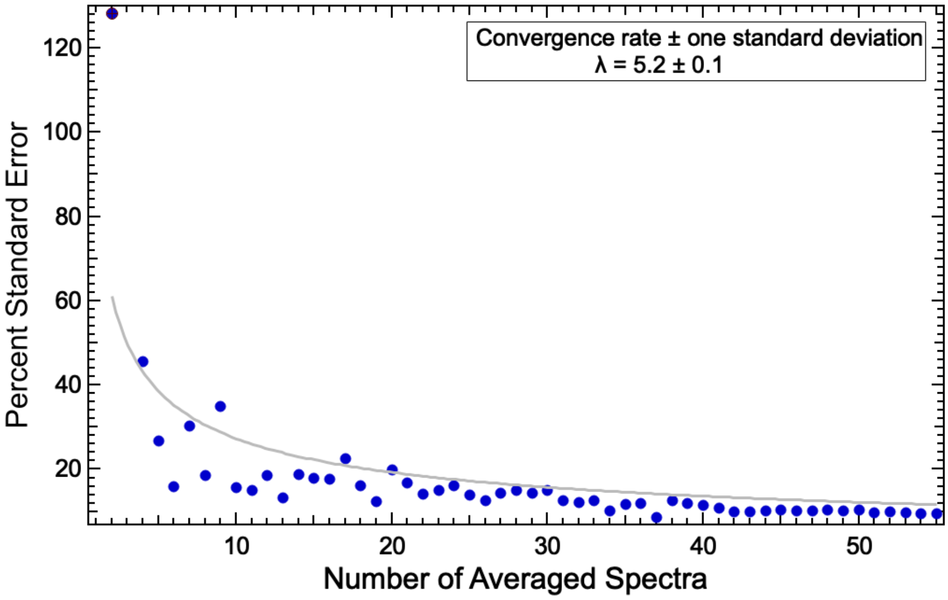

**Figure A.18:** Convergence of the percent SE of the PIR biomarker $I_{1453}/I_{781}$ for increasing numbers of spectra in the average spectrum of *E. coli* sample three. $\lambda$ is the rate of convergence which gives an indication of the level of heterogeneity of the biomarker for the sample.

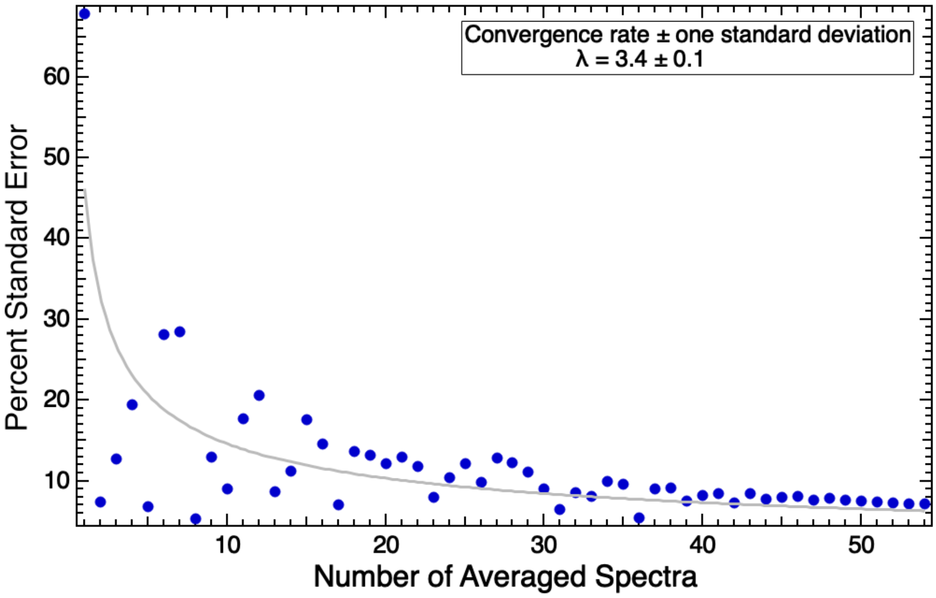

**Figure A.19:** Convergence of the percent SE of the PIR biomarker $I_{1453}/I_{1481}$ for increasing numbers of spectra in the average spectrum of *E. coli* sample one. $\lambda$ is the rate of convergence which gives an indication of the level of heterogeneity of the biomarker for the sample.

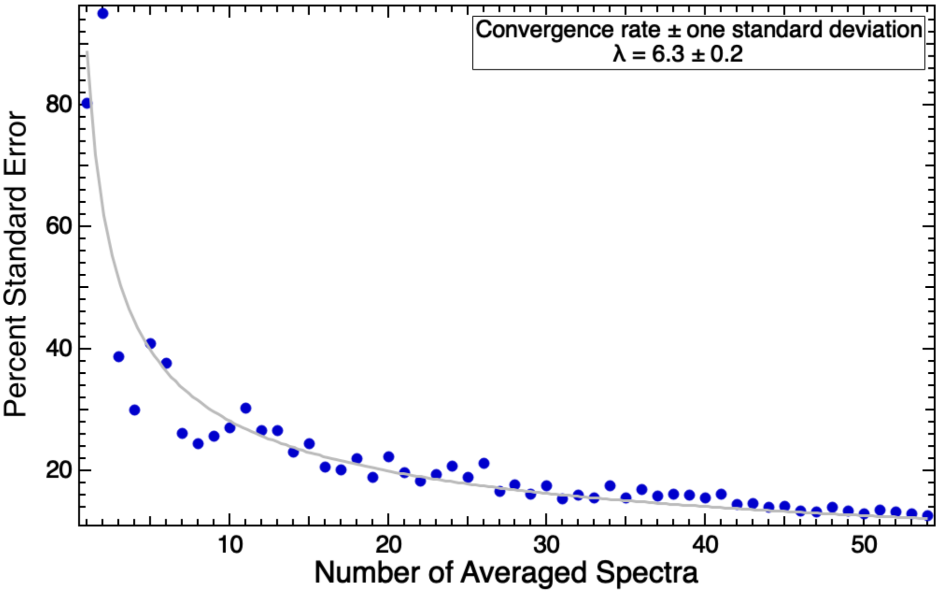

**Figure A.20:** Convergence of the percent SE of the PIR biomarker $I_{1453}/I_{1481}$ for increasing numbers of spectra in the average spectrum of *E. coli* sample two. $\lambda$ is the rate of convergence which gives an indication of the level of heterogeneity of the biomarker for the sample.

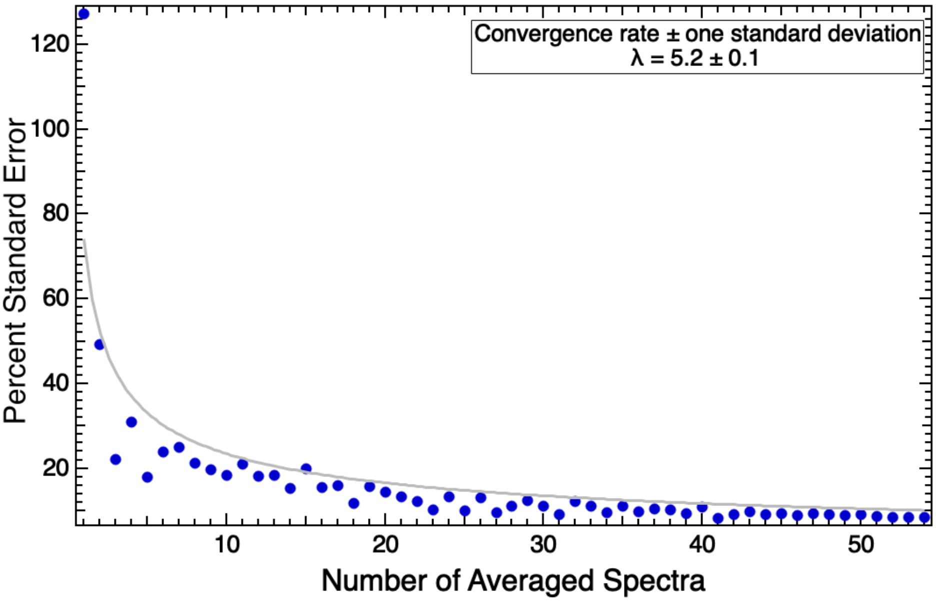

**Figure A.21:** Convergence of the percent SE of the PIR biomarker $I_{1453}/I_{1481}$ for increasing numbers of spectra in the average spectrum of *E. coli* sample three. $\lambda$ is the rate of convergence which gives an indication of the level of heterogeneity of the biomarker for the sample.

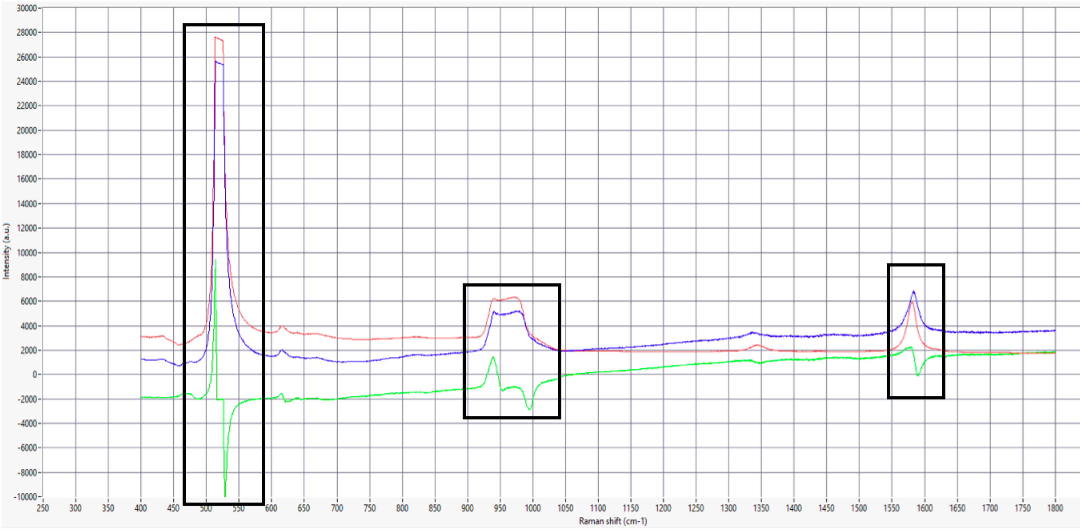

**Figure A.22:** Background subtraction of the graphene signals from the *E. coli* interfaced with graphene spectrum. The blue spectrum is the fingerprint region (600 - 1800 cm$^{-1}$) of the Raman spectrum collected from the *E. coli* interfaced with graphene, the *E. coli* signatures are drowned out by graphene signals. The red spectrum is a Raman spectrum of graphene, used for subtraction of the graphene signals from the interfaced spectrum. The green is the resultant spectrum of the background subtraction. The background subtraction leaves regions of noise in the spectrum, which could be mistaken for Raman bands of *E. coli* or interrupt the Raman signals. This noise is indicated on the image using a black box

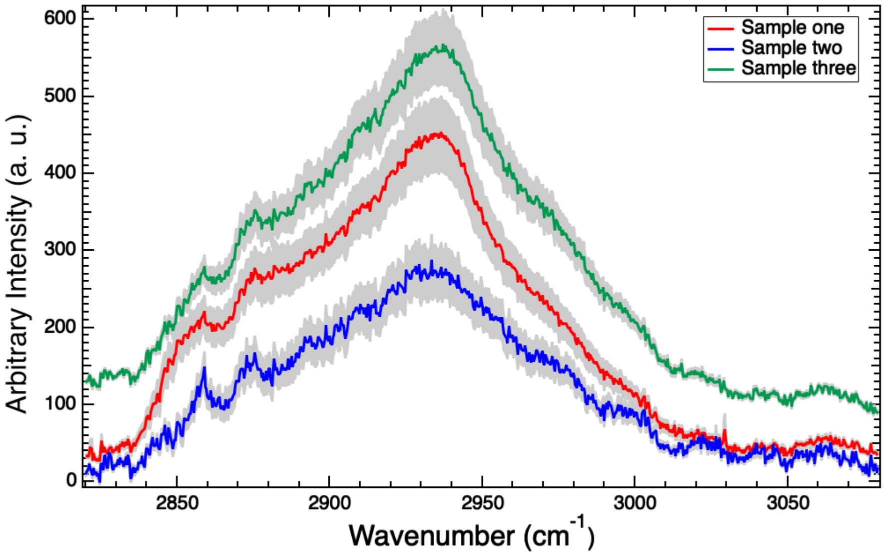

**Figure A.23:** The high wavenumber region (2800 - 3100 cm$^{-1}$) of the Raman spectra representative of three *E. coli* interfaced with graphene replicates. The *E. coli* was placed onto the graphene following growth to interface. The spectra were collected from the cells on the graphene surface. Each spectrum is an average of 45 - 55 individual Raman spectra. The grey envelope represents the standard error of the mean of the averaged spectrum.

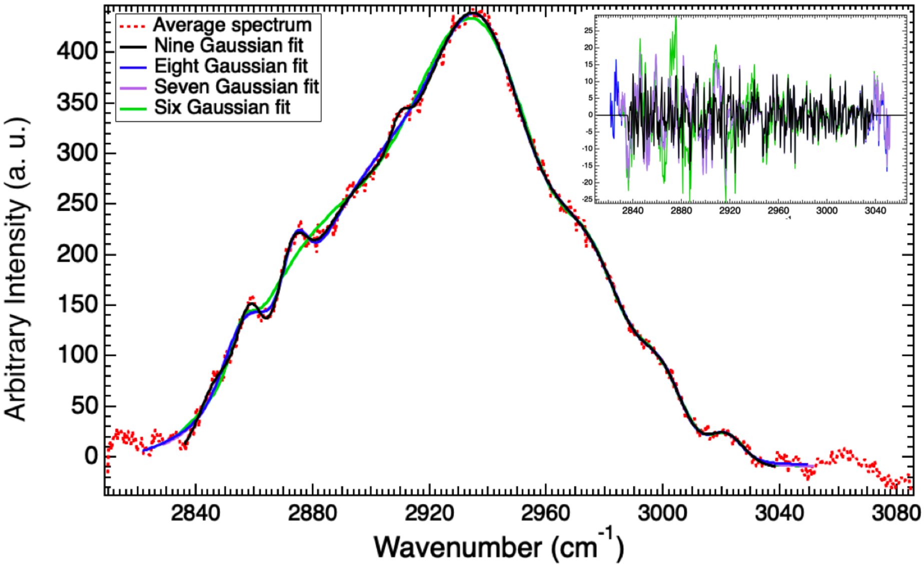

**Figure A.24:** Band fittings of the high wavenumber region of the Raman spectrum of *E. coli* interfaced with graphene performed using different numbers of Gaussians to determine which achieves the best fitting for data. The inset shows the resultant residuals from the fittings. The nine Gaussian fit produces the best fitting of the data reflected through achieving the smallest residual.

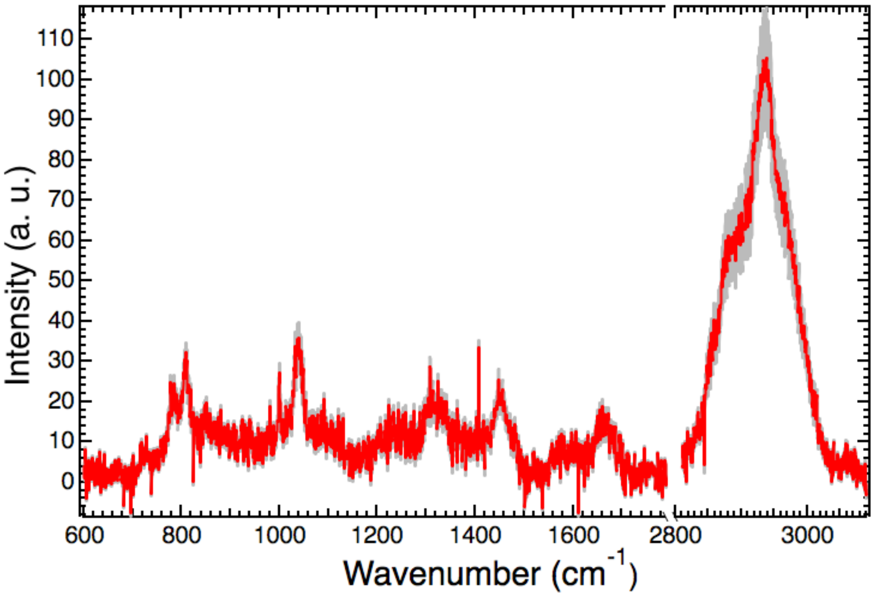

**Figure A.25:** Average spectrum of *E. coli* cultured with graphene. This is an average of the raw spectra. The cells were washed and air-dried onto a $CaF_2$ disc following which the Raman spectra were collected. This spectrum is an average of 55 individual Raman spectra collected from random points across the sample. The grey represents the SE of the mean of the averaged spectrum. The additional noise in the spectra may be due to artefacts in the sample from cell culturing with graphene.

# Bibliography

[1] C. L. Ventola. The antibiotic resistance crisis: Part 1: Causes and threats. *Pharmacy and Therapeutics*, 40(4):277, 2015.

[2] World Health Organization. Antimicrobial resistance: Global report on surveillance. 2014.

[3] R. Laxminarayan, A. Duse, C. Wattal, A. KM Zaidi, H. FL Wertheim, N. Sumpradit, E. Vlieghe, G. L. Hara, I. M. Gould, H. Goossens, et al. Antibiotic resistance? The need for global solutions. *The Lancet Infectious Diseases*, 13(12):1057, 2013.

[4] S. B. Levy and B. Marshall. Antibacterial resistance worldwide: Causes, challenges and responses. *Nature Medicine*, 10(12s):122, 2004.

[5] A. Cassini, L. D. Högberg, D. Plachouras, A. Quattrocchi, A. Hoxha, G. S. Simonsen, M. Colomb-Cotinat, M. E. Kretzschmar, B. Devleesschauwer, M. Cecchini, et al. Attributable deaths and disability-adjusted life-years caused by infections with antibiotic-resistant bacteria in the EU and the European Economic Area in 2015: A population-level modelling analysis. *The Lancet Infectious Diseases*, 2018.

[6] World Health Organisation et al. Tackling drug-resistant infections globally: Review on antimicrobial resistance. 2017.

[7] J. Davies and D. Davies. Origins and evolution of antibiotic resistance. *Microbiology and Molecular Biology Reviews*, 74(3):417, 2010.

[8] P.R. Moore, A. Evenson, T.D. Luckey, E. McCoy, C.A. Elvehjem, E.B. Hart, et al. Use of sulfasuxidine, streptothricin, and streptomycin in nutritional studies with the chick. *Journal of Biological Chemistry*, 165(2):437, 1946.

[9] E. Hershberger, S. F. Oprea, S. M. Donabedian, M. Perri, P. Bozigar, P. Bartlett, and M. J. Zervos. Epidemiology of antimicrobial resistance in *Enterococci* of animal origin. *Journal of Antimicrobial Chemotherapy*, 55(1):127, 2005.

[10] E. Y. Klein, T. P. Van Boeckel, E. M. Martinez, S. Pant, S. Gandra, S. A. Levin, H. Goossens, and R. Laxminarayan. Global increase and geographic convergence in antibiotic consumption between 2000 and 2015. *Proceedings of the National Academy of Sciences*, 115(15):E3463, 2018.

[11] M. N. Ragheb, M. K. Thomason, C. Hsu, P. Nugent, J. Gage, A. N. Samadpour, A. Kariisa, C. N. Merrikh, S. I. Miller, D. R. Sherman, et al. Inhibiting the evolution of antibiotic resistance. *Molecular Cell*, 73(1):157, 2019.

[12] P. Eduardo A. Da Silva and J. C. Palomino. Molecular basis and mechanisms of drug resistance in *Mycobacterium tuberculosis*: classical and new drugs. *Journal of Antimicrobial Chemotherapy*, 66(7):1417, 2011.

[13] UN Habitat. *State of the world's cities 2012/2013: Prosperity of cities*. Routledge, 2013.

[14] C. A. Michael, D. Dominey-Howes, and M. Labbate. The antimicrobial resistance crisis: Causes, consequences, and management. *Frontiers in Public Health*, 2:145, 2014.

[15] A. Revelas. Healthcare–associated infections: A public health problem. *Nigerian Medical Journal: Journal of the Nigeria Medical Association*, 53(2):59, 2012.

[16] S. O. Samuel, O. O. Kayode, O. I. Musa, G. C. Nwigwe, A. O. Aboderin, T. A. T. Salami, and S. S. Taiwo. Nosocomial infections and the challenges of

control in developing countries. *African Journal of Clinical and Experimental Microbiology*, 11(2):102, 2010.

[17] A. Amato-Gauci. *Annual Epidemiological Report on Communicable Diseases in Europe: Report on the status of communicable diseases in the EU and EEA/EFTA countries*. European Centre for Disease Prevention and Control, 2007.

[18] World Health Organization *et al.* Health care without avoidable infections: The critical role of infection prevention and control. Technical report, 2016.

[19] V. D. Rosenthal. Health-care-associated infections in developing countries. *The Lancet*, 377(9761):186, 2011.

[20] A. I. Hidron, J. R. Edwards, J. Patel, T. C. Horan, D. M. Sievert, D. A. Pollock, S. K. Fridkin, and *et al.* Antimicrobial-resistant pathogens associated with healthcare-associated infections: Annual summary of data reported to the national healthcare safety network at the centers for disease control and prevention, 2006–2007. *Infection Control & Hospital Epidemiology*, 29(11):996, 2008.

[21] J. M. Rangel, P. H. Sparling, C. Crowe, P. M. Griffin, and D. L. Swerdlow. Epidemiology of *Escherichia coli* O157:H7 outbreaks, United States, 1982-2002. *Emerging Infectious Diseases*, 11(4):603, 2005.

[22] Public Health England. English surveillance programme for antimicrobial utilisation and resistance (ESPAUR) report 2018–2019, 2019.

[23] European Centre for Disease Prevention and Control. The bacterial challenge: Time to react. *ECDC*, 2009.

[24] S. C. Davies and N. Gibbens. UK five year antimicrobial resistance strategy 2013 to 2018. *London: Department of Health*, 2013.

[25] R. Kelly, G. Zoubiane, D. Walsh, R. Ward, and H. Goossens. Public funding for research on antibacterial resistance in the JPIAMR countries, the Euro-

pean Commission, and related European Union agencies: A systematic observational analysis. *The Lancet Infectious Diseases*, 16(4):431, 2016.

[26] S. J. Howard, M. Catchpole, J. Watson, and S. C. Davies. Antibiotic resistance: Global response needed. *The Lancet Infectious Diseases*, 13(12):1001, 2013.

[27] A. K. Geim and K. S. Novoselov. The rise of graphene. *World Scientific*, page 11, 2010.

[28] R. N. Gomes, I. Borges, A. T. Pereira, A. F. Maia, M. Pestana, F. D. Magalhães, A. M. Pinto, and I. C. Gonçalves. Antimicrobial graphene nanoplatelets coatings for silicone catheters. *Carbon*, 139:635, 2018.

[29] J. C. Meyer, A. K. Geim, M. I. Katsnelson, K. S. Novoselov, T. J. Booth, and S. Roth. The structure of suspended graphene sheets. *Nature*, 446(7131):60, 2007.

[30] K. S. Novoselov, A. K. Geim, S. V Morozov, D. A. Jiang, Y. Zhang, S. V. Dubonos, I. V. Grigorieva, and A. A. Firsov. Electric field effect in atomically thin carbon films. *Science*, 306(5696):666, 2004.

[31] L. Zou, L. Wang, Y. Wu, C. Ma, S. Yu, and X. Liu. Trends analysis of graphene research and development. *Journal of Data and Information Science*, 3(1):82, 2018.

[32] A. H. C. Neto, F. Guinea, N. M. R. Peres, K. S. Novoselov, and A. K. Geim. The electronic properties of graphene. *Reviews of Modern Physics*, 81(1):109, 2009.

[33] M. S. Dresselhaus, A. Jorio, M. Hofmann, G. Dresselhaus, and R. Saito. Perspectives on carbon nanotubes and graphene Raman spectroscopy. *Nano Letters*, 10(3):751, 2010.

[34] A. K. Geim and A. H. MacDonald. Graphene: Exploring carbon flatland. *Physics Today*, 60(8):35, 2007.

[35] K. S. Novoselov, D. Jiang, F. Schedin, T. J. Booth, V. V. Khotkevich, S. V. Morozov, and A. K. Geim. Two-dimensional atomic crystals. *Proceedings of the National Academy of Sciences*, 102(30):10451, 2005.

[36] L. M. Malard, M. A. A. Pimenta, G. Dresselhaus, and M. S. Dresselhaus. Raman spectroscopy in graphene. *Physics Reports*, 473(5-6):51, 2009.

[37] C. Lee, X. Wei, J. W. Kysar, and J. Hone. Measurement of the elastic properties and intrinsic strength of monolayer graphene. *Science*, 321(5887):385, 2008.

[38] M. A. Lodes, F. S. Kachold, and S. M. Rosiwal. Mechanical properties of micro-and nanocrystalline diamond foils. *Philosophical Transactions of the Royal Society A: Mathematical, Physical and Engineering Sciences*, 373(2038):20140136, 2015.

[39] E. J. Siochi. Graphene in the sky and beyond. *Nature Nanotechnology*, 9(10):745, 2014.

[40] M. I. Katsnelson. Graphene: carbon in two dimensions. *Materials Today*, 10(1-2):20, 2007.

[41] K. S. Novoselov, A. K. Geim, S. V. Morozov, D. Jiang, M. I. Katsnelson, I. V. Grigorieva, S. V. Dubonos, and A. A. Firsov. Two-dimensional gas of massless Dirac fermions in graphene. *Nature*, 438(7065):197, 2005.

[42] J. Pernot, C. Tavares, E. Gheeraert, E. Bustarret, M. Katagiri, and S. Koizumi. Hall electron mobility in diamond. *Applied Physics Letters*, 89(12):122111, 2006.

[43] B. Wang, J. Ryu, S. Choi, G. Song, D. Hong, C. Hwang, X. Chen, B. Wang, W. Li, H. Song, et al. Folding graphene film yields high areal energy storage in lithium-ion batteries. *ACS Nano*, 12(2):1739, 2018.

[44] M. F. El-Kady and R. B. Kaner. Scalable fabrication of high-power graphene micro-supercapacitors for flexible and on-chip energy storage. *Nature Communications*, 4:2446, 2013.

[45] Y. Wang, L. Wang, T. Yang, X. Li, X. Zang, M. Zhu, K. Wang, D. Wu, and H. Zhu. Wearable and highly sensitive graphene strain sensors for human motion monitoring. *Advanced Functional Materials*, 24(29):4666, 2014.

[46] A. K. Sundramoorthy and S. Gunasekaran. Applications of graphene in quality assurance and safety of food. *Trends in Analytical Chemistry*, 60:36, 2014.

[47] H. Hirai, H. Tsuchiya, Y. Kamakura, N. Mori, and M. Ogawa. Electron mobility calculation for graphene on substrates. *Journal of Applied Physics*, 116(8):083703, 2014.

[48] K. I. Bolotin, K. J. Sikes, Z. Jiang, M. Klima, G. Fudenberg, J. Hone, P. Kim, and H. L. Stormer. Ultrahigh electron mobility in suspended graphene. *Solid State Communications*, 146(9-10):351, 2008.

[49] Graphenea. https://www.graphenea.com.

[50] J. Chen, L. Li, W. G. Cullen, E. D. Williams, and M. S. Fuhrer. Tunable kondo effect in graphene with defects. *Nature Physics*, 7(7):535, 2011.

[51] J. Dong, H. Wang, H. Peng, Z. Liu, K. Zhang, and F. Ding. Formation mechanism of overlapping grain boundaries in graphene chemical vapor deposition growth. *Chemical Science*, 8(3):2209, 2017.

[52] D. H. Jung, C. Kang, J. E. Nam, J. Kim, and J. S. Lee. Size and density of graphene domains grown with different annealing times. *Bulletin of the Korean Chemical Society*, 34(11):3312, 2013.

[53] S. Bae, H. Kim, Y. Lee, X. Xu, J. Park, Y. Zheng, J. Balakrishnan, T. Lei, H. R. Kim, Y. I. Song, et al. Roll-to-roll production of 30-inch graphene films for transparent electrodes. *Nature Nanotechnology*, 5(8):574, 2010.

[54] P. Nguyen and V. Berry. Graphene interfaced with biological cells: Opportunities and challenges. *The Journal of Physical Chemistry Letters*, 3(8):1024, 2012.

[55] R. Lakshmanan and N. Maulik. Graphene-based drug delivery systems in tissue engineering and nanomedicine. *Canadian Journal of Physiology and Pharmacology*, 96(9):869, 2018.

[56] S. Syama and P. V. Mohanan. Comprehensive application of graphene: Emphasis on biomedical concerns. *Nano-Micro Letters*, 11(1):6, 2019.

[57] Z. Gu, W. Song, S. H. Chen, B. Li, W. Li, and R. Zhou. Defect-assisted protein HP35 denaturation on graphene. *Nanoscale*, 2019.

[58] W. Wu, Q. Yu, P. Peng, Z. Liu, J. Bao, and S.S. Pei. Control of thickness uniformity and grain size in graphene films for transparent conductive electrodes. *Nanotechnology*, 23(3):035603, 2011.

[59] A. Matsubayashi, Z. Zhang, J. U. Lee, and V. P. LaBella. Microstructure fabrication process induced modulations in CVD graphene. *AIP Advances*, 4(12):127143, 2014.

[60] Y. Liu, Z. Liu, W. S. Lew, and Q. J. Wang. Temperature dependence of the electrical transport properties in few-layer graphene interconnects. *Nanoscale Research Letters*, 8(1):335, 2013.

[61] M. S. Dresselhaus, G. Dresselhaus, K. Sugihara, I. L. Spain, and H. A. Goldberg. Graphite fibers and filaments. 5, 1988.

[62] J. R. Ferraro. Introductory Raman spectroscopy. 2003.

[63] Z. Yan and A. R. Barron. Characterization of graphene by Raman spectroscopy. *Open Stax-CNX Modul.: http://cnx. org/content/m34667/1.2/-29 June*, 2010.

[64] A. C. Ferrari, J. C. Meyer, V. Scardaci, C. Casiraghi, M. Lazzeri, F. Mauri, S. Piscanec, D. Jiang, K. S. Novoselov, S. Roth, et al. Raman spectrum of graphene and graphene layers. *Physical Review Letters*, 97(18):187401, 2006.

[65] A. Jorio, G. F. Dresselhaus, R. Saito, and G. Dresselhaus. Raman spectroscopy in graphene related systems. 2011.

[66] R. Beams, L. G. Cançado, and L. Novotny. Raman characterization of defects and dopants in graphene. *Journal of Physics: Condensed Matter*, 27(8):083002, 2015.

[67] I. Childres, L. A. Jauregui, W. Park, H. Cao, and Y. P. Chen. Raman spectroscopy of graphene and related materials. *New Developments in Photon and Materials Research*, 1, 2013.

[68] M. S. Dresselhaus, A. Jorio, and R. Saito. Characterizing graphene, graphite, and carbon nanotubes by Raman spectroscopy. *Annual Review of Condensed Matter Physics*, 1(1):89, 2010.

[69] M. Bruna, A. K. Ott, M. Ijas, D. Yoon, U. Sassi, and A. C. Ferrari. Doping dependence of the Raman spectrum of defected graphene. *ACS Nano*, 8(7):7432, 2014.

[70] B. Tang, H. Guoxin, and H. Gao. Raman spectroscopic characterization of graphene. *Applied Spectroscopy Reviews*, 45(5):369, 2010.

[71] J. Li, G. Wang, H. Zhu, M. Zhang, X. Zheng, Z. Di, X. Liu, and X. Wang. Antibacterial activity of large-area monolayer graphene film manipulated by charge transfer. *Scientific Reports*, 4:4359, 2014.

[72] K. Krishnamoorthy, M. Veerapandian, L.H. Zhang, K. Yun, and S. J. Kim. Antibacterial efficiency of graphene nanosheets against pathogenic bacteria via lipid peroxidation. *The Journal of Physical Chemistry C*, 116(32):17280, 2012.

[73] Y. Tu, M. Lv, P. Xiu, T. Huynh, M. Zhang, M. Castelli, Z. Liu, Q. Huang, C. Fan, H. Fang, and R. Zhou. Destructive extraction of phospholipids from *Escherichia coli* membranes by graphene nanosheets. *Nature Nanotechnology*, 8(8):594, 2013.

[74] L. Dellieu, E. Lawarée, N. Reckinger, C. Didembourg, J. J. Letesson, M. Sarrazin, O. Deparis, J. Y. Matroule, and J. F. Colomer. Do CVD grown graphene films have antibacterial activity on metallic substrates? *Carbon*, 84:310, 2015.

[75] O. Akhavan and E. Ghaderi. Toxicity of graphene and graphene oxide nanowalls against bacteria. *ACS Nano*, 4(10):5731, 2010.

[76] B. Luan, T. Huynh, L. Zhao, and R. Zhou. Potential toxicity of graphene to cell functions via disrupting protein–protein interactions. *ACS Nano*, 9(1):663, 2014.

[77] L. Teng, X. Wang, X. Wang, H. Gou, L. Ren, T. Wang, Y. Wang, Y. Ji, W. E. Huang, and J. Xu. Label-free, rapid and quantitative phenotyping of stress response in *E. coli* via ramanome. *Scientific Reports*, 6(1):34359, 2016.

[78] Y. Zhang, S. F. Ali, E. Dervishi, Y. Xu, Z. Li, D. Casciano, and A. S. Biris. Cytotoxicity effects of graphene and single-wall carbon nanotubes in neural phaeochromocytoma-derived PC12 cells. *ACS Nano*, 4(6):3181, 2010.

[79] A. Sasidharan, L. S. Panchakarla, P. Chandran, D. Menon, S. Nair, C. N. R. Rao, and M. Koyakutty. Differential nano-bio interactions and toxicity effects of pristine versus functionalized graphene. *Nanoscale*, 3(6):2461, 2011.

[80] T. R. Nayak, H. Andersen, V. S. Makam, C. Khaw, S. Bae, X. Xu, P. R. Ee, J. Ahn, B. H. Hong, G. Pastorin, et al. Graphene for controlled and accelerated osteogenic differentiation of human mesenchymal stem cells. *ACS Nano*, 5(6):4670, 2011.

[81] S. K. Rastogi, G. Raghavan, G. Yang, and T. Cohen-Karni. Effect of graphene on nonneuronal and neuronal cell viability and stress. *Nano Letters*, 17(5):3297, 2017.

[82] S. Uskoković-Marković, V. Kuntić, D. Bajuk-Bogdanović, and I. Holclajtner-Antunović. Surface-enhanced Raman scattering (SERS) biochemical applications. 2017.

[83] Z. Liu, Z. Guo, H. Zhong, X. Qin, M. Wan, and B. Yang. Graphene oxide based surface-enhanced Raman scattering probes for cancer cell imaging. *Physical Chemistry Chemical Physics*, 15(8):2961, 2013.

[84] S. Liu, T. H. Zeng, M. Hofmann, E. Burcombe, J. Wei, R. Jiang, J. Kong, and Y. Chen. Antibacterial activity of graphite, graphite oxide, graphene oxide, and reduced graphene oxide: membrane and oxidative stress. *ACS Nano*, 5(9):6971, 2011.

[85] S. Szunerits and R. Boukherroub. Antibacterial activity of graphene-based materials. *Journal of Materials Chemistry B*, 4(43):6892, 2016.

[86] O. Clermont, S. Bonacorsi, and E. Bingen. Rapid and simple determination of the *Escherichia coli* phylogenetic group. *Applied and Environmental Microbiology*, 66(10):4555, 2000.

[87] F. R. Blattner, G. Plunkett, C. A. Bloch, N. T. Perna, V. Burland, M. Riley, J. Collado-Vides, J. D. Glasner, C. K. Rode, G. F. Mayhew, et al. The complete genome sequence of *Escherichia coli* K-12. *Science*, 277(5331):1453, 1997.

[88] K. Todar. Todar's online textbook of bacteriology, 2004.

[89] Jeff Dahl. Image of Gram negative cell wall, 2008.

[90] G. Reshes, S. Vanounou, I. Fishov, and M. Feingold. Cell shape dynamics in *Escherichia coli*. *Biophysical Journal*, 94(1):251, 2008.

[91] R. J. Allen and B. Waclaw. Bacterial growth: A statistical physicist's guide. *Reports on Progress in Physics*, 82(1):016601, 2018.

[92] C. S. Edén and H. A. Hansson. *Escherichia coli* pili as possible mediators of attachment to human urinary tract epithelial cells. *Infection and Immunity*, 21(1):229, 1978.

[93] P. J. Mears, S. Koirala, C. V. Rao, I. Golding, and Y. R. Chemla. *Escherichia coli* swimming is robust against variations in flagellar number. *Elife*, 3:e01916, 2014.

[94] A. T. Asmar, J. L. Ferreira, E. J. Cohen, S. Cho, M. Beeby, K. T. Hughes, and J. Collet. Communication across the bacterial cell envelope depends on the size of the periplasm. *PLoS Biology*, 15(12):e2004303, 2017.

[95] K. C. Huang, R. Mukhopadhyay, B. Wen, Z. Gitai, and N. S. Wingreen. Cell shape and cell-wall organization in Gram-negative bacteria. *Proceedings of the National Academy of Sciences*, 105(49):19282, 2008.

[96] V. R. F. Matias, A. Al-Amoudi, J. Dubochet, and T. J. Beveridge. Cryo-transmission electron microscopy of frozen-hydrated sections of *Escherichia coli* and *Pseudomonas aeruginosa*. *Journal of Bacteriology*, 185(20):6112, 2003.

[97] R. S. Roy, P. Yang, S. Kodali, Y. Xiong, R. M. Kim, P. R. Griffin, H. R. Onishi, J. Kohler, L. L. Silver, and K. Chapman. Direct interaction of a vancomycin derivative with bacterial enzymes involved in cell wall biosynthesis. *Chemistry & Biology*, 8(11):1095, 2001.

[98] H. Lodish, A. Berk, S. L. Zipursky, P. Matsudaira, D. Baltimore, and J. Darnell. Molecular cell biology 4th Edition. *National Center for Biotechnology Information, Bookshelf*, 2000.

[99] C. Sohlenkamp and O. Geiger. Bacterial membrane lipids: Diversity in structures and pathways. *FEMS Microbiology Reviews*, 40(1):133, 2016.

[100] T. J. Silhavy, D. Kahne, and S. Walker. The bacterial cell envelope. *Cold Spring Harbor Perspectives in Biology*, 2(5):414, 2010.

[101] Y. Kamio and H. Nikaido. Outer membrane of *Salmonella typhimurium*: Accessibility of phospholipid head groups to phospholipase C and cyanogen bromide activated dextran in the external medium. *Biochemistry*, 15(12):2561, 1976.

[102] S. Narita, S. Matsuyama, and H. Tokuda. Lipoprotein trafficking in *Escherichia coli*. *Archives of Microbiology*, 182(1):1, 2004.

[103] D. R. Dixon and R. P. Darveau. Lipopolysaccharide heterogeneity: Innate host responses to bacterial modification of Lipid A structure. *Journal of Dental Research*, 84(7):584, 2005.

[104] B. Lugtenberg. Composition and function of the outer membrane of *Escherichia coli*. *Trends in Biochemical Sciences*, 6:262, 1981.

[105] Y. Wang. The function of OmpA in *Escherichia coli*. *Biochemical and Biophysical Research Communications*, 292(2):396, 2002.

[106] Y. Rosenfeld and Y. Shai. Lipopolysaccharide (Endotoxin)-host defense antibacterial peptides interactions: role in bacterial resistance and prevention of sepsis. *Biochimica et Biophysica Acta (BBA)-Biomembranes*, 1758(9):1513, 2006.

[107] D. N. Medearis, B. M. Camitta, and E. C. Heath. Cell wall composition and virulence in *Escherichia coli*. *Journal of Experimental Medicine*, 128(3):399, 1968.

[108] C. García-Timermans, P. Rubbens, F. Kerckhof, B. Buysschaert, D. Khalenkow, W. Waegeman, A. G. Skirtach, and N. Boon. Label-free Raman characterization of bacteria calls for standardised procedures. *Journal of Microbiological Methods*, 151:69, 2018.

[109] J. W. Bioger. Treatment of *Staphylococcal* infections with penicillin by intermittent sterilization. *Lancet Oct*, 14:497, 1944.

[110] S. K. Govers, A. Adam, H. Blockeel, and A. Aertsen. Rapid phenotypic individualization of bacterial sister cells. *Scientific Reports*, 7(1):8473, 2017.

[111] M. Acar, J. T. Mettetal, and A. Van Oudenaarden. Stochastic switching as a survival strategy in fluctuating environments. *Nature Genetics*, 40(4):471, 2008.

[112] D. I. Ellis and R. Goodacre. Metabolic fingerprinting in disease diagnosis: biomedical applications of infrared and Raman spectroscopy. *The Analyst*, 131(8):875, 2006.

[113] E. M. J. Schotsmans, A. S. Wilson, R. Brettell, T. Munshi, and H. G. M. Edwards. Raman spectroscopy as a non-destructive screening technique for studying white substances from archaeological and forensic burial contexts. *Journal of Raman Spectroscopy*, 45(11-12):1301, 2014.

[114] R. Pätzold, M. Keuntje, and A. Anders-von Ahlften. A new approach to non-destructive analysis of biofilms by confocal Raman microscopy. *Analytical and Bioanalytical Chemistry*, 386(2):286, 2006.

[115] L. Ashton, K. Lau, C. L. Winder, and R. Goodacre. Raman spectroscopy: lighting up the future of microbial identification. *Future Microbiology*, 6(9):991, 2011.

[116] S. Stöckel, J. Kirchhoff, U. Neugebauer, P. Rösch, and J. Popp. The application of Raman spectroscopy for the detection and identification of microorganisms. *Journal of Raman Spectroscopy*, 47(1):89, 2016.

[117] A. Germond, T. Ichimura, T. Horinouchi, H. Fujita, C. Furusawa, and T. M. Watanabe. Raman spectral signature reflects transcriptomic features of antibiotic resistance in *Escherichia coli*. *Communications Biology*, 1(1):85, 2018.

[118] H. Zhou, D. Yang, N. P. Ivleva, N. E. Mircescu, S. Schubert, R. Niessner, A. Wieser, and C. Haisch. Label-Free in Situ Discrimination of Live and Dead Bacteria by Surface-Enhanced Raman Scattering. *Analytical Chemistry*, 87(13):6553, 2015.

[119] C. Xie and Y. Q. Li. Confocal micro-Raman spectroscopy of single biological cells using optical trapping and shifted excitation difference techniques. *Journal of Applied Physics*, 93(5):2982, 2003.

[120] M. F. Escoriza, J. M. Van Briesen, S. Stewart, and J. Maier. Raman spectroscopic discrimination of cell response to chemical and physical inactivation. *Applied Spectroscopy*, 61(8):812, 2007.

[121] T. N. K. Zu, A. I. M. Athamneh, R. S. Wallace, E. Collakova, and R. S. Senger. Near-real-time analysis of the phenotypic responses of *Escherichia*

coli to 1-butanol exposure using Raman spectroscopy. *Journal of Bacteriology*, 196(23):3983, 2014.

[122] B. B. Nepple, I. Flynn, and R. Bachofen. Morphological changes in phototrophic bacteria induced by metalloid oxyanions. *Microbiological Research*, 154(2):191, 1999.

[123] S. S. Nanda, D. K. Yi, and K. Kim. Study of antibacterial mechanism of graphene oxide using Raman spectroscopy. *Scientific Reports*, 6(1):28443, 2016.

[124] Z. Movasaghi, S. Rehman, and I. U. Rehman. Raman Spectroscopy of Biological Tissues. *Applied Spectroscopy Reviews*, 42(5):493, 2007.

[125] S. Huffer, M. E. Clark, J. C. Ning, H. W. Blanch, and D. S. Clark. Role of alcohols in growth, lipid composition, and membrane fluidity of yeasts, bacteria, and archaea. *Applied and Environmental Microbiology*, 77(18):6400, 2011.

[126] H. Wu, J. V. Volponi, A. E. Oliver, A. N. Parikh, B. A. Simmons, and S. Singh. In vivo lipidomics using single-cell Raman spectroscopy. *Proceedings of the National Academy of Sciences*, 108(9):3809, 2011.

[127] K. Czamara, K. Majzner, A. Selmi, M. Baranska, Y. Ozaki, and A. Kaczor. Unsaturated lipid bodies as a hallmark of inflammation studied by Raman 2D and 3D microscopy. *Scientific Reports*, 7:40889, 2017.

[128] C. V. Raman. A new radiation. *Indian Journal of Physics*, 2:387, 1928.

[129] A. Smekal. Zur quantentheorie der dispersion. *Naturwissenschaften*, 11(43):873, 1923.

[130] S. Lohumi, M. S. Kim, J. Qin, and B-K. Cho. Raman imaging from microscopy to macroscopy: Quality and safety control of biological materials. *Trends in Analytical Chemistry*, 93:183, 2017.

[131] D. L. Andrews. Raman scattering and spectral interpretation. pages 8–1 to 8–10, 2014.

[132] Teknova. https://www.teknova.com/.

[133] A. Rouf, V. Kanojia, H. R. Naik, B. Naseer, and T. Qadri. An overview of microbial cell culture. *Journal of Pharmacognosy and Phytochemistry*, 6(6):1923, 2017.

[134] M. D. Rolfe, C. J. Rice, S. Lucchini, C. Pin, A. Thompson, A. D. S. Cameron, M. Alston, M. F. Stringer, R. P. Betts, J. Baranyi, et al. Lag phase is a distinct growth phase that prepares bacteria for exponential growth and involves transient metal accumulation. *Journal of Bacteriology*, 194(3):686, 2012.

[135] J. Monod. The growth of bacterial cultures. *Annual Review of Microbiology*, 3(1):371, 1949.

[136] M. Bittel, C. B. Y. Cordella, A. Assaf, S. Jouanneau, M. J. Durand, and G. Thouand. Potential of Raman spectroscopy to monitor arsenic toxicity on bacteria: Insights toward multiparametric bioassays. *Environmental Science and Technology*, 49(20):12324, 2015.

[137] P. Sniegowski. Evolution: bacterial mutation in stationary phase. *Current Biology*, 14(6):R245, 2004.

[138] B. W. Peterson, P. K. Sharma, H. C. van der Mei, and H. J. Busscher. Bacterial cell surface damage due to centrifugal compaction. *Applied and Environmental Microbiology*, 78(1):120, 2012.

[139] R. S. Pembrey, K. C. Marshall, and R. P. Schneider. Cell surface analysis techniques: what do cell preparation protocols do to cell surface properties? *Applied and Environmental Microbiology*, 65(7):287, 1999.

[140] C. H. Bell. The effects of centrifugation and filtration as pre-treatement in bacterial retention studies. *Journal of Young Investigators*, 2005.

[141] N. Ramli, N. A. Nayan, H. W. Lee, and S. S. Embong. Analysis of the effect of growth parameters on graphene synthesized by chemical vapor deposition. *Journal of Nanoelectronics and Optoelectronics*, 10(1):50, 2015.

[142] M. Regmi, M. F. Chisholm, and G. Eres. The effect of growth parameters on the intrinsic properties of large-area single layer graphene grown by chemical vapor deposition on Cu. *Carbon*, 50(1):134, 2012.

[143] G. Kalita and M. Tanemura. Fundamentals of chemical vapor deposited graphene and emerging applications. *Graphene Materials: Advanced Applications*, page 41, 2017.

[144] S. Naghdi, K. Y. Rhee, M. T. Kim, B. Jaleh, and S. J. Park. Atmospheric chemical vapor deposition of graphene on molybdenum foil at different growth temperatures. *Carbon Letters* , 18:37, 2016.

[145] H. Ago, Y. Ito, N. Mizuta, K. Yoshida, B. Hu, C. M. Orofeo, M. Tsuji, K. Ikeda, and S. Mizuno. Epitaxial chemical vapor deposition growth of single-layer graphene over cobalt film crystallized on sapphire. *ACS Nano*, 4(12):7407, 2010.

[146] H. Kwon, J. M. Ha, S. H. Yoo, G. Ali, and S. O. Cho. Synthesis of flake-like graphene from nickel-coated polyacrylonitrile polymer. *Nanoscale Research Letters*, 9(1):618, 2014.

[147] T. J. Gnanaprakasa, Y. Gu, S. K. Eddy, Z. Han, W. J. Beck, K. Muralidharan, and S. Raghavan. The role of copper pretreatment on the morphology of graphene grown by chemical vapor deposition. *Microelectronic Engineering*, 131:1, 2015.

[148] HORIBA Scientic. Labspec 5 User Manual 12, 2010.

[149] T. Dieing, O. Hollricher, and J. Toporski. Confocal Raman microscopy. page 289, 2011.

[150] A. Walter, M. Reinicke, T. Bocklitz, W. Schumacher, P. Rösch, E. Kothe, and J. Popp. Raman spectroscopic detection of physiology changes in plasmid-bearing *Escherichia coli* with and without antibiotic treatment. *Analytical and Bioanalytical Chemistry*, 400(9):2763, 2011.

[151] W. Keeler and K. Leung. Confocal micro-Raman spectra of untreated and lethally treated *Escherichia coli* exposed to UV-B and violet light. *arXiv preprint arXiv:1701.01749*, 2017.

[152] T. J. Moritz, C. R. Polage, D. S. Taylor, D. M. Krol, S. M. Lane, and J. W. Chan. Evaluation of *Escherichia coli* cell response to antibiotic treatment by use of Raman spectroscopy with laser tweezers. *Journal of Clinical Microbiology*, 48(11):4287, 2010.

[153] H. Muhamadali, M. Chisanga, A. Subaihi, and R. Goodacre. Combining Raman and FT-IR spectroscopy with quantitative isotopic labeling for differentiation of *E. coli* cells at community and single cell levels. *Analytical Chemistry*, 87(8):4578, 2015.

[154] J. F. M. Almarashi, N. Kapel, T. S. Wilkinson, and H. H. Telle. Raman spectroscopy of bacterial species and strains cultivated under reproducible conditions. *Journal of Spectroscopy*, 27(5-6):361, 2012.

[155] K. Maquelin, L-P Choo-Smith, T. van Vreeswijk, H. P. Endtz, B. Smith, R. Bennett, H. A. Bruining, and G. J. Puppels. Raman spectroscopic method for identification of clinically relevant microorganisms growing on solid culture medium. *Analytical Chemistry*, 72(1):12, 2000.

[156] J. W. Chan, H. Winhold, M. H. Corzett, J. M. Ulloa, M. Cosman, R. Balhorn, and T. Huser. Monitoring dynamic protein expression in living *E. coli* bacterial cells by laser tweezers Raman spectroscopy. *Cytometry Part A*, 71A(7):468, 2007.

[157] E. J. G. Peterman, F. Gittes, and C. F. Schmidt. Laser-induced heating in optical traps. *Biophysical Journal*, 84(2):1308, 2003.

[158] D. P. Cherney, J. C. Conboy, and J. M. Harris. Optical-trapping Raman microscopy detection of single unilamellar lipid vesicles. *Analytical Chemistry*, 75(23):6621, 2003.

[159] K. Mlynáriková, O. Samek, S. Bernatová, F. Ružička, J. Ježek, A. Hároniková, M. Šiler, P. Zemánek, and V. Holá. Influence of culture media on microbial fingerprints using Raman spectroscopy. *Sensors*, 15(11):29635, 2015.

[160] K. C. Schuster, E. Urlaub, and J. R. Gapes. Single-cell analysis of bacteria by Raman microscopy: spectral information on the chemical composition of cells and on the heterogeneity in a culture. *Journal of Microbiological Methods*, 42(1):29, 2000.

[161] Z. Tu, Z. Liu, Y. Li, F. Yang, L. Zhang, Z. Zhao, C. Xu, S. Wu, H. Liu, H. Yang, et al. Controllable growth of 1–7 layers of graphene by chemical vapour deposition. *Carbon*, 73:252, 2014.

[162] S. M. Hussein, I. F. Crowe, N. Clark, M. Milosevic, A. Vijayaraghavan, F. Y. Gardes, G. Z. Mashanovich, and M. P. Halsall. Raman mapping analysis of graphene-integrated silicon micro-ring resonators. *Nanoscale Research Letters*, 12(1):600, 2017.

[163] J-U Lee, D. Yoon, H. Kim, S. W. Lee, and H. Cheong. Thermal conductivity of suspended pristine graphene measured by Raman spectroscopy. *Physical Review B*, 83(8):081419, 2011.

[164] S. Zhao, S. P. Surwade, Z. Li, and H. Liu. Photochemical oxidation of CVD-grown single layer graphene. *Nanotechnology*, 23(35):355703, 2012.

[165] G. Nandamuri, S. Roumimov, and R. Solanki. Chemical vapor deposition of graphene films. *Nanotechnology*, 21(14):145604, 2010.

[166] H. Bukowska, F. Meinerzhagen, S. Akcöltekin, O. Ochedowski, M. Neubert, V. Buck, and M. Schleberger. Raman spectra of graphene exfoliated on insulating crystalline substrates. *New Journal of Physics*, 13(6):063018, 2011.

[167] C-H Huang, H-Y Lin, C-W Huang, Y-M Liu, F-Y Shih, W-H Wang, and H-C Chui. Probing substrate influence on graphene by analyzing Raman lineshapes. *Nanoscale Research Letters*, 9(1):64, 2014.

[168] S. Roscher, R. Hoffmann, and O. Ambacher. Determination of the graphene–graphite ratio of graphene powder by Raman 2D band symmetry analysis. *Analytical Methods*, 11(9):1224, 2019.

[169] H. Zhou, W. J. Yu, L. Liu, R. Cheng, Y. Chen, X. Huang, Y. Liu, Y. Wang, Y. Huang, and X. Duan. Chemical vapour deposition growth of large single crystals of monolayer and bilayer graphene. *Nature Communications*, 4:2096, 2013.

[170] I. Goykhman, U. Sassi, B. Desiatov, N. Mazurski, S. Milana, D. de Fazio, A. Eiden, J. Khurgin, J. Shappir, U. Levy, and A. C. Ferrari. On-chip integrated, silicon–graphene plasmonic schottky photodetector with high responsivity and avalanche photogain. *Nano Letters*, 16(5):3005, 2016.

[171] T. Dieing, O. Hollricher, and J. Toporski. Confocal Raman microscopy. 158, 2011.

[172] A. Hermelink, A. Brauer, P. Lasch, and D. Naumann. Phenotypic heterogeneity within microbial populations at the single-cell level investigated by confocal Raman microspectroscopy. *Analyst*, 134(6):1149, 2009.

[173] M. Currie, J. D. Caldwell, F. J. Bezares, J. Robinson, T. Anderson, H. Chun, and M. Tadjer. Quantifying pulsed laser induced damage to graphene. *Applied Physics Letters*, 99(21):211909, 2011.

[174] M. Kalbac, A. Reina-Cecco, H. Farhat, J. Kong, L. Kavan, and M. S. Dresselhaus. The influence of strong electron and hole doping on the Raman intensity of chemical vapor-deposition graphene. *ACS Nano*, 4(10):6055, 2010.

[175] D. A. Boyd, W-H Lin, C-C Hsu, M. L. Teague, C-C Chen, Y-Y Lo, W-Y Chan, W-B Su, T-C Cheng, C-S Chang, et al. Single-step deposition of high-mobility graphene at reduced temperatures. *Nature Communications*, 6:6620, 2015.

[176] L. Mikoliunaite, R. D. Rodriguez, E. Sheremet, V. Kolchuzhin, J. Mehner, A. Ramanavicius, and D. R. T. Zahn. The substrate matters in the Raman spectroscopy analysis of cells. *Scientific Reports*, 5:13150, 2015.

[177] D. Tuschel. Selecting an excitation wavelength for Raman spectroscopy. 2016.

[178] M. Esfahani, T. Ioneda, and S. J. Wakil. Studies on the control of fatty acid metabolism III. Incorporation of fatty acids into phospholipids and regulation of fatty acid synthetase of *Escherichia coli*. *Journal of Biological Chemistry*, 246(1):50, 1971.

[179] A. G. Marr and J. L. Ingraham. Effect of temperature on the composition of fatty acids in *Escherichia coli*. *Journal of Bacteriology*, 84(6):1260, 1962.

[180] Q. Wu, W. H. Nelson, S. Elliot, J. F. Sperry, M. Feld, R. Dasari, and R. Manoharan. Intensities of *E. coli* nucleic acid Raman spectra excited selectively from whole cells with 251-nm light. *Analytical Chemistry*, 72(13):2981, 2000.

[181] O. Frank, J. Vejpravova, L. Kavan, and M. Kalbac. Raman spectroscopy investigation of defect occurrence in graphene grown on copper single crystals. *Physica Status Solidi (B)*, 250(12):2653, 2013.

[182] C-S Ho, N. Jean, C. A. Hogan, L. Blackmon, S. S. Jeffrey, M. Holodniy, N. Banaei, A. A. E. Saleh, S. Ermon, and J. Dionne. Rapid identification of pathogenic bacteria using Raman spectroscopy and deep learning. *Nature Communications*, 10:4927, 2019.

[183] A. Eckmann, A. Felten, A. Mishchenko, L. Britnell, R. Krupke, K. S. Novoselov, and C. Casiraghi. Probing the nature of defects in graphene by Raman spectroscopy. *Nano Letters*, 12(8):3925, 2012.

[184] Z. Luo, C. Cong, J. Zhang, Q. Xiong, and T. Yu. The origin of sub-bands in the Raman D-band of graphene. *Carbon*, 50(11):4252, 2012.

[185] D. Graf, F. Molitor, K. Ensslin, C. Stampfer, A. Jungen, C. Hierold, and L. Wirtz. Raman imaging of graphene. *Solid State Communications*, 143(1-2):44, 2007.

[186] V-M Liu, C-W Huang, B-J Lin, H-Y Lin, C-H Huang, F-Y Shih, W-H Wang, C-Y Liu, and H-C Chui. Probing substrate influence on graphene by fitting Raman signals with Voigt profile. In *Technical Digest of the Eighteenth Microoptics Conference*, page 1. IEEE, 2013.

[187] S. Berciaud, S. Ryu, L. E. Brus, and T. F. Heinz. Probing the intrinsic properties of exfoliated graphene: Raman spectroscopy of free-standing monolayers. *Nano Letters*, 9(1):346, 2008.

[188] R. Wang, S. Wang, D. Zhang, Z. Li, Y. Fang, and X. Qiu. Control of carrier type and density in exfoliated graphene by interface engineering. *ACS Nano*, 5(1):408, 2010.

[189] C. Casiraghi, S. Pisana, K. S. Novoselov, A. K. Geim, and A. C. Ferrari. Raman fingerprint of charged impurities in graphene. *Applied Physics Letters*, 91(23):233108, 2007.

[190] D. Yoon, Y-W Son, and H. Cheong. Strain-dependent splitting of the double-resonance Raman scattering band in graphene. *Physical Review Letters*, 106(15):155502, 2011.

[191] I. Delfino, G. Perna, M. Lasalvia, V. Capozzi, L. Manti, C. Camerlingo, and M. Lepore. Visible micro-Raman spectroscopy of single human mammary epithelial cells exposed to X-ray radiation. *Journal of Biomedical Optics*, 20(3):035003, 2015.

[192] A. Ghita, P. Matousek, and N. Stone. Sensitivity of transmission Raman spectroscopy signals to temperature of biological tissues. *Scientific Reports*, 8(1):8379, 2018.

[193] H. M. Sapers, J. Razzell Hollis, R. Bhartia, L. W. Beegle, V. J. Orphan, and J. P. Amend. The cell and the sum of its parts: Patterns of complexity

in biosignatures as revealed by deep UV Raman spectroscopy. *Frontiers in Microbiology*, 10:679, 2019.

[194] H. J. Butler, L. Ashton, B. Bird, G. Cinque, K. Curtis, J. Dorney, K. Esmonde-White, N. J. Fullwood, B. Gardner, P. L. Martin-Hirsch, et al. Using Raman spectroscopy to characterize biological materials. *Nature Protocols*, 11(4):664, 2016.

[195] K. Hamasha, Q. I. Mohaidat, R. A. Putnam, R. C. Woodman, S. Palchaudhuri, and S. J. Rehse. Sensitive and specific discrimination of pathogenic and nonpathogenic *Escherichia coli* using Raman spectroscopy a comparison of two multivariate analysis techniques. *Biomedical Optics Express*, 4(4):481, 2013.

[196] X. Li, C. W. Magnuson, A. Venugopal, J. An, J. W. Suk, B. Han, M. Borysiak, W. Cai, A. Velamakanni, Y. Zhu, et al. Graphene films with large domain size by a two-step chemical vapor deposition process. *Nano Letters*, 10(11):4328, 2010.

[197] S-M Lee, J-H Kim, and J-H Ahn. Graphene as a flexible electronic material: Mechanical limitations by defect formation and efforts to overcome. *Materials Today*, 18(6):336, 2015.

[198] M. Lobet, N. Reckinger, L. Henrard, and P. Lambin. Robust electromagnetic absorption by graphene/polymer heterostructures. *Nanotechnology*, 26(28):285702, 2015.

[199] Q. Wang, X. Zhai, M. Crowe, L. Gou, Y. Li, D. Li, L. Zhang, J. Diao, and B. Ji. Heterogeneous oxidization of graphene nanosheets damages membrane. *Science China Physics, Mechanics & Astronomy*, 62(6):64611, 2019.

[200] S. Reich and C. Thomsen. Raman spectroscopy of graphite. *Philosophical Transactions of the Royal Society of London. Series A: Mathematical, Physical and Engineering Sciences*, 362(1824):2271, 2004.

[201] R. Saito, A. Jorio, A. G. Souza Filho, G. Dresselhaus, M. S. Dresselhaus, and M. A. Pimenta. Probing phonon dispersion relations of graphite by double resonance Raman scattering. *Physical Review Letters*, 88(2):027401, 2001.

[202] Y. Lan, M. Zondode, H. Deng, J-A Yan, M. Ndaw, A. Lisfi, C. Wang, and Y-L Pan. Basic concepts and recent advances of crystallographic orientation determination of graphene by Raman spectroscopy. *Crystals*, 8(10):375, 2018.

[203] M. S. Dresselhaus and G. Dresselhaus. Light scattering in graphite intercalation compounds. In *Light Scattering in Solids III*, page 3. Springer, 1982.

[204] A. C. Ferrari and D. M. Basko. Raman spectroscopy as a versatile tool for studying the properties of graphene. *Nature Nanotechnology*, 8(4):235, 2013.

[205] V. Zólyomi, J. Koltai, and J. Kürti. Resonance Raman spectroscopy of graphite and graphene. *Physica Status Solidi (B)*, 248(11):2435, 2011.

[206] F. Tuinstra and J. L. Koenig. Raman spectrum of graphite. *The Journal of Chemical Physics*, 53(3):1126, 1970.

[207] T. M. G. Mohiuddin, A. Lombardo, R. R. Nair, A. Bonetti, G. Savini, R. Jalil, N. Bonini, D. M. Basko, C. Galiotis, N. Marzari, et al. Uniaxial strain in graphene by Raman spectroscopy: G peak splitting, Grüneisen parameters, and sample orientation. *Physical Review B*, 79(20):205433, 2009.

[208] P. Venezuela, M. Lazzeri, and F. Mauri. Theory of double-resonant Raman spectra in graphene: Intensity and line shape of defect-induced and two-phonon bands. *Physical Review B*, 84(3):035433, 2011.

[209] A. C. Ferrari and J. Robertson. Interpretation of Raman spectra of disordered and amorphous carbon. *Physical Review B*, 61(20):14095, 2000.

[210] N. S. Mueller, S. Heeg, M. P. Alvarez, P. Kusch, S. Wasserroth, N. Clark, F. Schedin, J. Parthenios, K. Papagelis, C. Galiotis, et al. Evaluating arbitrary strain configurations and doping in graphene with Raman spectroscopy. *2D Materials*, 5(1):015016, 2017.

[211] J. Zabel, R. R. Nair, A. Ott, T. Georgiou, A. K. Geim, K. S. Novoselov, and C. Casiraghi. Raman spectroscopy of graphene and bilayer under biaxial strain: bubbles and balloons. *Nano Letters*, 12(2):617, 2012.

[212] L. Chong, H. Guo, Y. Zhang, Y. Hu, and Y. Zhang. Raman study of strain relaxation from grain boundaries in epitaxial graphene grown by chemical vapor deposition on SiC. *Nanomaterials*, 9(3):372, 2019.

[213] Z. H. Ni, T. Yu, Y. H. Lu, Y. P. Wang, Y. Y.and Feng, and Z. X. Shen. Uniaxial strain on graphene: Raman spectroscopy study and band-gap opening. *ACS Nano*, 2(11):2301, 2008.

[214] R. Li, Z. Li, E. Pambou, P. Gutfreund, T. A. Waigh, J. R. P. Webster, and J. R. Lu. Determination of PMMA Residues on a Chemical-Vapor-Deposited monolayer of graphene by neutron reflection and atomic force microscopy. *Langmuir*, 34(5):1827, 2018.

[215] M. Xia, Z. Su, and S. Zhang. Raman spectra of bilayer graphene covered with Poly (methyl methacrylate) thin film. *AIP Advances*, 2(3):032122, 2012.

[216] E. Koo and S-Y Ju. Role of residual polymer on chemical vapor grown graphene by Raman spectroscopy. *Carbon*, 86:318, 2015.

[217] Y. Ahn, J. Kim, S. Ganorkar, Y-H Kim, and S-I Kim. Thermal annealing of graphene to remove polymer residues. *Materials Express*, 6(1):69, 2016.

[218] P. V. Pham. Cleaning of graphene surfaces by low-pressure air plasma. *Royal Society Open Science*, 5(5):172395, 2018.

[219] A. Suhail, K. Islam, B. Li, D. Jenkins, and G. Pan. Reduction of polymer residue on wet–transferred CVD graphene surface by deep UV exposure. *Applied Physics Letters*, 110(18):183103, 2017.

[220] A. C. Ferrari. Raman spectroscopy of graphene and graphite: Disorder, electron–phonon coupling, doping and nonadiabatic effects. *Solid State Communications*, 143(1-2):47, 2007.

[221] F. Bonaccorso, A. Lombardo, T. Hasan, Z. Sun, L. Colombo, and A. C. Ferrari. Production and processing of graphene and 2D crystals. *Materials Today*, 15(12):564, 2012.

[222] C. Stampfer, F. Molitor, D. Graf, K. Ensslin, A. Jungen, C. Hierold, and L. Wirtz. Raman imaging of doping domains in graphene on $\mathrm{SiO_2}$. *Applied Physics Letters*, 91(24):241907, 2007.

[223] L. G. Cançado, A. Jorio, E. H. M. Ferreira, F. Stavale, C. A. Achete, R. B. Capaz, M. V. O. Moutinho, A. Lombardo, T. S. Kulmala, and A. C. Ferrari. Quantifying defects in graphene via Raman spectroscopy at different excitation energies. *Nano Letters*, 11(8):3190, 2011.

[224] F. A. Mas'ud, H. Cho, T. Lee, H. Rho, T. H. Seo, and M. J. Kim. Domain size engineering of CVD graphene and its influence on physical properties. *Journal of Physics D: Applied Physics*, 49(20):205504, 2016.

[225] P. Y. Huang, C. S. Ruiz-Vargas, A. M. Van Der Zande, W. S. Whitney, M. P. Levendorf, J. W. Kevek, S. Garg, J. S. Alden, C. J. Hustedt, Y. Zhu, et al. Grains and grain boundaries in single-layer graphene atomic patchwork quilts. *Nature*, 469(7330):389, 2011.

[226] V. T. H. Pham, V. K. Truong, M. D. J. Quinn, S. M. Notley, Y. Guo, V. A. Baulin, M. Al Kobaisi, R. J. Crawford, and E. P. Ivanova. Graphene induces formation of pores that kill spherical and rod-shaped bacteria. *ACS Nano*, 9(8):8458, 2015.

[227] Z. Ni, Y. Wang, T. Yu, and Z. Shen. Raman spectroscopy and imaging of graphene. *Nano Research*, 1(4):273, 2008.

[228] A. C. Ferrari, J. C. Meyer, V. Scardaci, C. Casiraghi, M. Lazzeri, F. Mauri, S. Piscanec, D. Jiang, K. S. Novoselov, S. Roth, et al. The Raman fingerprint of graphene. *arXiv preprint cond-mat/0606284*, 2006.

[229] Y. Y. Wang, Z. H. Ni, T. Yu, Z. X. Shen, H. M. Wang, Y. H. Wu, W. Chen,

and A. T. Shen Wee. Raman studies of monolayer graphene: the substrate effect. *The Journal of Physical Chemistry C*, 112(29):10637, 2008.

[230] A. Das, S. Pisana, B. Chakraborty, S. Piscanec, S. K. Saha, U. V. Waghmare, K. S. Novoselov, H. R. Krishnamurthy, A. K. Geim, A. C. Ferrari, et al. Monitoring dopants by Raman scattering in an electrochemically top-gated graphene transistor. *Nature Nanotechnology*, 3(4):210, 2008.

[231] M. M. Lucchese, F. Stavale, E. H. M. Ferreira, C. Vilani, M. V. O. Moutinho, R. B. Capaz, C. A. Achete, and A. Jorio. Quantifying ion-induced defects and Raman relaxation length in graphene. *Carbon*, 48(5):1592, 2010.

[232] M. Bayle, N. Reckinger, A. Felten, P. Landois, O. Lancry, B. Dutertre, J-F Colomer, A-A Zahab, L. Henrard, J-L Sauvajol, et al. Determining the number of layers in few-layer graphene by combining Raman spectroscopy and optical contrast. *Journal of Raman Spectroscopy*, 49(1):36, 2018.

[233] Y-S No, H. K. Choi, J-S Kim, H. Kim, Y-J Yu, C-G Choi, and J. S. Choi. Layer number identification of CVD-grown multilayer graphene using Si peak analysis. *Scientific Reports*, 8(1):571, 2018.

[234] S. Pisana, M. Lazzeri, C. Casiraghi, K. S. Novoselov, A. K. Geim, A. C. Ferrari, and F. Mauri. Breakdown of the adiabatic Born–Oppenheimer approximation in graphene. *Nature Materials*, 6(3):198, 2007.

[235] H. Li, L. Daukiya, S. Haldar, A. Lindblad, B. Sanyal, O. Eriksson, D. Aubel, S. Hajjar-Garreau, L. Simon, and K. Leifer. Site-selective local fluorination of graphene induced by focused ion beam irradiation. *Scientific Reports*, 6:19719, 2016.

[236] J. Conroy, N. K. Verma, R. J. Smith, E. Rezvani, G. S. Duesberg, J. N. Coleman, and Y. Volkov. Biocompatibility of pristine graphene monolayers, nanosheets and thin films. *arXiv preprint arXiv:1406.2497*, 2014.

[237] K. S. Park, S. Kim, H. Kim, D. Kwon, Y-E K. Lee, S-W Min, S. Im, H. J. Choi, S. Lim, H. Shin, et al. Wafer-scale single-domain-like graphene by defect-

selective atomic layer deposition of hexagonal ZnO. *Nanoscale*, 7(42):17702, 2015.

[238] W. Liu, H. Li, C. Xu, Y. Khatami, and K. Banerjee. Synthesis of high-quality monolayer and bilayer graphene on copper using chemical vapor deposition. *Carbon*, 49(13):4122, 2011.

[239] X. Chen, L. Zhang, and S. Chen. Large area CVD growth of graphene. *Synthetic Metals*, 210:95, 2015.

[240] M. S. Dresselhaus, A. Jorio, A. G. Souza Filho, and R. Saito. Defect characterization in graphene and carbon nanotubes using Raman spectroscopy. *Philosophical Transactions of the Royal Society A: Mathematical, Physical and Engineering Sciences*, 368(1932):5355, 2010.

[241] B. Huet and J-P Raskin. Role of the Cu substrate in the growth of ultra-flat crack-free highly-crystalline single-layer graphene. *Nanoscale*, 10(46):21898, 2018.

[242] S. Sil, R. Mukherjee, N. S. Kumar, S. Aravind, J. Kingston, and U. K. Singh. Detection and classification of bacteria using Raman spectroscopy combined with multivariate analysis. *Defence Life Science Journal*, 2(4):435, 2017.

[243] E. Kastanos, A. Kyriakides, K. Hadjigeorgiou, and C. Pitris. A novel method for bacterial UTI diagnosis using Raman spectroscopy. *International Journal of Spectroscopy*, 2012.

[244] A. Assaf, C. B. Y. Cordella, and G. Thouand. Raman spectroscopy applied to the horizontal methods ISO 6579: 2002 to identify *Salmonella spp.* in the food industry. *Analytical and Bioanalytical Chemistry*, 406(20):4899, 2014.

[245] L. T. Kerr, H. J. Byrne, and B. M. Hennelly. Optimal choice of sample substrate and laser wavelength for Raman spectroscopic analysis of biological specimen. *Analytical Methods*, 7(12):5041, 2015.

[246] I. W. Schie and J. W. Chan. Estimation of spectra sample size for characterizing single cells using micro-Raman spectroscopy. *Journal of Raman Spectroscopy*, 47(4):384, 2016.

[247] S. Efrima and B. V. Bronk. Silver colloids impregnating or coating bacteria. *Journal of Physical Chemistry B*, 102(31):5947, 1998.

[248] H-U Gremlich and B. Yan. Infrared and Raman spectroscopy of biological materials. 2000.

[249] D. W. Shipp, F. Sinjab, and I. Notingher. Raman spectroscopy: techniques and applications in the life sciences. *Advances in Optics and Photonics*, 9(2):315, 2017.

[250] N. Kuhar, S. Sil, T. Verma, and S. Umapathy. Challenges in application of Raman spectroscopy to biology and materials. *RSC Advances*, 8(46):25888, 2018.

[251] P. Labhsetwar, J. A. Cole, E. Roberts, N. D. Price, and Z. A. Luthey-Schulten. Heterogeneity in protein expression induces metabolic variability in a modeled *Escherichia coli* population. *Proceedings of the National Academy of Sciences*, 110(34):14006, 2013.

[252] T. K. Wood, S. J. Knabel, and B. W. Kwan. Bacterial persister cell formation and dormancy. *Applied and Environmental Microbiology*, 79(23):7116, 2013.

[253] R. Manoharan, E. Ghiamati, S. Chadha, W. H. Nelson, and J. F. Sperry. Effect of cultural conditions on deep UV resonance Raman spectra of bacteria. *Applied Spectroscopy*, 47(12):2145, 1993.

[254] L. L. Kostiw, C. W. Boylen, and B. J. Tyson. Lipid composition of growing and starving cells of *Arthrobacter crystallopoietes*. *Journal of Bacteriology*, 111(1):103, 1972.

[255] V. W. Rowlett, V. K. P. S. Mallampalli, A. Karlstaedt, W. Dowhan, H. Taegtmeyer, W. Margolin, and H. Vitrac. Impact of membrane phospholipid alter-

ations in *Escherichia coli* on cellular function and bacterial stress adaptation. *Journal of Bacteriology*, 199(13):e00849–16, 2017.

[256] K. Tompa, M. Bokor, T. Verebélyi, and P. Tompa. Water rotation barriers on protein molecular surfaces. *Chemical Physics*, 448:15, 2015.

[257] C. García-Timermans, P. Rubbens, J. Heyse, R. Props, F-M Kerckhof, A. Skirtach, W. Waegeman, and N. Boon. Characterizing phenotypic heterogeneity in isogenic bacterial populations using flow cytometry and Raman spectroscopy. *bioRxiv*, page 545681, 2019.

[258] S. J. Webb. Mutation of bacterial cells by controlled desiccation. *Nature*, 213(5081):1137, 1967.

[259] M. Potts. Desiccation tolerance of prokaryotes. *Microbiology and Molecular Biology Reviews*, 58(4):755, 1994.

[260] V. Ragoonanan and A. Aksan. Heterogeneity in desiccated solutions: implications for biostabilization. *Biophysical Journal*, 94(6):2212, 2008.

[261] T. Nyström. Role of oxidative carbonylation in protein quality control and senescence. *The EMBO Journal*, 24(7):1311, 2005.

[262] H. Cho, T. Uehara, and T. G. Bernhardt. Beta-lactam antibiotics induce a lethal malfunctioning of the bacterial cell wall synthesis machinery. *Cell*, 159(6):1300, 2014.

[263] L. Hui, J. Huang, G. Chen, Y. Zhu, and L. Yang. Antibacterial property of graphene quantum dots (both source material and bacterial shape matter). *ACS Applied Materials & Interfaces*, 8(1):20, 2015.

[264] F. Perreault, A. F. De Faria, S. Nejati, and M. Elimelech. Antimicrobial properties of graphene oxide nanosheets: Why size matters. *ACS Nano*, 9(7):7226, 2015.

[265] E. Tegou, M. Magana, A. E. Katsogridaki, A. Ioannidis, V. Raptis, S. Jordan, S. Chatzipanagiotou, S. Chatzandroulis, C. Ornelas, and G. P. Tegos. Terms

of endearment: Bacteria meet graphene nanosurfaces. *Biomaterials*, 89:38, 2016.

[266] W. Hu, C. Peng, W. Luo, M. Lv, X. Li, D. Li, Q. Huang, and C. Fan. Graphene-based antibacterial paper. *ACS Nano*, 4(7):4317, 2010.

[267] K. Maquelin, C. Kirschner, L-P Choo-Smith, N. van den Braak, H. P. Endtz, D. Naumann, and G. J. Puppels. Identification of medically relevant microorganisms by vibrational spectroscopy. *Journal of Microbiological Methods*, 51(3):255, 2002.

[268] K. Czamara, K. Majzner, M. Z. Pacia, K. Kochan, A. Kaczor, and M. Baranska. Raman spectroscopy of lipids: A review. *Journal of Raman Spectroscopy*, 46(1):4, 2015.

[269] C. O. Gill and J. R. Suisted. The effects of temperature and growth rate on the proportion of unsaturated fatty acids in bacterial lipids. *Microbiology*, 104(1):31, 1978.

[270] T. A. Azam, A. Iwata, A. Nishimura, S. Ueda, and A. Ishihama. Growth phase-dependent variation in protein composition of the *Escherichia coli* nucleoid. *Journal of Bacteriology*, 181(20):6361, 1999.

[271] J. Gidden, J. Denson, R. Liyanage, D. M. Ivey, and Jackson O. Lay J. Lipid compositions in *Escherichia coli* and *Bacillus subtilis* during growth as determined by MALDI-TOF and TOF/TOF mass spectrometry. *International Journal of Mass Spectrometry*, 283(1-3):178, 2009.

[272] I. Notingher, S. Verrier, H. Romanska, A. E. Bishop, J. M. Polak, and L. L. Hench. In situ characterisation of living cells by Raman spectroscopy. *Journal of Spectroscopy*, 16(2):43, 2002.

[273] Z. D. Schultz and I. W. Levin. Vibrational spectroscopy of biomembranes. *Annual Review of Analytical Chemistry*, 4:343, 2011.

[274] J. T. Park and J. L. Strominger. Mode of action of penicillin. Biochemical basis for the mechanism of action of penicillin and for its selective toxicity. *Science*, 125(3238):99, 1957.

[275] A. Tomasz and S. Waks. Mechanism of action of penicillin: Triggering of the pneumococcal autolytic enzyme by inhibitors of cell wall synthesis. *Proceedings of the National Academy of Sciences*, 72(10):4162, 1975.

[276] R. B. Ghooi and S. M. Thatte. Inhibition of cell wall synthesis— Is this the mechanism of action of penicillins? *Medical Hypotheses*, 44(2):127, 1995.

[277] A. Sugimoto, A. Maeda, K. Itto, and H. Arimoto. Deciphering the mode of action of cell wall-inhibiting antibiotics using metabolic labeling of growing peptidoglycan in *Streptococcus pyogenes*. *Scientific Reports*, 7(1):1–12, 2017.

[278] N. Vajpai, L. Nisius, M. Wiktor, and S. Grzesiek. High-pressure NMR reveals close similarity between cold and alcohol protein denaturation in ubiquitin. *Proceedings of the National Academy of Sciences*, 110(5):E368–E376, 2013.

[279] I. K. Ventouri, D. B. A. Malheiro, R. L. C. Voeten, S. Kok, M. Honing, G. W. Somsen, and R. Haselberg. Probing protein denaturation during size-exclusion chromatography using native mass spectrometry. *Analytical Chemistry*, 92(6):4292–4300, 2020.

[280] E. C. López-Díez, C. L. Winder, L. Ashton, F. Currie, and R. Goodacre. Monitoring the mode of action of antibiotics using Raman spectroscopy: Investigating subinhibitory effects of amikacin on *Pseudomonas aeruginosa*. *Analytical Chemistry*, 77(9):2901, 2005.

[281] T. Basu and R. K. Poddar. Effect of ethanol on *Escherichia coli* cells. Enhancement of DNA synthesis due to ethanol treatment. *Folia Microbiologica*, 39(1):3, 1994.

[282] A. Colniță, N. Dina, N. Leopold, D. Vodnar, D. Bogdan, S. Porav, and L. David. Characterization and discrimination of Gram-positive bacteria using

Raman spectroscopy with the aid of principal component analysis. *Nanomaterials*, 7(9):248, 2017.

[283] M. Myintzu Hlaing, B. Wood, D. McNaughton, D. Ying, and M. A. Augustin. Raman spectroscopic analysis of *Lactobacillus rhamnosus* GG in response to dehydration reveals DNA conformation changes. *Journal of Biophotonics*, 10(4):589, 2017.

[284] N. Kaji, M. Ueda, and Y. Baba. Direct measurement of conformational changes on DNA molecule intercalating with a fluorescence dye in an electrophoretic buffer solution by means of atomic force microscopy. *Electrophoresis*, 22(16):3357–3364, 2001.

[285] C. Possoz, J. Newmark, N. Sorto, D. J. Sherratt, and M. E. Tolmasky. Sublethal concentrations of the aminoglycoside amikacin interfere with cell division without affecting chromosome dynamics. *Antimicrobial Agents and Chemotherapy*, 51(1):252, 2007.

[286] P. R. Carey, G. R. Whitmer, M. J. Yoon, M. N. Lombardo, M. Pusztai-Carey, H. Heidari-Torkabadi, and T. Che. Measuring drug-induced changes in metabolite populations of live bacteria: Real time analysis by Raman spectroscopy. *The Journal of Physical Chemistry B*, 122(24):6377, 2018.

[287] D. Fourmy, M. I. Recht, S. C. Blanchard, and J. D. Puglisi. Structure of the A site of *Escherichia coli* 16S ribosomal RNA complexed with an aminoglycoside antibiotic. *Science*, 274(5291):1367, 1996.

[288] J. Poehlsgaard and S. Douthwaite. The bacterial ribosome as a target for antibiotics. *Nature Reviews Microbiology*, 3(11):870, 2005.

[289] N. T. X. Nguyen, S. Sarter, N. H. Nguyen, and P. Daniel. Detection of molecular changes induced by antibiotics in *Escherichia coli* using vibrational spectroscopy. *Spectrochimica Acta Part A: Molecular and Biomolecular Spectroscopy*, 183:395, 2017.

[290] M. F. Siliakus, J. van der Oost, and S. W. M. Kengen. Adaptations of archaeal and bacterial membranes to variations in temperature, pH and pressure. *Extremophiles*, 21(4):651, 2017.

[291] L. A. Royce, P. Liu, M. J. Stebbins, B. C. Hanson, and L. R. Jarboe. The damaging effects of short chain fatty acids on *Escherichia coli* membranes. *Applied Microbiology and Biotechnology*, 97(18):8317, 2013.

[292] H. Zhang, H. L. Dolan, Q. Ding, S. Wang, and R. V. Tikekar. Antimicrobial action of octanoic acid against *Escherichia coli* O157: H7 during washing of baby spinach and grape tomatoes. *Food Research International*, page 108523, 2019.

[293] M. Wenzel, N. O. E. Vischer, H. Strahl, and L. W. Hamoen. Assessing membrane fluidity and visualizing fluid membrane domains in bacteria using fluorescent membrane dyes. *Bio-protocol*, 8(20):e3063–e3063, 2018.

[294] K. Gardikis, S. Hatziantoniou, K. Viras, M. Wagner, and C. Demetzos. A DSC and Raman spectroscopy study on the effect of PAMAM dendrimer on DPPC model lipid membranes. *International Journal of Pharmaceutics*, 318(1-2):118, 2006.

[295] H. L. Ennis. Inhibition of protein synthesis by polypeptide antibiotics I. Inhibition in intact bacteria. *Journal of Bacteriology*, 90(4):1102, 1965.